

# Monday Morning, October 29, 2012

## Spectroscopic Ellipsometry Focus Topic

Room: 19 - Session EL+TF+AS+EM+SS+PS+EN+NM-MoM

## Spectroscopic Ellipsometry for Photovoltaics and Semiconductor Manufacturing

**Moderator:** M. Creatore, Eindhoven University of Technology, the Netherlands, H. Wormeester, MESA+ Institute for Nanotechnology, University of Twente, Enschede, The Netherlands

8:20am **EL+TF+AS+EM+SS+PS+EN+NM-MoM1 Multichannel Spectroscopic Ellipsometry: Applications in I-III-V<sub>2</sub> Thin Film Photovoltaics**, *R.W. Collins, D. Attygalle, P. Aryal, P. Pradhan, N.J. Podraza*, University of Toledo, *V. Ranjan, S. Marsillac*, Old Dominion University **INVITED**

Multichannel spectroscopic ellipsometry (SE) has been applied successfully as an in situ, real time tool for optimizing, monitoring, and controlling multi-stage deposition processes in various thin film photovoltaics (PV) technologies. A particularly challenging process optimization problem involves the thermal co-evaporation of individual elements of Cu, In, Ga, and Se in a three-stage process, which has proven to produce high quality Cu(In<sub>1-x</sub>Ga<sub>x</sub>)Se<sub>2</sub> (CIGS) materials and high performance PV devices. This three-stage process provides a high level of flexibility in determining the phase, composition, and microstructure of the film, but also generates greater challenges in run-to-run reproducibility of the optimized process. Information extracted from real time SE measurements includes the evolution of the bulk layer and one or more surface layer thicknesses, as well as layer dielectric functions. The layer dielectric functions can be analyzed further to extract the phase and alloy compositions and the defect density or grain size, which can assist in understanding the fabrication process, in optimizing solar cells, and ultimately in monitoring and controlling the optimized process for improved reproducibility. In this study, the focus is on analysis of ellipsometric ( $\psi$ ,  $\Delta$ ) spectra acquired by real time SE in order to characterize (i) the structural and compositional evolution in (In,Ga)<sub>2</sub>Se<sub>3</sub> film growth from In, Ga, and Se fluxes in the first stage, (ii) the transition from Cu-poor to Cu-rich CIGS at the end of the second stage, which occurs under Cu and Se fluxes, and (iii) the transition from Cu-rich to the desired Cu-poor CIGS, which defines the end of the third and final stage, and occurs under a second application of In, Ga, and Se fluxes. After the transition from Cu-poor to Cu-rich material in the second stage, a Cu<sub>2-x</sub>Se phase near the surface of the bulk layer is tracked. In the Cu-rich to Cu-poor transition, this Cu<sub>2-x</sub>Se phase has fully reacted with In, Ga, and Se to form CIGS. Studies using a standard Mo substrate and 2  $\mu$ m thick CIGS for solar cells have also revealed features in the ( $\psi$ ,  $\Delta$ ) spectra characteristic of the anticipated changes in the near surface phase composition as established by detailed modeling on thinner and smoother films. Although careful analysis of real time SE is expected to provide quantitative information on the surface properties and their evolution in this case of solar cells, control of the deposition has been successful simply by monitoring real time changes in the ellipsometric ( $\psi$ , $\Delta$ ) spectra.

9:00am **EL+TF+AS+EM+SS+PS+EN+NM-MoM3 Contribution of Plasma Generated Nanoparticles to the Growth of Microcrystalline Silicon Deposited from SiF<sub>4</sub>/H<sub>2</sub>/Argon Gas Mixtures**, *J.-C. Dornstetter, S. Kasouit, J.-F. Besnier*, Total S.a, France, *P. Roca i Cabarrocas*, LPICM-CNRS, Ecole Polytechnique, France

Despite the low fabrication cost of thin film silicon solar modules, this type of technology remains non competitive in main stream markets because of the high BOS costs, due to the low energy conversion efficiency of this type of modules (~10%). We have recently shown that microcrystalline silicon films deposited using SiF<sub>4</sub>/H<sub>2</sub>/Argon RF capacitive plasmas have excellent structural and transport properties, compared to films deposited using conventional SiH<sub>4</sub>/H<sub>2</sub> mixtures, allowing for a very good carrier collection, even for thick cells, and Voc values of 0.55 V, without device optimization, thus opening up the path for the realization of high performance solar cells. However, little is known so far about the growth mechanism of this type of materials and the reason for such interesting properties. Studies of silicon thin films deposition from SiF<sub>4</sub>/H<sub>2</sub> mixes, under conditions different from ours, suggested that the growth is due to the deposition of SiF<sub>2</sub> radicals, followed by the abstraction of fluorine by hydrogen. Previous work within our group has also shown that deposition occurs only when particles are present in the plasma, and that growth starts from crystallites without any amorphous phase. We present here a systematic study of the growth of

microcrystalline films, together with the composition of nanoparticles attracted by thermophoresis to cold traps located both on the walls of the plasma chamber and in the fore line as a function of deposition conditions. The composition of the deposit on the traps is found to be amorphous at low power/ low hydrogen conditions and becomes crystalline when either of them increases. This correlates well with an increase in atomic hydrogen concentration in the plasma, as estimated by actinometry. The crystalline fraction of the deposited film was measured using in-situ ellipsometry and was found to correlate with the composition of the deposit on the cold traps. Deposition rate is drastically reduced when a water cooled trap is installed on the walls of the plasma chamber, and switches off at high H<sub>2</sub> flow rates. Under these conditions, TEM and AFM images, show that at the initial stages of the growth the film is constituted of sparse, hexagonal crystalline particles, having sizes on the order of few tens of nanometers. We interpret the data above as a result of plasma-generated nanocrystals being a significant contribution to the deposited film. This may explain the excellent electronic properties of the films, as the particles are formed in the bulk of the plasma region, free from energetic ions bombardment. We will correlate the structural properties and the film growth mechanisms to the properties of solar cells.

9:20am **EL+TF+AS+EM+SS+PS+EN+NM-MoM4 Multichannel Spectroscopic Ellipsometry for CdTe Photovoltaics: from Materials and Interfaces to Full-Scale Modules**, *P. Koirala, J. Chen, X. Tan, N.J. Podraza*, The University of Toledo, *S. Marsillac*, Old Dominion University, *R.W. Collins*, The University of Toledo

Real time spectroscopic ellipsometry (RTSE) has been implemented in studies of the evolution of the semiconductor structural and optical properties during sputter deposition of thin film polycrystalline CdS/CdTe solar cells on transparent conducting oxide (TCO) coated glass substrates. Analysis of the real time optical spectra collected during CdS/CdTe deposition requires an optical property database as a function of measurement temperature for all substrate components. These include not only soda lime glass, but also an SiO<sub>2</sub> layer and three different SnO<sub>2</sub> layers. We report optical functions parameterized versus temperature for the glass substrate and its overlayers starting from room temperature and ending at elevated temperature above which the semiconductor layers are deposited. In fact, such a database has additional applications for on-line, through-the-glass monitoring applications of coated glass at elevated temperature. In the RTSE studies, knowledge of the temperature dependent optical functions of the substrate components enables an accurate substrate temperature determination before the onset of deposition and is critical for accurate extraction of the semiconductor layer optical properties. We implement RTSE to study the filling process of the surface roughness modulations on the top-most SnO<sub>2</sub> substrate layer and modification of the optical properties of this layer. This modification is further studied post-deposition by infrared spectroscopic ellipsometry. In addition to providing information on interface formation to the substrate during film growth, RTSE also provides information on the bulk layer CdS growth, its surface roughness evolution, as well as overlying CdTe interface formation and bulk layer growth. Information from RTSE at a single point during solar cell stack deposition assists in the development of a model that can be used for mapping the completed cell stack properties, which can then be correlated with device performance. Independent non-uniformities in the layers over the full area of the cell stack enable optimization of cell performance combinatorially.

9:40am **EL+TF+AS+EM+SS+PS+EN+NM-MoM5 Determination of Electronic Band Gaps from Optical Spectra**, *R.A. Synowicki*, J.A. Woollam Co., Inc.

The band gap of a material  $E_g$  is defined theoretically as the lowest energy for electronic transition from the valence to conduction bands in a solid. For an ideal material free of defects this is the photon energy or wavelength where the optical properties change from transparent to absorbing. However, real materials contain defects which cause absorption to begin below the band gap (i.e. the Urbach Tail) making determination of the true band gap position difficult. For example, in a solar cell the measured absorption edge represents the onset of transitions first due to defects, then from band to band. Empirical methods used to determine the band gap in real materials with defects include the Tauc plot and the Mott-Davis plot. More theoretical mathematical dispersion models such as the Tauc-Lorentz, Cody-Lorentz, and Herzinger-Johs models have been developed which include an adjustable band gap parameter. The various plots and dispersion model methods will be discussed and applied to different materials measured optically via spectroscopic ellipsometry, intensity transmission, reflection, absorption, or a combination of these methods.

10:00am **EL+TF+AS+EM+SS+PS+EN+NM-MoM6 Optical Modeling of Plasma-Deposited ZnO: Extended Drude and its Physical Interpretation**, *H.C.M. Knoops, M.V. Ponomarev, J.W. Weber, N. Leick, B.W.H. van de Loo, Y.G. Melese, W.M.M. Kessels, M. Creatore*, Eindhoven University of Technology, the Netherlands

High-quality transparent conductive oxides such as ZnO are important due to their electrical and optical properties. To improve these properties the responsible physical processes have to be understood. Traditionally, charge-carrier-scattering processes are investigated by combining morphology data and Hall measurements. This contribution discusses the extensive optical modeling of plasma-deposited ZnO and how its interpretation directly provides insight into the relevant charge-carrier-scattering processes at different length scales. The interpretation is generalized to the concept of frequency-dependent resistivity, which is used to explain the applicability of different Drude models.

Thin films (50-1000 nm) of Al-doped and undoped ZnO were deposited using an expanding thermal plasma MOCVD process.<sup>1</sup> Conditions of high pressure and high diethyl zinc flow allowed for dense films with low electrical resistivities (e.g.,  $4 \times 10^{-4} \Omega \text{ cm}$  at 300 nm). The films were analyzed with variable-angle spectroscopic ellipsometry (SE) (0.75 – 5.0 eV), FTIR reflection spectroscopy (0.04 – 0.86 eV), Four-point-probe (FPP), and Hall measurements.

The SE and FTIR data were combined and fitted with classical and extended Drude<sup>2</sup> models. The high intensity of the Drude in the FTIR range resulted in a high sensitivity with which the carrier concentration and mobility could even be determined for thin (~40 nm) undoped ZnO films. An extended Drude model was needed to correctly model the SE energy range, which was explained by the dominance of ionized impurity scattering and a reduction of this scattering for higher photon energies. The grain-boundary-scattering mobility could be determined by the difference between optical and Hall mobilities.<sup>3</sup> When combined with FPP results, the effective mobility can be determined from these optical techniques without the use of Hall measurements. The optical response above the band gap was modeled by a PSEMI or Tauc-Lorentz oscillator model, where a broadening and shift of the transition was seen for increasing carrier concentration.<sup>4</sup>

These insights and a generalized view of electron scattering in ZnO at different length scales will be presented.

1. Ponomarev et al., *J. Appl. Phys.* **Submitted** (2012)
2. Ehrmann and Reineke-Koch, *Thin Solid Films* **519**, 1475 (2010)
3. Steinhäuser et al., *Appl. Phys. Lett.* **90**, 142107 (2007)
4. Fujiwara and Kondo, *Phys. Rev. B* **71**, 075109 (2005)

10:40am **EL+TF+AS+EM+SS+PS+EN+NM-MoM8 The Ellipsometric Response of Single-Crystal Silicon to Doping**, *H.G. Tompkins*, Consultant

The current wisdom is that for ellipsometry in the UV-vis-NIR spectral range, doping of single-crystal silicon can be ignored. We study the ellipsometric response of silicon doped with arsenic at various levels. We also studied the response after implant (before activation) and after the activation (anneal). We find that for samples implanted with  $1 \times 10^{18}$  atoms/cm<sup>3</sup>, the single-crystal silicon was not amorphized. Implants of  $2 \times 10^{19}$  atoms/cm<sup>3</sup> and higher left an amorphous layer on the surface of the wafer the thickness of which was about the depth of the implant. Activation of the sample implanted with  $2 \times 10^{19}$  atoms/cm<sup>3</sup> returned the sample to single-crystal silicon and the ellipsometric response in the UV-vis-near-IR is essentially that of undoped silicon. However, the response in the mid-IR is that the extinction coefficient is no longer zero. For samples implanted with  $2.5 \times 10^{20}$  atoms/cm<sup>3</sup> and greater, annealing did not return the UV-vis-near-IR ellipsometric response to that of single-crystal silicon. Although this amount of other material (arsenic) is still less than about one tenth of one percent, our conjecture is that the microstructure simply could not be returned to that of a single crystal. As with the lower doped sample, the mid-IR spectral region showed significant increase in the extinction coefficient.

11:00am **EL+TF+AS+EM+SS+PS+EN+NM-MoM9 The Effect of Stress on the Optical Properties Semiconductor Films**, *A.C. Diebold, G.R. Muthinti, M. Medikonda, T.N. Adam*, College of Nanoscale Science and Engineering, University at Albany, *A. Reznicek, B. Doris*, IBM Research at Albany Nanotech

Here we review the impact of stress on the complex dielectric function of semiconductor films measured using spectroscopic ellipsometry. Two relevant examples of stressed semiconductor layers are pseudomorphic epitaxial layers fabricated during semiconductor manufacturing and strained silicon on insulator (sSOI) wafers. Stress is known to shift the energies of direct gap critical point transitions in semiconductors. The biaxial stress in pseudomorphic films grown on silicon wafers can be as high as that used during opto-elastic studies of bulk semiconductors. The amount of stress in

un-relaxed, pseudomorphic films of  $\text{Si}_{1-x}\text{Ge}_x$  on Si (100) reaches 1 GPa for alloys with 20% Ge and is more than 3 GPa for films with > 50% Ge. The bi-axial stress in sSOI is typically ~1 GPa. An elastic theory approach for the effect of strain on the  $k^*p$  determined band structure and optical transition energy is well known. Both low shear stress and high shear stress approximations can apply to the shift in transition energy depending on the magnitude of the spin orbit splitting energy vs the magnitude of the shear stress. Until recently it was difficult to obtain sets of samples that test both approximations. Here we discuss results from our recent study of pseudomorphic films of  $\text{Si}_{1-x}\text{Ge}_x$  on Si (100) from  $x=0.05$  to 0.75 which covers both low and high shear regimes. We also present our recent study of the dielectric function of thinned sSOI which illustrates the impact of stress on the optical transitions for the Si layer on sSOI. All of these samples are examples of new materials being used in semiconductor research. The results of this study are directly transferred into cleanroom spectroscopic ellipsometry systems used for process control during manufacturing.

11:20am **EL+TF+AS+EM+SS+PS+EN+NM-MoM10 Numerical Ellipsometry: Spectroscopic n-k Plane Analysis of Thin Films Growing on Unknown Layered Substrates**, *F.K. Urban, D. Barton*, Florida International University

Spectroscopic ellipsometry measurements on thin films commonly make use of prior knowledge of the structure and optical properties of the underlying substrate. However, imprecision in substrate statistics propagates into the solution for the film of interest. Thus it is more accurate to have a method for solving for film properties which simultaneously obtains whatever is needed about the substrate. And it makes solutions possible whether or not book data or previous substrate solutions are available. In this work we apply Complex Analysis in the n-k plane to achieve solutions employing the well-know reflection equations. The method is carried out at each measured wavelength and does not necessitate an *a-priori* assumption of optical property dependencies on wavelength. The mean square error has been improved by many orders of magnitude, a selected limit of  $10^{-14}$  as opposed to 1 to 30 or so for least squares. Thus the full accuracy of the ellipsometer is now available for more accurate measurements of film thickness and optical properties. The method requires six measurements during growth. The first is used to determine the relationship between  $R_p$  and  $R_s$  at the film-substrate interface. The following four are used to uniquely determine the values of  $R_p$ ,  $R_s$ , and film  $n$ ,  $k$ , and  $d$ . The final measurement confirms the unique solution. Suitability of the model is tested by comparing measurements at two of more wavelengths for self consistency. Results for  $n$  and  $k$  of the growing film are examined across the measurement spectrum in comparison with parameterizations in common use.

## Electronic Materials and Processing

### Room: 9 - Session EM+TF+OX+GR-MoM

#### High-k Dielectrics for MOSFETs I

**Moderator:** A.C. Kummel, University of California San Diego

8:20am **EM+TF+OX+GR-MoM1 Surface Preparation and Dielectric Growth for Graphene-based Devices**, *R.M. Wallace*, University of Texas at Dallas **INVITED**

In addition to interesting physics, numerous device applications are under investigation for graphene. Many of these devices require an interaction of graphene with dielectrics, and require a thorough understanding of the graphene/dielectric interface. As practical device applications require large area graphene, CVD methods have been employed to synthesize graphene and typically involve a wet chemical transfer process, which can leave residues that impact device behavior. This talk will review recent progress in the investigation of CVD graphene growth, transfer and dielectric growth processes with an emphasis on in-situ studies of the surfaces produced by these processes and the resultant electrical behavior. This work is supported by the NRI SWAN Center.

9:00am **EM+TF+OX+GR-MoM3 Antimonide-Based P-Channel MOSFET: Progress and Challenges**, *S. Oktyabrsky, A. Greene, S. Madiseti, P. Nagaiah, M. Yakimov, R. Moore, S. Novak, H. Bakhru, V. Tokranov*, University at Albany-SUNY **INVITED**

Development of p-type MOSFETs using new materials is an important goal to provide a further scaling of CMOS circuits. Although Ge is still considered as a main candidate for novel p-channels due to its superior bulk transport properties, recent progress in strained III-Sb channels and MOS technologies makes it a good competitor in particular for deeply scaled devices. The materials parameters affecting MOSFET's figures-of-merit are

reviewed with the emphasis on strain in quantum wells (QWs), effective mass, density of states and mobility.

Progress in development of materials for III-Sb channels is reported. Optimization of MBE growth of metamorphic buffers and GaSb on lattice-mismatched GaAs substrates has resulted in "step-flow" growth mode of GaSb with monolayer-high steps on the surface,  $\sim 10^7 \text{ cm}^{-2}$  dislocation density and bulk hole mobility  $860 \text{ cm}^2/\text{Vs}$ . Optimization of strain in QWs provided the highest Hall mobility of  $1020 \text{ cm}^2/\text{Vs}$  at sheet hole density of  $1.3 \times 10^{12} \text{ cm}^{-2}$  obtained for  $\text{In}_{0.36}\text{Ga}_{0.64}\text{Sb}$  with compressive strain of 1.8%. Hole mobility in QW channel was benchmarked against the thickness of top semiconductor AlGaSb barrier. The effect of interface-related scattering hole mobility in the channel was found to be significantly less than e.g. for n-InGaAs, that might be due to stronger localization of holes in QWs.

Two approaches to fabricate high-quality III-Sb/high-k interface were studied: all *in-situ*  $\text{Al}_2\text{O}_3$  or  $\text{HfO}_2$  gate oxides, and *ex-situ* atomic layer deposited (ALD)  $\text{Al}_2\text{O}_3$  with InAs top semiconductor capping layer. Interface with *in-situ* MBE gate oxides was found to improve with *in-situ* deposited a-Si interface passivation layer (IPL). Interfaces with better thermal stability, reduced interface trap density and hysteresis were observed on both n- and p- type GaSb MOSCaps with the IPL. P-type MOSFETs with  $\text{HfO}_2$  showed a maximum drain current of 23 mA/mm for a  $3 \mu\text{m}$  gate length. Use of a-Si IPL has also resulted in a significant (over an order of magnitude) reduction of the hole density in QWs and corresponding negative flat band voltage shift and drop of mobility which becomes remote Coulomb scattering-limited. An interface with ALD  $\text{Al}_2\text{O}_3$  was improved by a thin 2nm interface layer of InAs which was treated with HCl or  $(\text{NH}_4)_2\text{S}$  immediately prior to ALD process. Optimized annealing further improved the C-V characteristics, reduced interface trap density down to  $10^{12} \text{ cm}^{-2}\text{eV}^{-1}$ , leakage current and MOSFET subthreshold slope down to 200 mV/dec. Increasing annealing temperature to and above  $450^\circ\text{C}$  drastically degraded C-V characteristics due to low thermal budget of antimonides.

9:40am **EM+TF+OX+GR-MoM5 Interface Study of the Atomic Layer Deposited  $\text{Al}_2\text{O}_3$  on  $\text{Al}_{0.25}\text{Ga}_{0.75}\text{N}$** , X. Qin, B. Brennan, H. Dong, R.M. Wallace, The University of Texas at Dallas

Due to the high two-dimensional electron gas (2-DEG) density, AlGaIn/GaN high electron mobility transistors (HEMTs) are recognized as key devices for high power and low noise applications. However, the associated large gate leakage current degrades the performance of AlGaIn HEMTs. In order to solve this problem, MOS-HEMTs have been developed, in which the incorporation of a high-k gate dielectric layer can overcome the drawbacks.

In this work, the native and treated  $\text{Al}_{0.25}\text{Ga}_{0.75}\text{N}$  surface chemical states and structure of were studied by x-ray photoelectron spectroscopy (XPS), ion scattering spectroscopy (ISS) and low energy electron diffraction. Different chemical treatment processes including  $(\text{NH}_4)\text{OH}$ ,  $(\text{NH}_4)_2\text{S}$  and HF were studied, followed by atomic layer deposition (ALD)  $\text{Al}_2\text{O}_3$  layers on  $\text{Al}_{0.25}\text{Ga}_{0.75}\text{N}$ . The oxidation states of the  $\text{Al}_{0.25}\text{Ga}_{0.75}\text{N}$  interface and  $\text{Al}_2\text{O}_3$  deposition process were studied by in-situ XPS analysis. In addition, ex-situ atomic force microscopy (AFM) was used to observe the surface topography before and after the  $\text{Al}_2\text{O}_3$  deposition. According to the XPS results, it is found that chemical treatments could remove the native  $\text{Al}_2\text{O}_3$  but were not effective to eliminate the Ga oxide, and the growth rate of  $\text{Al}_2\text{O}_3$  is low on the native and treated  $\text{Al}_{0.25}\text{Ga}_{0.75}\text{N}$  samples. The AFM images show that there are many pin holes in the surface of  $\text{Al}_{0.25}\text{Ga}_{0.75}\text{N}$ . Studies of  $\text{HfO}_2$  deposition will also be presented.

This work is supported by the AOARD under AFOSR Grant No. FA2386-11-1-4077

10:00am **EM+TF+OX+GR-MoM6 Ideal Monolayer Nitridation of Semiconductors using a Nitrogen Radical Generator**, A.T. Lucero, J. Kim, University of Texas at Dallas

Thin silicon nitride films have long been desirable for various applications. Suggested uses range from surface and interface passivation to ultra-thin dielectric layers. Traditional deposition techniques are low pressure chemical vapor deposition (LPCVD) and plasma enhanced chemical vapor deposition (PECVD). High quality LPCVD films require high processing temperatures, and PECVD exposes the substrate to damaging plasma and electric potentials. While both techniques are suitable for many applications, there are some instances where both processes are too harsh.

In this paper, we report the growth of silicon nitride using a remote nitrogen radical generator system. Growth temperatures range from room temperature to  $400^\circ\text{C}$ , and growth time is varied from two minutes to one hour. Film composition is analyzed using x-ray photoelectron spectroscopy (XPS) and morphology is checked using atomic force microscopy. Results indicate that surface nitrogen saturation can be reached at both low temperatures and short exposure times, and that the reaction is self limiting, terminating at one monolayer. Film thickness is approximately one

Angstrom, as determined by XPS. Results for silicon and III-V passivation will be discussed.

We would like to thank Toshiba Mitsubishi-Electric Industrial Systems Corporation for providing the nitridation system used in this study.

11:00am **EM+TF+OX+GR-MoM9 Characterization of ALD Laminated Gate Dielectrics on GaN MOSCAPs**, D. Wei, T. Hossain, Kansas State University, N. Nepal, N.Y. Garces, Naval Research Laboratory, H.M. Meyer III, Oak Ridge National Laboratory, C.R. Eddy, Jr., Naval Research Laboratory, J.H. Edgar, Kansas State University

To improve the efficiency of GaN based power electronic devices there is tremendous and growing interest in employing metal-insulator-semiconductor (MIS) transistors. As with all compound semiconductors, there is a significant challenge in forming an electronic quality dielectric-semiconductor interface. Thus, there is a need to better understand and improve the dielectric-semiconductor interface quality in order to improve the overall performance of the device.

This research focuses on the benefits and properties of  $\text{Al}_2\text{O}_3$ ,  $\text{TiO}_2$  and  $\text{TiO}_2\text{-Al}_2\text{O}_3$  nanolaminate thin films deposited on GaN and GaOx/GaN by plasma-assisted atomic layer deposition (PA-ALD) for gate dielectric development. Correlations were sought between the films' structure, composition, and electrical properties. The gate dielectrics were approximately 15nm thick as determined by spectroscopic ellipsometry. The interface carbon concentration, as measured by x-ray photoelectron spectroscopy (XPS) depth profile, was lower for  $\text{Al}_2\text{O}_3/\text{GaN}$  than  $\text{TiO}_2/\text{GaN}$ , and the nanolaminate structure did not decrease the carbon concentration. However, carbon was not detected at the interface for the GaN samples pretreated by annealing in  $\text{O}_2$  for 30 minutes at  $800^\circ\text{C}$ . Also, according to XPS, the  $\text{Al}_2\text{O}_3$  films had a better coverage than  $\text{TiO}_2$ . The RMS roughness of  $\text{TiO}_2$  and  $\text{Al}_2\text{O}_3$  top layers were  $\sim 0.53\text{nm}$  and  $\sim 0.20\text{nm}$  respectively, as determined by atomic force microscopy. The dielectric constant of  $\text{Al}_2\text{O}_3$  on GaOx/GaN was greatly increased compared to that of the  $\text{TiO}_2\text{-Al}_2\text{O}_3$  and pure  $\text{Al}_2\text{O}_3$  on GaN substrate. In addition, the  $\text{Al}_2\text{O}_3$  deposited on the GaOx/GaN showing no hysteresis in capacitance-voltage (C-V) characteristics, which is corresponding with a negligible carbon concentration from the XPS depth profile. These results indicate the promising potential of plasma ALD deposited  $\text{Al}_2\text{O}_3$  serving as the gate oxide on GaOx/GaN based MOS devices.

11:20am **EM+TF+OX+GR-MoM10 Passivation of Interfacial Defects in GaAs and Other III-Vs**, J. Robertson, Cambridge University, UK  
**INVITED**

It has always been harder to make FETs from GaAs than Si, because of 'Fermi level pinning' and the difficulty of passivating its surfaces. These issues were discussed by Spicer et al [1] in the 'unified defect model' and Hasegawa [2] is his 'Disorder Induced Gap states' model. Since 1997 it was possible to make inverted GaAs MOSFETs using the epitaxial Gadolinium gallium oxide [3]. The main impetus now is to use atomic layer deposition (ALD) to make scalable FETs [4], as recently achieved by Intel [5]. The obvious question is why (In)GaAs is much harder to passivate than Si. The early answer was its poor native oxide. But since the advent of good ALD  $\text{HfO}_2$  or  $\text{Al}_2\text{O}_3$  oxides on Si, this answer is deficient, as they should also work on GaAs [6]. The underlying reason for defects is not stress, it must be chemical. I show that it arises from the polar bonding of GaAs [7], and a driving force to keep the surface Fermi level in a gap. The electron counting rule of Pashley [8] that describes surface reconstructions is shown to be a variant of auto-compensation, and it works more generally [9]. It leads to a continuous generation of defects if it is not satisfied. So the answer is to deposit oxide layers that meet this rule, and also to break any surface reconstructions that may lead to As-As dimers [9]. Diffusion barriers are also crucial to a good passivant, on GaAs or on Ge.

1. W E Spicer, et al, J Vac Sci Technol 16 1422 (1979); Phys Rev Lett 44 420 (1980)
2. H Hasegawa, et al, J Vac Sci Technol B 5 1097 (1987)
3. M Hong et al, Science 283 1897 (1997)
4. P D Ye et al, App Phys Lett 83 180 (2003)
5. M Radosavljevic, et al, Tech Digest IEDM (2009) p13.1
6. C Hinkle, et al, Curr Opin Solid State Mat Sci 15 188 (2011)
7. W Harrison, J Vac Sci Technol 16 1492 (1979)
8. M D Pashley, Phys Rev B 40 10481 (1989)
9. J Robertson, L Lin, App Phys Letts 99 222906 (2011); 98 082903 (2011)

### Graphene Growth

**Moderator:** M. Spencer, Cornell University, V.D. Wheeler, U.S. Naval Research Laboratory

8:20am **GR+EM+NS+PS+SS+TF-MoM1 Synthesis Ingredients Enabling Low Noise Epitaxial Graphene Applications, D.K. Gaskill, L.O. Nyakiti, V.D. Wheeler, U.S. Naval Research Lab, A. Nath, George Mason Univ., V.K. Nagareddy, Newcastle University, UK, R.L. Myers-Ward, N.Y. Garces, S.C. Hernandez, S.G. Walton, U.S. Naval Research Lab, M.V. Rao, George Mason Univ., A.B. Horsfall, Newcastle Univ., UK, C.R. Eddy, Jr., U.S. Naval Research Lab, J.S. Moon, HRL Labs LLC**

Sensors made from graphene flakes have demonstrated single molecule detection [Schedin *et al.*, Nat Mat 6, 652 (2007)]; this ultra-sensitivity is likely due to the high crystalline quality of the graphene and the associated relative lack of defects that give rise to noise. The low noise nature of high quality graphene should also facilitate other applications, e.g., low-noise amplifiers. Combined with the unique ambipolar property of graphene field effect transistors (FETs), the low noise character of graphene would significantly advance the performance of frequency multipliers, mixers and high-speed radiometers. To exploit these applications, high quality, reproducible wafer-scale epitaxial graphene (EG) with minimal thickness variations and defects are essential requirements. Here, crucial graphene synthesis elements required to achieve the wafer-scale quality goal are described. Understanding the effect of substrate misorientation as well as hydrogen etch and Si sublimation conditions for graphene synthesis on the (0001) SiC surface is essential to achieve improved and reproducible wafer-scale graphene quality. For example, the impact of processing factors such as temperature control, laminar gas flow and substrate rotation on large area EG uniformity are described using examples created in an Aixtron SiC epitaxy reactor. In addition, managing SiC step formation on the nominal (0001) orientation is significant for achieving uniform EG thickness on terraces and to minimize additional growth at the step edges; this is illustrated using data from atomic force microscopy and scanning electron microscopy images in combination with Raman spectroscopy maps and x-ray photoelectron spectroscopy analysis. Managing step formation combined with optimal growth leads to the suppression of the Raman defect "D" band confirming minimal grain boundaries and defects, which are additional sources of electronic noise. Lastly, contactless Leighton resistivity maps of 75 mm wafers are used to illustrate the overall uniformity of optimally synthesized graphene as well as to show the resistance state-of-the-art, with individual wafers exhibiting about a  $\pm 3\%$  relative variation. Examples of the impact of this synthesis approach on chemical sensors devices and FETs will be shown, each exhibiting 1/f noise behavior down to 1 Hz and possessing noise spectral densities similar to reports from exfoliated graphene. Hence, careful control of EG formation across the wafer results in improved quality which subsequently leads to the reduction or elimination of additional noise sources from graphene defects that would then adversely affect device performance.

8:40am **GR+EM+NS+PS+SS+TF-MoM2 Growth of Graphene by Catalytic Decomposition of Ethylene on Cu(100) and Cu(111) With and Without Oxygen Predosing, Z.R. Robinson, P. Tyagi, T. Mowll, C.A. Ventrice, Jr., University at Albany- SUNY, K. Clark, A.-P. Li, Oak Ridge National Laboratory**

Graphene growth on Cu substrates has become one of the most promising techniques for the mass production of graphene, and therefore significant effort has been put into developing growth conditions that lead to large area, defect and grain boundary free graphene films. One key consideration is the influence that the underlying copper substrate has on the growth of the graphene. In order to study this, graphene growth on Cu(100) and Cu(111) was carried out in a UHV system. The samples were heated using an oxygen series button heater. The hydrocarbon pressure was measured using a capacitive manometer instead of an ion gauge, which could cause dissociation of the hydrocarbon molecules. Initially, it was found that annealing the crystals to 900 °C resulted in impurity segregation at the surface. Several cycles of sputtering at 600 °C were required to remove all bulk impurities so that the surface remained clean even after annealing to 900 °C. Initial attempts to grow graphene by annealing each crystal to temperatures as high as 900 °C in UHV, followed by backfilling the chamber with up to  $5 \times 10^{-3}$  torr of  $C_2H_4$  did not result in graphene formation. It was found that by first backfilling the chamber with  $C_2H_4$  and then raising the temperature from 25 °C to 800 °C, graphene growth could be achieved. A four-domain epitaxial overlayer is observed for the Cu(100) surface. Pre-dosing the Cu(100) with oxygen at 300 °C, which forms a saturation coverage of chemisorbed oxygen, was found to result in a 2-

domain graphene overlayer using similar growth conditions. A study of the effect of oxygen pre-dosing on the growth of graphene on Cu(111) has been initiated.

9:00am **GR+EM+NS+PS+SS+TF-MoM3 Impact of Growth Parameters on Uniformity of Epitaxial Graphene, L.O. Nyakiti, V.D. Wheeler, R.L. Myers-Ward, J.C. Culbertson, U.S. Naval Research Laboratory, A. Nath, George Mason University, N.Y. Garces, U.S. Naval Research Laboratory, J. Howe, Oak Ridge National Laboratory, C.R. Eddy, Jr., D.K. Gaskill, U.S. Naval Research Laboratory**

Epitaxial graphene (EG) offers a facile method for attaining large area graphene for device applications. Since wafer uniformity and thickness control is vital, a systematic study of the parameters affecting the EG growth process was performed and the optimal conditions for obtaining uniform morphology and high electronic quality were determined. EG was synthesized in a low pressure Ar flowing ambient on  $8 \times 8 \text{ mm}^2$  6H-SiC(0001) substrates that were offcut  $0.8^\circ$  from the basal plane, using an Aixtron VP508 reactor. The samples were placed on a rotating  $\sim 100$  mm diameter susceptor and excellent EG layer uniformity and run-to-run reproducibility were obtained. The investigation focused upon the critical synthesis parameters of temperature (T) (1520-1660°C) and time (t) (15-60 min), an *in-situ*  $H_2$  etch conditions (1520-1600°C for 10-30min). Morphology, layer thickness, chemical analysis, and strain variations across the samples were characterized using electron microscopy, AFM, XPS and  $\mu$ -Raman spectroscopy. Large-area van der Pauw Hall effect was performed to quantify the graphene mobility ( $\mu$ ), and carrier density. Results show that growth T and t had the most significant impact on EG electronic and morphological properties. For example, synthesis at 1660°C for 30min resulted in 4-8 monolayers (ML) and a step-bunched morphology with high concentration of wrinkles originating from the step-edge and pinned at the nearest terrace edge. Other morphological features were pits primarily located at the step edges having a depth  $\sim 20$ nm and density  $6.4 \times 10^6 \text{ cm}^{-2}$ . In contrast, EG synthesis at 1520°C for 30min results in uniform ML coverage along the terrace width that is devoid of pits and wrinkles. Mobility was found to have a drastic dependence on graphene thickness. Under optimal conditions, 1-2 ML were obtained and  $\mu$  as high as  $1240 \text{ cm}^2 \text{ V}^{-1} \text{ s}^{-1}$  was achieved; in contrast, for EG with  $>2$  ML  $\mu \sim 550 \text{ cm}^2 \text{ V}^{-1} \text{ s}^{-1}$ , presumably due to interlayer interaction and electronic screening. XPS C1s and Raman 2D spectra of EG grown on substrates after undergoing *in-situ*  $H_2$  etch at different times did not show shifts in peak position/intensity suggesting lack of etch time dependence on EG electronic or structural quality. Yet etch conditions affect the final morphology, as EG synthesis performed after an *in-situ*  $H_2$  etch at 1600°C resulted in step-bunched morphology with step heights 5-10nm, whereas, substrates etched at 1520°C had EG with step-heights 10-15nm. In addition other growth parameters investigated were found to be of secondary importance, including: Ar pressure, flow rates, and sample cool down conditions.

9:20am **GR+EM+NS+PS+SS+TF-MoM4 Uniform Epitaxial Growth of Charge Neutral Quasi-Free-Standing Monolayer Graphene on a 6H-SiC(0001) Surface by Combination of Metal Silicidation and Intercalation, H. Shin, I. Song, C.-Y. Park, J.R. Ahn, Sungkyunkwan University, Republic of Korea**

Intrinsic high mobility of graphene are much reduced in graphene devices by various factors. Two critical factors degrading mobility are uniformity in an atomic structure such as number of a layer and an interaction with a substrate. Recently Shuai-Hua Ji *et al.* reported quantitatively that conductivity is much reduced by one sixth when electrons pass through a boundary between monolayer and bilayer graphene at a step edge in comparison to conductivity of monolayer graphene. This suggests that uniformity of number of graphene layer is a more crucial factor than expected. In particular, in epitaxial graphene on SiC, the uniformity of number of layer is an intrinsic and serious problem because Si is more rapidly sublimated near a step edge in the formation of epitaxial graphene by thermal evaporation of Si and, subsequently, epitaxial graphene with different layers coexists intrinsically on a terrace. Another factor degrading mobility is an interaction between graphene and a substrate. In epitaxial graphene, the interaction was reduced by intercalation of metal or molecule such as H, F, and Au between graphene and a substrate, which results in quasi freestanding graphene. Various charge neutral quasi freestanding graphene has been reported, but the charge neutrality was found at an optimal coverage of an intercalated element and annealing temperature. This makes it difficult to achieve spatially homogeneous charge neutrality of quasi freestanding graphene, and a method with a broad range of coverage and temperature is demanded. We demonstrate that charge neutral quasi freestanding monolayer graphene can be grown uniformly without coexistence of a buffer layer and a bilayer graphene which limit mobility of epitaxial monolayer graphene. Because coexistence of two different phases is inevitable on a SiC surface, uniform monolayer graphene was produced based on two different phases, a Si-rich phase and a C-rich phase called a

buffer. Pd was deposited on both the Si-rich and C-rich phases and annealed up to 900°C. The Si-rich phase produced Pd silicide and charge neutral quasi freestanding monolayer graphene was produced on the Pd silicide while, on the C-rich phase, Pd was intercalated between the buffer layer and SiC resulting in charge neutral quasi freestanding monolayer graphene, where the quasi freestanding monolayer graphene on two different regions was connected atomically. The combination of Si silicidation and intercalation result in uniform charge neutral quasi freestanding uniform monolayer on a SiC surface, where the electronic and atomic structures were observed using angle-resolved photoemission spectroscopy and scanning tunneling microscopy.

9:40am **GR+EM+NS+PS+SS+TF-MoM5 Epitaxial Graphene on Ir(111) - A Playground for the Fabrication of Graphene Hybrid Materials**, *T.W. Michely*, Universität zu Köln, Germany **INVITED**

Carefully optimizing the growth of graphene on Ir(111) yields a virtually defect free, weakly bound epitaxial monolayer ranging from quantum dot sizes to macroscopic extension. In the talk I will show how this system can be used to construct new types of graphene based materials. Specifically, patterned adsorption of transition metals results in dense cluster arrays with exciting magnetic and catalytic properties. Intercalation underneath the graphene allows one to manipulate the properties of graphene itself, e.g. its ability to adsorb atoms and molecules as well as its magnetism.

10:40am **GR+EM+NS+PS+SS+TF-MoM8 Graphene Growth Studied with LEEM, PEEM, EELS, ARPES, MEIS, and STM**, *R.M. Tromp, J.B. Hannon, M.W. Copel, S.-H. Ji, F.M. Ross*, IBM T.J. Watson Research Center **INVITED**

We have studied the growth of graphene on a variety of substrates, including SiC (both Si and C terminated), polycrystalline Cu and Ni foils, as well as single-crystal Ni foils. Low Energy Electron Microscopy (LEEM) and Photo Electron Emission Microscopy (PEEM) offer the unique opportunity to follow the growth in real time, as it proceeds at high temperature, and in the presence of processing gases such as disilane (for growth on SiC) or ethylene (for growth on the metal substrates). Low Energy Electron Diffraction (LEED) allows us to determine crystallographic orientations as well as atomic structure of areas well below a micrometer in extent. Information on electronic structure can be obtained from the plasmon loss features using Electron Energy Loss Spectroscopy (EELS), or from Angle Resolved Photo Electron Spectroscopy (ARPES). These spectroscopic experiments are carried out in the LEEM/PEEM microscope using an in-line energy filter with which energy and angle resolved analysis of the electrons can be performed on selected areas. Finally, to obtain information on the layer-by-layer evolution of the graphene films, particularly on SiC, we have used isotope sensitive Medium Energy Ion Scattering (MEIS), to follow the growth by thermal decomposition of  $^{12}\text{C}$  vs  $^{13}\text{C}$  graphene monolayers from a three-bilayer thick  $\text{Si}^{13}\text{C}$  homoepitaxial film grown on a SiC substrate. Taken together, these results provide a comprehensive view of the growth of graphene films. In this talk, we will review the most salient results of these studies, and their relevance to the use of graphene films for electronic applications. To address the latter, we will discuss the results of three-probe STM experiments in which we measured the excess resistivity of a graphene sheet as it crosses an atomic step of the underlying substrate.

11:20am **GR+EM+NS+PS+SS+TF-MoM10 Spatial Confinement of Epitaxy of Graphene on Microfabricated SiC to Suppress Thickness Variation**, *H. Fukidome, T. Ide, H. Handa*, RIEC, Tohoku Univ., Japan, *Y. Kawai*, Tohoku Univ., Japan, *F. Fromm*, Univ. Erlange-Nürnberg, Germany, *M. Kotsugi, T. Ohkouchi*, JASRI/SPring-8, Japan, *H. Miyashita*, Tohoku Univ., Japan, *Y. Enta*, Hiroasaki Univ., Japan, *T. Kinoshita*, JASRI/SPring-8, Japan, *Th. Seyller*, Univ. Erlange-Nürnberg, Germany, *M. Suemitsu*, RIEC, Tohoku Univ., Japan

Epitaxial graphene on SiC (EG) is promising owing to a capability to produce high-quality film on a wafer scale [1]. One of the remaining issues is microscopic thickness variation of EG near surface steps, which induces variations in its electronic properties and device characteristics. To suppress the variation, spatial confinement of surface reactions is effective. The spatial confinement using substrate microfabrication, for instance homoepitaxy and sublimation on microfabricated Si substrates, can induce self-ordering of steps, and even produce step-free surfaces [2]. The spatial confinement is therefore anticipated effective to obtain EG without the thickness variation.

We have for this reason applied the spatial confinement to the epitaxy of graphene on 6H-SiC(0001). For the spatial confinement, 6H-SiC(0001) substrates were microfabricated by using electron beam lithography and fast atomic beam etching using sulfur hexafluoride [3, 4]. Epitaxial graphene on the microfabricated 6H-SiC(0001) substrates was obtained by annealing at 1923 K in Ar ambience [2]. It is verified by using low energy electron

microscopy (LEEM) and photoemission electron microscopy (PEEM) that step-free SiC surface and EG without thickness variation can be formed on smaller patterns [4]. This result clearly demonstrates that the spatial confinement is effective for the epitaxy of graphene on SiC. Furthermore, Raman spectroscopy and LEEM reveals that the spatial confinement can suppress the fluctuations of the electronic properties, e.g. (unintentional) doping in EG [4].

In conclusion, we have demonstrated that the spatial confinement of EG is effective to control both structural and electronic properties. This novel technique can boost the development of electronic devices based on EG.

[References]

- [1] K. V. Emstev et al., Nature Mater. 8 (2009) 203.
- [2] Y. Homma et al., Jpn. J. Appl. Phys. 35 (1996) L241.
- [3] T. Ide et al., accepted for the publication in Jpn. J. Appl. Phys.
- [4] H. Fukidome et al., submitted.

11:40am **GR+EM+NS+PS+SS+TF-MoM11 Three-Dimensional Graphene Architecture Growth and Its Facile Transfer to Three-Dimensional Substrates**, *J.-H. Park*, Sungkyunkwan University, Republic of Korea, *H.-J. Shin, J.Y. Choi*, Samsung Advanced Institute of Technology, Republic of Korea, *J.R. Ahn*, Sungkyunkwan University, Republic of Korea

Recent development of large area graphene synthesis on metal layer by chemical vapor deposition (CVD) or epitaxial growth on silicon carbide (SiC) opened the possibility for applications such as transparent electrodes for ITO replacement. For instance, graphene has been demonstrated for use in a liquid crystal display (LCD) and/or organic light emitting diode (OLED) test cell as a bottom electrode. However, the actual device, e.g., an active-matrix (AM) LCD, operates by switching individual elements of a display, using a thin-film transistor (TFT) for each pixel. Here, the pixel electrode of a display should extend down to the transistor's source or drain, thereby making contact with a via hole, which demands that a three-dimensional (3D) architecture electrode be deposited on a flat surface as well as its side walls. Although large-area graphene growth can be applied for a wide range of applications, 3D graphene architecture growth has not been realized for actual devices due to the original limitation of planar graphene growth. Herein, we demonstrate for the first time 3D graphene architecture growth and its facile transfer to a planar and/or 3D substrate. To prevent agglomeration of nano-scale metal catalyst by the CVD process, we chose a SiC system. Graphene, a few layers thick, was epitaxially grown on a pre-patterned SiC substrate with nano-size thickness which was produced by photolithography and dry etching. Graphene on a vertical facet of the SiC pattern with a few-hundred nanometers in height was perfectly prepared using this approach, contrary to the CVD method. Furthermore, we suggest the use of a facile transfer method of graphene on SiC to a SiO<sub>2</sub> substrate using thermal release tape after hydrogen intercalation. In spite of the troublesome transfer issue of SiC, the geometry of the 3D graphene was perfectly transferred onto the planar SiO<sub>2</sub> as well as the 3D SiO<sub>2</sub> structure. In other words, the 3D graphene architecture was maintained as a floating cap structure on planar SiO<sub>2</sub> and the vertical facet of the 3D SiO<sub>2</sub> structure was well covered. Moreover, the graphene bottom layer without a 3D cap and the inverted bowl structure in the 3D graphene architecture were selectively transferred by controlling intercalation and pressure. These approaches could provide a beneficial method for preparing a 3D graphene architecture as well as for modifying the ordered structure to be utilized in real devices.

**Oxide Heterostructures-Interface Form & Function**  
**Focus Topic**

**Room: 7 - Session OX+EM+MI+NS+TF-MoM**

**Structure-Property Relationships in Epitaxial Oxide Interfaces**

**Moderator: E.I. Altman, Yale University**

8:20am **OX+EM+MI+NS+TF-MoM1 Role of Dual-laser Ablation in Controlling Mn Oxide Precipitation during the Epitaxial Growth of Mn Doped ZnO Thin Films with Higher Doping Concentrations**, *D. Mukherjee, M. Hordagoda, R.H. Hyde, N. Bingham, H. Srikanth, P. Mukherjee, S. Witanachchi*, University of South Florida

The low solubility of Mn (equilibrium limit of 13 %) and precipitation of Mn oxides at slightly higher Mn doping (> 4 %) have remained major obstacles in the growth of Mn doped ZnO (ZnO:Mn) thin films for potential spintronic applications. In this work, epitaxial ZnO:Mn thin films were deposited on c-cut Al<sub>2</sub>O<sub>3</sub> (0001) substrates, with increasing Mn

concentrations from 2 to 12 %, using the dual-laser ablation process. In this process, an excimer (KrF) laser and a CO<sub>2</sub> laser pulses are spatially and temporally overlapped onto the target surface. Initially the target is heated by the CO<sub>2</sub> laser to produce a transient molten layer, from which the slightly time-delayed KrF laser initiates the ablation. Ablation for a momentary liquid target not only results in a drastic reduction of particulates in the deposited films but also overcomes the problem of non-congruent ablation of the ZnO:Mn target, leading to stoichiometric film deposition. Moreover, the optimum coupling of the laser energies produces an ablation plume that has a broader angular distribution, compared to the plume generated by KrF pulse alone, as observed from the intensified-charge-coupled-detector (ICCD) images of the ablated plumes. This allows the deposition of uniform films over larger area. Further, the higher ionization of the ablated species as seen in the optical emission spectra (OES) of the dual-laser ablated plumes leads to enhanced gas phase reaction and better film morphology and crystallinity. X-ray diffraction studies revealed that the dual-laser deposited ZnO:Mn films were single crystalline with no secondary phase formation even at 12 % doping while single-laser deposited ZnO:Mn films showed secondary Mn oxide phases. Room temperature magnetic measurements showed ferromagnetism (FM) with enhanced saturation magnetization ( $M_s$ ) values from 1.3 emu/cm<sup>3</sup> for 2 % ZnO:Mn films to 2.9 emu/cm<sup>3</sup> for 12 % ZnO:Mn films. In- and out-of-plane magnetization revealed absence of magnetic anisotropy. Further, temperature dependent Hall measurements showed a strong correlation between the effective carrier densities and the observed FM. All these measurements suggested a carrier mediated mechanism of FM in ZnO:Mn thin films. Using both the experimental data and theoretical analysis the FM in less conducting ZnO:Mn films was described by a bound magnetic polaron model whereas that in highly conducting films was consistent with a carrier mediated interaction via RKKY exchange mechanism.

8:40am **OX+EM+MI+NS+TF-MoM2 Structural Characterization of Heterojunction *n*-ZnO/*p*-NiO Thin Films Epitaxially Deposited on (0002)Al<sub>2</sub>O<sub>3</sub> Substrates**, *Y.H. Kwon*, Sungkyunkwan University, Republic of Korea, *J.H. Lee*, KAIST, Republic of Korea, *S.H. Chun*, Sungkyunkwan University, Republic of Korea, *J.Y. Lee*, KAIST, Republic of Korea, *H.K. Cho*, Sungkyunkwan University, Republic of Korea

Recently, oxide semiconductors with superior electrical properties have been considered as candidates to replace Si based electronics. Furthermore, their thermally and chemically stable characteristic is preferable for devices. Especially, among a lot of oxides, ZnO based semiconductors have been extensively investigated to apply in wide application such as thin film transistor and light emitting diode. ZnO is an intrinsic *n*-type semiconductor which characteristic comes from Zn interstitials and O vacancies. And band-gap and exciton binding energy are 3.37 eV and 60 meV, respectively, which is suitable for optical application operating in ultra-violet region. Therefore, *p-n* homojunction diode structure combined with *n*-ZnO and *p*-ZnO having well matched interface had been studied by a lot of researchers.[1] However, it was not reliable since *p*-type ZnO synthesized by doping of group V elements is unstable and return to the *n*-type by self-compensation.[2]

Therefore, *p-n* heterojunction diode composed of *n*-ZnO and stable *p*-type oxide such as Cu<sub>2</sub>O and NiO was alternatively studied.[3] Among the *p*-type oxides, NiO with wide direct band-gap (3.7 eV) have been expected to apply in optical applications. And conductivity of NiO could be significantly controlled by Li<sup>+</sup> doping. Furthermore, according to T. Dutta et. al., (111) plane of NiO could well matched with (0002) of ZnO by domain match epitaxy.[4]

In this study, heterojunction diode structure was fabricated with *n*-type ZnO and *p*-type NiO on [0002] oriented Al<sub>2</sub>O<sub>3</sub> substrates. RF magnetron sputtering method was used for deposition of NiO and ZnO films. After the deposition of NiO films at 400°C in O<sub>2</sub> atmosphere, ZnO films were grown at 600°C and in Ar and O<sub>2</sub> mixed gas atmosphere. XRD result showed the NiO films were fabricated with high crystallinity and preferred orientation of [111]<sub>NiO</sub>. And sixfold symmetry of (100)<sub>NiO</sub> plane obtained by phi-scan indicates that the NiO films were bi-epitaxially grown on Al<sub>2</sub>O<sub>3</sub> substrates. In addition, electrical properties of NiO showed relatively low resistivity (1.648 Ωcm) and high mobility (14.52 cm<sup>2</sup>/Vs) due to Li<sup>+</sup> doping. Sixfold symmetry of (1-102)<sub>ZnO</sub> observed at phi-scan result indicates that ZnO films were also epitaxially grown on [111] oriented NiO films.

#### REFERENCES

- [1] F. Zhuge, L. Zhu, Z. Ye, D. Ma, J. Lu, J. Huang, F. Wang, Z. Ji, S. Zhang, Applied Physics Letters, 87 (2005) 092103.
- [2] C. Park, S. Zhang, S.H. Wei, Physical Review B, 66 (2002) 073202.
- [3] H. Kawazoe, H. Yanagi, K. Ueda, H. Hosono, MRS Bulletin, 25 (2000) 28.
- [4] T. Dutta, P. Gupta, A. Gupta, J. Narayan, Journal of Applied Physics, 108 (2010) 083715.

9:00am **OX+EM+MI+NS+TF-MoM3 Manipulating the Electrostatic Boundary Conditions of Polar Interfaces**, *Y. Hikita*, SLAC National Accelerator Laboratory

INVITED

Transition metal oxides (TMO) offer various functionalities ranging from electronic devices to environmental catalysts [1, 2]. Often, the central part of such devices is the interface between different materials. In order to improve their device performance, control of charge transport across these interfaces is essential. Originally developed in semiconductor heterostructures, interface band alignment control is based on the interface electrostatic boundary conditions and is one of the most fundamental methods to tune the carrier transport across interfaces [3]. Given their strongly ionic nature and their accessibility to multiple valence states, the TMO interface should be more suitable than covalent semiconductors for manipulating interface band alignments. Here we focus on epitaxial metal-semiconductor Schottky interfaces between perovskite oxides to demonstrate the effectiveness of this technique. I will present two SrTiO<sub>3</sub> based perovskite Schottky junctions in which the interface energy barriers were modulated by interface dipoles controlled on the atomic scale [4]. Further, I will present the application of this technique in the form of an all-oxide hot electron transistor [5].

1. R. Ramesh and D. G. Schlom, MRS Bull. **33**, 1006 (2008).
2. J. Suntivich *et al.*, Science **334**, 1383 (2011).
3. F. Capasso *et al.*, Appl. Phys. Lett. **46**, 664 (1985).
4. Y. Hikita *et al.*, Phys. Rev. B **79**, 073101 (2009).
5. T. Yajima *et al.*, Nature Mater. **10**, 198 (2011).

11:20am **OX+EM+MI+NS+TF-MoM10 Strain-induced Oxygen Vacancy Ordering at SrTiO<sub>3</sub>/La<sub>0.5</sub>Sr<sub>0.5</sub>CoO<sub>3</sub> Interfaces, and its Impact on Magnetic "Dead" Layers**, *S. Bose, M. Sharma, M. Torija*, University of Minnesota, *J. Gazquez, M. Varela*, Oak Ridge National Laboratory, *J. Schmitt, C. He*, University of Minnesota, *S. El-Khatib*, American University of Sharjah, United Arab Emirates, *M. Laver, J. Borchers*, NIST Center for Neutron Research, *C. Leighton*, University of Minnesota

The remarkable functionality and epitaxial compatibility of complex oxides provides many opportunities for new physics and applications in oxide heterostructures. Perovskite cobaltites provide an excellent example, being of interest for solid oxide fuel cells, oxygen separation membranes, catalysis, ferroelectric RAM, resistive switching memory, and oxide spintronics. However, the same delicate balance between phases that provides this diverse functionality also leads to a serious problem - the difficulty of maintaining desired properties close to the interface with other oxides. Although this problem is widespread, manifests itself in several ways, and could present a significant roadblock to the development of heterostructured devices for oxide electronics, there is no consensus as to its origin. In our work, using SrTiO<sub>3</sub>(001)/La<sub>1-x</sub>Sr<sub>x</sub>CoO<sub>3</sub> as a model system, we have combined epitaxial growth via high pressure oxygen sputtering [1] with high resolution x-ray diffraction, atomic resolution scanning transmission electron microscopy (STEM) and electron energy loss spectroscopy (EELS), and detailed magnetic, transport, and neutron scattering measurements to determine the fundamental origin of the deterioration in interfacial transport and magnetism [2,3]. The effect is found to be due to nanoscopic magnetic phase separation in the near-interface region driven by a significant depletion in interfacial hole doping due to accumulation of O vacancies. This occurs due to a novel mechanism for accommodation of lattice mismatch with the substrate based on formation and long-range ordering of O vacancies [4]. This fundamental link between strain state and O vacancy formation and ordering is explored in detail in this presentation. We demonstrate that the O vacancy density, depth profile, and ordering vector can all be controlled via strain, leading to a potential mechanism to substantially improve interfacial properties.

UMN support from NSF and DOE (neutron scattering). ORNL support from DoE; UCM support from the European Research Council.

- [1] Torija *et al.*, J. Appl. Phys. **104** 023901 (2008); Sharma *et al.*, J. Vac. Sci. Technol. **29** 051511 (2011).
- [2] Torija *et al.*, Adv. Mater. **23** 2711 (2011).
- [3] Sharma *et al.*, Phys. Rev. B., **84** 024417 (2011). [4] Gazquez *et al.*, Nano. Lett. **11** 973 (2011).

11:40am **OX+EM+MI+NS+TF-MoM11 Fabrication and Characterization of Titanium Oxide Films with Tunable Stiffness**, *K. Gottlieb-Vainshtein, O. Girshevitz, C.N. Sukeinik*, Bar Ilan University, Israel, *D. Barlam*, Ben Gurion University, Israel, *E. Kalfon-Cohen, S.R. Cohen*, Weizmann Institute of Science, Israel

The design of surfaces with controlled stiffness is attractive for a variety of applications ranging from controlling cell growth to mechanical and electrical engineering design. Here, the creation of layered composites with tunable surface stiffness has been achieved by coating a soft PDMS

polymer with a stiff film of amorphous titanium oxide with thickness varying from 2 to 50 nm. The oxide layer is smooth (6 nm rms roughness at 2  $\mu\text{m}^2$  image size), and crack-free. Air plasma treatment was used to form a silica surface layer on the soft polymer base to promote adhesion of the titania overlayer. To gain insight into the mechanics of the layered structure, nanomechanical quantification has been performed using different experimental approaches, as well as modeling studies. The surface mechanical properties of the samples have been probed using both instrumented nanoindentation and atomic force microscopy—based nanomechanical characterization. These results have been compared to finite element analysis (FEA) simulations.

By fitting the FEA simulations with experimental curves it is shown that the hard titania film and softer PDMS substrate individually maintain their characteristic elastic moduli, while the stiffness of the vertical nanocomposite can be controllably modified by changing the thickness of the stiff layer. Liquid phase deposition of the oxide allows control of its thickness at the nm level. During an indentation cycle, the stiff layer transmits the stress to the underlying PDMS base by deformation of its overall shape, but only negligible compression of the film thickness.

This synthetic approach can be quite versatile, and can, in principle, be extended to different oxides and a wide range of thicknesses. It allows control of surface properties while maintaining bulk material properties. This exploratory work is a first step towards defining the range of surface stiffnesses that can be achieved in this way, as well as developing general methodologies for their characterization.

## Plasma Science and Technology

Room: 24 - Session PS+EM-MoM

### Atmospheric Plasma Processing and Micro Plasmas

Moderator: S.G. Walton, Naval Research Laboratory

#### 8:20am PS+EM-MoM1 Plasma Science and Applications in the Spatial Realm Below 1 mm: Recent Advances in Microcavity/Microchannel Plasmas, J.G. Eden, University of Illinois at Urbana Champaign INVITED

The last decade has witnessed the rapid emergence of microcavity plasmas, a new subfield of plasma science and technology that pursues the fundamental physics and applications of low temperature, nonequilibrium plasma confined in at least one dimension to nominally  $< 1$  mm. By melding plasma science with photolithography and other micro/manufacturing techniques adapted from the integrated circuits and materials science communities, it has become possible to observe plasma behavior and realize electronic/photonic/chemical devices that were inaccessible previously. With all due respect to Captain Kirk, plasmas are now able “to go where no [plasma] has gone before.” This presentation will highlight recent advances in microcavity plasma science, such as the realization of plasma confined to  $< 3$   $\mu\text{m}$ . Interfacing a gas phase ( $e^-$  - ion) plasma with an  $e^-$  -  $h^+$  plasma in a semiconductor to yield an  $n^+pn$  plasma bipolar junction transistor will be described. A new form of thin, flat lighting (“lighting tiles”) available in sheets as large as 900  $\text{cm}^2$  in area will be demonstrated, and massively-parallel plasmachemical processing of gases/vapors in arrays of microchannel plasmas will be described.

#### 9:00am PS+EM-MoM3 Development and Limitations of Microplasma Arrays on Silicon Operating in DC, R. Dussart, M. Kulsreshath, L. Schwaederle, V. Felix, P. Lefauchaux, O. Aubry, T. Tillocher, S. Sozias, GREMI - Polytech Orleans/CNRS, France, L.J. Overzet, University of Texas at Dallas

Arrays of microreactors built from silicon wafers in clean room facilities were first proposed and developed about ten years ago by G. Eden's team [1]. They consist of Micro Hollow Cathode Discharges (MHCD) operating in parallel in DC or in AC. One of the remarkable properties of these MHCDs relies on the fact that they can operate in DC, in a stable regime at atmospheric pressure, without evolving to an arc regime [2]. Potential applications of these new technological devices are numerous and include different domains such as lighting, detection, local treatments, sensors, lab on chip, treatment and micromachining processing, instrumentation... In this paper, we will focus on DC operation of microdischarges working in helium or in argon. The microreactor geometry was investigated to achieve the best results in terms of life time and ignition. Although we were able to ignite up to 1024 microdischarges (100  $\mu\text{m}$  diameter holes), we observed many spikes on the current waveform, which indicate that microplasmas are not so stable. The quite short life time of our microdevices which varies from few minutes to few hours could be linked to these spikes, which actually cause significant damages. Taking into account our observations by Scanning Electron Microscope, our optical characterization and our electrical measurements, we propose a mechanism explaining the

appearance of the damages, which shorten the lifetime of our microdischarges. Finally, we will give some indications to delay the damage mechanisms and to increase the life time of the microplasma arrays.

#### References

[1] J G Eden, S-J Park, N P Ostrom, S T McCain, C J Wagner, B A Vojak, J Chen, C Liu, P von Allmen, F Zenhausern, D J Sadler, C Jensen, D L Wilcox and J J Ewing, *J. Phys. D: Appl. Phys.* 36 2869–2877 (2003)

[2] K. H. Schoenbach, R. Verhappen, T. Tessnow, P. F. Peterkin, W. Byszewski, *Appl. Phys. Lett.* 68, 13 (1996)

#### 9:20am PS+EM-MoM4 A Foldable Microplasma-Generation Device on a Paper Substrate Operating under Atmospheric Pressure, Y.J. Yang, J.H. Tsai, Y.C. Liao, Y.W. Lu, C.C. Hsu, National Taiwan University, Taiwan, Republic of China

The fabrication of plasma generating devices on paper substrates is presented. The device was fabricated using a screen print process. Stable helium plasmas were ignited in two parallel electrodes with a gap of 237 to 710  $\mu\text{m}$  by a DC power source. When the plasma was ignited with a 0.2  $\mu\text{L}$  salt solution droplet with trace amount of metallic elements applied to the discharge gap, clear metallic emission lines emanated from the plasma. The result suggests that this paper-based device can be used in analytical applications. We demonstrate that a stable helium plasma can be sustained when the substrate is flat, rolled, and folded along various orientations. Microarrays were also fabricated on paper substrates. Stable array of discharges can be ignited by an AC power source with a frequency between 50 Hz to 10 kHz. Preliminary results show that a  $10^*10$  discharge array can be ignited under different atmospheres such as argon, helium, and air by properly adjusting the parameters. This work was supported by National Science Council of Taiwan, the Republic of China (100-2628-E-002-012 and 101-3113-E-002-002).

#### 9:40am PS+EM-MoM5 Cold Atmospheric Microplasma Arrays for Processing of Flexible Materials, J. Hopwood, A. Hoskinson, C. Wu, N. Miura, Tufts University INVITED

Microplasmas offer a pathway to atmospheric pressure plasma processing using low-temperature, low-cost substrates. Unlike arc and torch technologies, the atmospheric microplasma typically operates near room temperature. Corona discharges share this distinction, but modern microplasma devices produce electron densities that are several orders of magnitude greater than the corona. The combination of low gas temperature and high electron density suggests that a unique process window exists for deposition, etching, and surface modification of flexible materials at atmospheric pressure. In this lecture, we describe the plasma physics of a steady-state microplasma excited by 1 GHz microwave power. Spatially resolved laser diode absorption, imaging spectroscopy, and electrical probe measurements show that the individual microdischarge has an intense inner core surrounded by a cooler region that is rich in metastable atoms. These physical insights are combined with data from deposition experiments using acetylene mixed with a helium gas flow. High densities of electrons and energetic species produced by steady-state microplasmas are believed to be crucial to quality film formation at one atmosphere. Finally, we explore scaling the microplasma toward roll coating geometries. Linear arrays of microplasmas are excited from a single microwave power source through the use of resonant energy sharing. This technique allows over 100 microplasmas to operate in parallel without the usual problem of instabilities induced by ionization overheating and negative differential discharge resistance. This work was supported in part by the U.S. Department of Energy under award No. DE-SC0001923 and by the National Science Foundation under Grant No. CBET-0755761.

#### 10:40am PS+EM-MoM8 Nucleation of Nanodiamond Clusters at Ambient Pressure via Microplasma Synthesis, A. Kumar, P.A. Lin, A. Xue, R.M. Sankaran, Case Western Reserve University

Since their discovery, nanodiamonds have been an active area of research due to their unique size, chemical stability, high thermal conductivity, and biocompatibility.<sup>1</sup> Nanodiamonds have been detected in outer space (meteorites, interstellar dust) and synthetically produced by high pressure/high temperature (HPHT) and detonation processes. In addition to their potential technological use, the formation of nanodiamond is of great scientific interest. While bulk graphite is more stable than bulk diamond at lower pressures and temperatures (e.g. ambient conditions), recent modeling has suggested that nanometer-sized particles of diamond-phase carbon could be thermodynamically favored at these same conditions as a result of surface energy considerations.<sup>2</sup>

Previously, microplasmas have been shown to be capable of nucleating high-purity nanometer-sized metal nanoparticles from vapor precursors.<sup>3</sup> Here, we present a study of nanodiamond synthesis at atmospheric pressure using a similar microplasma process. Ethanol vapor was used as a carbon

precursor for the nucleation of carbon clusters. Aerosol measurements confirm that carbon clusters less than 6 nm in mean diameter are nucleated in the microplasma. *In situ* optical emission spectroscopy (OES) indicates the presence of C<sub>2</sub> dimers and atomic H species which have been linked to diamond nucleation. The collected product is characterized by several techniques including micro Raman spectroscopy, X-ray diffraction (XRD), X-ray photoelectron spectroscopy (XPS), and high-resolution transmission electron microscopy (HRTEM). Results confirm the presence of nanodiamond with uniform sizes of ca. 3 nm in diameter and crystal structures corresponding to known phases of diamond. The synthesis of nanodiamond at low pressure may allow new technologies to be realized, and help explain their formation in extraterrestrial material.

1. V. N. Mochalin *et al.*, "The properties and applications of nanodiamonds", *Nat. Nanotech.* 7, 11 (2012).
2. P. Badziag *et al.*, "Nanometre-sized diamonds are more stable than graphite", *Nature* 343, 244 (1990).
3. A. Kumar *et al.*, "New insights into plasma-assisted dissociation of organometallic vapors for gas-phase synthesis of metal nanoparticles", *Plasma Proc. Polym.*, in review.

11:00am **PS+EM-MoM9 Atmospheric Pressure Plasma Effects on the Adhesive Bonding Properties of Stainless Steel and Epoxy Composites**, T.S. Williams, H. Yu, P. Yeh, J. Yang, R.F. Hicks, University of California, Los Angeles

An atmospheric pressure helium and oxygen plasma has been used for the surface preparation of 410 stainless steel and carbon-fiber epoxy laminates prior to bonding them together. Lap shear results for stainless steel coupons and carbon-fiber epoxy laminates demonstrated an 80% and a 150% increase in bond strength, respectively, after plasma activation. Following 7 days of aging, wedge crack extension tests revealed a crack extension length of 7.0 mm and 2.5 mm for the untreated and plasma activated steel. The untreated stainless steel had 30% cohesive failure compared to 97% for steel activated with the plasma. Surface analysis by X-ray photoelectron spectroscopy showed that carbonaceous contamination was removed by plasma treatment, and specific functional groups, e.g. carboxylic acids, were formed on the surface. These functional groups promoted strong chemical bonding to the epoxy film adhesive. Atmospheric pressure plasmas are an attractive alternative to abrasion techniques for surface preparation prior to bonding. The process is easily automated, does not damage the materials, and has no environmental, health and safety concerns.

11:20am **PS+EM-MoM10 Numerical Simulation of Gas Heating in a Capacitively Coupled Microcell Plasma at Atmospheric Pressure**, T. Yagisawa, T. Makabe, Keio University, Japan

A microcell plasma at atmospheric pressure has been widely investigated. One of the biggest advantages is in the capability to produce a small-size and high-density plasma, broadening a range of applications such as nanomaterial synthesis, light sources, biomaterial processing, green technology and so on. With decreasing the size of the reactor, the ratio of volume to surface area also decreases. Under these circumstances, the contribution of the wall surface to the loss of charged and neutral particles becomes much larger. The energy is accumulated in the plasma in the form of a thermal energy by the interaction between energetic ions and gas molecules and the ion impact on the wall. Therefore, the effects of local heating of gas molecule on the plasma structure is of great importance particularly in a microcell plasma at high pressure.

In this study, the two-dimensional (2D) structure of a capacitively coupled microcell plasma (CCP) driven at radio frequency (13.56 MHz) with the power of ~4.7 W cm<sup>-3</sup> is numerically investigated in a sealed cylindrical chamber at atmospheric pressure. Pure argon is considered as a parent gas molecule, where electron, Ar<sup>+</sup>, Ar<sub>2</sub><sup>+</sup> and long-lived metastable atom (Ar<sup>m</sup>) are traced in the simulation. In order to discuss the effects of local gas heating, the governing system consisting of a coupled set of models is developed: a neutral transport model including the gas temperature T<sub>g</sub>, a conventional plasma model in gas phase, as well as a heat conduction model in solid phase. Large amount of metastable atom ~10<sup>14</sup> cm<sup>-3</sup> makes huge influence on the plasma structure via stepwise ionization process caused by low energy electrons (~4.3 eV), as well as metastable pooling. The temperature dependence of the thermal conductivity (~ T<sub>g</sub><sup>1/2</sup>) of argon is considered and the result is compared with that of constant thermal conductivity. The local peak of gas temperature T<sub>g</sub> ~ 600 K appears due to the Joule heating by energetic ions in the sheath region in front of the powered electrode, resulting in the local reduction of gas density N<sub>g</sub>(r) under the constant gas pressure. Taking the gas heating into account, electron density increases by the enhancement of reduced field E/N<sub>g</sub>(r). In addition, electron density distribution slightly expands toward the radial direction.

11:40am **PS+EM-MoM11 Reactions at the Interface of Plasmas and Aqueous Electrodes: Identifying the Role of Electrons**, M. Witzke, Case Western Reserve University, P. Rumbach, D.B. Go, University of Notre Dame, R.M. Sankaran, Case Western Reserve University

Plasmas formed at the surface of or inside liquids have been of historical interest for the potential to mediate electrochemical reactions with gaseous species.<sup>1</sup> Recently, there has been technological interest in plasma/liquid systems for a wide range of applications including nanomaterials synthesis, water treatment, and medicine. However, the nature of reactions at the plasma/liquid interface remains poorly understood. Specifically, since plasmas are a source of electrons, ions, UV light, and radicals, it has been difficult to isolate and identify the role of the various species on reactions that occur in the liquid phase.

Here, we present evidence of electrolytic reactions at the plasma/liquid interface. Experiments were carried out with a non-thermal, atmospheric-pressure, direct-current microplasma jet formed at the surface of an aqueous electrolyte. The plasma was operated as the cathode with a Pt foil immersed in solution as the anode. To isolate the role of electrons, we selected model electrolytic reactions such as the conversion of ferricyanide [Fe(CN)<sub>6</sub><sup>3-</sup>] to ferrocyanide [Fe(CN)<sub>6</sub><sup>4-</sup>] which can be easily monitored by UV-vis absorbance spectroscopy.<sup>2</sup> Cyclic voltammetry was performed to verify that ferricyanide was not dissociated. Alternatively, using acidic solutions, hydrogen gas was detected by mass spectrometry, indicating that protons (H<sup>+</sup>) are electrochemically reduced by the plasma.<sup>3</sup> Overall, these results reveal the significant role electrons can play in plasma/liquid systems.

1. J. Gubkin, *Ann. Phys. Chem. N. F.* 32, 114 (1887).
2. M. Witzke *et al.*, *J. Am. Chem. Soc.* 133, 17582 (2011).
3. M. Witzke *et al.*, submitted.

# Monday Afternoon, October 29, 2012

## Spectroscopic Ellipsometry Focus Topic

Room: 19 - Session EL+TF+BI+AS+EM+SS-MoA

## Spectroscopic Ellipsometry: From Organic and Biological Systems to Inorganic Thin Films

Moderator: M.S. Wagner, The Procter & Gamble Company

2:00pm **EL+TF+BI+AS+EM+SS-MoA1 Biochemical Optical Sensors Based on Highly-Ordered Slanted Columnar Thin Films**, *D. Schmidt, K.B. Rodenhausen*, University of Nebraska-Lincoln, *J. VanDerslice, T.E. Tiwald, J.A. Woollam Co., Inc., E. Schubert, M. Schubert*, University of Nebraska-Lincoln

Highly-ordered three-dimensional nanostructure thin films offer substantially increased surface area for attachment of organic layers, and in addition, new detection principles due to the physical properties of the nanostructures. For example, upon material attachment the optical birefringence of the nanostructures changes due to screening of polarization charges. Because of these advantages, highly-ordered three-dimensional nanostructure thin films lend themselves as suitable candidates for studying of organic attachments as well as for low-cost humidity sensing, for example.

We utilize glancing angle electron-beam deposition for fabrication of highly spatially coherent metal slanted columnar thin films. Subsequently, the nanostructures may be further functionalized with thin conformal coatings by means of atomic layer deposition. The ellipsometry model analysis and resulting anisotropic optical properties of hybrid metal slanted columnar thin films determined by generalized spectroscopic ellipsometry in the visible and near-infrared spectral region will be discussed. We will be reviewing research in this area and report in particular on in-situ monitoring of organic attachments using ellipsometry combined with quartz crystal microbalance with dissipation. Exemplarily, we discuss studies of fibronectin protein adsorption, octanethiol chemisorption (self-assembled monolayer growth) on platinum coated titanium slanted columnar thin films as well as relative humidity sensing.

2:20pm **EL+TF+BI+AS+EM+SS-MoA2 Studies of Optical Properties of Hybrid J-aggregates and Nanocrystal Quantum Dots Layers for Photonic Applications**, *K. Roodenko, H.M. Nguyen, L. Caillard, A. Radja, O. Seitz, Yu.N. Gartstein, A.V. Malko, Y.J. Chabal*, The University of Texas at Dallas

The integration of organic materials and inorganic nanocrystal quantum dots (NQDs) on the nanoscale offers the possibility of developing new photonic devices that utilize the concept of resonant energy transfer between an organic material and NQDs. Electromagnetic coupling that takes place between excitons—bound electron-hole pairs—at the interfaces of the hybrid composite can be utilized for light-emitting, photovoltaic and sensor applications.

As the key ingredients for the nanocomposite material system reported in this work are the J-aggregates (JA, dye self-assembled molecules) that have exceptional optical absorption due to their strong oscillator strength. NQDs on the other hand combine a variety of important properties, such as high quantum yields, excellent photo- and chemical stability, and size dependent, tunable absorption and emission. Excitation energy transfer in NQDs / J-aggregate hybrids is characterized by their strong excitonic transitions at room temperature with spectrally well-defined absorption and emission.

In order to understand the energy transfer mechanisms in such complex systems, optical properties of JA and NQDs/JA hybrid systems were characterized by means of spectroscopic ellipsometry and polarized IR spectroscopy.

Spectroscopic ellipsometry in 0.6-5 eV spectral range was employed to study optical properties of J-aggregates drop-casted on silicon surfaces. Thin JA films were found to exhibit strong optical anisotropy due to the specific molecular orientation of thin layers on Si substrates. Variation of optical properties due to the deposition of nanocrystal quantum dots (NQDs) was systematically studied for applications in new photonic devices that utilize excitonic energy transfer from NQDs to JA layer. Ellipsometric results were cross-referenced with atomic force microscopy (AFM) data to derive a quantitative understanding of the distribution of NQDs upon deposition on JA layer. Integration of hybrid colloidal NQD/JA structures could be potentially attractive for a range of optoelectronic applications.

2:40pm **EL+TF+BI+AS+EM+SS-MoA3 Love and Death, the Story of Most Proteins and Most Surfaces as Told by Spectroscopic Ellipsometry**, *T. Benavidez, K. Chumbuni-Torres, J.L. Felhofer, C.D. Garcia*, The University of Texas at San Antonio **INVITED**

Biosensors are analytical platforms that integrate a biological recognition element with a signal transducer. Because they have the potential to provide rapid, real-time, and accurate results, biosensors have become powerful tools in clinical and biochemical settings. Our group is particularly interested in the development of electrochemical biosensors based on enzymes adsorbed to nanomaterials. When integrated to microfluidic devices, these sensors offer sensitivity, portability, low cost, and the possibility of analyzing turbid samples. Adsorption was selected to immobilize the biorecognition element because it is one of the simplest and most benign methods, avoiding cross-linking reactions or additional components (such as entrapping polymers). Most importantly, as adsorption is a required (and sometimes limiting) step for any immobilization mechanism, the identification of key variables influencing this process can be applied to a variety of strategies. Although several techniques have been used to study the adsorption of proteins to nanomaterials,<sup>1</sup> only a few of them provide information about the kinetics of the process in real time. This is a critical aspect, as most of the post-adsorption conformational changes occur within a few minutes after the interaction.<sup>2</sup> Among those, reflectometry was used by our group to perform the first kinetic study related to the interaction of proteins with carbon nanotubes.<sup>3</sup> These kinetic studies have been recently extended to the interaction of enzymes (D-amino acid oxidase,<sup>4</sup> catalase,<sup>5</sup> and glucose oxidase<sup>6</sup>) by variable angle spectroscopic ellipsometry, which enabled a more thorough analysis of the interaction process with a much more versatile experimental design.<sup>7,8</sup> The use of VASE demonstrated that a number of variables, (being the amount of enzyme only one of them) can influence the biological activity of proteins adsorbed to the substrate. Furthermore, our results indicate that the activity of enzymes adsorbed to nanomaterials can be directly related to the kinetics of the adsorption process (dG/dt).<sup>5</sup>

Please see supplemental document for figures and footnotes.

3:40pm **EL+TF+BI+AS+EM+SS-MoA6 Detailed Photoresist and Photoresist Processing Studies using Spectroscopic Ellipsometry**, *C. Henderson*, Georgia Institute of Technology **INVITED**

Spectroscopic ellipsometry has become an invaluable tool for the study of a wide variety of thin film systems. In particular, it has become extremely valuable in the development and study of advanced photoresists and of lithographic processes used in the production of integrated circuits and other related semiconductor devices. In our work, we have used spectroscopic ellipsometry to study a variety of problems related to photoresists including swelling phenomena, exposure induced refractive index changes, and ultra-fast dissolution phenomena. We have combined spectroscopic ellipsometry with quartz crystal microbalance techniques to simultaneously study thin film optical properties, thickness, film mass, and film modulus. Such techniques have been particularly useful in understanding the dissolution properties of polymeric photoresists developed for 193 nm lithography. This talk will review some of the applications for spectroscopic ellipsometry in this field and in particular will highlight some of the results of our work made possible using spectroscopic ellipsometry.

4:20pm **EL+TF+BI+AS+EM+SS-MoA8 Ellipsometric Characterization of a Thin Titaniumoxide Nanosheets Layer**, *H. Wormeester, G. Maidecchi, S. Kumar, A. Kumar, A. ten Elshof, H.J.W. Zandvliet*, MESA+ Institute for Nanotechnology, University of Twente, The Netherlands

The photochemical properties of titaniumoxide make this a widely studied material. Of special interest is a thin nanostructured layer of such a material. A variety of a nanostructured material is the single sheet titaniumoxide that can be obtained by delaminating a layered titanate, with stoichiometry  $Ti_{1-x}O_{2+4x}$  ( $x=0.0875$ ). The slight titanium deficiency leads to a negatively charged nanosheet that can be used as a building block in a layer by layer assembled composite film [1]. In this work we used Langmuir Blodgett to deposit successive thin layers of nanosheets. The electronic properties of these layers were investigated with ellipsometry and Scanning Tunneling Microscopy (STM). The optical spectra show the well known absorption peak at 4.6 eV for titaniumoxide nanosheets. The optical spectra can be well modeled with a Cody-Lorentz dielectric function profile providing a bandgap of ... eV, a value also found from STM IV spectroscopy. The Cody-Lorentz profile also indicates a slight below band gap light absorption by the nanosheet material.

[1] T. Sasaki, Y. Ebina, T. Tanaka, M. Harada, M. Watanabe and G. Decher, Chem. Mater. 2001, 13, 4661

4:40pm **EL+TF+BI+AS+EM+SS-MoA9 Preparation of Abrupt LaAlO<sub>3</sub> Surfaces Monitored by Spectroscopic Ellipsometry**, C.M. Nelson, M. Spies, L.S. Abdallah, S. Zollner, Y. Xu, H. Luo, New Mexico State University

LaAlO<sub>3</sub> is a polar perovskite oxide, used as a single-crystal substrate in oxide epitaxy. It has created much interest for novel electronic applications, because a two-dimensional electron gas is formed at LaAlO<sub>3</sub>/SrTiO<sub>3</sub> heterostructures. The purpose of our work is twofold: First, we are interested in an accurate determination of the complex refractive index of LaAlO<sub>3</sub> at room temperature. Second, we studied the impact of various cleaning methods on the abruptness of the LaAlO<sub>3</sub> surface.

We obtained a commercial single-side polished LaAlO<sub>3</sub> substrate with 2-inch diameter and a (100) pseudo-cubic surface orientation. The surface was polished with an rms roughness below 0.8 nm. We determined the ellipsometric angles  $\psi$  and  $\Delta$  for LaAlO<sub>3</sub> at 300 K from 0.7 to 6.5 eV. For a bulk insulator with a clean smooth surface, the phase change  $\Delta$  should be zero or  $\pi$  below the band gap. In practice, this never happens, because surfaces are covered with overlayers (adsorbed organic or water vapors). Surface roughness has a similar effect on the ellipsometric spectra as a surface overlayer. Even for an abrupt bulk/air interface, there is a thin (~0.5nm) transition region where the electron wave functions leak from the crystal into the ambient. For the as-received sample, the data were described with a Tauc-Lorentz model for LaAlO<sub>3</sub>, plus 2.1 nm of surface layer thickness (described as an effective medium with 50% density of the bulk). After ultrasonic cleaning in acetone, the overlayer thickness decreased to 1.8nm. Next, we mounted the wafer in a UHV cryostat, pumped down to below 10<sup>-8</sup>Torr, and acquired an ellipsometric spectrum at 70°. The surface layer thickness was reduced to 1.2 nm, presumably because a part of the adsorbed surface layer (especially water) desorbed under vacuum.

So far, everything worked as expected, but here it gets interesting: We heated the sample to 700 K for about an hour to desorb the remaining surface overlayer. After cooling down to 300 K, we measured the ellipsometric angles again at 70° angle of incidence from 0.7 to 6.5 eV. The ellipsometric angle  $\Delta$  at 2 eV was reduced to below 0.2°, consistent with a surface layer thickness of less than 1 Å, much less than the surface roughness specified by the supplier (8 Å).

In conclusion, a macroscopically smooth and clean LaAlO<sub>3</sub> surface was prepared by ultrasonic cleaning of the wafer in acetone, followed by heating in UHV to 700 K. The resulting surface layer thickness was below 1 Å, as measured by spectroscopic ellipsometry. We will report Tauc Lorentz parameters. We will also describe the temperature dependence of the LaAlO<sub>3</sub> dielectric function from 77 to 700 K. This work was supported by NSF (DMR-11104934).

5:00pm **EL+TF+BI+AS+EM+SS-MoA10 Determination of the Refractive Index of a Gold-Oxide Thin Film Using X-Ray Photoelectron Spectroscopy and Spectroscopic Ellipsometry**, K. Cook, G.S. Ferguson, Lehigh University

A two-step procedure will be presented for measuring the complex refractive index of an electrochemically produced oxide film on a gold surface. In the first step, the composition and the thickness of the oxide film were determined using angle-resolved X-ray photoelectron spectroscopy. The experimental composition defined the system, thereby avoiding assumptions about the film stoichiometry that would otherwise be required. The value of thickness derived from these measurements was then used to calculate  $n$  and  $k$  from ellipsometric data collected across the visible spectrum (350 - 800 nm).

## Electronic Materials and Processing

Room: 9 - Session EM+TF+OX+GR-MoA

### High-k Dielectrics for MOSFETS II

Moderator: C.L. Hinkle, University of Texas at Dallas, H.J. Kim, National Institute of Aerospace (NIA)

2:00pm **EM+TF+OX+GR-MoA1 "6.1" Family: The Next Generation of III-V Semiconductors for Advanced CMOS: Epitaxial Growth and Passivation Challenges**, C. Merckling, A. Alian, A. Firrincelli, S. Jiang, M. Cantoro, J. Dekoster, M. Caymax, M. Heyns, IMEC, Belgium **INVITED**  
The integration of high carrier mobility materials into future CMOS generations is presently being studied in order to increase drive current capability and to decrease power consumption in future generation CMOS devices. If III-V materials are the candidates of choice for n-type channel

devices, antimonide-based III-V semiconductors present the unique property of owning both high electrons (InSb) and holes (GaSb) mobilities, which triggered much of the interest in these III-Sb compounds for advanced CMOS. Moreover recent simulations have demonstrated that higher hole mobility could be found in strained III-antimonides compounds, suggesting the possibility of an all III-antimonide solution for full III-V based CMOS. In this work we studied the heteroepitaxy of 6.1 family semiconductors (GaSb, AlSb & InAs) on various III-V and Si substrates as well as the passivation of such semiconductors.

The relatively large lattice parameter of "6.1" semiconductors makes the growth and the integration on standard surfaces difficult. But is it possible to grow such semiconductors fully relaxed with low defect density due to the formation of a highly periodic array of 90° misfit dislocations at the III-Sb/substrate interface. In this contribution both MBE and MOVPE growth techniques have been studied in order to propose novel integration scheme on Si substrate.

In a second part, we will focus on the passivation of these III-V semiconductors. Because III-V surfaces are very sensitive to oxygen compounds, this will generate the formation of native oxide. This undesirable interlayer will contribute aggressively to the high density of surface states within the energy band gap, resulting in Fermi level pinning which disturbs the basic III-V MOSFET-operation. In this context both ex-situ and in-situ Al<sub>2</sub>O<sub>3</sub> high-k gate dielectric deposition by standard ALD or MBD processes is reported. The interface is abrupt without any substantial interfacial layer, and is characterized by high conduction and valence band offsets. Finally, MOS capacitors showed well-behaved C-V with relatively low  $D_{it}$  along the band gap. Such a  $D_{it}$  profile is promising for the future devices and suggests possibility to attain a low subthreshold swing.

2:40pm **EM+TF+OX+GR-MoA3 Improving Nucleation and Passivation of Ge(100) via H<sub>2</sub>O and H<sub>2</sub>O<sub>2</sub> Dosing**, T. Kaufman-Osborn, K. Kiantaj, J.S. Lee, A.C. Kummel, University of California San Diego

Germanium is a promising candidate for potential channel materials due to its higher hole and electron mobility. To minimize the oxide-semiconductor interfacial defect density, a proper passivation layer must be used before the oxide layer is deposited. In this study, a monolayer of H<sub>2</sub>O chemisorbs is shown to activate TMA chemisorption due to the Ge-OH bonds catalyzing the formation of an ultrathin passivation layer which can serve as an ideal ALD nucleation template on a Ge surface. However, since H<sub>2</sub>O chemisorption results in equal density of Ge-H and Ge-OH sites on the Ge(100), H<sub>2</sub>O can only provide a maximum of 0.5 monolayer of Ge-OH sites, limiting the TMA nucleation density. By using H<sub>2</sub>O<sub>2</sub> dosing, the density of Ge-OH sites can be doubled thereby increasing the potential TMA nucleation density. This study compares the passivation of the Ge(100) surface via H<sub>2</sub>O and H<sub>2</sub>O<sub>2</sub>, for the application of nucleating ALD growth on the surface, using scanning tunneling microscopy (STM) and scanning tunneling spectroscopy (STS).

A saturation H<sub>2</sub>O dose onto Ge(100) resulted in 0.85 ML coverage of -OH and -H species chemisorbed on the surface. The remaining unreacted atoms on the surface have half filled dangling bond states causing a large local amount of conduction band edge states in the bandgap. The Ge-OH and Ge-H sites on the surface have limited thermal stability. Annealing the H<sub>2</sub>O/Ge(100) sample to 100°C significantly reduces the H<sub>2</sub>O coverage due to the recombinative desorption of H<sub>2</sub> or H<sub>2</sub>O.

A saturation dose of H<sub>2</sub>O<sub>2</sub> on Ge(100) at 25°C results in a coverage of 0.95 ML of Ge-OH species chemisorbed on the surface with very few unreacted sites. Compared to a H<sub>2</sub>O dose, H<sub>2</sub>O<sub>2</sub> provides more than double the number of reactive Ge-OH sites thereby increasing the number of potential ALD nucleation sites. In contrast to the H<sub>2</sub>O passivated surface, annealing the H<sub>2</sub>O<sub>2</sub>/Ge surface to 100°C generates no additional dangling bond sites and even eliminates the dangling bonds present from the 25°C dose and forms a highly ordered surface of Ge-OH bonds. The improved coverage of Ge-OH sites allows for increased nucleation density of O-Al bonds and also minimizes the dangling bonds which are considered as the major source of interfacial trap states (D<sub>it</sub>). The improved thermal stability allows for an increased thermal budget during ALD cycles. STS measurements show that TMA nucleation on the H<sub>2</sub>O<sub>2</sub> functionalized Ge(100) surface unpins the Fermi level and has a wide bandgap with no band edge states demonstrating very good interface quality.

3:00pm **EM+TF+OX+GR-MoA4 Electrical and Physical Characteristics of High-k/Metal Gate MOS Devices on MBE-Grown Germanium on Silicon Using Aspect Ratio Trapping**, S.R.M. Anwar, C. Buie, N. Lu, M.J. Kim, C.L. Hinkle, University of Texas at Dallas

Due to its high hole mobility and relative compatibility with Si CMOS processing, Ge has long been considered as a replacement channel material for PMOS devices. Selective area growth of Ge channels on bulk Si substrates would be ideal for minimizing fabrication costs and allowing the co-implementation of other materials (III-Vs for NMOS). However, due to

the 4.2% lattice mismatch between Ge and Si, unacceptably high dislocation densities ( $\sim 10^9 \text{ cm}^{-2}$ ) are created during this heteroepitaxy.

In this work, we investigate the fabrication of MOS gate stacks on MBE-grown Ge on Si using Aspect Ratio Trapping (ART)<sup>1,2</sup> to reduce Ge defect density. ART is a growth technique that allows for the reduction of defects for lattice mismatched materials by trapping the threading dislocations into the sidewalls of patterned nanoscale trenches in which the epitaxial growth takes place. This technique has the added benefit of producing the necessary geometric structure required for highly scaled tri-gate devices while reducing defect density simultaneously. Surface roughness and defect density dependence on growth temperature and growth rate will be discussed as will be the effect of varying the trench geometry. RHEED, XRD, XPS, TEM, EPD, AFM, SEM, and IPE data are correlated with growth conditions to produce high quality heteroepitaxial growth. Data will be presented demonstrating the use of low-temperature buffer layers in conjunction with low-growth rate bulk Ge results in a reduction in threading dislocations of 2-3 orders of magnitude.

MOS devices were fabricated on the MBE-grown Ge on Si samples. A high-quality interface was obtained using a DI-H<sub>2</sub>O surface functionalization by pre-pulsing the H<sub>2</sub>O 50 times in the atomic layer deposition (ALD) chamber at 250 °C.<sup>3</sup> A thin interfacial Al<sub>2</sub>O<sub>3</sub> film was deposited by ALD at 250 °C followed by forming gas anneal (FGA) performed for 30 minutes at 350 °C. This FGA step converts the surface functionalized oxide to a thin layer of GeO<sub>2</sub> resulting in improved electrical performance. 2.5 nm of HfO<sub>2</sub> was then deposited by ALD. 10 nm of RF sputtered TiN was deposited as the gate metal followed by low-temperature anneals in various ambients to tune the effective work function of the HfO<sub>2</sub>/TiN gate stack.<sup>4</sup> A final FGA for 30 minutes at 350 °C completed device processing. These devices show excellent PMOS characteristics and will be discussed.

This work is supported by the SRC Global Research Corporation.

- 1 J.-S. Park, *et al.*, *Appl. Phys. Lett.* **90**, 052113 (2007).
- 2 J. Bai, *et al.*, *Appl. Phys. Lett.* **90**, 101902 (2007).
- 3 S. Swaminathan, *et al.*, *J. Appl. Phys.* **110**, 094105 (2011).
- 4 C. L. Hinkle, *et al.*, *Appl. Phys. Lett.* **100**, 153501, (2012).

**3:40pm EM+TF+OX+GR-MoA6 In Situ Infrared Spectroscopy Study on the Temperature Dependence on the Growth Mechanism of Atomic Layer Deposition of Al<sub>2</sub>O<sub>3</sub> on InP(100).** W. Cabrera, The University of Texas at Dallas, I.M. Povey, Tyndall National Institute, Y.J. Chabal, The University of Texas at Dallas

One of the current challenges in fabricating III-V-based electronics is the growth of an interfacial layer during the atomic layer deposition (ALD) of high-k dielectrics on III-V substrates, which has led to poor quality electrical properties. A process that can mitigate this problem is the “clean-up” effect that occurs when trimethylaluminum (TMA) is deposited by atomic layer deposition during the formation of Al<sub>2</sub>O<sub>3</sub>. A recent theoretical study suggests that the principal pathway in the “clean-up” effect of TMA on the native oxides of GaAs and InGaAs involves oxygen gettering. In this work, *in-situ* infrared absorption spectroscopy has been used to investigate the temperature dependence of the native oxide and the interface formation during Al<sub>2</sub>O<sub>3</sub> deposition using TMA and deuterium oxide (D<sub>2</sub>O) on chemically-treated InP(100) surfaces. Upon annealing a degreased sample to 300°C, compositional changes are observed, as evidenced by new absorption features in the region of 900-1250 cm<sup>-1</sup> of the infrared spectrum prior to TMA exposure. The initial native oxide, comprised in part of In(PO<sub>3</sub>)<sub>3</sub> is transformed into an InPO<sub>4</sub>-rich surface. Upon TMA exposure at 300°C, there is a clear loss of In(PO<sub>3</sub>)<sub>3</sub> and gain of InPO<sub>4</sub> (at 1007 and 1145 cm<sup>-1</sup>, respectively) along with the formation of Al-O bonds (absorption band at 800 cm<sup>-1</sup>). These observations are consistent with the “clean up” effect observed on GaAs<sub>3</sub> and InGaAs<sub>4</sub>, and on InP(100)<sub>5</sub> where TMA preferentially withdraws oxygen from the native oxide forming Al-O bonds. However, the TMA reduces In(PO<sub>3</sub>)<sub>3</sub> and fosters the formation of InPO<sub>4</sub>. Furthermore, TMA exposure of the native oxide at lower deposition temperatures (150°C) gives rise to methoxy (CH<sub>3</sub>) formation as evidenced by the appearance of a band centered at 1475 cm<sup>-1</sup>. This indicates that TMA not only withdraws oxygen from the native oxide but also transfers a methyl group to the surface oxygen, which may lead to carbon contamination at the interface. Al<sub>2</sub>O<sub>3</sub> oxide films are formed after 10 TMA and D<sub>2</sub>O cycles on both degreased native oxide and chemically treated (HF and (NH<sub>4</sub>)<sub>2</sub>S) InP(100) substrates, although the quality is higher on the (HF and (NH<sub>4</sub>)<sub>2</sub>S)-treated surface. A more clearly defined LO phonon mode is detected for that surface, suggesting that a denser oxide is formed.

- 1 S. Klejna et. al, *J. Phys. Chem. C*, **116**, (2012) 643-654
- 2 M. M. Frank et. al, *Appl. Phys. Lett.* **82** (2003) 4758
- 3 C. L. Hinkle et. al, *Appl. Phys. Lett.*, **92** (2008) 071901

4 M. Milojevic, et. al *Appl. Phys. Lett.*, **93**, (2008) 202902

5 B. Brennan et. al, *Appl. Phys. Exp.*, **4** (2011) 125701

**4:00pm EM+TF+OX+GR-MoA7 Ultimate Scaling of High-k Gate Dielectrics: Current Status and Challenges.** T. Ando, M.M. Frank, E.A. Cartier, B.P. Linder, J. Rozen, IBM T.J. Watson Research Center, K. Choi, GLOBALFOUNDRIES, V. Narayanan, IBM T.J. Watson Research Center

**INVITED**

Current status and challenges of aggressive equivalent-oxide-thickness (EOT) scaling of high-k gate dielectrics via higher-k (>20) materials and interfacial layer (IL) scavenging techniques are reviewed [1]. La-based higher-k materials [2, 3] and La-silicate IL with HfO<sub>2</sub> [4] showed aggressive EOT values (0.5–0.8 nm), but with large effective workfunction (EWF) shifts toward the Si conduction band edge, limiting their application to nFET. Further exploration for pFET-compatible higher-k materials is needed. Meanwhile, IL scavenging is a promising approach to extend Hf-based high-k dielectrics to future nodes [4, 5]. Remote-scavenging techniques enable EOT scaling below 0.5 nm. We will review IL scavenging techniques from the viewpoints of (1) IL growth condition; (2) Choice of scavenging element; (3) Location of scavenging element; (4) Choice of high-κ material and (5) Maximum process temperature. Careful choice of materials and processes based on these considerations is indispensable. Mobility-EOT trends in the literature suggest that short-channel performance improvement is attainable with aggressive EOT scaling via IL scavenging or La-silicate formation. However, extreme IL scaling is accompanied with loss of EWF control [6] and with severe penalty in reliability [7]. Therefore, highly precise IL thickness control in an ultra-thin IL regime (<0.5 nm) will be the key technology to satisfy both performance and reliability requirements for future CMOS devices.

This work was performed by the Research alliance Teams at various IBM Research and Development Facilities.

- [1] T. Ando, *Materials* **2012**, *5*, 478-500 [2] H. Arimura et al., *Electron Device Lett.* **2011**, *32*, 288–290 [3] L. F. Edge et al., *Appl. Phys. Lett.* **2011**, *98*, 122905 [4] T. Ando et al., *IEDM 2009*, 423-426 [5] L. Å. Ragnarsson et al., *IEDM 2009*, 663-666 [6] T. Ando et al., as discussed at *SISC 2011* [7] E. A. Cartier et al., *IEDM 2011*, 18.4.1-18.4.4

**4:40pm EM+TF+OX+GR-MoA9 AR-XPS Study of Al<sub>2</sub>O<sub>3</sub>/In-based III-V Interfaces after Annealing under Vacuum at Low Temperature.** E. Martinez, H. Grampeix, O. Desplats, CEA, LETI, MINATEC Campus, France, A. Herrera-Gomez, O. Ceballos-Sanchez, CINVESTAV-Unidad Queretaro, Mexico, J. Guerrero, K. Yckache, F. Martin, CEA, LETI, MINATEC Campus, France

III-V semiconductor substrates are a potential solution for MOSTETs down scaling below the 16 nm technological node. Indium based semiconductors, such as InGaAs, InAs and InP are promising compounds to improve the speed of operation. The quality of the interface between these high mobility substrates and the gate oxide is of crucial importance to preserve the devices electrical properties. Aluminium oxide is used to remove the As oxide (“self-cleaning” effect). The gate-last scheme is preferred to control of the high-k/III-V since it involves low temperature post deposition annealing [1]. State-of-the-art control of this interface has been obtained with annealing at 400°C under vacuum [2]. In this work we focus on the impact of low temperature annealing under vacuum on the quality of the Al<sub>2</sub>O<sub>3</sub>/In-based III-V interfaces. We have studied the interfacial oxides formed between alumina and III-V substrates such as InGaAs, InAs and InP. Annealing at 600°C under ultra high vacuum (UHV) is first performed and compared to thermal treatments at 600°C and 400°C at 3 10<sup>-4</sup> mbar. Substrate passivation is done with NH<sub>4</sub>OH (4 %). The 3-nm thick alumina is deposited by Atomic Layer Deposition (ALD) using TMA and H<sub>2</sub>O as precursor and oxidant. Angle-resolved photoelectron spectroscopy (AR-XPS) has been carried out to investigate the interfacial chemical bonding states. Consistent and robust analysis of the As 3d, P 2p, Ga 3d and In 3d core levels was carried out through the simultaneous fitting method [3]. At 600°C, we show that, on InGaAs, no interfacial oxides are created after annealing under UHV, whereas a thin interfacial InGaO<sub>x</sub> is observed under secondary vacuum. A clear difference between the three substrates is observed after annealing at 400°C under 3 10<sup>-4</sup> mbar. In particular, the indium oxidation and the relative stability of interfacial oxides are substrate dependant. On InAs, indium hydroxide is formed after annealing, by OH release from TMA/H<sub>2</sub>O deposited alumina. This is not the case with additional elements such as Ga and P, which react with residual species to create their respective oxides. On InGaAs, a regrowth of InGaO<sub>x</sub> is observed after anneal, as a result of preferential oxidation of Ga. On InP, the InPO<sub>x</sub> interfacial oxide seems to decrease after anneal. **Acknowledgements** This work was performed with financial support from the MOS35 project funded by the French National Research Agency. Measurements were carried out at the NanoCharacterization Centre (NCC) of MINATEC. [1] H. Zhao et al., *Appl. Phys. Lett.* **95**, 253501 (2009)[2] Y.

**5:00pm EM+TF+OX+GR-MoA10 Effect of a H<sub>2</sub> Plasma Pre-treatment on the Reduction of Native Oxides at the PEALD Al<sub>2</sub>O<sub>3</sub>/InAs Interface, E. Cleveland, L. Ruppalt, J.B. Boos, B. Bennett, J. Champlain, S.M. Prokes, Naval Research Laboratory**

The integration of high-*k* dielectrics with high mobility III-V semiconductor materials has attracted extensive interest recently as an alternative to Si-based complementary metal-oxide semiconductor (CMOS) applications at the 16 nm node and beyond. Among the III-V semiconductors, InAs is a promising material as the channel material in metal-oxide-semiconductor field-effect transistors (MOSFETs) due to its extremely high electron mobility and high saturation velocity. However, problems arise in the fabrication of high performance channel MOSFETs due to the poor quality of the gate oxide/InAs interface. InAs has a highly reactive surface and on exposure to air will form a native oxide layer composed of In<sub>2</sub>O<sub>3</sub> and As<sub>2</sub>O<sub>3</sub>. The complexity of these native oxides leads to the formation of a relatively high density of interface states which in turn act as charge traps thus pinning the Fermi level and degrading device performance. Wet-chemical treatments based on HCl and (NH<sub>4</sub>)<sub>2</sub>S have been found to be an effective means of removing these oxides, however, due to the rapid re-oxidation and lack of reproducibility a better means of interface cleaning is needed. Recently, there has been much interest in the field of surface cleaning combined with atomic layer deposition (ALD) in order to deposit high quality dielectrics on III-V semiconductor materials, such as InAs and GaSb. Therefore, we examined the use of a H<sub>2</sub> plasma as a means to obtain an oxide-free InAs interface prior to the deposition of high-*k* Al<sub>2</sub>O<sub>3</sub> via plasma enhanced atomic layer deposition (PEALD). Ex-situ XPS, AFM, and C-V measurements were performed to establish the effect of the plasma exposure time, temperature and rf power on the removal of the native oxide. It will be demonstrated that by removing or reducing the native oxides on the InAs surface that the density of interface defects at the Al<sub>2</sub>O<sub>3</sub>/InAs interface can be reduced and enhance the electrical performance. Similar work done on GaSb will be discussed, where XPS spectra revealed a significant reduction in Sb-O features for longer H<sub>2</sub> plasma exposures as the peaks associated with Ga-O increased. C-V measurements of fabricated MOSCAPS also found that samples treated with longer H<sub>2</sub> plasma exposures exhibited better C-V characteristics.

## Graphene and Related Materials Focus Topic

### Room: 13 - Session GR+EM+ET+NS+TF-MoA

#### Electronic Properties and Charge Transport

**Moderator:** T.W. Michely, Universität zu Köln, Germany

**2:00pm GR+EM+ET+NS+TF-MoA1 Influence of Substrate Offcut on Electrical and Morphological Properties of Epitaxial Graphene, R.L. Myers-Ward, V.D. Wheeler, L.O. Nyakiti, T.J. Anderson, F.J. Bezares, J.D. Caldwell, A. Nath, N. Nepal, C.R. Eddy, Jr., D.K. Gaskill, U.S. Naval Research Laboratory**

The promise of graphene-based device technologies is critically dependent on uniform wafer-scale graphene films and is most directly met through epitaxial graphene (EG) growth on silicon carbide (SiC) substrates. An essential parameter which influences this uniformity is the substrate offcut, as any deviation will result in a local change in the terrace width, impacting the growth rate and step-bunched heights observed after EG formation. For nominally on-axis SiC substrates, typical offcuts can range from ~0° to ~1° off-axis toward the [11-20] direction. Offcuts approaching 0° produce wide terraces with short step-bunched heights which offers the possibility of reduced anisotropy of transport properties [M. Yakes, et al., Nano Lett. 10(5), 1559 (2010)] and improved EG layer uniformity. Thus, it is of interest to understand the influence of substrate offcut on carrier mobility, surface morphology, step heights, and graphene growth rate. This study investigates EG grown on a unique single 3-inch substrate possessing a large variation in offcut, from +0.1 to -1° toward the [11-20] direction, enhancing the information obtained on offcut influence while eliminating other substrate influences. X-ray diffraction rocking curve and peak position maps of the (0012) reflection were performed prior to growth to evaluate the crystalline quality and local offcut, respectively. Electron mobilities of EG films were determined by van der Pauw Hall measurements. Surface morphology of the EG was investigated with scanning electron microscopy, while the step heights and terrace widths were measured using atomic force microscopy.

For a given set of conditions (1620°C for 30 min in 10 slm Ar), the EG morphology is dominated by straight steps that become wavy in character as the offcut decreases to zero degrees. Close to zero degrees, the step direction rotates from [11-20] to the [1-100] direction and the steps become further distorted. The step bunch heights generally decreased (from 8 to 3 nm) as the offcut decreased and the terrace widths increased (from 0.3 to ~3 μm); however, for the latter, the trend is interrupted near zero degrees offcut. In addition to such morphological assessments, the impact of growth parameters, where the growth temperatures investigated were 1540, 1580 and 1620 °C and growth times were 15, 30 and 45 min, on the electrical and structural properties of EG grown on this unique substrate will be reported. For example, samples grown at 1540 °C for 30 min on witness substrates with offcuts ranging from ~ 0.4 to 0.9° had large area mobilities ranging from 780 to 1100 cm<sup>2</sup>/Vs, where larger offcuts led to lower mobilities.

**2:20pm GR+EM+ET+NS+TF-MoA2 Direct Determination of Dominant Scatterer in Graphene on SiO<sub>2</sub>, J. Katoch, D. Le, T.S. Rahman, M. Ishigami, University of Central Florida**

Freely suspended graphene sheets display high-field effect mobility, reaching 2'105 cm<sup>2</sup>/V s. Yet, suspended graphene sheets are fragile and impractical for most experiments and applications. Graphene sheets on SiO<sub>2</sub> are easier to handle but possess low-carrier mobilities, which can vary by an order of magnitude from sample to sample. Poor and unpredictable transport properties reduce the utility of SiO<sub>2</sub>-bound graphene sheets for both fundamental and applied sciences. Therefore, understanding the impact of substrates is crucial for graphene science and technology.

We have measured the impact of atomic hydrogen with kinetic energy less than 250 meV on the transport property of graphene sheets as a function of hydrogen coverage and initial, pre-hydrogenation field-effect mobility. The saturation coverages for different devices are found to be proportional to their initial mobility, indicating that the number of native scatterers is proportional to the saturation coverage of hydrogen. In order to understand this correlation between the field effect mobility and the apparent affinity of atomic hydrogen to graphene, we have performed a detailed temperature programmed desorption study on hydrogen-dosed graphene sheets. Atomic hydrogen is found to physisorb on graphene with activation energy for desorption of 60 ± 10 meV, consistent with our theoretical calculations. The associated charge transfer expected for such small desorption energy indicates that atomic-scale defects and ripples are not responsible for determining the mobility of graphene on SiO<sub>2</sub> and that charged impurities in substrates define the transport property of graphene on SiO<sub>2</sub>.

1. J. Katoch, J.H. Chen, R. Tsuchikawa, C. W. Smith, E. R. Mucciolo, and M. Ishigami, Physical Review B Rapid Communications, 82, 081417 (2010).

**2:40pm GR+EM+ET+NS+TF-MoA3 Tuning Electronic Properties of Graphene by Controlling its Environment, K.I. Bolotin, Vanderbilt University**

**INVITED**

Every atom of graphene, a monolayer of graphite, belongs to the surface. Therefore, the environment of graphene -- the substrate onto which graphene is deposited and any coating on top of graphene -- intimately affects the properties of graphene. In this talk, we demonstrate that both the mechanical and electrical properties of graphene can be tuned by varying its environment.

First, we discuss the dependence of electrical transport in graphene on the dielectric constant (*k*) of graphene's environment. For graphene in vacuum (*k*=1) we observe very strong electron-electron interactions leading to robust fractional quantum Hall effect at temperatures up to 15K. By suspending graphene in liquids, we explore the regime of dielectric constants between ~1.5 and ~30. We observe the dependence of carrier scattering in graphene on *k* and demonstrate large values for room temperature mobility (>60,000 cm<sup>2</sup>/Vs) in ion-free liquids with high *k*. We also explore the rich interplay between the motion of ions inside liquids and transport of electrons in graphene. We observe signatures due to streaming potentials and Coulomb drag between ions in the liquid and electrons in graphene.

We also briefly address the mechanical properties of graphene and their dependence on graphene's environment. We demonstrate that the built-in strain, the substrate adhesion force and even the thermal expansion coefficient of graphene depend on the substrate supporting graphene.

3:40pm **GR+EM+ET+NS+TF-MoA6 Study of Impurity-Induced Inelastic Scattering on Suspended Graphene by Scanning Confocal Micro-Raman Spectroscopy, L.W. Huang, C.S. Chang, Academia Sinica, Taiwan, Republic of China**

We utilized a polymer-based procedure to transfer the CVD-grown graphene onto a TEM copper grid. The heat treatment was performed on the graphene membrane in an argon/ hydrogen (Ar/H<sub>2</sub>) atmosphere at 400 °C. After the transfer and heat treatment, TEM images, acquired by an ultra-high-vacuum transmission electron microscopy (UHV-TEM), demonstrated areas with distinguishable impurity distribution on the suspended graphene membrane. These areal impurity distributions can also be mapped by the scanning Raman spectroscopy correspondingly, indicating the influence of impurity-induced inelastic scattering. The results of this experiment show that the intensity ratio of Raman spectra 2D band over G band ( $I_{2D}/I_G$ ) is proportional to minus fourth power of the inelastic scattering rate.

4:00pm **GR+EM+ET+NS+TF-MoA7 The Adsorption of Molecules with Large Intrinsic Electrostatic Dipoles on Graphene, L. Kong, Univ. of Nebraska-Lincoln, G.J. Perez Medina, Univ. of Nebraska-Lincoln, Univ. of Puerto Rico, J. Colón Santana, Univ. of Nebraska-Lincoln, L. Rosa, Univ. of Nebraska-Lincoln, Univ. of Puerto Rico, L. Routaboul, P. Braunstein, Maître de conférences de l'Université de Strasbourg, France, B. Doudin, Institut de Physique et Chimie des Matériaux de Strasbourg, France, C.-M. Lee, J. Choi, Kyung Hee Univ., Korea, P.A. Dowben, Univ. of Nebraska-Lincoln**

Both gold and graphene are excellent conductors, and one might expect that both conductors would fully screen the photoemission and inverse photoemission final states of a molecular adsorbate, but in fact this is not the case. The comparison of the electronic structure of p-quinonoid zwitterionic type molecules with a large intrinsic dipole of 10 Debyes adsorbed on both gold and graphene on copper substrates, shows that the interaction between the adsorbate molecules and graphene is very weak, confirming that graphene is chemically inert. We find that the photoemission and inverse photoemission final states are well screened for p-quinonoid zwitterionic dipolar molecules on gold. This is not observed in the case of this quinonoid zwitterion adsorbed on graphene on copper. This weaker screening is evident in a larger highest occupied molecular orbital to lowest unoccupied molecular orbital gap for the molecules on graphene. The larger highest occupied molecular orbital to lowest unoccupied molecular orbital gap for the molecules on graphene indicates that a much weaker screening on the photoemission and inverse photoemission final states for these dipolar molecules on graphene than that on gold. This work is reviewed in the context of other studies of molecular adsorption on graphene.

4:20pm **GR+EM+ET+NS+TF-MoA8 Growth of and Interactions in Epitaxial Graphene Layers, A. Bostwick, Lawrence Berkeley National Laboratory, A. Walter, Th. Seyller, Lawrence Livermore National Laboratory, K. Horn, E. Rotenberg, Lawrence Berkeley National Laboratory**

**INVITED**

The electronic properties of graphene has been investigated using angle-resolved photoemission spectroscopy at the MAESTRO\* facility of the ALS\*\* synchrotron in Berkeley, California. This laboratory is unique in its ability to grow sophisticated samples for *in situ* study using angle-resolved photoemission spectroscopy, and to subtly alter their properties by engineering their surfaces by chemical doping or thickness control. In this talk I will discuss the electronic properties of graphene, focusing on the role of dopants to control the charge density and as defects to disrupt the metallic conduction. By measuring the spectrum of "plasmaronic" quasiparticle excitations, we can demonstrate the scale-free nature of the Coulomb interaction in Dirac systems. Such effects are readily observed on quasi-free standing graphene samples doped with long-range scatterers. Doping with short-range scatterers, on the other hand, results in a loss of conduction which we interpret as a manifestation of strong (Anderson) localization.

\*Microscopic and Electronic Structure Observatory

\*\*Advanced Light Source

5:00pm **GR+EM+ET+NS+TF-MoA10 Squeezing of the Graphene Dirac Cone Observed by Scanning Tunneling Spectroscopy, J. Chae, S. Jung, Y. Zhao, N.B. Zhitenev, J.A. Stroscio, Center for Nanoscale Science and Technology / NIST, A. Young, C. Dean, L. Wang, Y. Gao, J.C. Hone, K.L. Shepard, P. Kim, Columbia University**

The single-particle spectrum of graphene is described by massless Dirac quasiparticles with a linear energy-momentum dispersion relation. In this talk I examine the effect of electron interactions on the graphene energy dispersion as a function of both excitation energy  $E$  away from the Fermi energy and density  $n$ . To analyze the dispersion, we measure the Landau levels (LLs) in graphene on a hexagonal boron nitride (hBN) insulator in

low magnetic fields by scanning tunneling spectroscopy. The experiments were performed in a custom designed cryogenic scanning tunneling microscope system operating at 4 K with applied magnetic fields from 0 T to 8 T. The graphene devices were fabricated by the method detailed in Dean *et al.* [1]. The disorder in graphene on hBN is reduced in comparison with the previous measurements in graphene on SiO<sub>2</sub> [2] allowing us to observe the LLs in fields as low as 0.5 T. By fitting the LL energies obtained at constant density, we find that the energy dispersion remains linear, characterized by a momentum-independent renormalized velocity. However, the renormalized velocity is density dependent, showing a strong increase as the charge neutrality point is approached. The overall spectrum renormalization can be described as a *squeezing* of the Dirac cone angle due to electron-electron interactions at low densities. Interestingly, we also find that the renormalization of the dispersion velocity is affected by the local disorder potential and magnetic field, which is not described by current theory.

[1]. C. Dean, A. Young, I. Meric, C. Lee, L. Wang, S. Sorgenfrei, K. Watanabe, T. Taniguchi, P. Kim, K. L. Shepard, and J. Hone, *Nature Nanotech.* 5, 722–726 (2010).

[2]. S. Jung, G. M. Rutter, N. N. Klimov, D. B. Newell, I. Calizo, A. R. Hight-Walker, N. B. Zhitenev, and J. A. Stroscio, *Nature Phys.* 7, 245–251 (2011).

5:20pm **GR+EM+ET+NS+TF-MoA11 Interfacial Interaction of Graphene and Metal Surfaces Investigated by Resonant Inelastic X-ray Scattering, L. Zhang, University of Science and Technology of China, Advanced Light Source, J.H. Guo, Advance Light Source, J.F. Zhu, University of Science and Technology of China**

The synthesis of graphene on metal surfaces by chemical vapor deposition (CVD) is the most promising method to prepare single-layer and large-area graphene, which is a prerequisite for the fabrication of graphene-based electronic devices. Therefore, the graphene/metal interfaces have attracted much attention due to their importance in graphene synthesis by CVD processes. In this presentation, we report our recent studies on the electronic structure and band dispersion of graphene on different metal surfaces (Cu, Ir and Ni) by the means of X-ray absorption spectroscopy (XAS), X-ray emission spectroscopy (XES) and resonant inelastic X-ray scattering (RIXS). The XAS spectra for graphene on metal surfaces show strong  $\pi^*$  and  $\sigma^*$  resonant features, indicating that the single-layer graphene films preserve the intrinsic symmetry of graphite. The resonant XES spectra of graphene on different metal surfaces change dramatically, especially for the features of  $\pi^*$  resonances, which can be directly related to the different strength of hybridization between graphene and metal substrates. These significant spectra changes have been proved to be an effective measure for the bonding strength of graphene on different substrates: strong band dispersion can be observed when the interaction between graphene and metal substrate is weak (such as Cu), while the band dispersion is seriously disturbed when a strong hybridization between graphene and metal substrate (such as Ni) exists. These results provide basic understanding of graphene/metal interfacial interaction, which helps to develop graphene-based electronic devices with high performances.

## Nanomanufacturing Science and Technology Focus Topic

**Room: 16 - Session NM+NS+MS+EM-MoA**

### ALD and Scalable Processes for Nanomanufacturing

**Moderator: T.S. Mayer, Penn State University**

2:00pm **NM+NS+MS+EM-MoA1 From R&D Towards Industrial Atomic Layer Deposition: Challenges in Scaling up, M. Putkonen, Benq Oy, Finland**

More and more ALD-enabled applications are emerging. Most of the ALD processes and applications are first demonstrated by small scale experiments. In optimal cases, the innovations lead to material-application combinations which have solid commercial interest. In the subsequent verification and pilot production phase, there is need for increased throughput and reduced costs also for the ALD processed materials.

There are two main features of ALD, that should be optimized when industrial scale production is being considered. Firstly, in large-area coating processes, more attention should be paid to the properties of the precursors. For large-area coatings, large doses of precursors are delivered to the substrates, preferably in very short pulses in order to keep the total cycle time as short as possible. This often requires either DLI-type sources or increased vapor pressure (i.e. increased thermal stability of metal precursors). In addition, although the ALD chemistry should be surface

controlled and not dependent on the substrate surface area, deposition rates and film uniformities are habitually dependent on the tool configuration.

Secondly, ALD has so far been largely confined to laboratories due to non-availability of efficient, larger scale, high-throughput ALD systems. Whereas sputtering and CVD have been mainstream coating tools for decades, ALD has only recently started to gain acceptance as a mainstream industrial coating method. For example, ALD is widely seen as the desired manufacturing technology for producing high-quality functional layers for solar cells and packaging materials, but ALD is commonly considered too slow for high throughput manufacturing. However, large-area batch ALD tools, such as the Beneq P800, can operate up to 10 m<sup>2</sup> batch sizes and still maintain ALD cycle times in the range of 3-5 s. Currently, industrial ALD is diffusing into various industrial thin film areas where single wafer, batch or roll-to-roll ALD is the preferred coating method.

In this presentation, we discuss the different requirements for single wafer, conventional batch, cross-flow batch as well as spatial ALD deposition processes and tools for large throughput applications. In addition to conventional Al<sub>2</sub>O<sub>3</sub> and TiO<sub>2</sub> processes, SiO<sub>2</sub> processes are used as examples when scaling up chemistry from single wafer to batch ALD. In addition, process transfer from an R&D scale Beneq TFS 200R rotating drum reactor to the true roll-to-roll Beneq WCS 500, developed for OLED encapsulation applications, is discussed in detail. Results of the studies using this system are presented including temperature dependence of growth rate, RI and WVTR measurements.

#### 2:20pm NM+NS+MS+EM-MoA2 Enabling ALD for Semiconductor Manufacturing, D. Chu, Applied Materials Inc. INVITED

Atomic layer deposition (ALD) is being extensively studied for semiconductor applications because of its precise, atomic level thickness control for very thin films; ALD is extremely conformal and the overall thermal budget is lower than its CVD alternatives. However, ALD is inherently slow which makes it cost prohibitive.

Adoption of ALD processes into manufacturing requires consideration of multiple factors. At Applied Materials, we focus on three main areas to enable ALD for volume manufacturing.

1. Atomic level engineering to create differentiated solutions that boost device performance.
2. Tool architecture and methods to allow integration of multiple films without vacuum break. This is particularly of importance when films scale to Angstrom level, stability of the film becomes an issue. Extendable tool architectures allow integration of other films such as capping layers and pre-post treatments to address this issue
3. Accelerate adoption of standalone ALD films by improving manufacturability and productivity while maintaining single wafer performance

Example applications and challenges for each area will be discussed in this paper.

#### 3:00pm NM+NS+MS+EM-MoA4 Migration to ALD Techniques in the Semiconductor Industry: Pattern Effects, Microloading and Film Thickness Variability in Dielectric Thin Films Deposition, M.P. Belyansky, IBM Semiconductor R&D Center

The continuation of scaling in the microelectronics industry is having a profound effect on thin film deposition techniques and processes. One of the consequences of the scaling is a decrease in average film thickness to accommodate the shrinking device dimensions which amplifies the problem of film thickness variability. Most of the CVD deposition techniques and tooling are reaching the limit of reliable thickness control of very thin films. At the same time, circuit designs are becoming more complex, which leads to significant pattern density variation on macro scale. Therefore CVD technology is facing a tremendous challenge in controlling film thickness and properties across variable pattern density which has been one of the major reasons that facilitated the transition to ALD-like deposition techniques and processes in the industry.

The paper discusses the microloading effect (dependence of thin film deposition rate on pattern density) as well as other manifestations of pattern effects in the semiconductor manufacturing. The data shows the effect of microloading on the variation of as deposited film thickness across features of different size as well as for identical features with different pattern density in the surrounding areas. The microloading performance of CVD and ALD silicon oxide and silicon nitride dielectric thin films is covered as well as methods aimed at quantifying and improving thin film variability. The effects of major process parameters, precursor chemistry and tool design on the thin films microloading performance are delineated. Thin films step coverage over a nano scale feature and pitch to pitch film thickness dependence for CVD and ALD dielectric processes are also discussed.

#### 3:40pm NM+NS+MS+EM-MoA6 Interface Analysis of PEALD TaCN Deposited on HfO<sub>2</sub> using Parallel Angle Resolved X-ray Photoelectron Spectroscopy for sub-20nm Gate Last CMOS Transistors, F. Pierrat, ST Microelectronics, France, V. Beugin, R. Gassilloud, P. Michallon, CEA Grenoble, France, L. Dussault, B. Pelissier, LTM - MINATEC - CEA/LETI, France, C. Leroux, CEA Grenoble, France, P. Caubet, ST Microelectronics, France, C. Vallée, LTM - MINATEC - CEA/LETI, France

Sub-20 nm high-k/metal CMOS devices require about 2 nm thin metal gate electrode with adapted work function (WF) and chemical inertness regarding the high-k dielectric sub-layer. TaCN material deposited by Plasma Enhanced Atomic Layer Deposition (PE-ALD) has been investigated as a possible gate electrode candidate [1-2]. Depending on the carbon content TaCN can presents a *p-type* behavior with a WF from 4.5 to 4.7eV [3]. Besides plasma used for deposition may have an impact on the under-layer dielectric such as an increase of the EOT [4]. A deviation from bulk material characteristics of the metal gate WF is induced by the intimate bond linking environment at high-k/TaCN interface, but these chemical mechanisms are still unclear. Thus, in this work, interface of TaCN and HfO<sub>2</sub> dielectric is carefully analyzed by X-Ray Photoelectron Spectrometry (XPS), using Ta4f, Hf4f, O1s, C1s, N1s and Si2p core levels, and obtained bonding environments are correlated to work function extracted from MOS capacitors.

Thanks to chemical stability of SiO<sub>2</sub> [5], bonding environments of TaCN/SiO<sub>2</sub> and HfO<sub>2</sub>/SiO<sub>2</sub> stacks were chosen as reference for XPS analysis. Then, by comparing TaCN deposited on HfO<sub>2</sub> spectra with these references, the evolution of the chemical environments can be determined, thus a mechanism of interaction between the two materials is proposed. Furthermore, it appeared that, when deposited on HfO<sub>2</sub>, TaCN oxidation is higher than on SiO<sub>2</sub>, which is attributed to the higher capacity of HfO<sub>2</sub> to have O deficiency [6].

In addition, TaCN/HfO<sub>2</sub>/SiO<sub>2</sub> stack was measured using Parallel Angle Resolved XPS (PARXPS) in order to build a depth composition profile. This profile confirms the modifications of chemical environment such as oxidation of the electrode close to high-k/metal interface, it also shows N penetration in HfO<sub>2</sub>, which could be induced by plasma densification.

Finally, electrical results from MOS capacitors with TaCN/HfO<sub>2</sub>/SiO<sub>2</sub> stacks and TiN/W plug have shown an evolution of the *p-like* metal flat band voltage (V<sub>fb</sub>) with plasma conditions. The modifications of chemical bonding environment observed at the high-k/metal interface can give insight on this deviation of V<sub>fb</sub> with plasma.

[1] W. S. Hwang, D. Chan, B. Jin Cho, IEEE Transactions on Electron Devices, 55, (2008)

[2] H. Zhu and R. Ramprasad, Journal of Applied Physics 109, 083719 (2011)

[3] H. N. Alshareef, et al., Electrochemical and Solid-State Letters, 11, H182 (2008)

[4] H. C. Shin and C. Hu, Semiconductor Science Technologie, 11, 463, (1996)

[5] M. Zier, et al., Applied Surface Science 252, 234 (2005)

[6] G. D. Wilk, R. M. Wallace and J. M. Anthony, Journal of Applied Physics 89, 5243 (2001)

#### 4:20pm NM+NS+MS+EM-MoA8 Atmospheric Pressure Atomic Layer Deposition of Al<sub>2</sub>O<sub>3</sub> using Trimethylaluminum and Ozone, M.B. Mousa, D.H. Kim, C.J. Oldham, G.N. Parsons, North Carolina State University

Atomic layer deposition (ALD) is used for nanoscale coatings with high uniformity and precise thickness control. Currently, most commercial ALD processes operate in batch mode. Expanding to ambient pressure can increase throughput and facilitate its integration for applications such as smart textiles, flexible electronics and synthetic polymer coatings. We find that under certain flow conditions in the trimethylaluminum (TMA)/water ALD process for Al<sub>2</sub>O<sub>3</sub>, increasing the reactor pressure from ~ 2 Torr to 760 Torr can produce excess film growth per cycle.

For this work, we studied ALD of Al<sub>2</sub>O<sub>3</sub> using TMA/O<sub>3</sub> and compared growth at ~ 2 Torr to that at 760 Torr in a flow tube reactor. We measured film thickness by ellipsometry and surface morphology by AFM. Also, we plan to monitor in-situ growth using a quartz crystal microbalance (QCM). At 2 Torr, by changing the ozone and TMA exposure times, we saw clear ALD saturation at ~ 0.45 Å/cycle at 170°C. A shorter purging time after the ozone exposure tends to increase the growth per cycle. Deposition at higher pressure results in growth rates between ~0.3 and 0.6 Å/cycle at 205°C, with lower growth rates obtained under higher gas flow rate conditions. For both the water and O<sub>3</sub> processes at 760 Torr, a low gas flow rate of 0.5 standard liters per minute (slm) in our flow-tube reactor leads to a high growth rates of ~3 Å/cycle (for water) and 0.6 Å/cycle (for O<sub>3</sub>). For the water process at 760 Torr, increasing the flow rate to 10 slm somewhat

decreases the growth per cycle to  $\sim 1.35 \text{ \AA/cycle}$ . However, for the  $\text{O}_3$  processes at 760 Torr, we need only a relatively small increase to 1.5 slm to achieve growth of  $0.3 \text{ \AA/cycle}$ . This could be due to enhanced ozone desorption kinetics compared to the rate of water desorption under the conditions used. Also interestingly, we find for the water process that films deposited at high pressure have higher surface roughness than films deposited at low pressure. These results will help to identify the key parameters for new continuous atmospheric pressure ALD reactors designs.

**4:40pm NM+NS+MS+EM-MoA9 An Industrial Solution for Surface Passivation of c-Si using  $\text{AlO}_x$  Film Deposited by In-line Atmosphere Chemical Vapor Deposition.** *K. Jiang*, Gebr. Schmid GmbH + Co, Germany, *K.O. Davis*, University of Central Florida, *C. Demberger*, *H. Zunft*, *H. Haverkamp*, Gebr. Schmid GmbH + Co, Germany, *W.V. Schoenfeld*, University of Central Florida, *D. Habermann*, Gebr. Schmid GmbH + Co, Germany

Among the different dielectric passivation layers for crystalline silicon (c-Si) solar cells,  $\text{AlO}_x$  has recently received a great attention due to its excellent chemical and field effect passivation performance for p-type c-Si surface. It offers great promise as a rear-side passivation material for passivated emitter and rear cell (PERC) designs. However, up to this point in time, most of the development has been based on laboratory scale deposition systems and methods. Common approaches for synthesizing these passivation layers are thermal or plasma-assisted atomic layer deposition (ALD), whose deposition rates are typically too low ( $< 10 \text{ nm/min}$ ) to be compatible with high-volume manufacturing. Other deposition methods like PECVD or spatial separated ALD enable an increase in deposition rate by one order of magnitude (i.e.  $100 \text{ nm/min}$ ). An industrially-compatible deposition technique with low processing cost, easy-handling, compact size, and high throughput that still retains comparable passivation performance to ALD films remains a challenging task.

Using an in-line atmosphere chemical vapor deposition (APCVD) tool, we have synthesized amorphous  $\text{AlO}_x$  films from precursors of trimethylaluminum and  $\text{O}_2$ , yielding a maximal deposition rate of up to  $150 \text{ nm/min}$  per wafer. Deposition rate is determined by the film thickness divided by wafer transportation time through the CVD injector. Both top view and the cross-sectional SEM images present an intact  $\text{AlO}_x/\text{Si}$  interface. A smooth surface is shown without any outgassing (blistering) after deposition and a subsequent firing step. The as-deposited layers exhibit an over stoichiometric O/Al ratio of 1.65–1.75 due to the incorporation of an OH group inside the layer. For both high and low doped p-type c-Si wafers deposited with APCVD  $\text{AlO}_x$ , excellent surface passivation is achieved with a maximum effective surface recombination velocities ( $S_{\text{eff,max}}$ ) of  $8 \text{ cm/s}$  following by a firing step. These findings are attributed to the buildup of a large negative charge ( $Q_f \approx -3 \times 10^{12} \text{ cm}^{-2}$ ) and low interface defect density ( $D_{\text{it}} \approx 4 \times 10^{11} \text{ eV}^{-1}\text{cm}^{-2}$ ) following the firing process. It is believed that the incorporated OH group plays an essential role during the firing step. During the annealing/firing step, a certain degree of dehydration takes place (i.e. Al sites bonded OH termination start to bond via an O bridge), which may involve an octahedral to tetrahedral coordination change. This could facilitate the negative charge formation and release of atomic H for passivating the Si dangling bonds at the  $\text{AlO}_x/\text{Si}$  interface.

This data implies a high application potential of APCVD  $\text{AlO}_x$  for low cost industrial solar cell applications.

**5:00pm NM+NS+MS+EM-MoA10 Solution Based Processing of Floating Gate Memory using Additive-Driven Self-Assembly and Nanoimprint Lithography.** *J. Watkins*, University of Massachusetts

**INVITED**

Polymer and polymer-inorganic hybrid materials organized at the nanoscale are at the heart of many devices that can be created on flexible substrates for applications in energy generation and storage, microelectronics, optoelectronics, communications and sensors. The challenge is to produce these materials using process platforms and materials sets that are environmentally and economically sustainable and can be scaled for cost-effective, high value-added manufacturing. Here we describe a resource efficient, additive approach based on roll-to-roll coating of self-assembled hybrid materials. Specifically we report that nanostructured templates with periodic spherical, cylindrical, and lamellar morphologies exhibiting sub-10 nm domains can be easily obtained through the blending of commercially available disordered polymer surfactants with commodity homopolymers that selectively associate with one segment of the surfactant. We further demonstrate that order in the surfactant systems and in block copolymer templates can be induced by nanoparticle additives that undergo multi-point hydrogen bonding with one of the segments of the polymer template. These additives, which include metal and semiconducting nanoparticles, fullerenes, and other active components, impart functionality to the device. The strong interactions further enable particle loadings of more than 40% in

the target phase, resolving a crucial constraint for many applications. These systems can be scaled in our newly constructed R2R processing facility, which includes a custom microgravure coater for hybrid materials that is equipped for in-line substrate planarization and a precision R2R UV-assisted nanoimprint lithography (NIL) tool.

We illustrate the capabilities of these approaches by the fabrication of floating gate field effect transistor memory devices. For this application, the charge trapping layer is comprised of well-ordered polymer/gold NP composites prepared via additive-driven self-assembly; the addition of gold nanoparticles that selectively hydrogen bond with pyridine in poly(styrene-*b*-2-vinyl pyridine) copolymers yields well-ordered hybrid materials at gold nanoparticle loadings of more than 40 wt.%. The charge trapping layer is sandwiched between a dielectric layer and a poly(3-hexylthiophene) semiconductor layer. We can achieve facile control of the memory windows by changing the density of gold nanoparticles. The devices show high carrier mobility ( $> 0.1 \text{ cm}^2/\text{Vs}$ ), controllable memory windows (0–50V), high *on/off* ratio ( $> 10^5$ ) between memory states and long retention times. Strategies for patterning of the device using NIL will be discussed.

## Electronic Materials and Processing

Room: 9 - Session EM-TuM

### Electrical Testing and Defects in III-V's

**Moderator:** E.M. Vogel, Georgia Institute of Technology,  
E.X. Zhang, Vanderbilt University

#### 8:00am EM-TuM1 Characterization, Modeling and Control of Fermi Level Pinning Phenomena at III-V High-k MOS Gate Stack Interfaces, H. Hasegawa, Hokkaido University and RIKEN, Japan **INVITED**

III-V high mobility channel materials are currently drawing attention as possible material candidates for devices to continue scaling of CMOS transistors on the Si platform. Here, construction of high performance high-k MOS gate stacks is the key issue. Such gate stacks are also needed for various gate controlled III-V nanowire and nanodot devices for "Beyond CMOS" applications.

The purpose of this paper is to review the present status of understanding and control of "Fermi level pinning (FLP)" phenomena at III-V metal-gate high-k gate stack interfaces whose atomic level control is vitally important for success of above approaches. FLP at the insulator-semiconductor (I-S) interface deteriorates efficiency and stability of gate control of carriers while FLP at the metal-insulator (M-S) interface deteriorates the control capability of the threshold voltage of the MOSFET.

First, various models on FLP at I-S and M-S interfaces are reviewed, paying attention to chemical trends of pinning at Schottky barriers and MOS capacitors formed on GaAs and other III-V materials. Extremely complicated C-V behavior of ALD high-k dielectric/GaAs MOS capacitors is explained by the authors' disorder induced gap state (DIGS) model [1] where a U-shaped donor-acceptor gap state continuum causes pinning. Importance of the location of the charge neutrality level (CNL) [2] is pointed out for channel material selection, showing superiority of InGaAs over GaAs and others.

Then, various efforts to remove FLP at III-V I-S interfaces by inserting interface passivation layers are reviewed. In particular, authors' efforts to realize pinning-free high-k MOS interfaces on GaAs and InGaAs, using the silicon interface control layer (Si ICL) are described. Here, the Si ICL is an MBE-grown ultrathin Si interlayer which is proposed first by the authors [2,3] and now extended to construction of high-k MOS gate stacks. The structure has been investigated by XPS, contactless C-V and STM/STS methods and by ex-situ PL and MOS C-V measurements [4-7].

Finally, the FLP issue at metal-high-k Schottky interfaces is briefly discussed.

[1]H. Hasegawa and H. Ohno, J. Vac. Sci. Technol, B4, 1130 (1986) [2]H. Hasegawa, M. Akazawa et al J. Vac. Sci. Technol. B 7, 870 (1989), [3]H. Hasegawa, M. Akazawa, et al Jpn. J. Appl. Phys., 27, L2265 (1988) [4]M. Akazawa and H. Hasegawa, J. Vac. Sci. Technol. B25, 1481(2007)[5]M. Akazawa and H. Hasegawa, J. Vac. Sci. Technol. B26,(2008)1569 [6]M. Akazawa, A.Domanowska, B. Adamowicz and H. Hasegawa, J. Vac. Sci. Technol. B27, 2028(2009) [7]M. Akazawa and H. Hasegawa, Appl. Surf. Sci., 256, 5708(2010)

#### 8:40am EM-TuM3 An Investigation into the Origin of Anomalous Frequency Dispersion in Accumulation Capacitance of MOS Devices on III-V Substrates, R.V. Galatage, D.M. Zhernokletov, H. Dong, B. Brennan, C.L. Hinkle, R.M. Wallace, University of Texas at Dallas, E.M. Vogel, Georgia Institute of Technology

Anomalous frequency dispersion in accumulation is a commonly observed feature in experimental capacitance-voltage (C-V) characteristics of III-V metal-oxide-semiconductor (MOS) devices. Different models have been proposed to explain the origin of this frequency dispersion. One model attributes this dispersion to tunneling of the carriers into a disordered region caused by oxidation of the III-V substrate which is close to the interface between the III-V substrate and an insulator.<sup>1,2</sup> Another model attributes this dispersion to border traps located inside the high-k dielectric.<sup>3,4</sup> In this work, we use both HfO<sub>2</sub> and Al<sub>2</sub>O<sub>3</sub> with several interface treatments to differentiate between these two models.

MOS capacitors are fabricated on As-decapped n-In<sub>0.53</sub>G<sub>0.47</sub>As and n-GaAs substrates with either atomic layer deposited (ALD) HfO<sub>2</sub> or Al<sub>2</sub>O<sub>3</sub> dielectrics. An As-cap initially grown on the n-In<sub>0.53</sub>G<sub>0.47</sub>As surface to avoid spurious oxidation is thermally desorbed to leave a pristine surface. ALD HfO<sub>2</sub> and Al<sub>2</sub>O<sub>3</sub> is then deposited onto substrates prepared with several conditions: (1) *in situ* on the oxide free surface, (2) *ex situ* with a 10% ammonium sulfide and immediate transfer to ALD (<3 min exposure to air),

(3) *ex situ* with a 10% ammonium sulfide treatment and ~30 min exposure to air prior to ALD. Companion GaAs samples receive similar *ex situ* ammonium sulfide treatments, air exposure times and ALD dielectrics for comparison. A detailed analysis of the effect of the different disordered region thicknesses and different dielectrics on the accumulation frequency dispersion and interface trap density (D<sub>it</sub>) distribution will be presented. Correlation of electrical results to X-ray photoelectron spectroscopy (XPS) analysis will also be presented.

This work is sponsored by SRC FCRP Materials Structures and Devices Center and the National Science Foundation under ECCS Award No. 0925844.

[1] H. Hasegawa and T. Sawada, IEEE Trans. Electron Devices 27(6), 1055 (1980).

[2] A. M. Sonnet, C. L. Hinkle, H. Dawei, G. Bersuker, and E. M. Vogel, IEEE Trans. Electron Devices, 57, 2599 (2010).

[3] Y. Yuan, L. Q. Wang, B. Yu, B. H. Shin, J. Ahn, P. C. McIntyre, P. M. Asbeck, M. J. W. Rodwell, and Y. Taur, IEEE Electron Device Lett.32 (4), 485 (2011).

[4] E. J. Kim, L. Wang, P. M. Asbeck, K. C. Saraswat, and P. C. McIntyre, Appl. Phys. Lett.96 (1), 012906 (2010).

#### 9:00am EM-TuM4 Evaluation of Atomic Layer Deposited High-k Dielectrics on GaAs, H.J. Lim, Y.J. Choi, S.H. Lee, Seoul National University, Republic of Korea, J.H. Ku, N.I. Lee, Samsung Electronics Co. Ltd., Republic of Korea, H.J. Kim, Seoul National University, Republic of Korea

GaAs is a promising channel material for sub-20nm logic MOSFET due to high electron mobility. However the instability of its native oxide is considered to generate high density of interface states that can induce Fermi level pinning and frequency dispersion in capacitance-voltage (C-V) curve. Although a variety of dielectric materials have been investigated over the past 4 decades to improve interface properties, a few positive results have been reported: Ga<sub>2</sub>O<sub>3</sub> (Gd<sub>2</sub>O<sub>3</sub>) grown by molecular beam epitaxy (MBE) and Al<sub>2</sub>O<sub>3</sub> and HfO<sub>2</sub> grown by atomic layer deposition (ALD). In this study, n-type GaAs MOSCAP's were fabricated with ALD SiO<sub>2</sub>, Al<sub>2</sub>O<sub>3</sub>, La<sub>2</sub>O<sub>3</sub>, and HfO<sub>2</sub>, and measurements of C-V hysteresis, flatband voltage shift ( $\Delta V_{fb}$ ), and frequency dispersion were performed to investigate the dependence of electrical properties on dielectric materials and to find dielectrics suitable for a stable MOSCAP operation.

Only HfO<sub>2</sub> revealed good electrical characteristics with a C-V hysteresis of < 80 mV and  $\Delta V_{fb}$  of 40 mV under constant stress time and voltage, while SiO<sub>2</sub>, Al<sub>2</sub>O<sub>3</sub>, and La<sub>2</sub>O<sub>3</sub> showed significantly degraded characteristics with a C-V hysteresis of > 700mV hysteresis and  $\Delta V_{fb}$  of 200mV. But even though a single HfO<sub>2</sub> dielectric layer had good electrical characteristics, the stacked HfO<sub>2</sub>/SiO<sub>2</sub> dielectric layer on GaAs showed the degraded characteristics like a single SiO<sub>2</sub> layer, indicating that the electrical characteristics were mainly dependent not on bulk properties but on the interface properties with GaAs. X-ray photoelectron spectroscopy (XPS) analysis revealed that SiO<sub>2</sub>, Al<sub>2</sub>O<sub>3</sub>, and La<sub>2</sub>O<sub>3</sub> dielectrics produced more elemental As (As<sup>0</sup>) than HfO<sub>2</sub> did at the interface. In addition, for SiO<sub>2</sub>, Al<sub>2</sub>O<sub>3</sub> and La<sub>2</sub>O<sub>3</sub> dielectrics, As were detected on the top surface of dielectrics by Auger electron spectroscopy (AES) measurement, implicating that the origin of degradation was related with the amount of elemental As, which might diffuse out and induce vacancy defects during subsequent annealing process, at the interface.

Frequency dispersion characteristics in a C-V measurement were also compared. HfO<sub>2</sub> showed huge frequency dispersion of about 280 % ( $\Delta C_{1kHz-1MHz}/C_{1MHz}$ ) while SiO<sub>2</sub>, Al<sub>2</sub>O<sub>3</sub>, and La<sub>2</sub>O<sub>3</sub> resulted in the relatively small dispersion of about 50% unlike the C-V hysteresis tendency. However, HfO<sub>2</sub> on thin SiO<sub>2</sub> led to small dispersion similar to SiO<sub>2</sub>. Frequency dispersion was strongly correlated with the interface state density (D<sub>it</sub>). Therefore, we can conclude that both hysteresis and frequency dispersion in a C-V measurement are dependent on the interface properties of dielectrics, especially the amount of elemental As and D<sub>it</sub> level, respectively.

#### 9:20am EM-TuM5 High Energy XPS and Electrical Characterisation Studies of Metal Oxide Semiconductor Structures on Si, GaAs and InGaAs, G.J. Hughes, L.A. Walsh, Dublin City University, Ireland, P.K. Hurley, J.H. Lin, Tyndall National Laboratory, Ireland, J.C. Woicik, National Institute of Standards and Technology **INVITED**

In this work synchrotron radiation based hard x-ray photoelectron spectroscopy (HAXPES) measurements have been used to study the intrinsic electronic properties of high-k dielectric metal oxide semiconductor (MOS) structures on Si, GaAs and InGaAs substrates. The

MOS structures were prepared with both high (Ni) and low (Al) workfunction metal layers 5nm thick on both n and p doped semiconductor substrates. CV and IV measurements were also performed on an identical sample set where the top metal contact was 160 nm thick to facilitate electrical measurements, and Ni was replaced with Ni/Au, 70/90 nm thick, respectively. The 4150 eV photon energy used in the HAXPES measurements gave a photoemission sampling depth of ~15 nm ensuring that signals were simultaneously detected from the substrate, the 8 nm thick dielectric layers as well as the top metal contact. The binding energy of core levels in photoemission are referenced with respect to the Fermi level, therefore changes in the binding energy of a particular core level reflect differences in the position of the Fermi level in the semiconductor band gap. For the MOS structures fabricated using SiO<sub>2</sub>/Si, changes in the Fermi level positions and differences in the potential drops across the dielectric layers have been directly correlated with the metal workfunction differences observed in the CV and GV measurements. The MOS structures on ammonium sulphide passivated n (Si - 5x10<sup>17</sup> cm<sup>-3</sup>) and p (Zn - 5x10<sup>17</sup> cm<sup>-3</sup>) doped GaAs substrates were fabricated by the atomic layer deposition (ALD) of 8 nm thick Al<sub>2</sub>O<sub>3</sub> dielectric layers. A binding energy difference of 0.6 eV was measured between the GaAs core levels of the n and p doped substrates, independent of metal work function indicating that the Al<sub>2</sub>O<sub>3</sub>/GaAs interface is strongly pinned. Lattice matched 0.2 μm thick In<sub>0.53</sub>Ga<sub>0.47</sub>As layers, with both n and p doping (~4x10<sup>17</sup> cm<sup>-3</sup>), were grown by MOCVD on InP n<sup>+</sup> and p<sup>+</sup> substrates, respectively. Al<sub>2</sub>O<sub>3</sub> dielectric layers 8 nm thick were then deposited ex-situ by ALD on the native oxide and ammonium sulphide treated InGaAs surfaces. Binding energy measurements for the core levels of native oxide covered n-type doped InGaAs substrates with no metal cap were found to be consistently (~0.3 eV) higher than p-type samples reflecting the fact that the Fermi level is in a different position in the band gap. Deposition of the metals with different workfunctions resulted in limited movement of the Fermi level, indicating the partially pinned nature of the InGaAs/Al<sub>2</sub>O<sub>3</sub> interface. Corresponding changes in the potential across the dielectric layer were also measured.

10:40am **EM-TuM9 Metastable Centers and Localized States in AlGaN/AlN/GaN Heterostructures Studied by C-V, Admittance Spectroscopy, and DLTS.** *A.Y. Polyakov, N.B. Smirnov, A.V. Govorkov, E.A. Kozhukhova*, Institute of Rare Metals, Russian Federation, *S.J. Pearton, F. Ren, L. Lu*, University of Florida, *S.Y. Karpov*, Soft-Impact, Ltd, Russian Federation, *W. Lim*, Samsung LED, Republic of Korea

A set of AlGaN/AlN/GaN high electron mobility transistor (HEMT) structures with Al composition in the AlGaN barrier changing from 20% Al to 50% Al was grown by metalorganic chemical vapor deposition (MOCVD) on sapphire and studied by means of capacitance-voltage C-V measurements, admittance spectroscopy, reverse deep levels transient spectroscopy. C-V and admittance measurements were performed in the dark and after illumination. The results suggest the presence in the AlGaN barriers of deep negatively charged traps of high concentration measurably shifting C-V characteristics to more positive voltages. The density of negatively charged centers can be increased by cooling at high reverse bias. These centers are believed to have a relatively high barrier for capture of electrons. Their thermal activation energy is estimated as 0.6-0.85 eV, the optical ionization energy is close to 1.7 eV. The presence of such centers explains lower than expected from modeling threshold voltages of the studied structures. Admittance spectroscopy also reveals consistent presence of features corresponding to apparent activation energy 0.11-0.13 eV for measurements at reverse voltages corresponding to a peak in AC conductance dependence on bias. These peaks in conductance and steps in admittance were attributed to transitions from the ground state in the triangular well near the AlN/GaN interface to the quasi continuum of excited states in the well with subsequent thermal emission into the conduction band. For samples illuminated at low temperature admittance spectra show unusual peaks in conductance with the activation energy close to the activation energy of thermal emission from the traps responsible for persistent photoconductivity.

11:00am **EM-TuM10 Characterizations of Proton-irradiated GaN and 4H-SiC by KOH Etching.** *H.-Y. Kim*, Korea University, *Y.J. Shin, W. Bahng*, Korea Electrotechnology Research Institute, *J. Kim*, Korea University

We investigated the variations of the free electron concentrations and the etch pits such as threading screw dislocation (TSD), threading edge dislocation (TED) and mixed dislocation on proton-irradiated GaN and 4H-SiC. High energy protons create the radiation-induced defects (RD) such as single V<sub>Si</sub>, V<sub>C</sub> and interstitials, which can act as the carrier traps. Before proton irradiation, the energy loss and the penetration depth of the high-energy protons were assessed by Monte Carlo simulation (SRIM). Proton irradiations were performed on the sidewall and backside (carbon face of 4H-SiC) of the samples to examine the experimental proton-penetration depth. The irradiated fluence of the 6 and 8 MeV protons were 5x10<sup>15</sup> cm<sup>-2</sup>.

High-energy protons gradually lose their energy by Coulomb interactions until they approach to specific depth where protons collide with the lattice atoms and create the point defects. The free electron concentrations of pre-irradiated GaN and 4H-SiC were 4x10<sup>16</sup> cm<sup>-3</sup> and 5x10<sup>18</sup> cm<sup>-3</sup>, respectively. The free carrier concentrations of proton irradiated GaN and SiC showed less than 1x10<sup>16</sup> cm<sup>-3</sup>, which can be calculated from the Raman scattering. After proton irradiation, 4H-SiC was etched in molten KOH at 530 °C for 3 min to compare the shape of the etch pits before and after proton irradiation. It was reported that the different kinds of etch pit were apparently distinguished at low-doped SiC, while the classification of the etch pit on highly doped SiC were very difficult. We observed the effect of the free carrier concentrations to the shape and the size of the etch pits. The results of molten KOH etched proton irradiated 4H-SiC showed different etch pits which were clearly distinguished. The TSDs were approximately 2-3 times larger than TEDs in proton-irradiated sample. After 1700 °C thermal annealing, the free electron concentrations were partially recovered. The differences of TEDs and TSDs were less evident after thermal annealing due to the recovery of the free electron concentrations. More details will be discussed.

11:20am **EM-TuM11 Trapping Centers in High -k Dielectrics for MOS Devices.** *P. Lenahan*, Pennsylvania State University **INVITED**

This presentation will review experimental evidence with regard to trapping centers in high dielectric constant gate stacks in metal oxide semiconductor (MOS) devices. The presentation will deal primarily with hafnium oxide based systems on silicon. The presentation will include discussion of silicon/dielectric interface traps, trapping centers within the interlayer dielectric between the silicon and the high -k material, and defects in hafnium oxide. Most of the experimental evidence with regard to the physical and chemical nature of these trapping centers comes from electron paramagnetic resonance (EPR) and electrically detected magnetic resonance (EDMR). The presentation will thus emphasize EPR and EDMR measurements along with "electronic" measurements on these systems. An attempt will be made to link device processing, defect structures, and defect densities to the electronic properties of these high -k MOS systems.

**Graphene and Related Materials Focus Topic**  
**Room: 13 - Session GR+AS+EM+MI+MN-TuM**

**Optical, Magnetic, Mechanical and Thermal Properties**

**Moderator:** K.I. Bolotin, Vanderbilt University

8:00am **GR+AS+EM+MI+MN-TuM1 Characterization of Magnetically Tunable Iron Nanorod Coated Graphene Nanoplatelets.** *S.D. Johnson, M.H. Gowda, S.-F. Cheng, N.Y. Garces, B. Feigelson, F.J. Kub, C.R. Eddy, Jr.*, U.S. Naval Research Laboratory

Composites made from iron coated graphene nanoplatelets (GNPs) show promise for applications such as, magnetic switches, electromagnetic interference shielding, and electromagnetic waveguides due to the large conductivity of GNPs combined with the magnetism of iron. Additionally, this composite can be easily formed into millimeter thick sheets making it a promising composite for other applications.

We report a novel method to synthesize iron oxide compound onto GNP using microwave hydrothermal synthesis at 60° C and reaction times between 10 and 120 minutes. Scanning electron microscopy imaging reveals iron oxide nanorods approximately 100 nm long adhered to the GNPs for reaction times as short as 10 minutes. X-ray photoemission spectroscopy reveals that the iron/carbon ratio remains constant across these reaction times. The resistivity of the composite increases with reaction time from 0.2 to 0.6 ohm-cm. Saturation magnetization and coercive field values follow a decreasing trend with increasing reaction time. From 10 to 120 minutes saturation magnetization decreases by 70% from 170 emu/g and coercive field decreases by 40% from 52 Oe. Remnant magnetization of around 0.7 memu/g remains constant throughout. We also report the temperature-dependent magnetic response of the compound across the Morin transition, which for submicron particles of α-Fe<sub>2</sub>O<sub>3</sub> is near 250 K.

Preliminary results suggest that while the nanorod size and quantity remains constant with reaction time, the resistive and magnetic properties change. This may suggest that we are tuning the magnetism of the system by changing the iron structure between the ferromagnetic γ-Fe<sub>2</sub>O<sub>3</sub> and the antiferromagnetic α-Fe<sub>2</sub>O<sub>3</sub>.

8:20am **GR+AS+EM+MI+MN-TuM2 Dynamical Origin of Blue Photoluminescence from Graphene Oxide**, *A.L. Exarhos, M.E. Turk, P.M. Vora, J.M. Kikkawa*, University of Pennsylvania

The tunable broadband emission from graphene oxide (GO) has sparked significant interest in research regarding its potential for band gap engineering. Here, we use polarization sensitive time-resolved optical spectroscopy to study the spectral diffusion and sub-picosecond dynamics of the excited carriers in GO and photo-exposed GO, where photo-exposure has been demonstrated to constitute a reducing condition. In steady state measurements, a significant blueshifting of the photoluminescence (PL) is observed with photo-exposure. This blueshift correlates with a marked difference in the temporal behavior of the PL from GO and photo-exposed GO. The PL spectra are very similar at short delay times, but an increased non-radiative recombination rate in the exposed GO leads to a decreased lifetime in the material. Utilizing in-plane polarization memory measurements, we examine the electron-hole polarization in these systems which can probe excitonic effects and help to provide a better understanding of the role of the  $sp^2$  graphene lattice in GO and exposed GO. We further discuss the relevance of our data to the origins of PL in these systems.

A.L.E. gratefully acknowledges the support of NSF DMR-0907226. M.E.T., P.M.V., and the construction of a Kerr gate system are supported by the Department of Energy Office of Basic Energy Sciences Award DE-SC0002158.

8:40am **GR+AS+EM+MI+MN-TuM3 Spin-Transport and Magnetism in Graphene**, *R. Kawakami*, University of California, Riverside **INVITED**

Graphene is an attractive material for spintronics due to its high mobility and the low intrinsic spin-orbit and hyperfine coupling, which should lead to excellent spin transport properties. In 2007, graphene became the first material to exhibit gate tunable spin transport and spin precession at room temperature. However, the spin injection efficiency was low and the spin lifetime was much shorter than predicted theoretically. In this talk, I will report on our progress in this area. The low spin injection efficiency into graphene is due to the conductivity mismatch between the ferromagnetic metal (Co) spin injector and the single layer graphene (SLG). To alleviate this problem and enhance the spin injection efficiency, we developed atomically smooth MgO tunnel barriers by utilizing a  $TiO_2$  seed layer. With tunneling contacts, the non-local spin signal is found to be as high as 130 ohms at room temperature, with a spin injection efficiency of 30%. In addition to improving the spin injection efficiency, the tunneling contacts were found to improve the spin lifetime as well. This indicates that the short spin lifetimes reported before are due to the contact-induced spin relaxation from the ferromagnetic electrodes. Using tunneling contacts, we investigate spin relaxation in single layer graphene (SLG) and bilayer graphene (BLG). At low temperatures, contrasting behaviors of gate voltage dependence of the spin lifetime are observed between SLG and BLG, which suggest different mechanisms for spin relaxation in SLG and BLG. A final topic of interest is magnetism and the formation of magnetic moments in graphene. While there is substantial theoretical work on magnetic moments generated by hydrogen adatoms and lattice vacancies, the experimental situation is less clear. We have developed a new method for detecting magnetic moment formation based on scattering of pure spin currents in graphene spin valves. We will report the progress on our efforts to identify magnetism with this approach.

10:40am **GR+AS+EM+MI+MN-TuM9 A "How To" for Magnetic Carbon**, *H. Ohldag*, SLAC National Accelerator Laboratory, *E. Arenholz, T. Tyliczszak*, Lawrence Berkeley National Laboratory, *D. Spemann, R. Hoehne, P. Esquinazi, M. Ungureanu, T. Butz*, University of Leipzig, Germany

While conventional wisdom says that magnetic materials have to contain some metallic atoms, the confirmation of intrinsic magnetic order in pure metal free carbon represents an ultimate and general scientific breakthrough because of the fundamental importance of carbon as an elemental building block of organic as well as inorganic matter. The common controversy raised across all disciplines is whether the magnetism of carbon is intrinsic or induced by other elements. We address this controversy by providing clear experimental evidence that metal free carbon can be ferromagnetic at room temperature using dichroism x-ray absorption spectro-microscopy. For this purpose we acquired soft x-ray microscopy images of magnetic structures on a thin carbon film that have been produced by irradiation with a focused 2.25MeV proton beam. Our element specific magnetic probe shows no indication of magnetically ordered Fe, Co or Ni impurities in these samples. In a second step we investigate the particular electronic states that are involved in carbon magnetism and find that the carbon p-states as well as C-H bonds show a magnetic moment, indicating that hydrogenation plays a crucial role in developing the ferromagnetic order. Our surface sensitive approach reveals that the magnetism at the surface of the irradiated graphite samples is much larger than in the bulk of the

sample. We observe a surface magnetic moment similar to what is typically present in classical ferromagnetic 3d transition metals.

#### REFERENCES

P.Esquinazi et al., *Magnetic order in graphite: Experimental evidence, intrinsic and extrinsic difficulties*, Journal of Magnetism and Magnetic Materials, Vol 322, 1156 (2010).

H. Ohldag et al., *p-Electron ferromagnetism in metal free carbon probed by soft x-ray dichroism*, Phys. Rev. Lett. 98, 187204 (2007) H. Ohldag et al., *The role of hydrogen in room temperature ferromagnetism at graphite surfaces*, New J. Phys. 12 123012 (2010)

11:00am **GR+AS+EM+MI+MN-TuM10 From Graphene to Amorphous Carbon by Sublimation and Condensation**, *B. Steele, R. Perriot, V. Zhakhovsky, I.I. Oleynik*, University of South Florida

The mechanisms of the non-equilibrium melting process of graphene and the structure of the liquid phase of carbon was studied by molecular dynamics (MD). Graphene undergoes a non-equilibrium melting process at high temperature and low pressure as the carbon chains are formed out of the graphene sheet, thus making up a transient liquid phase of carbon. As the chains expand the material sublimates to a low dense gas of carbon chains. Under higher pressure the gas phase will condense to an intermediate porous phase of carbon with a significant  $sp^2$  fraction of atoms, followed by the liquid phase, and finally an amorphous phase. Mechanisms of melting of graphene, including formation of topological and Stone Wales (SW) defects in two and three dimensions will be discussed.

# Tuesday Afternoon, October 30, 2012

## Electronic Materials and Processing

Room: 9 - Session EM-TuA

### Materials and Processes for Advanced Interconnects

**Moderator:** J. Bielefeld, Intel Corporation, S. King, Intel Corporation

2:00pm **EM-TuA1 Interface Engineering of Porous and Non-Porous ILD Layers Using Molecular Layer Deposition for Interconnect Applications.** *J. Bielefeld*, Intel Corporation, *H. Zhou*, *P. Loscutoff*, Stanford University, *S. Clendinning*, Intel Corporation, *S.F. Bent*, Stanford University

As the dimensions continue to scale in interconnect processing, having a stable and controlled interface between the metal line and the dielectric material becomes more and more important. Molecular Layer Deposition (MLD) has been investigated as a method of growing thin films on dielectric surfaces which act as metal barriers, as blocking layers and as adhesion promoters. The advantage of MLD growth over conventional self-assembled monolayer (SAM) processing is the ability of MLD to easily grow films of varying thickness with tunable chemical functionality.

In this paper, we will discuss the growth and thermal stability of poly-urea-based MLD thin films on both porous and non-porous Carbon Doped Oxide (CDO) dielectric surfaces and compare this work to similar MLD films grown on conventional SiO<sub>2</sub>. A variety of characterization techniques, including thermal stress test, secondary ion mass spectrometry, x-ray photoelectron spectroscopy, and electron microscopy, were used to determine film composition, film stability, film adhesion, and degree of penetration into porous substrates. We investigate the importance of surface preparation on the anchoring of MLD films to CDO surfaces. Surface preparation is especially important when growing controlled layers on the surface of a porous dielectric, and we show that surface treatments influence the depth of penetration of the MLD film within porous CDO. Finally, we examine the deposition of thin metal films on top of MLD coated CDO layers (both blanket and patterned) and we show that the metal deposition process impacts both the MLD stability and the metal penetration into the ILD.

2:20pm **EM-TuA2 Synchrotron X-ray Scattering Investigation of Morphological Stability of Cu Thin Film Interfaces.** *A.P. Warren*, University of Central Florida, *M.F. Toney*, Stanford Synchrotron Radiation Lightsource, *K. Barkak*, Carnegie Mellon University, *I.I. Kravchenko*, Oak Ridge National Laboratory, *K.R. Coffey*, University of Central Florida

Nanomeric films of pure Cu continue to attract attention due to their widespread use as interconnect material in the semiconductor community. Among the various engineering and scientific challenges posed by the continued use of Cu is its high surface mobility, which is well known to result in both electromigration and stress induced void formation in interconnects. The use of barrier/adhesion layers greatly improves the reliability of Cu interconnects. Nonetheless, the diffusion of Cu along the Cu/barrier interface is not well understood. Addressing the thermal stability and morphological evolution of Cu/barrier interfaces with the intent of quantifying interfacial diffusivities is the ultimate goal of this research.

Synchrotron x-ray scattering was used to study the evolution of interface roughness with annealing for a series of Cu thin films. The films were encapsulated in SiO<sub>2</sub> or Ta / SiO<sub>2</sub> and prepared by sputter deposition. Specular x-ray reflectivity was used to determine the root mean square roughness for both the upper and the lower Cu / SiO<sub>2</sub> (or Cu / Ta ) interfaces. The lateral roughness was studied by diffuse x-ray reflectivity. Annealing the films at 600°C resulted in a smoothing of only the upper interface for the Cu / SiO<sub>2</sub> samples, while the lower Cu / SiO<sub>2</sub> interfaces and both interfaces for the Ta encapsulated films did not evolve significantly. As a function of roughness wavelength, the upper Cu / SiO<sub>2</sub> interfaces exhibited a roughness decay with annealing that was only 12.5% of that expected for classical capillarity driven smoothing of a free surface.

Continued work is focusing on further quantifying the interface kinetics for Cu/barrier systems. Using e-beam lithography methods, we have patterned a grating onto the surface of Cu thin films. Subsequent encapsulation and annealing will be carried out to study the effects of time and temperature on the patterned interface.

2:40pm **EM-TuA3 Interconnect Scaling for 10nm and Beyond.** *Z. Tokei*, IMEC, Belgium **INVITED**

The rapid introduction of different interconnect schemes enabled sustained scaling towards advanced technology nodes. Enablers are dimensional and

material scaling together with system level aspects. Both logic and memory chips require tight pitch interconnecting lines with some common aspects and at the same time some different requirements. From material and dimensional scaling point of view logic interconnects demand tight pitch metal lines with low-k dielectrics, while emerging memories demand high current (or voltage) through tight pitch metal lines embedded into silicon oxide or air gaps. Conventional interconnects are built using multilevel damascene recently added with multiple patterning techniques leading to increased complexity. In order to break down the barrier and pave the way for 10nm technologies and beyond further material innovation along with non-conventional integration schemes and potentially system architecture modification will be necessary. Copper interconnects will require less than 2nm cladding layer or eventually the complete omission of conventional Ta-based diffusion barriers. Copper based metallization is expected to extend to 15nm critical dimensions although the number of elements through alloying and various liners increases already today. At 10nm and below alternatives to Cu wiring without a reliability issue is a candidate. For thin film deposition self assembled mono-layers, electroless and CVD/ALD techniques are becoming important, while novel dielectrics increasingly rely on self-assembling chemistries. This talk will focus on options that are being considered for 10nm and beyond. While several aspects will be mentioned, the main emphasis will be put on material innovation. Examples and case studies will be detailed for dielectric and metal options along with the relevant material characterization. Examples include defect characterization in low-k materials, phase identification and stress measurements in metal lines.

4:00pm **EM-TuA7 High Throughput Crystal Orientation Mapping of Nanometric Cu: Impact of Surface and Grain Boundary Scattering on Electrical Resistivity.** *X. Liu*, Carnegie Mellon Univ., *A. Darbal*, Nanomegas, *K. Ganesh*, Univ. of Texas at Austin, *G. Rohrer*, *D. Choi*, Carnegie Mellon Univ., *P. Ferreira*, Univ. of Texas at Austin, *B. Yao*, *T. Sun*, *A.P. Warren*, Univ. of Central Florida, *M.F. Toney*, Stanford Synchrotron Radiation Lab, *K.R. Coffey*, Univ. of Central Florida, *K. Barkak*, Carnegie Mellon Univ.

Due to limitations in characterizing twin boundaries in nanocrystalline Cu, it has been difficult to account for twin boundary scattering in the quantitative analysis of the resistivity size effect. In this study, a recently developed high throughput electron diffraction based metrology method in the transmission electron microscope, known as ASTAR<sup>TM</sup>, is employed to obtain crystal orientation maps in two SiO<sub>2</sub> and 6 SiO<sub>2</sub>/Ta<sub>38</sub>Si<sub>14</sub>N<sub>48</sub> encapsulated nanocrystalline Cu thin films. In ASTAR<sup>TM</sup>, a dedicated hardware unit is used for precession and automated scanning of a nanosized quasi-parallel electron beam probe. A high speed external optical camera is then used for rapid acquisition of spot diffraction patterns. The acquired spot patterns are indexed automatically using a template matching algorithm. Significant improvement in the reliability of the orientation maps is achieved with electron beam precession. The use of precession reduces the dynamical effects and increases the number of spots in the diffraction pattern. The use of rapidly acquired spot patterns and the robust template matching algorithm make ASTAR<sup>TM</sup> highly suitable for obtaining large datasets of crystal orientations. Analysis of the orientation maps of the Cu films shows a significant fraction of incoherent twin boundaries, indicating a potentially higher resistivity contribution from twin boundary scattering than previously assumed. Including the mixture of coherent and incoherent twin boundaries in the study of the resistivity size effect shows that the contribution from grain boundary scattering is still the dominant resistivity size effect in Cu, compared to surface scattering. Inclusion of the twin boundary mixture in a quantitative model shows the resistivity data to be best described by the Fuchs Sondheimer surface scattering model and the Mayadas Shatzkes grain boundary scattering model, combined using Matthiessen's rule (simple summation), with a surface specularly coefficient,  $p = 0.50$ , and a grain boundary reflection coefficient,  $R = 0.26$ . These values can be compared with values of  $p = 0.52$  and  $R = 0.43$  obtained in previous studies where the presence of twin boundaries was not considered. The potential to separately quantify electron scattering at twin boundaries and non-twin grain boundaries, the role of surface roughness, measured by x-ray reflectivity using synchrotron radiation, and the role of voids, measured using high angle annular dark field imaging in the transmission electron microscope, will also be discussed.

4:20pm **EM-TuA8 Developing Robust Ultra-Low-k Dielectric ( $\kappa \leq 2.55$ ) Materials using Novel Characterization Techniques for the 20nm Node and Beyond**, D.R. Kioussis, Z. Sun, Y. Lin, GLOBALFOUNDRIES, A. Madan, N. Klymko, C. Parks, S. Molis, IBM Semiconductor R&D Ctr, E.T. Ryan, GLOBALFOUNDRIES, E. Huang, S.M. Gates, A. Grill, IBM T.J. Watson Res. Center, B. Kim, J.K. Kim, Samsung Electronics Co. Ltd., Korea, D. Restaino, T.H. Lee, IBM Semiconductor R&D Ctr, S. Hosadurga, IBM Research Group, S.A. Cohen, IBM T.J. Watson Res. Center, K. Virwani, IBM Research - Almaden

As the semiconductor industry pushes feature miniaturization limits beyond the 20nm node, novel interline dielectric materials with low dielectric constants ( $k$ -value), so called ultra low- $k$  (ULK) materials ( $k < 2.55$ ), are targeted to prevent capacitive crosstalk, interline leakage and reduced power consumption of advanced integrated circuits (IC). These materials are commonly porous (>15%) and organic in nature, which necessarily incur compromises in either the thermal or mechanical integrity with respect to more traditional dense low- $k$  and SiO<sub>2</sub> dielectrics. Porous organosilicate glass ULK films with  $k$ -values 2.4 - 2.55 deposited by PECVD and cured via UV irradiation were first put into production at the 45nm node to further minimize RC delay. These ULK materials incorporate a large number of methyl (Si-CH<sub>3</sub>) groups and pores into Si-O based network structures. The methyl groups disrupt the Si-O bond network, which tend to lower density and also lower polarizability making the film hydrophobic. Lower density, reduced polarizability, and greater hydrophobicity decrease the  $k$ -value. Introduction of porosity is used to further lower the  $k$ -value but other critical film properties, such as fracture toughness are affected. A viable ULK material must survive "damage" sustained from a series of processing steps that include dual-damascene (DD) litho, RIE, stripping and cleaning, CMP, and packaging. The reliability of devices containing these multi-layer DD stacks depends heavily on the chemical and mechanical stability of the dielectric, as this is the material and structural template in which the IC functionality is laid. Damage mechanisms occur when ULK is exposed to RF-plasma during etching or ashing. Subsequent moisture adsorption leads to the increase of effective  $k$ -value degrading performance. The integration challenges of ULK are significant, such as plasma damage, chip packaging, and ILD/metal barrier compatibility issues. Substantial optimization of the ULK properties via quick turn methods is crucial for successful integration in advanced 20 nm generations. This study will discuss optimization of the material properties of single or dual precursor based ULK films through the use of different process chemistry and tuning of material deposition and UV curing parameters to meet the integration and packaging requirements. Quick turn characterization techniques were used to determine critical film properties. Correlation between film properties to the degree of plasma damage and mechanical integrity of ULK will be shown. We will show that careful modification of the ULK properties to minimize damage resulted in the successful integration at the 20nm node.

4:40pm **EM-TuA9 Reflection Electron Energy Loss Spectroscopy Investigation of Band Gap and Defect States in Low- $k$  and High- $k$  Dielectrics**, B. French, S. King, Intel Corporation

Electrical leakage in high- $k$  metal gate transistors and low- $k$ /Cu interconnect structures is a growing, vital concern as the nano-electronics industry moves to sub-16 nm technology nodes and continues to implement new materials. In order to understand the various possible leakage mechanisms in low- $k$ /Cu interconnects, knowledge of the band gap and defect states in low- $k$  and high- $k$  dielectrics is needed but has gone largely unreported in many cases. In this regard, we have utilized Reflection Electron Energy Loss Spectroscopy (REELS) to determine the band gap of numerous single crystalline and amorphous low- $k$  and high- $k$  dielectric materials. We demonstrate that for standard single crystalline materials such as Quartz, 6H-SiC, and GaN, REELS band gap measurements agree with known values. For amorphous low- $k$  and high- $k$  thin film materials, we further demonstrate that REELS band gap measurements in most cases agree with optical measurements of the same materials. However in some cases, we have observed that the REELS analysis can be complicated by the existence of defect states within the band gap of these materials. While troublesome for band gap measurements, we demonstrate that this sensitivity can be utilized to determine the energy level of various defects in pristine and sputter damaged low- $k$  SiOC:H dielectrics and in some cases identify the chemical identity of the defect.

5:00pm **EM-TuA10 The Effects of Plasma Exposure and Vacuum-Ultraviolet Radiation on Photopatternable Low- $k$  Dielectric Materials**, M.T. Nichols, K. Mavrakakis, University of Wisconsin-Madison, Q. Lin, IBM T.J. Watson Research Center, J.L. Shohet, University of Wisconsin-Madison

Silsesquioxane-based photopatternable low- $k$  (PPLK) dielectric materials[1] are promising alternatives to existing low- $k$  dielectrics due to the reduction of BEOL integration complexity. However, processing-induced damage due to reactive species and energetic particles has been previously found to be

problematic for low- $k$  organosilicate dielectrics. Thus, for successful integration, the effects of charged-particle bombardment and photon irradiation (particularly in the vacuum ultraviolet range) must be characterized. In order to examine these effects, I-V and C-V characteristics were made on PPLK samples before and after exposure to a variety of argon plasma exposure conditions. Plasma parameters were varied between each exposure so that each sample was subjected to a range of charged particle and photon fluxes. In order to examine the effects of photon irradiation alone, PPLK samples were also exposed to monochromatic synchrotron radiation over energies varying from 5 to 15 eV. It was found that both charged-particle bombardment and photon irradiation have deleterious effects, resulting in increased magnitude of leakage currents and increased flat-band voltage shifts. VUV-exposed samples also exhibited increased leakage currents, but this effect was found to be strongly dependent on photon energy.

This work has been supported by the Semiconductor Research Corporation under Contract 2008-KJ-1871 and by the National Science Foundation under Grant CBET-1066231.

[1] Q. Lin, S.T. Chen, A. Nelson, et al., **Proc. Of SPIE** 7639, 76390J (2010)

5:20pm **EM-TuA11 A Survey of Alternative Methods for Curing Porous SiCOH Films**, N. LiCausi, V. Kamineni, GLOBALFOUNDRIES, S. Ohsiek, H. Geisler, M. Weisheit, M. Majer, GLOBALFOUNDRIES, Germany, E.T. Ryan, GLOBALFOUNDRIES

SiCOH films have been used in advanced semiconductor devices to enable continued scaling of interconnect integration. The further scaling of ultra low  $k$ -value (ULK) films has necessitated a move to porous SiCOH films. Porosity is intentionally introduced to decrease the dielectric  $k$ -value and therefore reduce interconnect RC delay. However, this porosity also leads to reduced mechanical strength and presents substantial challenges to integration and packaging.

Nanoporous thin films can be formed with PECVD of a SiCOH film with embedded porogen clusters. The porogen can either be supplied by a second porogen precursor or using a single precursor containing an embedded porogen fragment. The porogen is then removed with curing. Currently the industry favors UV assisted thermal curing to simultaneously drive out porogen (forming the porous structure) and enable cross-linking of the film matrix (Si-O-Si bond formation). However, prior investigation claims that this porogen is not completely removed, leaving porogen residue in the pores [1]. It is believed that cross-linking of the film matrix inhibits porogen removal and inversely, porogen residue prevents efficient cross-linking. Subsequently, this can lead to degraded electrical and mechanical performance.

A new approach under review uses a two-step curing procedure. First porogen is removed from the film with a novel film treatment. This step targets porogen removal, but does not cross-link the film's matrix. An example of this is remote H<sub>2</sub>/He plasma (H radical exposure) [2]. After removing the porogen, a traditional UV assisted thermal cure strengthens the film and drives out any remaining porogen. We evaluated this and two similar approaches and observed the same qualitative trends. Generally speaking, when using conventional curing techniques there is an unavoidable tradeoff between  $k$ -value and mechanical performance. However, the two-step process results in films which have both increased mechanical strength and improved electrical performance.

Films have been evaluated electrically ( $k$ -value, breakdown voltage, leakage current). Film structure (porosity and pore size distribution), mechanical properties (Young's modulus) and film composition were measured with ellipsometry porosimetry, nanoindentation and XPS/FTIR, respectively. The UV absorption peaks related to porogen residue have also been measured using vacuum ultraviolet spectroscopic ellipsometry.

[1] A.M. Urbanowicz, K. Vanstreels, D. Shamiryan, S.D. Gendt and M.R. Baklanova, *Electrochem. Solid St.* **12** (2009).

[2] A.M. Urbanowicz, K. Vanstreels, P. Verdonck, D. Shamiryan, S. De Gendt and M.R. Baklanov, *J. Appl. Phys.* **107** (2010).

5:40pm **EM-TuA12 Metallization Challenges in Integration of Soft Dielectric Materials**, R. Chebiam, C. Jezewski, B. Krist, H. Yoo, J. Clarke, Intel Corporation

In order to take advantage of reduction in transistor gate delay at smaller dimensions, back-end interconnect (RC) delay has to be minimized. One of the methods of reducing the system capacitance is by reducing the dielectric constant of ILD's at each technology node. There is an observed trend that modulus and hardness of dielectric films degrades with decreasing  $k$  value. This is either due to increased carbon content or increased porosity. Ultra low- $k$  materials ( $k < 2.2$ ) are well known to be susceptible to damage during the patterning process. However, there has been little focus on the damage resulting from the metallization process (barrier/seed, plate, and CMP). In

this study we use a spin-on dielectric (K~2.2) with E =4.5GPa and H= 0.3GPa to investigate metallization damage. The soft ILD shows little feature size blowout post metallization for large feature sizes (>100nm). However, features size blowout of ~10-18 % is seen for sub 100nm features post metallization compared to pre-metallization. Feature blow out appears to be driven by dielectric densification and to a less extent from material etch out. Densification damages the dielectric by increasing the k value and hence must be minimized. The origin of the feature size blowout can be traced to an energetic barrier or seed deposition process. For example, a high resputter PVD barrier process has similar blowout compared to an ALD Liner process. When the energy of barrier /seed process was decreased blowout was reduced, but this was accompanied by poorer sidewall coverage which will result in degraded gapfill and reliability. The key challenge can then be highlighted as developing a low energy barrier/seed process that has good sidewall coverage (conformality) and no feature blowout to enable ultra low-k dielectrics integration.

# Tuesday Afternoon Poster Sessions

## Spectroscopic Ellipsometry Focus Topic

Room: Central Hall - Session EL+TF+AS+EM+SS-TuP

## Spectroscopic Ellipsometry Poster Session

**EL+TF+AS+EM+SS-TuP1 Ellipsometric Characterization of Iron Pyrite (FeS<sub>2</sub>) and Samarium Sesquisulfide (Sm<sub>2</sub>S<sub>3</sub>) Thin Films.** A. Sarkar, N.J. Ianno, University of Nebraska-Lincoln, J.R. Brewer, Rare Earth Solar

Iron pyrite (FeS<sub>2</sub>) and samarium sesquisulfide (Sm<sub>2</sub>S<sub>3</sub>) are transition metal chalcogenides characterized as absorbing semiconductors with bandgaps of 0.95 eV and 1.8 eV respectively. Synthesis of both *n*-type and *p*-type samples have been reported in the form of single crystals and thin films for both materials. As a result of these properties they have received considerable interest as photovoltaic absorber materials. We present the characterization of FeS<sub>2</sub> and Sm<sub>2</sub>S<sub>3</sub> thin films using spectroscopic ellipsometry. FeS<sub>2</sub> thin films were synthesized by sulfurizing DC magnetron sputtered iron films and reactive ion sputtered iron (III) oxide films in H<sub>2</sub>S / Ar atmosphere. Sm<sub>2</sub>S<sub>3</sub> thin films were synthesized by reactive ion sputtering of Sm in an H<sub>2</sub>S / Ar atmosphere. This analysis gives the optical properties of chalcogenide films from near-UV (300 nm) to the mid-IR (20 μm). This can then be correlated to the structural and electronic properties as well. The analysis is corroborated with results obtained from Raman spectroscopy, scanning electron microscopy, profilometry, X-ray diffraction (XRD), and Van der Pauw measurements. The ellipsometric results can be used to access different processing methods for synthesizing FeS<sub>2</sub> and Sm<sub>2</sub>S<sub>3</sub>, to determine the presence of different phases and intermediate products. This work will lay the foundation for employing *in situ* ellipsometry as a process monitor and quality control tool during manufacture of earth abundant chalcogenide thin films.

**EL+TF+AS+EM+SS-TuP2 Temperature Dependence of the Dielectric Function of Germanium by Spectroscopic Ellipsometry.** A.A. Medina, L.S. Abdallah, S. Zollner, New Mexico State University

Germanium has important applications in photovoltaics as a substrate for III/V triple-junction solar cells, especially in space vehicles and for terrestrial concentrator-based applications. Unfortunately, the optical properties of germanium (complex refractive index and absorption coefficient) and their temperature dependence (important to consider the effects of the space environment or the radiation-induced heating in concentrators) are not as well known as for silicon, which limits the accuracy of modeling for solar cells and Ge-based optical interconnects. In this work, we report precision measurements of the complex refractive index of germanium from 0.5 to 6.6 eV at room temperature using variable-angle spectroscopic ellipsometry. To improve accuracy, especially at photon energies below 2 eV, we used a Berek waveplate compensator. By cleaning a commercial Ge wafer in isopropanol followed by deionized water, we were able to reduce the native oxide thickness to 1.3 nm. Heating the wafer in UHV at 700 K did not reduce the oxide thickness further. (The oxide thickness can be determined with precision measurements of  $\Delta$  below the band gap on a single-side polished wafer.) From the ellipsometric angles of the Ge wafer measured at three angles of incidence (65, 70, and 75°), we calculated the dielectric function from 0.5 to 6.6 eV, by correcting for the effects of a native oxide.

Mounting our wafer in a compact UHV cryostat allowed temperature-dependent measurements from 80 to 700 K at 70° angle of incidence. Using similar methods as described above, we determined the dielectric function at different temperatures. We also determined the critical-point parameters (amplitude, energy, phase angle, and broadening) of the E<sub>0</sub>, E<sub>1</sub>, E<sub>1</sub>+ $\Delta_1$ , E<sub>0</sub>' , and E<sub>2</sub> critical points as a function of temperature. To separate the non-resonant contributions from the critical-point line shapes, we calculated the second derivative of the dielectric function with respect to photon energy and fitted the result to analytical line shapes with two-dimensional critical points. In general, our results are in good agreement with those of Viña *et al.* However, our results cover a wider spectral range and are more accurate because of the use of a compensator. Work is in progress to form thermal oxides on Ge wafers by annealing in oxygen, which will allow a multi-wafer analysis for Ge similar to work on Si by Herzinger *et al.*

This work was supported by NSF (HRD-0803171 and DMR-11104934) and the New Mexico Louis Stokes Alliance for Minority Participation.

Reference: L. Viña, S. Logothetidis, M. Cardona Phys. Rev. B **30**, 1979 (1984).

# Wednesday Morning, October 31, 2012

## Electronic Materials and Processing

Room: 9 - Session EM+TF-WeM

### Hybrid Electronic Materials and Interfaces

**Moderator:** M.R. Linford, Brigham Young University, A.J. Muscat, University of Arizona

8:00am **EM+TF-WeM1 Versatile Electron Beam Chemical Lithography on the Basis of Monomolecular Films, M. Zharnikov, University of Heidelberg, Germany** **INVITED**

The talk reviews recent progress in Electron Beam Chemical Lithography (EBCL) on the basis of monomolecular templates provided by self-assembled monolayers (SAMs). Due to the monolayer thickness of SAMs and molecular size of their structural building blocks, patterning down to few nanometers is in principle possible. Depending on the architecture of the SAM constituents, different EBCL strategies can be used [1]. In the case of aromatic backbone, selective modification of specific tail groups at the SAM-ambient interface can be exploited [1]. In the case of aliphatic backbone, irradiation-promoted exchange reaction between the molecules in the primary SAM and potential molecular substituents can be used [2]. A further promising technique within the EBCL framework is Electron Beam Activation Lithography which involves activation of the amino tail groups of the primary SAM template disabled by specific quencher moieties [3]. This method is especially useful for the fabrication of morphological patterns. EBCL can also be adapted for biological applications, based on protein-repelling templates [4]. One can either perform a direct writing in such a template, which can be both SAM-based and polymer-like, or apply irradiation-promoted exchange reaction with well-controlled parameters. Using the above techniques, chemical patterning and surface engineering on the length scale ranging from cm to nm can be performed. Not only simple dot or stripe structures, but complex gradient-like and biology-inspired patterns can be fabricated as will be demonstrated by representative examples.

[1] M. Zharnikov and M. Grunze, *J. Vac. Sci. Technol. B* **20**, 1793-1807 (2002).

[2] N. Ballav, S. Schilp, and M. Zharnikov, *Angew. Chem. Int. Ed.* **47**, 1421-1424 (2008).

[3] S. Schilp, N. Ballav, and M. Zharnikov, *Angew. Chem. Int. Ed.* **47**, 6786-6789 (2008).

[4] N. Ballav, H. Thomas, T. Winkler, A. Terfort, and M. Zharnikov, *Angew. Chem. Int. Ed.* **48**, 5833-5836 (2009); *Nature*, **460**, 308 (2009).

8:40am **EM+TF-WeM3 Covalently Linked Organic Monolayers on Silicon Surfaces: Making Them Better, Stronger, Faster!, H. Zuilhof, Wageningen University, Netherlands**

Covalently linked organic monolayers on silicon surfaces provide a prime example of hybrid electronic materials. Such systems are required on the one hand to passivate the Si surface, and on the other hand provide an optimal electrical link between the bulk of the Si semiconductor and the liquid with which it interacts.

To obtain an optimal passivation a highly dense monolayer is required, and we present novel agents and methods that yield a denser formation of the monolayers. At the same time monolayer formation can be made faster, which reduces the chance for competing silicon oxide formation. Finally, this combination of properties is desired for really thin monolayers, which drives research to allow attachment of small molecules. The paper will present a combination of such newly developed methods, properties of the resulting monolayers and an approach for further systematic improvements.

9:00am **EM+TF-WeM4 Probing the Intrinsic Organic/Semiconductor Interface, W. Peng, O. Seitz, R. Chapman, University of Texas at Dallas, E.M. Vogel, Georgia Institute of Technology, Y.J. Chabal, University of Texas at Dallas**

The electronic properties of organic/semiconductor interfaces are crucial for a variety of applications, such as organic dielectrics and organic/inorganic hybrid solar cells. However, the accurate characterization of these interfaces is prevented by the large tunneling current through the molecular layer. Moreover, standard fabrication methods, such as the formation of top metal contact via evaporation, cause damages during the processing even if applied directly with extreme caution. We present here a novel method to protect the interface with a layer of high- $\kappa$  dielectric ( $\text{Al}_2\text{O}_3$ ) gently deposited on top of the organic layer using atomic layer deposition. The metal precursor reacts with the carboxylic head group of the self-assembled

monolayer (SAM) layer without affecting the underlying SAM/Si interface. Due to the increase of the dielectric layer thickness ( $\text{SAM}+\text{Al}_2\text{O}_3$ ), a large reduction in tunneling leakage current occurs, and conductance voltage measurements can be implemented with a mercury probe setup. Moreover, the gate stack shows enough robustness to survive the entire MOS capacitor fabrication. Capacitance voltage measurements show small frequency dispersion and a low  $D_{it}$ , on the order of  $10^{11} \text{ cm}^{-2}\text{eV}^{-1}$ , for the intrinsic SAM/Si interface demonstrating inherent high quality when it is protected by the  $\text{Al}_2\text{O}_3$  layer.

9:20am **EM+TF-WeM5 Towards Organic Electronics: Methods for the Selective Deposition of Semiconductors and Metals, J. Yang, Z. Shi, K. Borner, A.V. Walker, University of Texas at Dallas**

We describe recent progress in our laboratories to build robust complex two- and three-dimensional molecular constructs. This work has important applications in photovoltaics, molecular and organic electronics, sensing, photonics and other technologies. Several recent developments are discussed including the chemical bath deposition of PbS, the UV photoassisted chemical vapor deposition of Al, and the formation of Ni and Cu nanowires on micron-scale patterned surfaces. Optimization and further development of these techniques requires a detailed understanding of the reaction pathways involved in the interaction of organic thin films with metals, organometallic compounds, ions, and other compounds.

9:40am **EM+TF-WeM6 Electroless Deposition of Co on  $\text{SiO}_2$  Surfaces Modified by an Aminosilane Self-Assembled Monolayer, R. Jain, A. Ng, E. White, A.J. Muscat, University of Arizona**

As device interconnects continue to shrink in size, the formation of diffusion barriers between dielectric and metal surfaces becomes more difficult. Self-assembled monolayers (SAMs) can be used to chemically activate a variety of surfaces, and their potential for uniform and defect-free monolayer formation makes them attractive alternatives for barrier layers. SAMs can also serve as adhesion layers to promote the electroless deposition (ELD) of metals on some dielectric surfaces. A 3-aminopropyltrimethoxysilane (APTMS) SAM was formed on a well-hydroxylated  $\text{SiO}_2$  surface and studied as a function of solvent (methanol, IPA, and toluene), APTMS concentration (5.72 mM and 57.2 mM), and post-deposition rinsing in methanol, IPA or chloroform depending on the solvent used. An aminopropylsilane monolayer with a thickness of  $7.8 \pm 0.2 \text{ \AA}$  and roughness of  $3 \pm 1 \text{ \AA}$  was formed at an APTMS concentration of 5.72 mM in methanol and IPA, but multilayers were formed in toluene, which were deposited at a rate of  $0.4 \pm 0.06 \text{ \AA/min}$  and roughness of  $31 \pm 18 \text{ \AA}$ . The N 1s XPS peak at a binding energy (BE) of 398.8 eV verified that a primary amine group ( $-\text{NH}_2$ ) was present together with an equal coverage of protonated amine ( $-\text{NH}_3^+$ ). Based on N 1s XPS peak areas, the molecular density of the aminopropylsilane monolayer was  $4.2 \pm 0.6 \text{ molecules/nm}^2$ , which is about equal to the accepted value of the OH group density on the Si surface. ELD processes are known to be sensitive to surface termination and require a metal catalyst, such as palladium, to activate the surface. A layer of Pd atoms was deposited by immersing the APTMS SAM surfaces in an 80 mM  $\text{PdCl}_2\text{-HCl}$  solution for 2 min, yielding one Pd atom bonded to two amine groups based on XPS peak areas. These results suggest that Pd atoms are bonded to primary amines rather than protonated amines resulting in a coverage of half of the N sites. Cobalt was plated by immersing the Pd-coated surface in a solution of 0.05 M  $\text{CoSO}_4$ , 0.2 M dimethylaminoborane (DMAB), and 0.01 M diethylenetriamine (DETA). Cobalt replaced the Pd atoms on the surface depositing a seed layer that auto-catalytically yielded a thick cobalt film on the surface. The thickness of the Co increased with the deposition time as verified by both the Co 2p peak at a BE of 777.2 eV and attenuation of the Si 2p peak with time. These results demonstrate that an aminopropyl silane adhesion layer binds metals such as Co. The next step is to test the effectiveness as a diffusion barrier.

10:40am **EM+TF-WeM9 Polymer-Colloidal Nanocrystal Hybrid Materials for Photovoltaic Applications, J. Xue, R. Zhou, P.H. Holloway, University of Florida** **INVITED**

Hybrid photovoltaic (PV) cells based on conjugated polymers and colloidal inorganic semiconductor nanoparticles have attracted significant attention as an alternative for all-organic solar cells. However, so far the highest efficiencies for hybrid PV cells have been limited to 2-3%, significantly lower than that of all-organic PV cells. One main reason for the lower performance is attributed to the complex interfaces and surfaces involving the inorganic nanocrystals.

Here we report our recent work that significantly improves the efficiency of hybrid PV cells to the 5% level. First, a 30-70% increase in the device efficiency was achieved by incorporating a solution-processed ZnO nanoparticle layer between the active layer and the cathode. This was

attributed to a combination of electronic, optical, chemical, and morphological effects, including blocking leakage of photogenerated holes to the cathode, optimizing the optical intensity profile in the hybrid active layer, minimizing recombination or quenching of photogenerated excitons and charge carriers. Maximum power conversion efficiencies of 2.5% and 3.5% were achieved with a high-gap polymer P3HT and a low-gap polymer PCPDTBT, respectively. The incorporation of the ZnO nanoparticle layer also drastically improves the stability of the hybrid PV cells.

We further demonstrated another 30-50% improvement in the efficiencies of hybrid PV cells by treating the hybrid active layer in an acetonitrile solution with 1% ethanedithiol (EDT). This leads to a maximum efficiency of ~5.0% for the EDT-treated hybrid PV cell with a PCPDTBT:CdSe nanorod active layer. Detailed characterizations of the hybrid active layers before and after the EDT treatment revealed no appreciable differences in their morphology and absorption spectra; however the phosphonic acid organic ligands on CdSe nanocrystals are more completely removed, and an improved electron mobility was obtained upon EDT treatment. We attribute the enhanced efficiency to more complete removal of exciton/charge recombination centers and the subsequent atomic layer passivation of the CdSe nanorod surface.

11:20am **EM+TF-WeM11** **Obtention of Deterministic Patterns through Wrinkling Formation**, *J.L. Yague, J. Yin, D. Eggenstiele, M.C. Boyce, K.K. Gleason*, Massachusetts Institute of Technology

Formation of wrinkles through buckling of a stiff coating on a compliant substrate can be found very commonly in nature. For instance, the epidermal ridges, which form our fingerprints, show a very unique pattern due to out-of-plane bending of the epidermis. The use of wrinkling to obtain patterned surfaces has become increasingly significant for a wide range of applications, such as: microfluidic, tunable wettability, stretchable electronics, photonics or anti-fouling surfaces. In this work, we demonstrate the ability to obtain labyrinth and herringbone patterns using a 2D stretching-releasing approach.

On top of a compliant substrate, an acrylate-based polymer is deposited by initiated chemical vapor deposition (iCVD). iCVD is a solvent-free method that yields a conformal thin coating on virtually any substrate, giving a controllable thickness and tunable structural, mechanical, thermal, wetting, and swelling properties. Monomer together with an initiator is introduced into a reactor chamber under vacuum, where the initiator is decomposed over resistively heated filaments to obtain radicals. Radicals and monomer are then adsorbed on a surface, which is kept at a controlled temperature to promote adsorption, to yield the polymer by the classical free-radical mechanism. Here, deterministic herringbone patterns are achieved through wrinkling of the polymer thin film. Furthermore, a simplified theoretical model is developed to predict the geometry of the ordered herringbone pattern. Depending on the experimental conditions is possible to control the features of such pattern. We report, for first time, the obtention of herringbone patterns with a jog angle lower than 90°. Finally, this method also provides a tool to determine the Young's modulus of the films based only on the characteristic wavelengths of the pattern.

11:40am **EM+TF-WeM12** **Surface Dynamics of Hybrid Silicon Interfaces Explored via Helium Atom Scattering**, *Z.M. Hund, R.D. Brown*, University of Chicago, *L.E. O'Leary*, California Institute of Technology, *D. Campi, M. Bernasconi, G. Benedek*, Università di Milano-Bicocca, Italy, *N.S. Lewis*, California Institute of Technology, *S.J. Sibener*, University of Chicago

Surface dynamical properties of methyl-terminated silicon(111) were investigated with energy and momentum resolved inelastic helium atom scattering measurements. The narrow energy distribution and nondestructive nature of neutral helium atom beams allow us to probe the vibrational dynamics of this hybrid organic-semiconductor interface. Time-of-flight experiments identify single phonon inelastic scattering events including, but not limited to, those attributed to Rayleigh wave excitations. We have mapped out the entire surface Brillouin zone along the nearest neighbor and next nearest neighbor azimuths,  $\langle 011 \rangle$  and  $\langle 121 \rangle$ , respectively. Our experimental results are in excellent agreement with density functional perturbation theory calculations, which provide a detailed description of the dispersion curves. The combination of experimental measurements with theoretical calculations allows us to determine the interfacial Si-Si force constants, including coupling between the molecular adlayer and the substrate, displacement fields, and mode polarizations. Helium atom scattering complemented with DFPT calculations allow us to quantify these effects. Additionally, isotopic effects were probed by mapping the dispersion curves for the perdeutero-methylated silicon surface. Our results will be discussed with respect to hydrogen-terminated Si(111).

# Wednesday Afternoon, October 31, 2012

## Electronic Materials and Processing

Room: 9 - Session EM+OX-WeA

### Oxides and Dielectrics for Novel Devices and Ultra-dense Memory

**Moderator:** J.F. Conley, Oregon State University, J. Kim, The University of Texas at Dallas

2:00pm **EM+OX-WeA1 Dielectric Requirements for a Novel Tunnel-FET Based on Room-Temperature Superfluidity in Graphene Double Layers**, L.F. Register, X. Mau, D. Reddy, D. Basu, W. Jung, I. Sodeman, D. Pesin, A. Hassibi, A.H. MacDonald, S.K. Banerjee, University of Texas at Austin

INVITED

The Bilayer pseudo-spin Field Effect Transistor (BiSFET) is a novel transistor concept based on possible room temperature superfluidity in two graphene layers separated by a thin dielectric. In principle, the switching energy per device could be on the scale of 10 zJ, over two orders of magnitude below estimates for "end-of the roadmap" CMOS transistors. However, at the time of writing, neither a BiSFET nor just such room temperature superfluidity have been demonstrated, and doing so poses substantial challenges both theoretical and experimental. Most significant among these challenge for this novel device concept now appear to be those associated with its novel dielectric requirements. In this presentation I will cover the basic concepts behind graphene superfluidity and BiSFET concepts, our current understanding—and limits to that understanding—of the requirements for condensate formation, and how these requirements could impact BiSFET design. In particular, I will compare and contrast the dielectric needs for the proposed BiSFET to those of conventional transistors.

2:40pm **EM+OX-WeA3 Interfaces and Surfaces in Tunnel Field-effect Transistors**, G. Xing, University of Notre Dame

INVITED

Abstract: It is now recognized that compound semiconductor tunnel field-effect transistors (TFETs) can retain MOSFET-like speed at low supply voltages given that on-current and voltage can be lowered in proportion. To achieve high on-current at low V<sub>dd</sub>, the staggered-gap and broken-gap AlGaSb/InAs heterojunctions and graphene are being developed. In this talk I will first outline the recent experimental progress in the development of interband tunnel transistors with sub-60 mV/decade subthreshold swing at Notre Dame. Subsequent discussions will be then focused on the impact of interfaces and surfaces of the transistor on the TFET performance, in particular, the interface between the gate dielectric and semiconductor as well as the semiconductor surface after transistor isolation etch.

4:00pm **EM+OX-WeA7 Resistive Switching Characteristics of Al<sub>2</sub>O<sub>3</sub>/TiO<sub>2</sub> Bilayer ReRAM dependent on Al<sub>2</sub>O<sub>3</sub> Thickness**, H.Y. Jeon, J.S. Lee, J.G. Park, W.C. Jang, H.T. Jeon, Hanyang University, Korea

The next generation nonvolatile memory (NGNVM) devices should satisfy the device properties such as high density, fast operation speed, low power consumption, and high reliability. Recently, many type-NGNVM candidates are extensively considered to replace the conventional nonvolatile memory devices; polymer random access memory (PoRAM), phase change random access memory (PRAM), spin transfer torque random access memory (STT-RAM), and resistive switching random access memory (ReRAM). Among the many type-NGNVMs, ReRAM has attracted a great deal of attention in semiconductor industry mainly due to its high density integration, long retention time, small cell size, and fast switching speed. Also, the ReRAM has the simple structure like metal/insulator/metal (MIM) structure allowing the fabrication of 3 dimensional stack and nano cross-bar structure. There are two types of resistive switching for ReRAM. One is unipolar resistive switching (URS) and the other is bipolar resistive switching (BRS). The URS means the operation of set (program) and reset (erase) are under the same polarity of bias, whereas the polarity of bias for set operation is opposite to that of bias for reset operation in the BRS. The URS type ReRAM needs current compliance to prevent hard breakdown of transition metal oxide (TMO) when measuring the resistive switching. The URS is usually observed in ReRAM using binary transition metal oxides such as NiO, TiO<sub>2</sub>, and Al<sub>2</sub>O<sub>3</sub>, while the BRS appeared in ReRAM using perovskite materials like Cr: SrZrO<sub>3</sub>, Pr<sub>0.7</sub>Ca<sub>0.3</sub>MnO<sub>3</sub>. Among many deposition methods for metal oxide, atomic layer deposition (ALD) has recently received a great interest for manufacture of ReRAM. Especially, remote plasma ALD is expected to enhance the reactivity between metal-organic precursor and reactant gas with minimal plasma damage on substrate, allowing the low impurity content and high density of the deposited films. In RPALD, plasma is

generated remotely outside of chamber. And the radicals and ions generated in plasma region enter into the chamber by a downstream flow for chemical reaction of deposition. In this study, we investigated URS switching behaviors of ReRAM using Al<sub>2</sub>O<sub>3</sub>/TiO<sub>2</sub> bilayer deposited by remote plasma atomic layer deposition (RPALD) method. The thickness of Al<sub>2</sub>O<sub>3</sub> layers was varied to observe the discrepancy of set/reset voltage and operation current level. The deposited Al<sub>2</sub>O<sub>3</sub> and TiO<sub>2</sub> films are perfectly amorphous structures and their binding states have nearly stoichiometric composition. When operating the ReRAM with different thickness ratio, the dependence of operation voltage and current level on the thickness of Al<sub>2</sub>O<sub>3</sub> layers was observed.

4:20pm **EM+OX-WeA8 High- k SrTiO<sub>3</sub> Dielectric by Plasma-Assisted Atomic Layer Deposition**, N.Y. Garces, D.J. Meyer, B.P. Downey, V.D. Wheeler, D.W. Zapotok, C.R. Eddy, Jr., U.S. Naval Research Laboratory

Strontium titanate (STO) is a promising material that offers the possibility of achieving large dielectric permittivity (k) constants for gate dielectric and other applications. Thin (~28 nm) STO films were deposited by remote plasma-assisted atomic layer deposition on the native oxide of n-type Si substrates in an Oxford Instruments FlexAL reactor at ~250°C using Bis(Tris-IsopropylCyclopentadienyl) Strontium, Tetrakis(dimethylamido)titanium as metal precursors, and a remote oxygen plasma as oxidizer. The general approach to deposit the ternary perovskite SrTiO<sub>3</sub> is by alternating the ALD of the constituents TiO<sub>2</sub> and SrO in a specific ratio to control such properties as the stoichiometric composition and dielectric constant [1,2]. The deposition temperature was chosen to give optimum growth uniformity for both SrO and TiO<sub>2</sub> and to avoid decomposition of the precursors. The growth rate of the STO films was ~ 0.14 nm/cycle, which is slightly higher than the combined growth rate of the individual components. Also, the STO growth rate and stoichiometry are highly dependent on the temperature of the strontium precursor.

Initial capacitance-voltage (C-V) and current-voltage (I-V) results on 50-250 μm diameter circular capacitors patterned on ALD SrO:TiO<sub>2</sub> (1:1) films were obtained. These dielectrics exhibited a moderate (~ 20) dielectric constant with reduced reverse-biased leakage current of ~1.6x10<sup>-5</sup> A/cm<sup>2</sup> but larger forward bias leakage current ~ 1.2x10<sup>-3</sup> A/cm<sup>2</sup> at 1V. Hysteresis in forward and reverse C-V sweeps was not observed, suggesting that these films are high-quality with limited or no slow time-constant charge trapping. After annealing the STO films at 550°C in N<sub>2</sub> for 5 min, a reduction in the oxide thickness by ~ 9% was measured, as well as a small increase in the dielectric constant to ~ 28 as a result of crystallization [3].

During this study, the overall thickness of the dielectric was held relatively constant, while the relative ratio of SrO:TiO<sub>2</sub> was varied to tune the stoichiometry of the films and to monitor changes in the dielectric constant, optical band gap, E<sub>g</sub>, and the electrical performance of the resulting oxides. The thickness, growth rates, and ALD mode behavior of STO, SrO, and TiO<sub>2</sub> oxides were evaluated by spectroscopic ellipsometry measurements. We will present electrical measurements of STO oxides of various compositions with optimized deposition conditions for the chosen precursors, as well as stoichiometry assessments by x-ray photoelectron spectroscopy.

1. Vehkamäki, et.al. *Chem. Vap. Deposition*, **7**, 75 (2001)
2. Popovici, et.al. *J. Electrochem. Soc.*, **157**, G1 (2009)
3. Langereis, et.al. *J. Electrochem. Soc.*, **158**, G34-G38 (2011)

4:40pm **EM+OX-WeA9 Micro-Antenna Coupled Nano-MIM Diodes: Modeling, Design, Processing and Application**, N. Goldsman, Univ. of Maryland, CoolCAD Electronics LLC, F. Yesilkoya, Univ. of Maryland, S. Potbhare, CoolCAD Electronics, LLC, M. Peckerar, Univ. of Maryland, A. Akturk, CoolCAD Electronics, LLC, K. Choi, Univ. of Maryland, W. Churaman, U.S. Army Research Lab, N.K. Dhar, DARPA/MTO INVITED

An antenna coupled to a diode can convert electromagnetic power into DC power, which can be integrated over time and stored on a capacitor or used to charge a battery. The combination of the antenna and diode is typically called a "Rectenna". We are interested in developing a rectenna that operates in the infrared region of the electromagnetic spectrum. The applications of interest for IR rectennas include self-powering circuits and infrared imagers.

The rectenna structure we focus on consists of a micro-antenna and a rectifying metal-insulator-metal (MIM) diode for converting electromagnetic wave induced alternating current on the antenna to a direct current. The antenna couples to ambient or directed electromagnetic (EM) radiation, and the diode rectifies the AC signal for DC current and power generation. The frequency or the wavelength of the EM signal dictates the physical dimensions of the antenna, and the operating frequency of the

diode. Here one of the main challenges in achieving DC output upon IR radiation is to fabricate a diode capable of operating in the infrared range of frequencies, and more specifically at 30 Terahertz corresponding to 10 micrometer infrared radiation or approximately 300K. To meet this challenge, we are fabricating metal-insulator-metal diode structures with oxide thicknesses of on the order a couple of nanometers or less.

An application of significant interest is a high resolution, high speed IR imager that can operate at room temperatures. Expanding from a single pixel to a complete large array is a challenge because the added complexity may give rise to electromagnetic coupling between adjacent elements, which needs to be accounted for. In addition, IR imaging, which corresponds to 30 terahertz region of operation, is special because it represents an 'in-between' region between radio and optical frequencies. At 10 micron wavelengths, the photons are typically too small in energy to economically convert their AC power into DC using semiconductor or quantum based photodetectors. At the same time, their frequency is too high to utilize standard PN or Schottky barrier diode based rectification. We thus explore the use of a micro-antenna coupled to a MIM diode for AC to DC conversion. A major difficulty here is to develop a diode that responds quickly enough to be forward biased during one part of the AC cycle and reverse biased to the other half of the cycle, without having the parasitic capacitance of the diode short out the signal. The rectenna we are developing uses a Nickel/Nickel-Oxide/Nickel (Ni-NiO-Ni) MIM structure, fabricated and designed using unique modeling and processing techniques.

**5:20pm EM+OX-WeA11 High-Electron-Mobility SiGe on Sapphire Substrate for Next Generation Ultrafast Chipsets, H.J. Kim, Y. Park, National Institute of Aerospace (NIA), H.-B. Bae, Korea Advanced Institute of Science and Technology, S.H. Choi, NASA Langley Research Center (NASA LaRC)**

In the conventional silicon-on-sapphire (SOS) technology with the epitaxy of Si on *r*-plane (1-102) sapphire, typical device region do not need reverse bias between the substrate and device area for electrical separation, because SOS wafer is separated by the sapphire itself, a best insulator. The advantage is that the sapphire insulator is very thick, which engenders an ultra-small capacitance and therefore it can reduce parasitic capacitance and leakage current at a high operating frequency. However, SOS wafer has a limitation in carrier mobilities due to the silicon material. The mobilities of SiGe can be a few times higher than those of silicon due to the high carrier mobilities of germanium (p-type Si: 430 cm<sup>2</sup>/V·s, p-type Ge: 2200 cm<sup>2</sup>/V·s, n-type Si: 1300 cm<sup>2</sup>/V·s, n-type Ge: 3000 cm<sup>2</sup>/V·s at 10<sup>16</sup> per cm<sup>3</sup> doping density). Therefore, RF devices which are made with rhombohedral SiGe on *c*-plane sapphire can potentially run a few times faster than RF devices on SOS wafers.

NASA Langley's rhombohedral epitaxy uses an atomic alignment of the [111] direction of cubic SiGe on top of the [0001] direction of the sapphire basal plane (*c*-plane). It shows a sample of rhombohedrally grown SiGe on *c*-plane sapphire with a single crystalline percentage of 95%. Twin defects exist only at the edge of the wafer. The electron mobilities of the tested samples are between those of single crystal Si and Ge. For instance, the electron mobility of 95% single crystal SiGe is 1538 cm<sup>2</sup>/V·s which is between 350 cm<sup>2</sup>/V·s (Si) and 1550 cm<sup>2</sup>/V·s (Ge) at 6x10<sup>17</sup> /cm<sup>3</sup> doping concentration. Typically, a rhombohedral single crystal SiGe has 2 or 3 times higher carrier mobility than monocrystalline silicon. If the defects in SiGe can be removed, transistors with higher operational frequencies can be fabricated for a new generation of ultrafast chipsets.

**5:40pm EM+OX-WeA12 Fabrication and Characterization of Metal-Insulator-Insulator-Metal (MIIM) Tunnel Diodes, A.N. Nasir, J.F. Conley, Oregon State University**

MIM tunnel diodes have been proposed for high speed applications such as hot electron transistors, IR detectors, and optical rectennas for IR energy harvesting as well as backplanes for LCDs. The majority of these applications require highly asymmetric and non-linear I-V behavior at low applied voltages. The standard approach to achieving asymmetric operation in MIM devices is through the use of metal electrodes with different workfunctions ( $\Phi_M$ ). However, the amount of asymmetry achievable using this method is limited by the  $\Phi_M$  difference that can be obtained using practical metals. In this work, we use an alternative approach to achieving asymmetric and non-linear operation – engineering of the insulating tunnel barrier using nanolaminate pairs of insulators with different bandgaps and band-offsets to produce asymmetric tunnel barriers. Electrons tunneling from one metal electrode to the other will see a different shape barrier depending on the direction of tunneling and the bias applied.

Recently, we found that atomic scale roughness at the bottom metal-insulator interface can dominate the I-V characteristics of MIM diodes, even overwhelming the influence of  $\Phi_M$  difference. By using the amorphous metal ZrCuAlNi (ZCAN) as an ultra-smooth bottom electrode in combination with high quality dielectrics deposited via ALD, we were able

to fabricate MIM diodes dominated by FN tunneling. In this work, nanolaminate insulator stacks consisting of either HfO<sub>2</sub>/Al<sub>2</sub>O<sub>3</sub>, Ta<sub>2</sub>O<sub>5</sub>/Al<sub>2</sub>O<sub>3</sub>, ZrO<sub>2</sub>/Al<sub>2</sub>O<sub>3</sub>, or HfO<sub>2</sub>/ZrO<sub>2</sub> are deposited on sputtered ZCAN bottom electrodes via ALD. Al dots form the top gate electrode.

MIIM I-V characteristics were found to be sensitive to the relative thickness as well as the arrangement of the individual dielectric layers. In the ZCAN / Al<sub>2</sub>O<sub>3</sub> / HfO<sub>2</sub> / Al orientation, the asymmetric tunnel barrier opposes the effect of the asymmetric  $\Phi_M$ , a larger current is measured at positive bias, and asymmetry is lower than for a neat Al<sub>2</sub>O<sub>3</sub> insulator device. However, in the ZCAN / HfO<sub>2</sub> / Al<sub>2</sub>O<sub>3</sub> / Al orientation, the asymmetric tunnel barrier enhances the asymmetric  $\Phi_M$ , a larger current is measured at negative bias, and asymmetry is greater than for neat Al<sub>2</sub>O<sub>3</sub> or HfO<sub>2</sub> insulator devices. High asymmetry is seen when conduction in both dielectric layers is dominated by FN tunneling rather than bulk limited mechanisms. Ta<sub>2</sub>O<sub>5</sub>/Al<sub>2</sub>O<sub>3</sub>, e.g., did not show an enhancement in asymmetry.

In conclusion, we have fabricated dual insulator MIIM diodes that exhibit improved asymmetry over single layer MIM diodes. These results represent an advancement of the understanding necessary to engineer thin film based MIM tunnel devices for microelectronics applications.

## **Graphene and Related Materials Focus Topic Room: 13 - Session GR+AS+EM+NS+SS-WeA**

### **Dopants and Defects in Graphene; Graphene Interfaces with Other Materials**

**Moderator:** D. Gunlycke, Naval Research Laboratory

**2:00pm GR+AS+EM+NS+SS-WeA1 Increasing Interface Bonding and Tuning Doping Behavior at Metal-Graphene-Metal Sandwich Contact, C. Gong, R.M. Wallace, K.J. Cho, Y.J. Chabal, The University of Texas at Dallas**

Two types of interfaces can be formed between metals and graphene depending on the strength of the metal-graphene interaction: weak (metal physisorption) and strong (metal chemisorption) interfaces. "Physisorption" interfaces (e.g., with Al, Ag, Cu, Ir, Pt and Au) are characterized by a larger metal-carbon distance (>3 Å) with some charge transfer between metal and graphene (i.e. doping of graphene) that maintains its overall  $\pi$ -band dispersion. "Chemisorption" interfaces (e.g. with Ni, Co, Pd, and Ti) are characterized by a smaller metal-carbon distance (<2.5 Å) and strong orbital hybridization between metal-*d* and carbon-*pz* orbitals, resulting in the destruction of the graphene's  $\pi$ -band dispersion around the Dirac point. Till now, only a small fraction of all available metals has been used as electrode materials for carbon-based devices due to metal-graphene interface debonding problems. The issue therefore is to keep graphene's intrinsic  $\pi$  bandstructure by using weakly interacting metals while enhancing the interface stability.

We report an enhancement of the bonding energy of weakly interacting metals by using a metal-graphene-metal sandwich geometry, without sacrificing the intrinsic  $\pi$ -electron dispersions of graphene that is usually undermined by strong metal-graphene interface hybridization. This sandwich structure further makes it possible to effectively tune the doping of graphene with an appropriate selection of metals. Density functional theory calculations reveal that the strengthening of the interface interaction is ascribed to an enhancement of interface dipole-dipole interactions. Raman scattering studies of metal-graphene-copper sandwiches are used to validate the theoretically predicted tuning of graphene doping through sandwich structures.

**2:20pm GR+AS+EM+NS+SS-WeA2 Defects in Two-Dimensional Materials and their Heterostructures, L. Adamska, I.I. Oleynik, University of South Florida**

Recent developments in graphene electronics have stimulated an interest in other two dimensional materials such as hexagonal boron nitride (BN) and molybdenum disulfide (MoS<sub>2</sub>). In contrast to graphene, BN and MoS<sub>2</sub> possess appreciable band gap and may form good interfaces with graphene, which opens up exciting opportunities for development of novel nanoelectronic devices. For practical applications, it is important to understand the effect of defects, which appear during growth and processing, on resulting electronic properties. The defects in graphene, BN, MoS<sub>2</sub> and their heterostructures have been investigated by first-principles density functional theory. Their effect on electronic properties including density of states and simulated STM images will be discussed.

4:00pm **GR+AS+EM+NS+SS-WeA7 Metal Oxide Growth and Characterization on CVD Graphene**, *A. Matsubayashi*, College of Nanoscale Science and Engineering, University at Albany

Thin metal oxide layers deposited on graphene can be utilized as dielectric barriers between metals and graphene to help isolate a metal contact from the graphene channel. This is important for graphene based spintronic devices as dielectric layers between the ferromagnetic electrode and graphene have been shown to increase the spin relaxation time measured utilizing non-local detection and spin precession measurements<sup>[1]</sup>. However, simply depositing metal oxide layers such as aluminum oxide on graphene results in non-uniform film lowering the quality of the interface barrier<sup>[2]</sup>. In addition it is important to understand the stoichiometry of the resulting film. We will present a systematic study of aluminum oxide layers grown on CVD (chemical vapor deposition) graphene under ultra-high vacuum conditions with and without titanium seed layers. The aluminum oxide layers with the titanium seed layers showed reduced surface roughness. The chemical and structural composition determined by XPS (X-ray photoelectron spectroscopy) will be also presented that shows full oxidation of the aluminum and partial oxidation of the titanium.

References:

- (1) E. I. Rashba, *Phys. Rev. B*, **62**, 16267 (2000)
- (2) W. Han *et al*, *Phys. Rev. Lett.*, **105**, 167202 (2010)

4:20pm **GR+AS+EM+NS+SS-WeA8 Bi-layer Graphene Growth on Ni(111): The Role of Monolayer Graphene Rotation**, *A. Dahal, A. Rafik*, University of South Florida, *P.W. Sutter*, Brookhaven National Laboratory, *M. Batzill*, University of South Florida

Bi-layer graphene synthesis by chemical vapor deposition is of importance for field effect devices because the band gap can be tuned in bi-layer graphene by an applied electric field. Here, we demonstrate that bi-layer graphene can be synthesized above 650°C by chemical vapor deposition on thin Ni(111) films grown on YSZ(111) substrates in ultra high vacuum (UHV). We characterize the bi-layer graphene growth by low energy electron microscopy (LEEM), Auger electron spectroscopy (AES) and low energy electron diffraction (LEED). Below 600 °C graphene grows in registry with the Ni(111) lattice and no second layer graphene is formed upon cooling. At 650 °C rotationally misaligned graphene domains are formed on Ni(111) and we observe second layer graphene to grow by carbon-segregation under those rotated monolayer graphene domains. The difference in second layer graphene nucleation and growth is explained by the graphene-Ni interaction, which is much stronger for graphene in registry with the substrate than for rotated graphene. The segregated second layer graphene sheet is in registry with the Ni(111) substrate and this suppresses further carbon-segregation, effectively self limiting graphene formation to two layers.

4:40pm **GR+AS+EM+NS+SS-WeA9 Energetic and Kinetic Factors of Graphene Nucleation on Cu**, *N. Safran, M.S. Arnold*, University of Wisconsin-Madison

Chemical Vapor Deposition (CVD) of graphene on Cu substrates uniquely allows for growth of uniform monolayer graphene and is a promising route for its scalable production for many industrial applications due to low cost. The growth is a purely surface driven process, due to carbon's low solubility in the Cu substrate, and relies on the Cu surface catalytically decomposing a carbon precursor (methane). As the growth of graphene proceeds across the surface, the reactivity of the Cu is passivated by the graphene, making the growth self-limiting to monolayer coverage. Research interest on the control of nucleation is intensifying, as the polycrystalline character of the graphene films can limit mobility, thermal conduction, and mechanical strength via grain boundaries.

In this paper, we study the nucleation dependencies of graphene at ambient pressure CVD in the context of surface nucleation theory. At low methane partial pressures, the concentration of carbon on the surface on the copper is low and carbon clusters cannot grow to a critical size for nucleation. As the partial pressure is increased, the methane partial pressure reaches a critical value and nucleation occurs. Tracking the critical pressure as a function of temperature from 880 to 1075° C, we have determined the formation energy of the critical graphene nucleus to be  $\sim 1.5$  eV/carbon atom, via the relation  $c_{nuc} \sim \exp(-E_{form}/k_B T)$ . Additionally, we have found that the nucleation density of the graphene varies by 5 orders of magnitude over this temperature range at the critical methane concentration. The results are described under the desorption controlled regime of surface cluster nucleation.

Growths near the critical methane concentration yield hexagonal growing graphene domains characteristic of attachment limited kinetics, while at higher rates yield other growth shapes. Characterization by Raman Spectroscopy has been used to identify defects in the graphene layers. We find that the Raman defect band (D-Band) scales with the root of the

nucleation density, indicating the majority of defects are located at the domain boundaries and the D-band intensity scales with the distance between them. Electrical mobility measurements show nearly constant values in samples across the range of temperatures indicating other limiting factors besides internal defects. Growths at 900° C yield  $\mu > 1000$  cm<sup>2</sup>/Vs, ON/OFF ratio  $\sim 10$ , and Raman D/G ratio  $< 1$ , demonstrating high quality of growth even at relatively low temperatures.

5:00pm **GR+AS+EM+NS+SS-WeA10 Magnetic Spin Reorientation Transition in Graphene Covered Cobalt on Iridium(111)**, *A.T. N'Diaye*, Lawrence Berkeley National Laboratory, *J. Coraux, N. Rougemaille, C. Vo-Van, O. Fruchart*, Institut NÉEL, CNRS & Université Joseph Fourier, France, *A.K. Schmid*, Lawrence Berkeley National Laboratory

One of graphene's promises is to be material for spintronic applications. While the influence of a magnet on graphene is under intense investigation by many groups little attention is given to the influence of graphene on a magnet.

With spin polarized low energy electron microscopy (SPLEEM) we studied thickness dependent spin reorientation transition on this system and compare with Co/Ir(111) without graphene. Monitoring the spin orientation in three dimensions while increasing the film thickness by one ML at a time, we find that the presence of graphene on the film at least doubles the thickness at which the spin reorientation from out-of-plane to in-plane occurs from 6ML Co to transition to 12ML-13ML at 300°C and to between 14ML and 20ML at room temperature.

We attribute the significant contribution of the graphene/Cobalt interface to the magnetic anisotropy energy to a strong hybridization of graphene with Cobalt in directional bonds.

This work was supported by the U.S. Department of Energy under Contract No. DE-AC02-05CH11231, by the French ANR contract ANR-2010-BLAN-1019-NMGEM and by the Alexander von Humboldt Foundation.

5:20pm **GR+AS+EM+NS+SS-WeA11 Nucleation and Growth of Rh and Au Clusters on Graphene Moiré/Ru(0001)**, *B. Habenicht*, Oak Ridge National Laboratory, *D. Teng*, Georgia Institute of Technology, *L. Semidey-Flecha*, Oak Ridge National Laboratory, *D. Sholl*, Georgia Institute of Technology, *Y. Xu*, Oak Ridge National Laboratory

Nanometer and sub-nanometer sized metal clusters may possess electronic and catalytic properties that differ greatly from those of the corresponding bulk metals. For potential applications, dense arrays of uniform metal clusters are desirable. However, the synthesis of such cluster materials remains a formidable challenge. Moiré superstructures that develop in graphene supported on certain metals have been shown to be viable templates for driving the formation of uniform metal clusters.[1] On graphene moiré (GM) on Ru(0001), dispersed clusters are obtained for Rh whereas Au coalesces into very large 2D islands.[2,3] We carry out a computational study to understand the disparate morphologies of Rh and Au clusters on GM/Ru(0001) via a multi-scale approach. DFT calculations are performed to study the adsorption and diffusion of the adatom and ad-clusters of Rh and Au on GM/Ru(0001) and the bonding mechanism between the metals, graphene, and Ru substrate. The potential energy landscape is then used to perform kinetic Monte Carlo simulations for the diffusion, nucleation, and growth of Rh and Au clusters. This approach allows us to predict the spatial and size distribution of the metal clusters and may be generally applicable to identifying the conditions necessary for obtaining desired cluster morphologies on GM.

- (1) N'Diaye, A. T.; Bleikamp, S.; Feibelman, P. J.; Michely, T. *Phys. Rev. Lett.* **2006**, *97*, 215501.
- (2) Zhou, Z.; Gao, F.; Goodman, D. W. *Surf. Sci.* **2010**, *604*, L31.
- (3) Xu, Y.; Semidey-Flecha, L.; Liu, L.; Zhou, Z.; Goodman, D.W. *Faraday Discuss.*, **2011**, *152*, 267.

5:40pm **GR+AS+EM+NS+SS-WeA12 Graphitic and Pyridinic N Species on N-doped HOPG Studied by STM, STS, PES and DFT**, *M. Sakurai*, *T. Shikano*, *D. Ushigome*, *T. Suzuki*, University of Tsukuba, Japan, *Y. Harada*, *M. Oshima*, University of Tokyo, Japan, *S. Casolo*, University of Milan, Italy, *M.I. Trioni*, ISTM, Italy, *G.F. Tantardini*, University of Milan, Italy, *T. Kondo*, *J. Nakamura*, University of Tsukuba, Japan

Nitrogen doped graphene and carbon nanotube have been reported to show superior catalytic activity or superior support effect in the fuel cell. However, effects of the dopant nitrogen on the modification of the electronic structure of such graphite-related materials have not been clarified because a wide variety of defects with different types of C-N bonding configurations can coexist in nitrogen doped graphite.

Here, we report comprehensive atomic-resolution characterization of the defects in a nitrogen-doped graphite surface by scanning tunneling microscopy (STM), scanning tunneling spectroscopy (STS), Photoemission spectroscopy (PES) and first-principles calculations based on the density functional theory (DFT). Nitrogen-doped graphite was produced by nitrogen ion bombardment of the HOPG (highly oriented pyrolytic graphite) followed by thermal annealing at about 900 K.

Two types of nitrogen species were identified at the atomic resolution. One is pyridinic N (N having two C nearest neighbors) with single-atom vacancy. The other is graphitic N (N having three C nearest neighbors). In the case of pyridinic N with single vacancy, the local electronic states of the non-bonding pz orbital of carbon are found to appear at occupied region near the Fermi level at the carbon atoms around pyridinic N. On the other hand, the local electronic states of the non-bonding pz orbital of carbon are found to appear at unoccupied region near the Fermi level at the carbon atoms around graphitic N.

These results indicate that in both cases more than 300 carbon atoms are found to be modified by the dopant N to show the non-bonding pz orbitals. Moreover, these results suggest that the graphitic-N and pyridinic-N as well as their surrounding carbon atoms may act as "acid" and "base", because their non-bonding pz orbitals appear at empty and occupied region, respectively.

### Late Breaking Session

**Room: 14 - Session LB+EM+GR+MN+TR-WeA**

### Select Topics in Surface and Interface Science

**Moderator:** C.R. Eddy, Jr., U.S. Naval Research Laboratory, J.M. Fitz-Gerald, University of Virginia

2:00pm **LB+EM+GR+MN+TR-WeA1 Degradation Kinetics of Hard Gold Tribofilms**, N. Argibay, M.T. Dugger, M.T. Brumbach, S.V. Prasad, Sandia National Laboratories

Hard gold coatings are low alloy (> 98% Au) films exhibiting relatively low friction, electrical contact resistance (ECR) and chemical reactivity, making them uniquely suited for use in dynamic electrical connections. Hardness is primarily a result of grain refinement achieved through alloying. At relatively low temperature (approx < 0.5Tm) the diffusion of codeposited and underlayer species toward the free surface, dominated by grain boundary and pipe diffusion, has been identified as a principal degradation pathway. The consequent formation of metal oxides deteriorates ECR and often contributes to increased wear and friction. A clear antagonistic relationship exists between the hardening mechanism that improves tribological performance and the diffusion phenomena that reduce useful lifespan. This talk focuses on the role of diffusion and film morphology on the aging and degradation of the tribological and electrical characteristics of hard gold films.

2:20pm **LB+EM+GR+MN+TR-WeA2 Effect of Nitrogen Concentration on the Surface Properties of Plasma Nitrided Tool Steels**, P. Abraha, J. Miyamoto, Meijo University, Japan

The nitriding of tool steel was performed in electron beam excited plasma using neutral nitrogen species and nitrogen ions. The plasma apparatus is composed of three regions: the discharge region, the acceleration region and the processing region. This set up has the advantage of controlling the energy and number of electrons involved in producing the plasma independently.

In this study, the control of the nitrogen concentration on the formation of the hard but brittle compound layer and the effect on the tribology of the tool steel surface were investigated. Electron probe micro-analyzer (EPMA) results revealed that nitrogen concentration of samples nitrided by neutral nitrogen species had deep diffusion layer before reaching the threshold value of 6% nitrogen concentration that is necessary for the formation of the compound layer. Whereas in the samples nitrided by nitrogen ions, compound layer was confirmed right from the onset of the nitriding process.

The results of our experiments show that in nitriding the tool steel for 6h, below the threshold value, a mirror finish surface (Ra=14nm) with a deep diffusion layer of (up to 80 micrometers) and a surface hardness of more than two times (1300 Hv) that of the untreated sample (600 Hv) were produced. Our results demonstrate that neutral species based nitriding is effective for high performance and high precision mechanical components

that require high hardness and wear resistance without altering the as finished dimensional accuracy, surface roughness and appearance.

2:40pm **LB+EM+GR+MN+TR-WeA3 High Strength Carbon Fiber Composite Wafers for Microfabrication**, L. Pei, K. Zufelt, R. VanFleet, R.C. Davis, J. Lund, K. Jones, B.D. Jensen, Brigham Young University, J. Abbott, M. Harker, M. Zappe, S. Liddiard, Moxtek

Carbon fiber composites are very high strength materials that could be enabling materials for micro and mesoscale applications. These materials have comparable strength to silicon but are much less brittle and can achieve four times higher strain. Several challenges must be overcome before carbon fiber composite devices can be fabricated on this scale. One challenge is the fabrication of ultra-thin wafers with low void density and low surface roughness. Another challenge is the ability to reliably machine the material into desired patterns. Here we present a method for curing carbon fiber wafers (~100  $\mu\text{m}$  thick) with low surface roughness, low void density, a modulus of 50 GPa, and a yield strength of ~3.6 GPa. These wafers are suitable for laser machining into high fidelity micro and mesoscale structures. We will present laser micromachined devices made from these wafers including a series of high strength support structures for ultrathin membranes and a high-dynamic-range accelerometer.

4:00pm **LB+EM+GR+MN+TR-WeA7 Selective Graphitization using Multi-Ion Beam Lithography**, J. Fridmann, Raith USA Inc., S. Tongay, University of California, Berkeley, M. Lemaire, A.F. Hebard, B. Gila, University of Florida, A. Nadzeyka, Raith GmbH, Germany, F. Ren, X. Wang, University of Florida, D.K. Venkatachalam, R.G. Elliman, Australian National University, Australia, B.R. Appleton, University of Florida

Promising techniques for growing graphene on SiC single crystals for electronic device fabrication include heating in UHV above the graphitization temperature ( $T_G$ )<sup>1</sup>; or processing them in vacuum using pulsed excimer laser<sup>2</sup>.

We report recent findings on the graphitization of SiC using a patterned Ga implantation, in which the implanted regions exhibit reduced  $T_G$  and enhanced graphitization above  $T_G$ . Here we report an approach that combines ion implantation, thermal or pulsed laser annealing (PLA), and multi-ion beam lithography (MIBL) to both pattern and synthesize graphene nanostructures on SiC single crystals at low temperatures. This approach utilizes a MIBL system developed at the University of Florida in collaboration with Raith for implantation/nanofabrication, in combination with thermal annealing in vacuum or PLA with a 25 ns pulsed ArF laser in air. To investigate the mechanisms and the effects of the implanted species, ion damage, and annealing, samples were also subjected to broad-area ion-implantations using facilities at the Australian National University.

It has recently been shown that implantation of Si, Ge, Au, or Cu followed by thermal annealing in vacuum below the  $T_G$  of SiC can selectively grow graphene only where the ions are implanted, and that graphene nanoribbons a few nanometers to microns wide can be formed using MIBL<sup>3</sup>. Additionally, we will show that graphene can be formed on implanted and/or unimplanted SiC by ArF PLA in air, at fluences from 0.4-1.2 J/cm<sup>2</sup>. AES, SEM, X-sectional TEM, micro-Raman analyses and heat flow simulations are presented to verify graphene growth and explain the effects and mechanisms involved.

1. C. Berger, Z. Song, T. Li, X. Li, A. Y. Ogbazghi, R. Feng, Z. Dai, A. N. Marchenkov, E. H. Conrad, P. N. First, and W. A. de Heer, J. Phys. Chem. 108, 19912 (2004)

2. Sangwon Lee, Michael F. Toney, Wonhee Ko, Jason C. Randel, Hee Joon Jung, Ko Munakata, Jesse Lu, Theodore H. Geballe, Malcolm R. Beasley, Robert Sinclair, Hari C. Manoharan, and Alberto Salleo; ACS Nano Vol.4, No. 12, 7524-7530 (2010).

3. S. Tongay, M. Lemaire, J. Fridmann, A. F. Hebard, B. P. Gila, and B. R. Appleton, Appl. Phys. Lett. 100, 073501 (2012).

4:20pm **LB+EM+GR+MN+TR-WeA8 Unrippling and Imaging of Extra-Large Free-Standing Graphene with Atomic Precision**, W.W. Pai, R. Breitweiser, Y.C. Hu, Y.C. Chao, National Taiwan University, Taiwan, Republic of China, Y.R. Tzeng, Institute of Nuclear Energy Research of Taiwan, Republic of China, L.J. Li, Academia Sinica, Taiwan, Republic of China, K.C. Lin, Catholic Fu Jen University, Taiwan, Republic of China

Nanoscale ripple is believed to be a common feature most manifested in free-standing graphene and is expected to play an important role in altering the coupling of graphene's electronic and geometric structures. Direct characterization of free-standing graphene ripple is challenging from atom-resolved transmission electron microscopy (TEM) due to its limited depth resolution. Recent scanning tunneling microscopy (STM) of free-standing graphene uses small suspended area (1 or 5 microns) samples and can introduce uncontrolled tension that alters the intrinsic graphene structure. Here we report an STM study of suspended extra-large (~4000 micron<sup>2</sup>) Cu

CVD graphene that was prepared with a resist-free transfer and characterize its electromechanical response in details. In our study, a series of controlled “Z-V” spectroscopy were carefully conducted. In Z-V spectroscopy, the tip displacement vs. sample bias in close-loop condition is recorded. This gives hints on the nature of interaction forces and the mechanical response of graphene. In contrast to a solid surface, the graphene membrane is very compliant and Z-V curves are characterized by a fast-rise regime and a plateau regime that follows. Graphene deformation up to 100 nm with simply a small  $\sim 1$  V bias ramp was observed. We discovered that our graphene is in best analogy with a curved rubber band that maintains quasi-static in shape until it is either pulled or pushed to tensile stress regimes. The graphene can be manipulated by the STM tip through electrostatic and van der Waals forces, with the latter being significant when it is repulsive. In its transit to tensile-stressed state, the graphene exhibits a series of sudden speed jump; we interpret these events as unripping of graphene ripples and render support with molecular dynamics (MD) simulation. Atom-resolved graphene images provide direct evidence of nanoscale structure ripples in its intrinsic state and the smoothing out of such ripples in the tensile regimes. Surprisingly, on rippled monolayer graphene, coexistence of triangular and hexagonal graphene lattices without tip condition change were observed. Our study provides a foundation to understand and control the electromechanical response of graphene (or other flexural atomic crystals) in its pristine two-dimensional form when subjected to a local proximal probe, therefore paves way to further investigate its structure-property correlation with atomic precision.

**4:40pm LB+EM+GR+MN+TR-WeA9 Ultrafast Charge Transfer at Monolayer Graphene Surfaces with Varied Substrate Coupling.** S. Lizzit, ELETTRA Sincrotrone Trieste, Italy, R. Larciprete, CNR, Institute of Complex Systems, Italy, P. Lacovig, ELETTRA Sincrotrone Trieste, Italy, K. Kostov, Bulgarian Academy of Sciences, Bulgaria, D. Menzel, Technische Universität München and Fritz Haber Institute, Germany

The importance and scientific appeal of graphene monolayers (Gr) are out of question, and investigations of its electronic properties abound. Most of these center on the most spectacular region, that around the Dirac cone, which is also the most relevant region for possible devices. But regions outside of this region are also important, since their correct representation requires basic understanding, and since they may relate to applications in photonics, photochemistry, and contact formation. Also, static investigations are more frequent than those of dynamics.

We present here the first investigation of electron dynamics at energies above the Fermi (and Dirac) energy but below the vacuum level [1]. To this purpose we used the core hole clock (CHC) method with adsorbed argon and measured the transfer rate of a localized electron (the 4s electron on core-excited Ar) to the surface of Gr monolayers with variable substrate coupling: strong but graded coupling for Gr on Ru(0001) (“valleys” and “hills”), and decoupled Gr ML on SiO<sub>2</sub>. We obtained the latter system by using the recently developed transfer-free approach [2] based on the synthesis of SiO<sub>2</sub> layers directly below Gr epitaxially grown on Ru(0001), through a stepwise reaction between intercalated silicon and oxygen. This method provides the optimal system to study the electronic properties of Gr using spectroscopic approaches, such as the CHC method.

We find strong variations of CT time between  $\sim 3$  fs (Gr ML strongly coupled to substrate on Ru(0001) “valleys”) and  $\sim 16$  fs (decoupled Gr on SiO<sub>2</sub>). A ratio of 1.7 is found between the “hills” and “valleys” of the corrugated Gr/Ru. The very fast CT on Gr/Ru valleys is interpreted as due to hybridized Ru orbitals “reaching through” the Gr layer which change with the relative Gr/Ru alignment and distance. On the decoupled Gr layers the intrinsic coupling to the Gr empty  $\pi^*$  states determines the CT time. The intermediate CT time for the Gr hills on Ru shows that these regions are far from the “decoupled” condition. The results contribute new information on the still controversial states of Gr/Ru, and shed light on the empty density of states above Gr surfaces and the coupling to them in an energy range possibly important for photonic applications of Gr, such as solar energy conversion.

[1] S. Lizzit, R. Larciprete, P. Lacovig, K.L.Kostov, D. Menzel, *in preparation*

[2] S. Lizzit *et al.* Nanoletters (2012) DOI: 10.1021/nl301614j

**5:00pm LB+EM+GR+MN+TR-WeA10 Fano Interference Effects in Hydrogen Intercalated Graphene.** A. Boosalis, T. Hofmann, University of Nebraska-Lincoln, R. Elmquist, M. Real, National Institute of Standards and Technology (NIST), M. Schubert, University of Nebraska-Lincoln

Graphene has been the focus of much recent research due to its unique electronic and optical properties, with potential for high performance electronics, tunable ultra-fast lasers, and transparent electrodes. Further development of graphene for commercial use requires effective large-area epitaxial production that maintains the desirable properties of exfoliated graphene. One such method of epitaxial graphene growth is thermal

sublimation of Si from SiC. Sublimation of Si from the Si-face (0001) is the most controllable but produces a  $(6\sqrt{3} \times 6\sqrt{3})R30^\circ$  surface reconstructed layer prior to graphene formation. This layer can be altered by subsequent hydrogen intercalation, resulting in quasi-free-standing (QFS) epitaxial graphene.

In order to determine the effect of hydrogen intercalation on the optical properties of graphene we performed spectroscopic ellipsometry experiments in a spectral range of 3 to 9 eV before and after hydrogen intercalation of buffer layer only carbon growth on 6H SiC (0001). Spectroscopic ellipsometry is a widely used technique for determining the optical properties of thin films, and can provide sensitivity to film quality, morphology, and strain. In the case of graphene sensitivity is obtained through the critical-point (CP) located at 5.1 eV and modified by a Fano interference. Analysis of absorption near the CP is achieved through a parameterized model dielectric function (MDF) which is varied until a best-match between model and experimental data is obtained.

Best-match model results show drastic changes in the imaginary part of the MDF between previous measurements of buffer layer only growth on SiC, and buffer layer growth after hydrogen intercalation. Buffer layer only growth exhibits a far greater absorption throughout the spectrum, with an exciton produced maximum energy point that is shifted toward the infrared from the CP energy. After hydrogen intercalation, the QFS graphene layer exhibits a lowered absorption with a maximum closer to that of the CP energy; displaying an MDF closer to that of theoretical predictions for graphene.

In conclusion, hydrogen intercalation of buffer layer carbon growth on SiC (0001) has been shown to produce QFS graphene with optical properties closest to that of theoretical predictions for graphene, further proving its effectiveness as a tool for large-area epitaxial graphene production. In addition, buffer layer carbon growth shows optical properties sufficiently different from that of graphene to allow spectroscopic ellipsometry to become a viable in-situ monitor for commercial production of hydrogen intercalated graphene on SiC.

**5:20pm LB+EM+GR+MN+TR-WeA11 In Situ Dry-Cleaning of Ge(100) Surface using H<sub>2</sub>O<sub>2</sub>.** K. Kiantaj, T. Kaufman Osborn, T.J. Kent, A.C. Kummel, University of California San Diego

Since Ge has higher hole and electron mobility compared to silicon, it is a good candidate for development of a new channel material in CMOS semiconductor devices. One of the obstacles in using Ge as a channel material is the high interface trap density between Ge and Ge native oxide. Air exposed Ge surfaces have a high density of defects and contaminants, but, in order to make optimal semiconductor devices, nearly perfect bonding between each unit cell and the gate oxide layer is required. Although there are many methods available for cleaning the Ge surface, the effectiveness of each of these methods highly depends on the cleanliness of the processing chambers. After cleaning, the Ge surface is typically functionalized with OH groups via water (H<sub>2</sub>O) or hydrogen peroxide (HOOH) during atomic layer deposition of the gate oxide. This OH functionalized surface ideally provides a high density of reactive sites for precursor nucleation. We have studied the effect of a very small amount of hydrocarbon in the processing chambers, and its effect on both the clean Ge surface and the OH functionalized surface since this may increase the density of interface traps and limit Equivalent Oxide Thickness (EOT) scaling. In-situ cleaned Ge surfaces as well as HOOH dosed surfaces have been studied after exposure to hydrocarbon contaminants with x-ray electron spectroscopy (XPS) and scanning tunneling microscopy (STM). An Argon ion source sputtering system was employed for in-situ cleaning of the Ge surface. After exposure to trace hydrocarbon contaminants, two different nanoscale features were observed by STM on the Ge and HOOH/Ge surfaces. One type of contamination denoted as carbon “nanoclusters” which are typically 0.3-0.5nm in height and 2-4nm in diameter. A distinctly different feature is observed on the Ge-OH terminated surface denoted as carbon “nanoflakes”. In contrast to nanoclusters, nanoflakes were only observed on the Ge surfaces dosed with low concentration hydrogen peroxide. In the next step, a high concentration hydrogen peroxide source in combination with an ozone source was employed to study the removal of the contaminants from the Ge surface. Several dosing conditions and sample temperatures were studied and optimized. As the result, an atomically clean Ge surface were achieved by employing an all-dry in-situ process. The all-dry cleaning procedure does not involve any ion-milling or wet-cleaning procedures as both of these methods involve surface etching and result in surface roughness which is not desirable for semiconductor devices.

5:40pm **LB+EM+GR+MN+TR-WeA12 Hf-based High-k Dielectrics for Ge MOS Stacks**, *S. Fadida, M. Eizenberg*, Technion Israel Institute of Technology, Israel, *L. Nyns, D. Lin, S. Van Elshocht, M. Caymax*, IMEC, Belgium

Ge has drawn much attention recently, being a leading candidate to serve as the channel material of future metal oxide field effect transistors (MOSFETs) due to its high carrier mobility with respect to Si. The interest in Ge is mostly because of its high hole mobility. Most of Ge related researches were focused so far on the challenge of Ge surface passivation. In this research we have moved on to the next challenge - finding a suitable high-k dielectric for a Ge-MOS stack. The high-k dielectric has to be chemically and thermally stable on top of the chosen passivation layer, have sufficiently high energy barriers with respect to Ge energy band edges, and have a large dielectric constant in order to obtain the required low effective oxide thickness (EOT). We have studied the chemical, structural and electrical properties of various Hf-based high-k dielectrics:  $\text{HfO}_2$ ,  $\text{Hf}_x\text{Zr}_{1-x}\text{O}_2$ ,  $\text{Hf}_x\text{Al}_{1-x}\text{O}_2$  and  $\text{Hf}_x\text{Gd}_{1-x}\text{O}_2$ . All high-k dielectrics (4 nm thick) were deposited by atomic layer deposition (ALD) on top of a constant passivation stack composed of a thin  $\text{GeO}_2$  layer (0.7 nm thick) followed by a thin (2 nm) ALD  $\text{Al}_2\text{O}_3$  layer. The  $\text{Al}_2\text{O}_3$  layer, which has high band offsets to Ge and  $\text{GeO}_2$ , was added since  $\text{HfO}_2$ , as many of the leading candidates for high-k dielectrics, are unstable on top of Ge or  $\text{GeO}_2$ . A thorough and systematic electrical and chemical characterization of this complex gate stack was carried out. The interesting results show that this challenge of seeking for a superior high-k is not detached from the passivation challenge. Surprisingly, we have found that although the passivation stack was kept constant for all systems studied, the apparent  $D_{it}$  (density of interface states) changes when the top high-k material is modified. Another interesting phenomenon is revealed when different methods of  $D_{it}$  characterization are compared - each method points out a different high-k as the one with the lowest  $D_{it}$ . These observations imply that the C-V characteristics do not reflect only the role of Ge interface traps, but also of traps throughout the whole stack, at least to a distance of 2.7 nm (the total thickness of the passivation stack) from the Ge surface. These results emphasize even more the great challenges in integrating Ge as a new channel material. We have also analyzed the band alignment for all high-k dielectrics using XPS with respect to the underlying layers. All high-k dielectrics have similar band gaps at the range of 5.2-5.9 eV. The conductance and valence band offsets with respect to Ge are all larger than 1 eV, which make them all suitable for Ge-MOSFETs in terms of band alignment.

## Surface Science

Room: 22 - Session SS+EM-WeA

## Semiconductor Surfaces

Moderator: M.A. Hines, Cornell University

2:00pm **SS+EM-WeA1 Local Characterization of Laterally Patterned GaN Polar Surfaces**, *J.D. Ferguson*, Virginia Commonwealth University, *J.K. Hite, M.A. Mastro, C.R. Eddy, Jr.*, U.S. Naval Research Laboratory, *A.A. Baski*, Virginia Commonwealth University

Using scanning probe microscopy techniques, we have investigated the topographic and electrical properties of lithographically defined Ga- and N-polar regions grown on the same surface of a GaN epilayer. These unique structures were created on N-polar substrates grown by either hydride vapor phase epitaxy (HVPE) or metalorganic chemical vapor deposition (MOCVD). A patented selective epitaxy process [1,2] was used to prepare the alternating polarity surfaces on the two separate substrate types. To produce adjacent stripes of alternating polarity on a single substrate, a thin inversion layer comprising AlN was selectively grown inside a nitride mask. After removing the mask, Ga- and N-polar GaN were simultaneously grown over the inversion layer and bare N polar substrate, respectively, using MOCVD. Atomic force microscope (AFM) topography images reveal that Ga-polar regions are smoother than N-polar ones by about two orders of magnitude (rms of  $\sim 0.5$  nm and  $\sim 50$  nm, respectively). Local current/voltage ( $I/V$ ) spectra obtained by conductive AFM indicate a lower turn-on voltage and higher conductivity for N polar regions, whereas Ga polar regions are insulating. Scanning Kelvin probe microscopy (SKPM) data show a surface potential drop of  $\sim 0.5$  V across the interface domain boundary ( $< 200$  nm lateral resolution) from the N- to the Ga polar regions on the HVPE substrate. A lower potential drop ( $\sim 0.2$  V) is seen across the N- to Ga- interface on the template, as well as inconsistent surface potential values ( $\pm 0.1$  V) for Ga-polar stripes. Using SKPM, the surface photovoltage (SPV), or the change in surface potential upon exposure to above-bandgap light, may also be measured for both surfaces simultaneously. Both samples show similar characteristics to previously studied polar GaN surfaces, where Ga-polar regions have higher initial SPV values ( $\sim 0.3$  V for HVPE,  $\sim 0.5$  V for MOCVD) than N-polar regions ( $\sim 0.2$

V for HVPE,  $\sim 0.3$  V for MOCVD). Restoration of the SPV signal after illumination is faster for Ga-polar regions, which is not consistent with previously studied bulk Ga-polar films. In summary, scanning probe methods can be used to distinguish Ga- versus N-polar GaN surface regions grown on the same GaN epilayer.

1. J.K. Hite, M.E. Twigg, M.A. Mastro, C.R. Eddy, Jr. and F.J. Kub, "Initiating Polarity Inversion in GaN Growth Using an AlN Interlayer", *Physica Status Solidi A* 208, 1504-1506 (2011).

2. J.K. Hite, N.D. Bassim, M.E. Twigg, M.A. Mastro, F.J. Kub and C.R. Eddy, Jr., "GaN Vertical and Lateral Polarity Heterostructures on GaN Substrates", *Journal of Crystal Growth* 332, 43-47 (2011).

2:20pm **SS+EM-WeA2 Systematic Prediction of Entropic Surface Reconstruction Stabilization on GaAs(001) from First Principles**, *J.C. Thomas, A. Van der Ven*, University of Michigan, *N.A. Modine*, Sandia National Laboratories, *J.M. Millunchick*, University of Michigan

Increasing evidence linking bulk material properties to surface structure has made critical the development of a comprehensive understanding of atomic-scale surface structure. This is particularly true in low-temperature-grown (LTG) GaAs, where As anti-site defects are incorporated at the As-rich growth surface. Unfortunately, GaAs(001) reconstruction stability is poorly characterized in this regime, where, in addition to the well-studied  $\beta 2 \times 4$  and  $c(4 \times 4)$  reconstructions, a " $\times 3$ " reconstruction is also observed. This " $\times 3$ " reconstruction has been difficult to characterize experimentally, and theoretical calculations have failed to identify a stable " $\times 3$ " reconstruction on GaAs(001). We have developed a systematic, rigorous procedure for predicting equilibrium surface structure and ordering behavior at finite temperature. By combining new and established techniques, our method overcomes difficulties of studying multicomponent surfaces from first principles, which has traditionally followed a painstaking trial-and-error approach.

Using our approach of directed structural enumeration and density functional theory calculation, we can efficiently identify stable and near-stable reconstructions of the GaAs(001) surface in order to identify the structure of the missing " $\times 3$ " reconstruction. Accounting for lattice vibrations and configurational entropy from first principles, we predict finite-temperature stability of a  $(4 \times 3)$  reconstruction over a range of  $\text{As}_4$  partial pressure at low temperature. Our results reveal a competition between vibrational entropy of the  $(4 \times 3)$  reconstruction and configurational entropy of the  $c(4 \times 4)$  reconstruction, which becomes entropically stabilized at higher temperatures. We find that this same  $(4 \times 3)$  reconstruction features prominently in calculated reconstruction phase diagrams for the wetting layer systems Bi/GaAs(001) and InAs/GaAs(001).

2:40pm **SS+EM-WeA3 3D Atomic Scale Structure Analysis of Semiconductor Nanostructures by Atom Probe Tomography and Cross-Sectional STM**, *P.M. Koenraad*, Eindhoven University of Technology, Netherlands **INVITED**

Present day semiconductor science depends heavily on the construction of precise nanostructures in which atomic scale details are of key importance in the understanding and utilization of such nanostructured semiconductor materials. It is thus of key importance to have techniques that allow such details to be assessed by novel microscopy techniques that can obtain, preferable in 3D, atomic resolution. In this presentation I will present recent results that we have obtained by two exciting techniques that allow for an atomic scale resolution. We have used cross-sectional Scanning Tunneling Microscopy (X-STM) and Atom Probe Tomography (APT) on a range semiconductor nanostructures such as quantum dots and rings. The X-STM technique offers a superb 2D true atomic resolution in a single atomic plane intersecting the nanostructure. Atom Probe Tomography is a technique that has recently become available for the analysis of semiconductor nanostructures. Laser induced field emission is used to get a full atomically resolved 3D map of the composition of semiconductor nanostructure. In the presentation I will apply and compare these techniques on quantum dots and rings that have been obtained by various growth procedures such as the traditional Stransky-Krastonow process, droplet epitaxy or by applying Sb during the dot formation process.

4:20pm **SS+EM-WeA8 Coverage-dependent Adsorption of a Bifunctional Molecule with a Rigid Spacer on the Ge(100)- $2 \times 1$  Surface**, *B. Shong, S.F. Bent*, Stanford University

Direct chemical functionalization of semiconductor surfaces with organic molecules has been gaining attention, in part due to its potential applications based on forming organic-inorganic interfaces with tailorable properties. Attachment of bifunctional molecule is important because of the possibility for manipulating the chemical properties of the surface to allow for successive reaction, for example by molecular layer deposition (MLD). Whether dual or single reaction occurs during adsorption of a bifunctional molecule is of critical interest. It is known that more singly-tethered

adsorbates typically form at higher coverages, but most previous studies focused only on a few discrete coverages.

In this study, we investigate coverage-dependent adsorption behavior of resorcinol (1,3-benzenediol) on the Ge(100)-2 × 1 surface. *In situ* X-ray photoelectron spectroscopy and Fourier transform infrared spectroscopy experiments along with density functional theory calculations are combined to determine the products and reaction pathways. First, the results support our previous conclusion that molecular geometry is an important factor in the reactivity and stereoselectivity of rigid bifunctional adsorbates.<sup>1</sup> Resorcinol is found to dually and singly attach on Ge(100) through its two hydroxyl groups, and the dually reacted adsorbate assumes only one configuration due to geometrical restrictions. Moreover, a detailed study with respect to coverage shows that the product distribution is strongly dependent on coverage in a nonlinear fashion with two distinct adsorption regimes. In the low coverage regime, a constant fraction of singly-attached adsorbates is observed, independent of coverage. On the other hand, the fraction of singly-bound adsorbates increases with coverage in the high coverage regime. The increase in singly-bound species at higher coverages is explained by surface crowding, with existing adsorbates blocking reactive sites. This study provides fundamental knowledge about the reactivity of bifunctional molecules on semiconductor surfaces.

<sup>1</sup>B. Shong, K. T. Wong, and S. F. Bent, *J. Phys. Chem. C* **116**, 4705 (2012).

4:40pm **SS+EM-WeA9 2012 AVS Medard Welch Award Lecture: Chemical Functionalization of H-terminated Silicon Surfaces, Y.J. Chabal\***, The University of Texas at Dallas **INVITED**

Silicon is best known for its oxide because of its propensity to oxidize and the remarkable properties of the Si/SiO<sub>2</sub> interface. Yet, oxidation is ill-defined and hard to control. Moreover, modification of chemically stable oxide surfaces mostly involves silanization, typically characterized by disorder and poor chemical stability in solution. The ability to functionalize oxide-free Si surfaces opens new opportunities for a broader range of applications. Precise modification of clean Si surfaces in an ultra-high vacuum environment leads to interesting chemistry but is not widely applicable. In contrast, wet chemical preparation of well-defined H-terminated Si surfaces provides a platform for both fundamental science and further applications. Much work has been done to functionalize H/Si using well known chemical procedures, such as UV- or catalyst-induced hydrosilylation with alkene molecules or halogens followed by Grignard chemistry. Relatively little attention has been placed on the role of structure in H-terminated surfaces for selective modification. Yet, just as structure is important in etching, it also plays a role during chemical modification of surfaces, as illustrated by the reaction of ammonia on stepped Si(111) surfaces.<sup>1</sup> Understanding the role of structure during HF etching is also critical to devise new methods for expanding the functionality of H-terminated surfaces. This talk illustrates this concept and shows that thermal chemistry is well suited to explore such effects. It discusses, for instance, the use of methoxylation of H-terminated Si(111) surfaces to provide a well-defined template for interesting surface chemistry and a broader range of functionalization,<sup>2</sup> such as the grafting of phosphonates, amines, and metal complexes.

<sup>1</sup> Dai, M., Y. Wang, J. Kwon, M.D. Halls, and Y.J. Chabal, *Nitrogen interaction with hydrogen-terminated silicon surfaces at the atomic scale. Nature Materials* **8**, 825 (2009).

<sup>2</sup> Michalak, D.J., S.R. Amy, D. Aureau, M. Dai, A. Esteve, and Y.J. Chabal, *Nanopatterning Si(111) surfaces as a selective surface-chemistry route. Nature Materials* **9**, 266 (2010).

5:20pm **SS+EM-WeA11 Wet Chemical Approach for Amino Functionalization of Oxide-free Si(111) Surfaces, T. Peixoto, P. Thissen, Y.J. Chabal**, University of Texas at Dallas

The ability to functionalize H-terminated Si surfaces with NH<sub>2</sub> groups is crucial for a number of applications, such as biomedical (bio-sensors), solid diffusion barrier films, single electron devices, MOSFETs and MEMS. The Si-N bond provides a versatile functionality for chemical modification. Although the creation of a well-defined and stable interface for the Si-N bonds has remained elusive, chlorosilanes have been shown to easily react with gas-phase or liquid ammonia and primary and secondary amines to achieve a stable silicon nitride bond<sup>1</sup>.

For fluorosilane surfaces, we have performed DFT calculations indicating that the kinetic barrier for the NH<sub>3</sub> reaction with Si-F surfaces is only slightly higher than for Si-Cl surfaces, suggesting the reaction should occur at moderate temperatures (<700C). The 1/3 ML Si-F and 2/3 ML Si-H nanopatterned<sup>2</sup> model surface has a tailorable distance between Si-F groups (from 6.8 Å for 1/3ML to 3.9 Å at higher coverages) allowing the adsorption mechanism to be investigated in detail (and evaluated by DFT

calculations) and the role of NH<sub>x</sub>-NH<sub>x</sub> interactions explored. We further show that the Si-F surface reacts with amino containing molecules (NH<sub>2</sub>-R-NH<sub>2</sub>), as evidenced by the reaction between Si-F and ethylenediamine at room temperature. Using these reactions we demonstrate that the amidation for the nanopatterned surface takes place for both small molecules (NH<sub>3</sub>) and larger amino chains (NH<sub>2</sub>-CH<sub>2</sub>-CH<sub>2</sub>-NH<sub>2</sub>) with similar kinetics. The surfaces were characterized using Fourier-transform infrared spectroscopy (FTIR) and x-ray photoelectron spectroscopy (XPS) to verify reaction mechanisms.

These results provide a fundamental understanding of the amidation reaction mechanism for achieving stable Si-N bonds using fluorosilanes surfaces. Achieving a well-defined and stable Si-N interface is significant for a number of important technological applications.

References:

[1] Tian, F.; Taber, D.F.; Teplyakov, A.V. *J. Am. Chem. Soc.* **2011**, *133*, (20769)

[2] Michalak, D. J.; Amy, S. R.; Aureau, D.; Dai, M.; Esteve, A.; Chabal, Y. *J. Nat. Mater.* **2010**, *9*, (266).

5:40pm **SS+EM-WeA12 Ammonia- and Amine-based Chemical Modification of Silicon Surfaces, A.V. Teplyakov**, University of Delaware  
Stable silicon-nitrogen bonds on surface of single crystalline silicon substrates can serve a variety of practical purposes. The main problem is that creating and controlling the formation of these bonds is done predominantly in the controlled ultra-high vacuum conditions. Here the formation of stable Si-N-based interfaces will be compared for vacuum procedures and for the wet chemistry-based methods. A number of compounds, including ammonia, amines, azides and nitro- and nitroso-compounds, dosed onto a clean silicon surface can yield stable Si-N bonds. However, designing surface reactions leading to contaminant-free interfaces that contain these bonds by wet chemistry methods has been a challenge. We will use multiple spectroscopy and microscopy techniques supplemented by density functional theory investigations to build interfacial systems based on Si-N bonds with ammonia and amines reacting with Cl-covered single crystalline silicon surfaces in a solvent at room temperature. Further transformations of the produced functionalized surfaces will also be discussed.

## Transparent Conductors and Printable Electronics Focus Topic

Room: 7 - Session TC+EM+AS-WeA

### Printable and Flexible Electronics

Moderator: G.S. Herman, Oregon State University

2:00pm **TC+EM+AS-WeA1 Metal Oxides and Organic Materials for Printed Electronics, A. Facchetti**, Polyera Corp. and Northwestern U. **INVITED**

Printed electronics is a new technology envisioning the fabrication of electronic devices using printing methodologies instead of conventional photolithography employed in the silicon industry. Metal oxide- and organic-based materials will be key players for this technology. In this presentation I will discuss our latest results in developing new printable organic semiconductors. Furthermore, I will describe amorphous and polycrystalline metal oxide formulations in which the corresponding films can be annealed at temperatures < 250 °C. For instance, solution-processed amorphous tin-doped indium oxide (ITO) films for TFT fabrication at temperatures < 250 °C can be achieved by controlling film precursor solution In<sup>3+</sup> vs. Sn<sup>4+</sup> molar ratio resulting in electron mobilities > 2 cm<sup>2</sup> V<sup>-1</sup>s<sup>-1</sup> and ~ 20 cm<sup>2</sup> V<sup>-1</sup>s<sup>-1</sup> for TFTs using SiO<sub>2</sub> and a self-assembled nanodielectric (SAND) as the gate dielectrics, respectively. Finally, a new general strategy for fabricating solution-processed metal oxide TFTs at dramatically lower temperatures (as low as 200 °C for all TFT electrical components) using self-energy generating combustion chemistry will be presented. Our results show that by tuning the gate dielectric-semiconductor interface dramatically enhances performance, yielding In<sub>2</sub>O<sub>3</sub>, IZO, IZTO, and IGZO /amorphous alumina gate dielectric TFTs having electron mobilities of 40 cm<sup>2</sup>/Vs and 13 cm<sup>2</sup>/Vs at T<sub>anneal</sub> = 250 °C and 200 °C, respectively.

2:40pm **TC+EM+AS-WeA3 Ion Dependence of Gate Dielectric Behavior of Beta-Aluminas in Transparent Oxide Field-Effect Transistors, Y. Liu, B. Zhang, H.E. Katz**, Johns Hopkins University  
Sodium beta-alumina (SBA) is an excellent gate dielectric material which can be used in low-voltage (2 V), solution-processed transparent oxide field-effect transistors (FETs). Sodium ions have been experimentally

\* Medard W. Welch Award Winner

proved to be the origin of the high capacitance observed in SBA gate dielectric. With this discovery, the investigation of dielectric properties of alumina with the incorporation of other alkali metal ions (for example  $K^+$ ,  $Li^+$ ) becomes compelling.

High field-effect mobility (about  $20 \text{ cm}^2 \cdot \text{V}^{-1} \cdot \text{s}^{-1}$ ), high saturation drain current (about 1 mA), and small subthreshold swing (about 200 mV/decade) were achieved in low-voltage (2 V), spin-coated zinc-tin-oxide (ZTO) FETs with potassium beta-alumina (PBA) and lithium beta-alumina (LBA) dielectrics. This proves that the incorporation of alkali metal ions in beta-aluminas is a general route to reduce operation voltage of transistors while achieve excellent electrical performance.

To investigate the effect of alkali metal ions on beta-alumina capacitance, beta-alumina Metal-Insulator-Metal (MIM) capacitors (PBA, LBA, and SBA) were analyzed in a frequency range from 100 Hz to 1 MHz. A tendency for beta-alumina capacitance to increase with increasing atomic number of alkali metal ions was observed. Besides, beta-alumina capacitance was found to decrease as temperature increases and LBA showed the strongest temperature dependence of capacitance. Moreover, capacitance of beta-aluminas with different thickness was measured and they were independent of thickness. With these results, electric double layer (EDL) structure was proposed as one way to explain the high capacitance of beta-alumina dielectrics. Ion exchange experiments showed significant diffusion of both lithium ion and potassium ion between PBA and  $LiNO_3$  solution; however, a high concentration difference did not seem to cause obvious diffusion of either lithium ion or potassium ion between LBA and  $KNO_3$  solution. This selective ion exchange behavior in beta-aluminas showed that the  $Al_2O_3$  matrix structure would be affected by the alkali metal ions incorporated, and/or that Li ions are much more strongly bound. Thus, varying intercalated ion types and concentrations can be a means of tuning frequency-dependent capacitance of alumina films.

3:00pm **TC+EM+AS-WeA4 Selection Rule of Preferred Doping Site for N-Type Transparent Conducting Oxides**, *S.-H. Wei*, National Renewable Energy Laboratory, *C. Li, J.B. Li*, Institute of Semiconductor Physics, CAS, China

Traditionally, it is believed that the conduction band edges of  $d^0$  or  $d^{10}$  oxides are derived mostly from cation  $s$  states, thus doping on anion sites is expected to cause less perturbation and produce shallow donor levels in these materials. Using first-principles calculations, we show that although this paradigm is applicable for more covalent oxides such as  $SnO_2$  where  $F_O$  is a better n-type dopant than  $Sb_{Sn}$ , for more ionic oxides such as ZnO, the conduction band edge actually contains a considerable amount of O  $s$  orbitals, thus  $F_O$  in ZnO causes larger perturbation and consequently produces deeper donor levels than cation site doping such as  $Al_{Zn}$ . The rule that anion site doping is preferred for more covalent oxides and cation site doping is preferred for more ionic oxides for n-type metal oxides should be general and can be used to guide future study of and search for functional oxide materials.

4:00pm **TC+EM+AS-WeA7 Single-Walled Carbon Nanotube Aerogel Based Elastic Conductors**, *K.H. Kim, Y. Oh, I. Lee, M.F. Islam*, Carnegie Mellon University **INVITED**

Flexible conductors of various shapes and sizes with high electrical stability under large elastic stretching and bending are of significant importance in diverse fields ranging from microelectronics to biological implants. A major roadblock in the development of flexible conductors is the disparity between elastomers and stiff conducting materials used in microelectronics. We have developed a novel scheme to create flexible conductors by completely backfilling a prefabricated conducting porous single wall carbon nanotube (SWCNT) three-dimensional network, called SWCNT aerogel, with an elastic polymer polydimethylsiloxane (PDMS). Our approach allowed us to control SWCNT dispersion quality, and tune shapes, sizes and thicknesses of the SWCNT-aerogel/PDMS composite films to make them transparent. The resistance of our stretchable conductors remains nearly unchanged under repeated stretch-release cycles up to a tensile strain of 100% and high bending strain. We believe that the simple but unique fabrication method can be combined with different types of elastic polymers for different electrical, mechanical or biological demands.

4:40pm **TC+EM+AS-WeA9 Networked Metal Nanowire-Polymer Composites for Flexible, Transparent and Conducting Devices**, *S. Narayanan, S. Fu, M.R. Bockstaller, L.M. Porter*, Carnegie Mellon University

Transparent conductive metal oxides (TCOs) exhibit inherent disadvantages such as limited supply, brittle mechanical properties, expensive processing that present major barriers for the more widespread economic use in applications such as flexible transparent conductors. A promising alternative route towards flexible, transparent conductive materials is based on silver nanowire network structures, which can be easily processed from solution.

We report a systematic analysis of the effect of nanowire geometry and solution processing on the network characteristics of nanowire deposits, and the associated electronic and optical properties of silver nanowire-based transparent electrodes. Ag nanowire (of average diameter  $\sim 100$  nm) films drop-cast from solution were shown to exhibit bulk-like electrical conductivity ( $\sim 2\text{-}50 \text{ } \Omega/\text{sq}$ ) and high transparency ( $\sim 70\text{-}75\%$ ). The electrical properties of nanowire networks were found to be sensitive to geometric parameters of the wire assembly that can be interpreted by use of percolation theory. At concentrations below the percolation threshold the sheet resistance increases dramatically, effecting a marked deviation from bulk-like behavior [1]. The dispersion of Ag nanowires in a conducting medium, like that of a conducting polymer was found to significantly reduce nanowire aggregation and thus decrease the percolation threshold. Preliminary results of spun-cast films of composites of these nanowire networks with PEDOT:PSS show higher transmittances ( $\sim 79\text{-}82\%$ ) with similar conductivities ( $\sim 10\text{-}170 \text{ } \Omega/\text{sq}$ ) combined with better film forming properties. The use of composites was found to bring about a consistent improvement in electrical conductivity with very little change in the transmittance. Samples prepared on flexible PET substrates showed no degradation in conductivity on flexing thereby showing ample promise for incorporating flexibility in such structures. Through analysis of microstructural characteristics of these films, a quantitative correlation of the density of nanowires with conductivity and transmittance will be presented. The advantages of using such a composite structure in reducing the percolation threshold will be discussed.

[1] Sukanta De *et al.* ACS Nano 4 12 (2010) 7064-7072

# Thursday Morning, November 1, 2012

## Electronic Materials and Processing

Room: 14 - Session EM+SS+AS+NS-ThM

## Nanoelectronic Interfaces, Materials, and Devices

Moderator: M. Filler, Georgia Institute of Technology

8:00am EM+SS+AS+NS-ThM1 **Tensilely Strained Ge Nanomembranes for Applications in Group-IV Infrared Photonics**, *R. Paiella*, Boston University **INVITED**

Single-crystal semiconductor nanomembranes have emerged as a new materials platform offering unique opportunities for strain engineering, by virtue of their ultrasmall thicknesses that result in extremely high thresholds for plastic deformation under stress. This talk will review our recent work aimed at exploiting this property for the development of CMOS-compatible group-IV semiconductor light sources for the technologically important near-infrared spectral region. It is well known that Si, Ge, and related alloys are very inefficient light emitters and generally unsuitable for laser action, due to the indirect nature of their fundamental energy bandgap. A possible solution to this important drawback is provided by the ability of biaxial tensile strain in Ge to lower the conduction-band edge at the direct ( $\Gamma$ ) point relative to the L-valley minima, until at a strain of about 1.9% the fundamental bandgap becomes direct. In our work, mechanically stressed Ge nanomembranes capable of accommodating the required strain levels have been developed, and used to demonstrate strong strain-enhanced photoluminescence. A maximum biaxial tensile strain of over 2% in a 24-nm-thick nanomembrane has been measured, above the accepted threshold for the formation of direct-bandgap Ge. A detailed theoretical model of the light-emission and optical gain properties of tensilely strained Ge has also been developed and applied to the measured luminescence spectra, providing evidence of population inversion at strain levels as low as about 1.4%. More recent work is focused on integrating optical cavities on these strained nanomembranes for the development of infrared photonic active devices.

8:40am EM+SS+AS+NS-ThM3 **Self-activating and Self-limiting Features of the Thermally Assisted Growth Mechanisms of Thin Oxide-, Nitride- and Carbide Films on Si Surfaces at Low Gas or Plasma Pressures**, *P. Morgen, J. Drews, R. Dhiman*, University of Southern Denmark, *Z.S. Li*, Aarhus University, Denmark

The thermally assisted growth of oxide-, nitride-, and carbide films on Si surfaces, in direct reactions, carried out with neutral gases or remote plasmas under ultrahigh vacuum background conditions, are self-limiting processes, reaching different thicknesses. The mechanisms have been studied using photoelectron spectroscopies with synchrotron radiation or conventional x-ray induced photoelectron spectroscopy (XPS). For the oxidation with neutral oxygen molecules, or microwave-excited remote oxygen plasmas, and for the nitride formation reaction with microwave-excited remote nitrogen plasmas, the "kinetics" (uptake versus exposure plots) is well described with a Hill-function. For the nitrogen reaction, the variation of the temperature causes the Hill parameters to vary because this reaction has more latitude than the oxidation, in temperature range and final thickness, as well as in the resulting structure of the nitride, going from amorphous to crystalline at higher temperatures. One known instance of the "Hill reaction" is a self-activating enzymatic-like reaction, and such a mechanism is believed to be relevant also in our systems. The carbide reaction is different, due to defects in the growing film, which allow a relatively unhindered transport of Si to the surface, where it reacts with carbon species arriving at the surface, from remote microwave-excited plasmas of methane. Thus the limiting thickness of SiC/Si (111) is around 100 nm, while the thickness of oxide is 0.8 nm, and the nitrides between 1 and 3 nm.

9:00am EM+SS+AS+NS-ThM4 **Functional Conductive Polymer to Inexpensive and Portable Chemiresistive Biosensor**, *D. Bhattacharyya, K.K. Gleason*, Massachusetts Institute of Technology

Extensive research has focused on developing different types of biosensors for detecting bio-threat risks and the occurrence of toxins in the food supplies. However, these food screening processes involve many steps, have high labor costs, reagent costs and time delays of at least 2-3 days to obtain reliable data. Despite the current availability of various types of sensors, limitations of the current state-of-the-art biosensors for molecular recognition of biomolecules are well known. Among these limitations are the unacceptably long process times required for detection and user non-compliance as a result of the excessive weight of the sensor modules coupled with the inflexibility of the sensor platforms for routine uses.

Chemiresistive biosensors detect changes in resistance when analyte molecules specifically bind to the sensor surface. Chemiresistive biosensing technique is attractive because it is label-free and can be developed for faster detection of analytes. In this work, oxidative chemical vapor deposition (oCVD) technique is employed for deposition of functional conductive copolymer thin films on the electro-spun fiber mats. The dry oCVD process allowed us to deposit uniform and conformal conducting -OH functional copolymeric film on the electro-spun fiber mat in a single step. For the proof-of-concept of the biosensor application, avidin molecules were covalently immobilized to the -OH functional groups. Various concentrations of biotin solutions were employed as the analytes. The responses and the response times of the devices were significantly improved when the high surface area electro-spun mat were used as a substrate in contrast to a flat substrate.

9:20am EM+SS+AS+NS-ThM5 **Semiconductor Nanomembranes for Biomedical Applications**, *J.A. Rogers*, University of Illinois at Urbana Champaign **INVITED**

Biology is curved, soft and elastic; silicon wafers are not. Semiconductor technologies that can bridge this gap in form and mechanics will create new opportunities in devices that adopt biologically inspired designs or require intimate integration with the human body. This talk describes the development of ideas for electronics that offer the performance of state-of-the-art, wafer-based systems but with the mechanical properties of a rubber band. We explain the underlying materials science and mechanics of these approaches, and illustrate their use in bio-integrated, 'tissue-like' electronics with unique capabilities for mapping cardiac electrophysiology, in both endocardial and epicardial modes, and for performing electrocorticography. Demonstrations in live animal models illustrate the functionality offered by these technologies, and suggest several clinically relevant applications.

10:40am EM+SS+AS+NS-ThM9 **Structure, Dynamics and Mechanism of a Single-Molecule Electric Motor**, *C.J. Murphy, C.H. Sykes*, Tufts University

Future nano-electronic devices, such as fluid pumps, sensors and switches, will rely on rotating molecules bound to surfaces as key components. To operate these devices, it is important to understand and direct molecular rotation at this interface. We utilized a Low Temperature Scanning Tunneling Microscope (LT-STM) to both drive and measure the rotation of a single asymmetric thioether molecule bound to a copper (111) surface. Due to the hexagonal arrangement of the underlying Cu atoms the rotor molecule has six favorable orientations, with an asymmetrical barrier to rotation around the Cu-S bond. The symmetry of this barrier is dependent on the surface bound chirality. Rotation of the molecule can be driven by either thermal or electrical means. In thermally driven systems, there is no preferred direction of rotation. In order to measure the rate of anisotropic rotation, the system is cooled to 5 K, and a tunneling current is applied to periodically excite the molecule, resulting in a flashing ratchet like mechanism of molecular rotation. The progression of molecular orientations relative to the tip can be determined by the exponential dependence of tunneling current on distance. This allows evaluation of the rate, direction and magnitude of rotation between these orientations in real time. We aim to further interrogate this novel mechanism for electrically-driven motion by quantifying the lifetime of the rotor in each stable orientation and the transitions between these states as a function of tunneling current and voltage.

11:00am EM+SS+AS+NS-ThM10 **Semiconductor Nanostructures for Efficient Thermoelectric Energy Conversion**, *Z. Aksamija*, University of Wisconsin Madison

Thermoelectric (TE) refrigeration using semiconductor-based nanostructures, such as nanowires, nanoribbons, and superlattices, is an attractive approach for targeted cooling of local hotspots inside integrated circuits due to inherently no moving parts, ease of miniaturization and on-chip integration, and the nanostructures' enhanced TE conversion efficiency. In addition, thermoelectric power generation enables the reuse of waste heat in a variety of applications, from low-power and energy-efficient designs to internal combustion engines and solar cells. Thermoelectric efficiency, measured by the figure-of-merit  $ZT$ , is dictated by the ratio of electronic power factor  $S^2\sigma$  over the total thermal conductivity. Consequently, largest gains in TE conversion efficiency have come from the ability to reduce thermal conductivity. This is especially true in nanostructures, where small physical dimensions lead to reduced thermal transport due to the scattering of lattice waves, or phonons, with the boundaries of the nanostructure. The design of efficient semiconductor thermocouples requires a thorough understanding of both charge and heat

transport; therefore, thermoelectricity in semiconductor-based nanostructures requires that both electronic and thermal transport are treated on equal footing. SOI nano-membranes and membrane-based nanowires and ribbons show promise for application as efficient thermoelectrics, which requires both high electronic power factor and low thermal conductivity. I will present numerical simulation and modeling of both carrier and phonon transport in ultrathin silicon nanomembranes and gated nanoribbons. We show that the thermoelectric response of Si-membrane-based nanostructures can be improved by employing the anisotropy of the lattice thermal conductivity, revealed in ultrathin SOI nanostructures due to boundary scattering, or by using a gate to provide additional carrier confinement and enhance the thermoelectric power factor. Furthermore, we explore the consequences of nanostructuring on silicon/germanium and SiGe alloy superlattices, and show that the drastic reduction of thermal conductivity in these structures comes from the increased interaction of lattice waves with rough interfaces and boundaries. Finally we demonstrate reduced thermal conductivity in both suspended and supported graphene nanoribbons (GNRs), which exhibit strong anisotropy due to interaction of lattice waves with line edge roughness (LER) and the competition between LER and substrate scattering. The talk will conclude with an outlook for future nanostructured thermoelectric based on nanocrystalline and nanocomposite semiconductors, and nanopatterned graphene.

11:20am **EM+SS+AS+NS-ThM11 UV Ozone Irradiation Induced Defect Formation in Graphene/PZT Devices**, C.X. Zhang, D.M. Fleetwood, M.L. Alles, R.D. Schrimpf, Vanderbilt University, E.B. Song, S. Kim, K. Galatsis, K.L. Wang, University of California at Los Angeles, E.X. Zhang, Vanderbilt University

Graphene based materials are promising candidates for integration into future integrated circuit technologies. Initial studies of the effects of electron-beam and proton irradiation have been performed on graphene materials, but there remain significant questions about the nature of the conductivity and the defects that influence its material and electronic properties. We have found that low-energy x-ray irradiation can lead to significant shifts in the charge neutral point and increases in resistance of suspended graphene layers and graphene layers on SiO<sub>2</sub>. For graphene-on-SiO<sub>2</sub> structures, the reaction oxygen atoms may be supplied either by ozone in the ambient air, or by the adjacent SiO<sub>2</sub> substrate. Similar reactions may be observed for hydrogen, for devices exposed to x-ray and/or UV ozone (UVO) irradiation. Moreover, we also have found that graphene/PZT ferroelectric field-effect transistors (FFETs) are sensitive to UVO irradiation. The conducting channel in these devices is a single graphene layer. The device functions as a nonvolatile memory with reverse hysteresis, where charge trapping and detrapping in the PZT layer leads to a large memory window that is robust to x-ray irradiation and/or memory state cycling. When these devices are exposed to UVO irradiation, the memory window of the device decreases slightly with exposure time. In addition, an increase is observed in the slope of the I-V curves, along with a small positive shift in current-voltage characteristics. These results are consistent with the formation of negatively charged surface states on the graphene layer during the UVO exposure, which are most likely associated with adsorbed oxygen. The degradation in the I-V characteristics recovers somewhat with room temperature annealing. At the AVS meeting, the detailed electrical response will be described, and a physical model will be presented for the UVO degradation and recovery mechanisms.

11:40am **EM+SS+AS+NS-ThM12 Switching Molecular Kondo Effect by Chemical Reactions**, H. Kim, ISSP, University of Tokyo, Japan, Y.H. Chang, KAIST, Korea, M.H. Chang, Korea University, Y.-H. Kim, KAIST, Korea, S.-J. Kahng, Korea University

Motivated by spintronics applications, the methods to control Kondo effect have been actively studied in magnetic adsorbates on metal surfaces using scanning tunneling microscopy, but they were limited to the processes that required external energy supply from scanning tunneling microscope tip. We report new methods to control molecular Kondo effect by using bimolecular chemical reactions. A chemical binding between diatomic molecules and Co-porphyrin was exploited to switch off, or reset the molecular Kondo effect. The Kondo effect was switched back on using scanning tunneling microscope manipulation as well as thermal desorption. These methods rely on the hybridized pairing of unpaired spins in d<sub>2</sub> and π\* orbitals of Co-porphyrin and diatomic molecules, respectively, as supported by our density functional theory calculation results. Our study opens up ways to control the molecular Kondo effect using an enormous variety of bimolecular chemical reactions.

12:00pm **EM+SS+AS+NS-ThM13 Quantifying the Local Seebeck Coefficient using Scanning Thermoelectric Microscopy (SThEM)**, J.C. Walrath, Y.H. Lin, K.P. Pipe, R.S. Goldman, University of Michigan

Thermoelectric (TE) devices allow reliable solid-state conversion of heat to electricity. The efficiency of a TE device is determined by the figure of

merit, ZT, which is sensitive to the Seebeck coefficient, S. Traditional S measurements are used to quantify thermally-induced electron transport on a macroscopic scale. A promising alternative method for nanoscale measurements of S is scanning thermoelectric microscopy (SThEM). In SThEM, an unheated scanning tunneling microscopy (STM) tip acts as a high-resolution voltmeter to measure the thermally-induced voltage, V, induced by a temperature gradient in a heated sample. SThEM has been utilized to measure V across a GaAs p-n junction [1], with the spatial profile of S determined through a comparison of the measured V with a simulation of a network of resistors and voltage sources, based upon a theoretical S-value [2]. Although this approach is useful for predicting the measured V, it does not provide a method for direct conversion of the measured V to a local S. We have developed a Fourier heat conduction model to calculate a temperature profile matrix, thereby enabling direct conversion between the measured V and the local S. According to our model, SThEM can be optimized by fine-tuning several parameters, including the cone angle of the STM tip and the relative thermal conductivity of the tip and sample. We applied our model to SThEM data across a GaAs p-n junction [1] and improved the agreement between the measured and theoretical S by 40%. Our progress towards SThEM measurements of CoSb<sub>3</sub> and InAs quantum dots will also be discussed. This material is based upon work supported by the Department of Energy under Award Number DE-PI0000012. Y.H. Lin and R.S. Goldman are supported in part by DOE under contract No. DE-FG02-06ER46339.

[1] H.K. Lyeo, A.A. Khajetoorians, L. Shi, K.P. Pipe, R.J. Ram, A. Shakouri, and C. K. Shih, *Science* **303**, 816 (2004).

[2] Z. Bian, A. Shakouri, L. Shi, H.K. Lyeo and C.K. Shih, *Appl. Phys. Lett.* **87**, 053115 (2005)

## Electronic Materials and Processing Room: 9 - Session EM-ThM

### Processing for Ultra Low Power Electronics + Semiconductor Heterostructures I

**Moderator:** S.A. Vitale, MIT Lincoln Laboratory, J.E. Ayers, University of Connecticut

8:00am **EM-ThM1 Advanced FinFET Process for 22nm and Beyond**, M. Masahara, T. Matsukawa, Y. Liu, K. Endo, S. Ouchi, National Institute of AIST, Japan

**INVITED**

#### 1. Introduction

One of the biggest challenges for the VLSI circuits with 22nm-node and beyond is to overcome the issue of a catastrophic increase in power dissipation of the circuit due to short channel effects (SCEs) and V<sub>th</sub> variation. Fortunately, double-gate FinFETs have a promising potential to overcome this issue due to their superior SCE immunity even with an undoped channel thanks to the 3D structure. This paper presents novel FinFET process technologies for 22nm-node and beyond.

#### 2. V<sub>th</sub> Tuning

The V<sub>th</sub> of the FinFET is determined by the gate workfunction (WF). A mid-gap metal gate (MG) such as TiN gives a relatively high V<sub>th</sub> (±0.4V) for both n- and pMOS FinFETs. In order to further reduce V<sub>th</sub>, we have developed a novel dual MG FinFET integration process by using metal interdiffusion technology. In this work, we selected a Mo (4.95eV) and Ta (4.25eV) combination, and demonstrated the integration of a Ta/Mo gate nMOS and Mo gate pMOS FinFET. A Ta diffuses into the underlying Mo layer, piles up at the metal/dielectric interface. Thus, by depositing Mo on both n- and pMOS and by stacking Ta on only pMOS, dual MG CMOS FinFETs with low V<sub>th</sub> (±0.2V) were successfully realized without any MG removal process.

By separating the two gates in the FinFET and using one to control the V<sub>th</sub>, we have succeeded in obtaining the great advantage of the post-fabrication flexible V<sub>th</sub> controllability. The fabricated independent double-gate FinFET (called 4T-FinFET) enabled V<sub>th</sub> to flexibly range from around 0.2V to 0.4V.

#### 3. V<sub>th</sub> Variation

So far we have investigated FinFET performance variability for undoped channels with TiN MG. By evaluating the influence of channel doping, fluctuation of gate length and that of fin thickness, we have also found that gate WF variation (WFV) is the dominant source of V<sub>th</sub> variation for the undoped TiN FinFET. We speculated that the WFV originates from randomly aligned TiN on rough sidewall channels due to line edge roughness of the patterned resist mask. Then in order to reduce the WFV, we fabricated FinFETs having smooth sidewall channels formed by using

orientation-dependent nanowet etching. It was found that  $\sigma V_{th}$ 's for the wet-etched case is significantly lower than that for the dry-etched case. This means that the smooth sidewall channels formed by using the nanowet etching well contribute to the reduction of the WFV.

#### 4. Summary

By introducing Ta/Mo dual metal gate technology, low  $V_{th}$  ( $\pm 0.2V$ ) can be obtained for CMOS FinFETs. By separating the DG,  $V_{th}$  can be tuned from 0.2V to 0.4V flexibly. Flattening of Si-fin sidewall channel is very promising for reducing  $V_{th}$  variations.

#### 9:00am EM-ThM4 Wideband Characterization for Optimized Performance in Low Voltage Low Power Applications, M. Emam, Incize, Belgium, J.-P. Raskin, Université Catholique de Louvain, Belgium

Portability and performance are becoming the main two keywords in any consumer or professional applications. Portable computers, mobile phones, handheld measurement instruments, and many other examples are all applications that need long battery lifetime while compromising the least at the performance level. Long battery lifetime is simply translated into less power consumption and hence operating at lower voltage schemes. This new approach requires solutions at all levels; including material, fabrication, device structure, circuit design, and system architecture. Wideband characterization is the bridge that links these levels together (especially material, fabrication and device structure levels) and provides the means to optimize this cycle of innovation for an optimized final product in the Low Voltage Low Power (LVLP) regime.

Wideband characterization is the process of measurement and extraction of many parameters of the Device-Under-Test (DUT) in order to fully understand its characteristics and be able to provide solutions for inconvenient performance aspects. Wideband characterization usually covers a wide range of frequency starting at a few Hz and going up to tens of GHz, depending on the characteristics to be studied. Recently, many high frequency techniques have been proposed to deeply understand and qualify new materials (especially wafers and substrates) and new devices (active devices such as transistors and passive devices such as inductors). These new techniques rapidly and efficiently define the advantages and the disadvantages of the material/device and precisely define the causes of malfunction or poor quality performance. The result is a shorter time-to-market thanks to less number of iterations between the different steps of final product fabrication.

This paper presents the importance of wideband characterization techniques for fabrication process. Examples are given for new substrate, new device structures and enhancement of existing and mature device structures. The objective is an optimized performance for a LVLP application.

#### 9:20am EM-ThM5 Ultra Low-Power (ULP) Current Logic Gates for Subthreshold-Triode Operation, K. Lam, Chinese University of Hong Kong, Hong Kong Special Administrative Region of China, T. Mak, Newcastle University, UK

Most logic gates used today are based on voltage-mode ideas, where the two binary states for 0 and 1 are represented using inverted logic on voltages. In carrying out the basic operations for AND and OR on two levels of voltages for 0 and 1, NAND gates and NOR gates are often required by using inverted logic and inverters are commonly used to get the logical computations functionally correct. It is straightforward to construct a NAND gate with two tightly coupled common drain and source N-channel MOSFET transistors. A properly chosen resistor from the supply voltage to the common drain will then realize the NAND function to the two voltage levels with a reasonable margin. For subthreshold operation with a supply voltage close to the threshold voltage, the gate switching speed is determined by the subthreshold swing.

There are limitations for these voltage-mode logic gates due to the lack of accuracy and inability to work on very small voltage levels less than the threshold voltage for ultra-low power applications. We explore the idea of current logic by making use of small currents at the subthreshold-triode region to overcome some of these limitations. Using current for the binary inputs of 0 and 1, the 2-input current-mode minimum circuit and maximum circuit are investigated to realize the logical functions of OR and AND gates for subthreshold-triode operation. Our previous work reported that in subthreshold-triode operation it is possible to obtain a subthreshold swing which can surpass the theoretical limit of 60 mV/dec at very small gate voltage less than 0.025V for the IMEC 90 nm process. Further simulation is focused on the evaluation of ULP current logic gates constructed using current-mode min-max circuits. A benchmark test on a dynamic programming network for solving transitive closure problem has been performed on using conventional voltage-mode NAND-NOR logic gates. The results will be compared with the proposed current-mode min-max circuits.

#### 9:40am EM-ThM6 Impact of Threading Dislocation Density and Dielectric Layer on I-V Characteristics of Schottky Diodes Fabricated from Ti and Epitaxially Grown p-Type Ge on Si, S. Ghosh, S.M. Han, University of New Mexico

Epitaxially grown Ge and III-V on Si have emerged as a promising candidate for the next generation high performance devices, including high-mobility complementary metal-oxide-semiconductor field-effect transistors. For high-mobility transistors integrated on Si substrates, in particular, managing dislocations and metal-semiconductor contacts has become an important engineering challenge. Herein, we have investigated the impact of threading dislocations and metal-semiconductor interfacial states on Schottky diode characteristics made of Ti and wafer-scale Ge grown on Si. For the purpose of comparison, we have grown epitaxial Ge on Si with two threading dislocation densities:  $2 \times 10^8$  and  $5 \times 10^7$   $\text{cm}^{-2}$ . The p-type carrier density in the Ge layer is approximately  $5 \times 10^{16}$   $\text{cm}^{-3}$ . To prevent Fermi-level pinning, we have also deposited a thin layer of  $\text{SiO}_2$  and  $\text{Al}_2\text{O}_3$  between Ti and Ge with varying thickness, ranging from 5 to 30 nm. With a thin dielectric layer (5 nm), Schottky diodes on two Ge epilayers resulted in an on/off current ratio of approximately 1. This result indicates that there is a significant amount of leakage current. When the dielectric thickness is optimized to 30 nm, we observe that the on/off ratio improves by a factor of 40 and 2000 for  $\text{SiO}_2$  and  $\text{Al}_2\text{O}_3$ , respectively. In the case of  $\text{Al}_2\text{O}_3$ , we were able to achieve an ideality factor of 1.67 at 300 K and the reverse leakage current density of  $\sim 4.3 \times 10^{-10}$   $\text{A}/\mu\text{m}^2$  at 300 K. The ideality factor increases to 2.44 at 77 K. This result suggests that the thermionic emission might be the dominant current transport mechanism for Schottky diodes fabricated from Ti and epitaxially grown p-type Ge on Si. However, the slight increase in ideality factor at low temperatures implies a change in the dominant current transport mechanism. In summary, the use of 30-nm-thick  $\text{Al}_2\text{O}_3$  between Ti and Ge provides improved I-V characteristics for the Schottky diodes. In this presentation, we will further discuss our latest approaches [1] to reduce the dislocations in the Ge epilayer to low  $10^6$   $\text{cm}^{-2}$  level and device characteristics of Schottky diodes fabricated on these low-dislocation-density Ge on Si substrates.

[1] Darin Leonhardt and Sang M. Han, *Appl. Phys. Lett.* 99, 111911 (2011).

#### 10:40am EM-ThM9 Heteroepitaxial Lattice Mismatch Stress Relaxation in Nonpolar and Semipolar GaN by Dislocation Glide, J. Speck, University of California, Santa Barbara

**INVITED**  
Light emitting devices, namely LEDs and laser diodes, grown on *c*-plane GaN suffer from large internal electric fields due to discontinuities in spontaneous and piezoelectric polarization effects which cause charge separation between holes and electrons in quantum wells and limits the radiative recombination efficiency. Nonpolar GaN devices, such as in the *m*-plane {1100}, are free from polarization related electric fields since the polar *c*-axis is parallel to any heterointerfaces. Semipolar GaN-based devices have reduced electric fields.

Nonpolar and semipolar nitride epitaxial layers have other striking differences from *c*-plane. Namely, in conventional *c*-plane GaN heteroepitaxy, there is no shear stress on the easiest slip plane – the (0001) or basal plane and the next easiest slip plane – the prismatic {1100} *m*-plane. Epitaxy of mismatched layers on nonpolar and semipolar GaN, there are significant shear stresses in the inclined *m*-planes and on the inclined *c*-plane. Significant lattice mismatch-related stresses can be relieved by misfit dislocation formation via threading dislocation glide.

In this talk, we present the progress in developing high quality relaxed semipolar templates. The predominant relaxation in semipolar InGaN on GaN or AlGaN on GaN, in orientations such as (1122) or (2021), proceeds via threading dislocation glide on the inclined basal plane, followed in many cases by prismatic slip [1]. Since semipolar GaN has only one (0001) plane, plastic relaxation results in crystallographic tilt which can easily be measured in on-axis x-ray rocking curves or reciprocal space maps and can be directly used to quantify the extent of plastic strain relaxation [2]. The initial misfit stress relaxation occurs by glide of pre-existing threading dislocations [3,4] at a thickness slightly greater than the Matthews-Blakeslee critical thickness; the development of pseudomorphic InGaN and AlGaN semipolar buffer layers via dislocation strain relaxation [5,6,7]; blue (1122) LDs in relaxed buffer layers [8]; green LEDs on relaxed buffer layers [9].

[1] F. Wu et al., *Appl. Phys. Lett.* 99, 251909 (2011).

[2] E.C. Young et al. *Appl. Phys. Express* 3, 011004 (2010).

[3] E.C. Young et al. *Appl. Phys. Express* 3, 111002 (2010).

[4] P.S. Hsu et al., *Appl. Phys. Lett.* 99, 081912 (2011).

[5] F. Wu et al. *J. Appl. Phys.* 109, 033505 (2011)

[6] A.E. Romanov et al., *J. Appl. Phys.* 109, 103522 (2011).

[7] E.C. Young et al. *Appl. Phys. Express*, 4, 061001 (2011).

[8] P.S. Hsu et al. *Appl. Phys. Lett.* 100, 021104 (2012).

11:20am **EM-ThM11 Electronically Unmixed State of a Statistical Two-Dimensional Ga-Si Semiconductor Alloy on Si(111).** *P. Ebert, S. Landrock*, Forschungszentrum Jülich, Germany, *Y. Jiang*, Peking University, China, *K.H. Wu*, Chinese Academy of Sciences, China, *E.G. Wang*, Peking University, China, *R.E. Dunin-Borkowski*, Forschungszentrum Jülich, Germany

Alloying different semiconductor compounds attracted wide attention, since the materials properties of the resulting semiconductor alloy can be continuously tuned by varying the composition. Hence one can engineer semiconductor materials with, e.g., intentionally designed band gaps, lattice constants, and/or optical properties. This approach possesses a large technical and economical interest, as it is the basis for defining the wavelength of most optoelectronic devices.

For such applications, it is crucial that the newly formed semiconductor alloy has spatially homogeneous electronic properties, i.e., the original materials' properties of the individual alloyed compounds merge into the desired new properties. This is in general assumed to be the case for most three-dimensional compound semiconductor alloys. With the ever shrinking dimensions of semiconductor devices, the semiconductor alloy layers are becoming increasingly thinner. Ultimately only monolayer thin alloy layers may be needed and then the concept of a globally homogeneous alloy band structure, different from that of its alloyed compounds, needs to be reassessed. The central question is if a two-dimensional semiconducting alloys would always exhibit a merged new band structure in analogy to three-dimensional semiconductor alloys, or if locally the different band structures of the constituent semiconductor compounds of the alloy persist.

In this paper, we present a two-dimensional Ga-Si  $\sqrt{3}\times\sqrt{3}$  semiconductor alloy on Si(111) substrates as model system. Using atomically and momentum resolved STM and STS, we demonstrate that the electronic structure, i.e., density of states, band gap, and band structure, is atomically localized and different at Si and Ga atoms. No intermixing and formation of new alloy related electronic properties are observed, as if no alloying ever happened. This unmixed state is discussed in terms of the particular bonding structure of the two-dimensional alloy.

11:40am **EM-ThM12 Atomistic Analysis of Ge on a-SiO<sub>2</sub> using an Empirical Interatomic Potential to Describe Selective Epitaxial Growth.** *Y. Chuang*, University of Pennsylvania, *Q. Li, D. Leonhardt, S.M. Han*, University of New Mexico, *T. Sinno*, University of Pennsylvania

Integration of Ge and III-V compound semiconductors on Si has received significant recent attention for the next-generation, high-mobility transistors and III-V optoelectronic and photovoltaic devices.[1] However, managing dislocations and film stress due to lattice mismatch and thermal expansion coefficient mismatch remains a significant engineering challenge. One possible solution is selective epitaxial growth (SEG) where the epitaxial layer is grown in select areas to simultaneously manage dislocations and stress. For SEG, a dielectric layer (e.g., SiO<sub>2</sub> and Si<sub>3</sub>N<sub>4</sub>) with open windows that expose the underlying Si is typically employed to reduce the contact area between the deposited epitaxial layer and Si substrate, resulting in lower mismatch stress and defect density.[2] The selectively grown epitaxial islands can be further grown laterally over the dielectric layer and coalesced into a continuous film. The SEG technique squarely relies on weak interaction between growth precursors and the dielectric film, which prevents random nucleation. For instance, we have previously reported that desorption and surface diffusion barriers of Ge adspecies on SiO<sub>2</sub> are  $0.44 \pm 0.03$  and  $0.24 \pm 0.05$  eV, respectively.[3, 4] Herein, we present an atomistic analysis of Ge on SiO<sub>2</sub> in order to validate a Tersoff-based model for Si-Ge-O [5, 6]. We compare simulation predictions to detailed experimental data for a variety of properties. In particular, we consider bulk SiO<sub>2</sub> structural parameters as a function of temperature, Si-SiO<sub>2</sub> and Ge-SiO<sub>2</sub> interface energies, and the Ge-on-SiO<sub>2</sub> desorption energy and diffusion behavior. We show that with a single fitting parameter, the potential model provides a good overall description of the Si-Ge-O system, while retaining the highly efficient nature of the Tersoff potential, making it a good choice for larger-scale atomistic studies of Ge-on-Si SEG. We conclude by showing example calculations of stress distributions in epitaxial Ge islands in an SEG system.

[1] H. Lafontaine, D. C. Houghton, N. L. Rowell and G. C. Aers, *Appl. Phys. Lett.* **69**, 1444 (1996).

[2] T. A. Langdo, C. W. Leitz, M. T. Currie, E. A. Fitzgerald, A. Lochtefeld and D. A. Antoniadis, *Appl. Phys. Lett.* **76**, 3700 (2000).

[3] Q. Li, J. L. Krauss, S. Hersee, and S. M. Han, *J. Phys. Chem. C* **111**, 779 (2007).

[4] D. Leonhardt and S. M. Han, *Surf. Sci.* **603**, 2624 (2009).

[5] J. Tersoff, *Phys. Rev. B* **39**, 5566 (1989).

[6] S. Munetoh, T. Motooka, K. Moriguchi and A. Shintani, *Comput. Mater. Sci.* **39**, 334 (2007).

## Electron Transport at the Nanoscale Focus Topic Room: 16 - Session ET+NS+EM-ThM

### Electron Transport at the Nanoscale: Nanowires and Junctions

**Moderator:** K. Clark, Oak Ridge National Laboratory, A.-P. Li, Oak Ridge National Laboratory

8:00am **ET+NS+EM-ThM1 Functional Imaging of Semiconductor Nanowires and Devices.** *L.J. Lauhon*, Northwestern University

**INVITED** Microscopy has played a central role in the advancement of nanoscience and nanotechnology by enabling the direct visualization of nanoscale structure, and by extension predictive models of novel physical behaviors. Correlated imaging of nanoscale structure *and* properties is an important frontier that can provide a rational basis for engineering new materials and devices. I will describe our approach to correlated functional imaging with a focus on semiconductor nanowires. Nanocrystal growth modes such as the vapor-liquid-solid process provide the ability to tailor nanoscale structure and composition in three dimensions, creating new opportunities in a range of applications including light harvesting and solid state lighting. In this context, we have explored a number of important processing-structure-property relationships using atom probe tomography, scanning transmission electron microscopy, Raman microspectroscopy, and scanning photocurrent microscopy. From these studies, we develop a more comprehensive understanding of the influence of geometry, size, defects, dopants, and interfaces on carrier generation, recombination, and transport in nanostructured materials. This quantitative approach to characterization of model systems aims to identify applications that can derive significant benefits from the adoption of unconventional nanostructured materials.

8:40am **ET+NS+EM-ThM3 Electronic Transport and Structure Relations in Self-Assembled GdSi<sub>2</sub> Quantum Wires.** *S.Y. Qin, T. Kim*, Oak Ridge National Laboratory, *Y. Zhang, W. Ouyang*, University of California Irvine, *H. Weitering*, The University of Tennessee, *C. Shih*, The University of Texas at Austin, *A.P. Baddorf*, Oak Ridge National Laboratory, *R. Wu*, University of California Irvine, *A.-P. Li*, Oak Ridge National Laboratory

Quantum wires are extremely narrow one-dimensional (1D) materials where electron motion is allowed only along the wire direction, and is confined in the other two directions. Quantum wires, as a smallest electronic conductor, are expected to be a fundamental component in all quantum electronic architectures. The electronic conductance in quantum wires, however, is often dictated by structural instabilities and electron localization at the atomic scale. Adding interwire coupling can often lead to the formation of charge density waves. In both cases, the metallic state is not stable and a metal to insulator transition (MIT) occurs at low temperature. [1] Here we show that robust metallic conductance can be stabilized by interwire coupling, while the isolated single nanowires exhibit a MIT due to quantum localization.

We grow the quantum wires of GdSi<sub>2</sub> on Si(100) and study the evolution of electronic transport as a function of temperature and interwire coupling as the quantum wires are self-assembled *wire-by-wire*. As shown in Fig. 1, individual nanowires have a width of 16.7 Å, a height of 4 Å, and lengths of micrometers. These nanowires can be grown either in the form of isolated nanowires or bundles with a number of constituent wires separated by an atomic interwire spacing. We perform the correlated study of electronic properties by utilizing both scanning tunneling microscopy and nanotransport measurements on the same nanowire. [2] The approach takes advantage of our developments in fabricating nanocontacts using a field-induced atom emission process to bridge the atomic wires and the mesoscopic transport electrodes. [3] A MIT is revealed in isolated nanowires, while a robust metallic state is obtained in wire bundles at low temperature. The results provide a rare glimpse of the intrinsic structure-transport relations and the influence of local environments at the atomic scale. This research was conducted at the Center for Nanophase Materials Sciences, which is sponsored at Oak Ridge National Laboratory by the Office of Basic Energy Sciences, U.S. Department of Energy.

1. Changgan Zeng, P.R.C. Kent, Tae-Hwan Kim, An-Ping Li, Hanno H. Weitering, *Nature Materials*, **7**, 539 (2008).

2. Shengyong Qin, Tae-Hwan Kim, Wenjie Ouyang, Yanning Zhang, Hanno H. Weitering, Chih-Kang Shih, Arthur P. Baddorf, Ruqian Wu, and An-Ping Li, *Nano letters*, **12** (2), 938 (2012).

3. Shengyong Qin, Sondra Hellstrom, Zhenan Bao, Boyan Boyanov, and An-Ping Li, *Appl. Phys. Lett.* **100** (11), 022211 (2012).

9:00am **ET+NS+EM-ThM4 Multi-Segment Nanowire Heterojunctions of AuGe and Ge: Fabrication and Electrical Transport**, X.D. Li, G.W. Meng, Chinese Academy of Sciences, China, S.Y. Qin, A.-P. Li, Oak Ridge National Laboratory

One-dimensional (1D) multiple segment nanostructures that contain heterojunctions between various metals and semiconductors are of great interest due to their fascinating chemistry and size-, shape-, and material-dependent properties. Here we report on the synthesis and electronic characterization of multi - segment nanowire (NW) junctions of Au1-xGex and Ge. The 1D heterostructures are grown with a low - temperature chemical vapor deposition process, assisted by electrodeposited Au NWs inside nanochannels of anodic aluminum oxide template.[1,2] The Au-catalyzed vapor-liquid-solid growth process simultaneously in multiple locations along the nanochannel, which leads to multi-segment Au1-xGex/Ge heterojunctions. The structures of the as-grown hybrid NWs, analyzed by using transmission electron microscopy and energy dispersive X-ray spectroscopy elemental mapping, show clear compositional modulation with variable modulation period and controllable junction numbers. Remarkably, both GeNW and Au1-xGexNW segments are single crystalline with abrupt interfaces and good crystallographic coherences. The electronic and transport properties of individual NW junctions are measured by using a multi-probe scanning tunneling microscope (STM). The semiconducting nature of Ge segments and the metallic behavior of Au1-xGex segments are examined by scanning tunneling spectroscopy (STS). The transport current-voltage curves across the heterojunctions show a characteristic rectifying behavior, which is discussed in association with the potential barriers at the junction. The high yield of multiple segment NW junctions and the ability to control predictably the properties of a metal-semiconductor can facilitate the applications in nanoelectronics and optoelectronics that harness multiple functionalities of hetero-interfaces.

[1] Li, X. D.; Meng, G. W.; Xu, Q. L.; Kong, M. G.; Zhu, X. G.; Chu, Z. Q.; Li, A. P. Controlled Synthesis of Germanium Nanowires and Nanotubes with Variable Morphologies and Sizes. *Nano Lett.* **2011**, *11*, 1704–1709.

[2] Li, X. D.; Meng, G. W.; Qin, S. Y.; Xu, Q. L.; Chu, Z. Q.; Zhu, X. G.; Kong, M. G.; Li, A. P. Nanochannel-Directed Growth of Multi-Segment Nanowire Heterojunctions of Metallic Au1-xGex and Semiconducting Ge. *ACS Nano* **2012**, *6*, 831–836.

9:20am **ET+NS+EM-ThM5 Single Charge Nano Memory using Nano Carbon Material**, K. Matsumoto, T. Kamimura, Osaka University, Japan  
Single charges nano memory which can shift the threshold voltage by the stored single charge and operated at room temperature was realized using the carbon nanotube as an ultra short channel of 10nm.

The double gate stack insulator layers of Al2O3(3nm) and SiNx (27nm) are deposited using the atomic layer deposition to the suspended carbon nanotube with source and drain electrodes of 70nm separation. The carbon nanotube channel was then surrounded by this double gate stack insulator layers and the gap between the source drain electrodes with the insulator layers reduced down to as small as 10nm. The gate metal was then deposited through this gap to form the gate electrode of 10nm.

The dependence of the drain current on the top gate bias shows weak oscillation along the gate bias with the period of 220mV. The oscillation is attributed to the single charge injection from CNT channel to the Al2O3/SiNx interface trap, which make the threshold voltage shift of 220mV. The injection of charge is regulated by the Coulomb blockade that stops the next charge to be injected to the trap. The around trip of the gate bias produces the hysteresis. The width of the hysteresis was also regulated by the single charge injection and shows the stepwise increase.

Thus, we have succeeded in fabricating the single charge memory operated at room temperature.

9:40am **ET+NS+EM-ThM6 Combining Atomic Structure, Local Band Alignment, and Electron Transport through Individual Semiconductor Nanowires using Scanning Tunneling Microscopy**, R. Timm, O. Persson, M. Hjort, M.T. Borgström, L. Samuelson, A. Mikkelsen, Lund University, Sweden

III-V semiconductor nanowires offer tremendous possibilities for device application in energy and information technology [1]. Due to their unique properties and extreme surface-to-volume ratio, it is both essential and challenging to investigate their atomic structure and to combine this information with electrical measurements on individual nanowires. Recently, we have managed to clean InAs nanowires from their native oxide and obtained first atomically resolved images of their side surfaces by using scanning tunneling microscopy (STM) [2]. Here, we present a systematic STM study covering various nanowire surface structures emerging from different III-V material systems and different crystal structures. By combining STM imaging with scanning tunneling

spectroscopy (STS) measurements we simultaneously study the surface structure and local electronic properties across the interfaces of nanowire heterostructures like polytypic nanowires, *p-n*-junctions, and material heterostructures.

In order to go further in combining local structural and electronic characterization as well as transport measurements of nanowire devices, we have developed a new method to perform STM/S on individual nanowires *in-situ* under device operation: For this, specific heterostructure nanowires, distributed on a SiO<sub>2</sub>/Si substrate, are contacted with metal electrodes defined by electron beam lithography. Using a combined Atomic Force Microscopy (AFM) / STM setup, we can first locate an individual nanowire in AFM mode and then acquire STM images and STS spectra on the contacted nanowire. Thus, we obtain the LDOS spatially resolved along the nanowire, even while the nanowire is externally biased via the metal contacts, allowing simultaneous transport studies. We will show and discuss initial results for different heterostructure nanowire devices, demonstrating the large potential of this new method.

Finally, we can also use the STM to measure electron transport through individual upright standing nanowires still on their growth substrate: After imaging the nanowires from top by STM [3], a point contact between the STM tip and the Au particle on top of the nanowire can be established in ultrahigh vacuum, thereby overcoming the problems in contacting single nanowires known from conventional setups. A high accuracy and reproducibility of this method has been demonstrated for InP and InAs nanowires with different doping levels [4] as well as for Schottky barrier measurements on Au/GaAs nanowires.

[1] Y. Li *et al.*, *Mater. Today* **9** (10), 18 (2006).

[2] E. Hilner *et al.*, *NanoLetters***8**, 3978 (2008).

[3] A. Fian *et al.*, *Nano Letters* **10**, 3893 (2010).

[4] R. Timm *et al.*, *submitted* (2012).

10:40am **ET+NS+EM-ThM9 Point-Contact Spectroscopy Study of Topological Insulators and Superconductors**, Z. Jiang, Georgia Institute of Technology

Recently, much attention has been given to an intriguing class of materials, the so-called topological insulators. This type of material exhibits a band gap in the bulk, but gapless states on the edge or surface, which are protected by topological order and cannot be analogized to previous conventional semiconductors or insulators. When topological insulators are in contact with a superconductor (e.g., Nb, a conventional *s*-wave superconductor), novel proximity effect occurs. Theory predicts that the proximity induced superconducting state is spinless and *p*-wave like, and Majorana bound states may appear at the edges. On the other hand, in a related research avenue topological superconductors are predicted to possess unconventional pairing symmetries and gapless surface Andreev bound states. Theoretically massless Majorana fermions could be realized in such materials and used as a building block for topological quantum computation.

Here we present our point-contact spectroscopy studies of topological insulators and superconductors. Specifically, we use a superconducting Nb tip to approach the surface of topological insulators and measure the interface conductance as a function of bias voltage, temperature and magnetic field. Indeed, we find that a superconducting state can be induced at the interface when the Nb tip is in good contact with the topological insulator, as evidenced by observation of a zero-bias conductance peak in the point-contact spectra at a temperature below the superconducting transition temperature of Nb. Such an induced superconducting state is robust even in a magnetic field up to 1T. In the study of topological superconductors, we use a normal-metal Au tip to approach the surface, and a zero-bias conductance peak is also observed. Owing to accurate control of the point-contact barrier strength (tip/sample) in our experiments, the obtained spectra are free of artificial background, and therefore can be quantitatively compared with existing theories; good agreement is achieved.

11:00am **ET+NS+EM-ThM10 Identifying and Measuring the State Variables in TaOx Memristors**, P.R. Mickel, M. Marinella, C.D. James, Sandia National Laboratories

We present evidence of the identification and characterization of a new state variable in TaOx memristors. Thus far, the state variable controlling the resistive switching has been believed to be the oxygen concentration in the conducting Ta filament. However, using voltage pulse measurements sensitive to small changes in resistance, we shown that the changing area of the conducting filament is in fact the dominant switching mechanism. The oxygen concentration in the Ta filament is shown to control the memristor resistance for low resistances, after which we observe a clear crossover to the area state variable dominated resistance range. Voltage and temperature dependence are investigated for the switching time-scales,  $\tau$ , and

magnitudes of filament area change, providing insight into their driving mechanisms and the resolution limits of their modulation.

11:20am **ET+NS+EM-ThM11 Terahertz Spectroscopy and Carrier Dynamics of Al Doped ZnO Nanowires**, *S. Balci, W. Baughman, D.S. Wilbert, G. Shen, N. Dawahre, P. Kung, S.M. Kim*, The University of Alabama

Terahertz time domain spectroscopy (THz-TDS) has been widely investigated for many applications in sensing and imaging technologies over the past two decades. Terahertz wave, with a frequency between 300GHz to 10THz, is especially attractive for various applications including security monitoring, biomedical imaging, high speed electronics and communications, and chemical and biological sensing. There is also an increasing interest for nondestructive testing using the THz waves because they have unique properties of propagation through certain media and cover a number of important frequencies. For such applications, THz-TDS has become a powerful tool and measurement technique that can probe carrier dynamics at high frequencies, and thus may yield a better understanding of the characteristics of high frequency optoelectronics and many other fundamental properties of materials. Using THz-TDS, one can determine the frequency dependence of basic properties of materials, including their complex dielectric constant, refractive index and electrical conductivity. Unlike conventional Fourier-Transform spectroscopy, THz-TDS is sensitive to both the amplitude and the phase of the wave, thereby allowing for a direct approach to determining complex values of material parameters with the advantage of high signal to noise ratio and coherent detection. In addition, it is possible to carry out THz-TDS experiments without any electrical contact to the sample being probed, which significantly facilitates electrical measurements on nanostructures and nanomaterials.

In this work, we investigated the physical properties of ZnO:Al nanowires (NWs) in using THz-TDS both at room temperature and elevated temperatures for the first time. ZnO NWs were grown by thermal chemical vapor deposition and in-situ doped with Al, which increased their electrical conductivity by one order of magnitude compared to undoped nanowires. THz-TDS measurements yielded the relative change in the transmitted THz electric field magnitude and phase caused by the samples being probed, which was used to extract the nanowire material refractive indices through mathematical iterative calculations. These subsequently allowed a determination of the complex conductivity, refractive index, and absorption coefficient. To obtain the carrier dynamics parameters, we showed that the Drude-Smith model had to be applied to the frequency dependent complex conductivity in order to determine the plasma frequency and relaxation time. To gain a better understanding of the dependence on doping, the measurements were performed for both undoped ZnO NWs and Al-doped ZnO NWs, as well as a function of temperature in each case.

11:40am **ET+NS+EM-ThM12 Probing Surface-Independent Minority Carrier Transport in Semiconductor Nanowires using Kelvin Probe Microscopy**, *A. Soudi, C. Hsu, Y. Gu*, Washington State University

In advancing semiconductor nanowire-based device technologies, a quantitative knowledge of carrier transport properties is required for a rational design of devices with controlled performance. The one-dimensional confinement of charge carriers and phonons can lead to novel transport properties, and thus represents an advantage of semiconductor nanowires in electronic and opto-electronic applications. However, due to the high surface-to-volume ratio, surface effects are prevalent in nanowires, and the measured carrier transport properties are usually dominated by surface-related processes, such as carrier trapping and recombination processes facilitated by surface states. To evaluate the intrinsic transport properties, especially those related to the confinement effects, the capability to probe surface-independent carrier transport properties is desired. Here we present studies of bulk limited minority carrier transport properties in semiconductor nanowires using the scanning Kelvin probe microscopy technique. Specifically, by measuring and modeling the spatial variations of the nanowire surface potential close to a nanowire-metal Schottky junction, both under an above-bandgap illumination and in the dark, the surface-independent minority carrier diffusion length was obtained.

## Transparent Conductors and Printable Electronics Focus Topic

Room: 7 - Session TC+EM+AS+TF+EN-ThM

## Transparent Conductors and Devices

Moderator: L.M. Porter, Carnegie Mellon University

8:20am **TC+EM+AS+TF+EN-ThM2 High Conductivity in Thin ZnO:Al Deposited by Means of the Expanding Thermal Plasma Chemical Vapor Deposition**, *K. Sharma, H.C.M. Knoops, M.V. Ponomarev*, Eindhoven University of Technology, The Netherlands, *R. Joy, M. Velden, D. Borsa, R. Bosch*, Roth and Rau BV, Germany, *W.M.M. Kessels, M. Creatore*, Eindhoven University of Technology, The Netherlands

Session: Transparent Conductors and Devices

The ever-increasing demand for transparent conducting oxides (TCO) for application in flat panel displays, light emitting diodes (LEDs), and thin film photovoltaics drives the present research in the field of TCOs. Aluminum-doped zinc oxide (ZnO:Al) is often referred to as a potential alternative to e.g. indium tin oxide. The ZnO:Al is considered appealing due to the relatively low cost, high abundance, non-toxicity, resistance to H<sub>2</sub> etching and, under specific conditions, surface texturing for light management/trapping. Thin ZnO:Al films (~ 100 nm) with low resistivity ( $2.5 \cdot 10^{-4}$  ohm\*cm) along with high transmission (> 85 %) are desirable in many devices. Furthermore, large area processing/ high throughput are essential pre-requisites for industrial applications.

ZnO:Al thin films (< 150 nm) have been deposited by using an in-line industrial expanding thermal plasma chemical vapor deposition (ETP-CVD) technique,<sup>1,2,3</sup> by means of O<sub>2</sub>/diethylzinc/trimethylaluminium mixtures. High diethyl zinc flow rate conditions<sup>2</sup> were applied, which enable the development of a conductive ( $5 \cdot 10^{-4}$  Ω·cm), 300 nm-thick ZnO:Al layer by promoting the development of a densely packed structure at early stages of growth, as very recently reported.<sup>2</sup>

In the present contribution, the effect of the dopant, i.e. trimethylaluminium, is investigated to further improve the electrical quality of even thinner ZnO:Al layers. ZnO:Al films were analyzed with spectroscopic ellipsometry, four point probe, hall measurements, X-ray photon spectroscopy (XPS), Rutherford backscattering (RBS), elastic recoil backscattering (ERD), and X-ray diffraction (XRD).

A remarkable low resistivity of  $5 \cdot 10^{-4}$  Ω·cm was measured for a ZnO:Al film with thickness of only 120 nm, characterized by a carrier concentration of  $1 \cdot 10^{21}$  cm<sup>-3</sup>, with an electron mobility in the range of 10-25 cm<sup>2</sup>/V · s.<sup>2,3</sup> The obtained mobility values are higher than previously reported value of 13 cm<sup>2</sup>/V · s for 300 nm thick ZnO:Al.<sup>2</sup> The improvement in terms of conductivity is attributed to the large hydrogen content ( $2.4 \cdot 10^{21}$  at/cm<sup>3</sup>) promoting the chemical passivation of the grain boundaries.

A broad characterization of highly conductive thin ZnO:Al films along with insights on charge transport process will be presented.

Reference List

1. B. Hoex *et al.*, Progress in Photovoltaics **13**, 705 (2005).
2. M. V. Ponomarev *et al.* Journal of Applied Physics **112**, 043708 (2012).
3. M. V. Ponomarev, *et al.*, Journal of Applied Physics **111**, 063715 (2012).

8:40am **TC+EM+AS+TF+EN-ThM3 Recent Progress in Oxide Semiconductors and Oxide TFTs**, *H. Hosono*, Tokyo Institute of Technology, Japan

Transparent conductive oxides (TCOs) and transparent oxide semiconductors (TOSs) have a long history since 1950s. The material design concept for TCOs looks almost established, i.e., ionic oxides p-block metals with an electronic configuration of (n-1)d<sup>10</sup>ns<sup>0</sup> and a spatial spread of ns orbitals which is enough to have large overlap with neighboring metal ns orbitals irrespective of intervening oxygen ion<sup>1</sup>. Concretely, most of the TCOs have been realized in the material systems of In<sub>2</sub>O<sub>3</sub>-SnO<sub>2</sub>-CdO-Ga<sub>2</sub>O<sub>3</sub>-ZnO. Materials based on light metal oxides such as Al<sub>2</sub>O<sub>3</sub> and SiO<sub>2</sub> have not been regarded as the candidates of TCOs. In 2002, we<sup>2</sup> reported high electronic conductivity in 12CaO·7Al<sub>2</sub>O<sub>3</sub> (C12A7) which had been a typical insulator and this discovery was followed by transparent conductivity in cubic SrGeO<sub>3</sub> in 2011.<sup>3</sup> These two materials are TCOs realized by a new material design concept.

As for TOS, the striking advances are seen in transparent amorphous oxide semiconductors (TAOS) in science and technology due to strong demand for active layer materials in thin film transistors (TFTs). Amorphous In-Ga-Zn-O (IGZO) TFTs, which was first reported in late 2004,<sup>4</sup> has adopted to drive high resolution displays of new iPad.<sup>5</sup> This is a first mass production of TOS

family. The major reasons for this adoption are high electron mobility (an order of larger than that of a-Si:H) and easy fabrication process. A major advance in TOS-TFTs is realization of p-channel TFTs and subsequent fabrication of C-MOS using ambipolar SnO.<sup>6)</sup>

In this talk, I review these progresses viewed from the electronic state of these materials.

- 1) H. Kawazoe, H. Yanagi, K. Ueda, and H. Hosono. *MRS Bull.*, 25, 28 (2000)
- 2) K. Hayashi, S. Mitsuishi, T. Kamiya, M. Hirano, H. Hosono, *Nature* 419, 462 (2002).
- 3) H. Mizoguchi, T. Kamiya, S. Mitsuishi, H. Hosono: *Nat. Commun.*, 2, 470 (2011).
- 4) K. Nomura, H. Ohta, A. Takagi, T. Kamiya, M. Hirano, H. Hosono, *Nature* 432, 488 (2004).
- 5) Sharp Press Release April 6, 2012
- 6) K. Nomura, T. Kamiya, and H. Hosono: *Adv. Mater.*, 23, 3431 (2011)

9:20am **TC+EM+AS+TF+EN-ThM5 Surface Functionalization of Amorphous Zinc Tin Oxide Thin Film Transistors**, G.S. Herman, M.S. Rajachidambaram, Oregon State University, A. Pandey, S. Vilayrganapathy, P. Nachimuthu, S. Thevuthasan, Pacific Northwest National Laboratory

Amorphous zinc tin oxide semiconductor materials have been studied primarily as the active semiconducting material for thin film transistors (TFT) for applications including transparent and flexible electronics. Due to the amorphous nature of these materials excellent uniformity can be obtained over large areas while still having reasonably high electron mobilities ( $>10 \text{ cm}^2/\text{Vs}$ ). Considerable control over the electrical properties of ZTO can be maintained, where insulating, semiconducting, and conductive films can be obtained by varying the processing and post-annealing conditions. We have recently characterized sputter-deposited zinc tin oxide (ZTO) as the active material for TFTs and found that the switching properties of ZTO are closely related to deposition, post-annealing, and electrical test conditions. In this presentation we will discuss bias stress induced instabilities for ZTO TFTs. We have found that devices with a backchannel exposed to the atmosphere have a positive subthreshold shift under positive bias, which can be well explained by a stretched exponential model. Using this model the shifts may be related to either electron trapping at the dielectric semiconductor interface or due to metastabilities of the active material. We have found that the adsorption of a self-assembled monolayer (SAM) on the backchannel of the TFT effectively passivates the device and significantly reduces the bias stress induced instabilities. In this study we will present contact angle measurements and x-ray photoelectron spectroscopy to better understand the interaction of the SAM with the ZTO surface, and the improved stability of the ZTO TFTs will be discussed in regards to the interfacial chemistry of the backchannel.

9:40am **TC+EM+AS+TF+EN-ThM6 Work Function and Valence Band Structure of Oxide Semiconductors and Transparent Conducting Oxides Grown by Atomic Layer Deposition**, A. Yanguas-Gil, Argonne National Laboratory, R.T. Haasch, University of Illinois at Urbana Champaign, J.A. Libera, J.W. Elam, Argonne National Laboratory

Atomic Layer Deposition offers a low-temperature, scalable route to the synthesis of a wide range of oxide semiconductors and transparent conducting oxides both in flat and high aspect ratio surfaces. We have carried out studies on the influence of concentration and spatial distribution on the electrical properties within the ZnO-SnO<sub>2</sub>-In<sub>2</sub>O<sub>3</sub> compositional map, including standard TCO materials such as Al:ZnO and ITO. We will present results on the work function and valence band structure of transparent conducting oxides grown by ALD using ex-situ UPS measurements, including the influence of the surface termination on the interfacial properties of the materials. Finally, the ability of ALD to tailor the surface and interfacial properties of TCOs based on its layer-by-layer nature will be discussed.

10:40am **TC+EM+AS+TF+EN-ThM9 Low Temperature, High Performance Solution-Processed Metal Oxide Thin Film Transistors formed by a 'Sol-Gel on Chip' Process**, H. Sirringhaus, University of Cambridge, UK **INVITED**

N-type amorphous mixed metal oxide semiconductors, such as ternary oxides, where M<sup>1</sup> and M<sup>2</sup> are metals such as In, Ga, Sn, Zn, have recently gained momentum because of high carrier mobility and stability and good optical transparency, but they are mostly deposited by sputtering. To date only limited routes are available for forming high-performance mixed oxide materials from solution at low process temperature  $< 250^\circ \text{C}$ . Ionic mixed metal oxides should in principle be ideal candidates for solution processible materials because the conduction band states derived from metal s-orbitals are relatively insensitive to the presence of structural disorder and high

charge carrier mobilities are achievable in amorphous structures. Here we report the formation of amorphous metal oxide semiconducting thin films via a 'sol-gel on chip' hydrolysis approach from soluble metal alkoxide precursors, which affords unprecedented high field-effect mobilities of  $10 \text{ cm}^2/\text{Vs}$ , reproducible and stable turn-on voltages  $V_{\text{on}} \gg 0 \text{V}$  and high operational stability at maximum process temperature as low as  $230^\circ \text{C}$ . We discuss the effect of film composition on device performance and stability.

11:20am **TC+EM+AS+TF+EN-ThM11 In Situ Measurements of Interface States and Junction Electrical Properties of Electrically Biased Metal /  $\beta$ -Ga<sub>2</sub>O<sub>3</sub> Structures**, H. Pham, X. Zheng, B. Krueger, M.A. Olmstead, F.S. Ohuchi, University of Washington

A significant issue in application of wide-band-gap transparent conducting oxides is formation of reliable ohmic and rectifying metal contacts. The metal-oxide interface properties are dominated by chemical reactions during growth and the resultant interface state distribution once the interface is formed. We have investigated interface formation between the wide band gap TCO  $\beta$ -Ga<sub>2</sub>O<sub>3</sub> ( $E_g = 4.8 \text{ eV}$ ) and the metals Pd, Ni, Ti and Al with in-situ x-ray photoemission spectroscopy (XPS) both during growth and during sputter profiling. The two techniques give very similar results, demonstrating that in this case sputter profiling does not significantly alter the interface chemistry. Consistent with the relative compound heats of formation, Ni and Pd show very little interface reaction with either Ga or O, while Ti interacts strongly with both Ga and O and Al interacts primarily with oxygen. Electrically, Ni and Pd have similar Schottky barriers on the intrinsically n-type oxide (about 0.9 eV), Ti forms a symmetric, nearly ohmic contact, while Al exhibits a smaller barrier (about 0.6 eV). To probe the nanoscopic origins of the Schottky contact behavior through the interface state energy distribution, we combined *in-situ* deposition of thin metal layers and application of forward/reverse biases to the metal-oxide junction with XPS measurements of the relative positions of the Ga<sub>2</sub>O<sub>3</sub> bands (via the Ga 3d or O 1s core level) and the metal Fermi level. The density of interface states determines the rate at which the Fermi level can be moved through the oxide band gap, so variation of the oxide core-level shift with respect to the bias voltage yields the interface state density. We find the metal and oxide bands maintain their relative alignment under forward bias (back-plane negative with respect to metal), while they separate at a rate about half that of the applied bias under reverse bias (positive bias with respect to metal).

11:40am **TC+EM+AS+TF+EN-ThM12 Atmospheric Pressure Dielectric Barrier Discharge (DBD) Post Annealing of Aluminium Doped Zinc Oxide (AZO) Films**, Y.L. Wu, E. Ritz, J. Hong, T.S. Cho, D.N. Ruzic, University of Illinois at Urbana Champaign

Aluminum-doped Zinc Oxide (AZO) is a material that has high electrical conductivity while being highly transparent at the same time. It could find many useful applications in our daily lives such as displays, mobile devices, solar cells, etc. Currently AZO films are considered as attractive alternatives to materials such as Indium Tin Oxide (ITO) due to its much cheaper cost and comparable high electrical conductivity. A process of depositing AZO film by dual DC magnetron system has been developed. Film thicknesses were measured to be about 300nm by stylus contact profilometer and transparency of greater than 90% in the visible range were measured with spectrophotometry methods. Film conductivities were in the order of  $10^{-3} \text{ Ohm-cm}$  with the four-point probe method. By using a Dielectric Barrier Discharge operating at atmospheric pressure, conductivity of film can be further lowered. A 500mm x 30mm line source operating at a Nitrogen flow of 250L/min was used and  $\sim 0.4 \text{ L/min}$  Hydrogen gas was also introduced into the discharge system to create Hydrogen radicals. A 10%-15% decrease in electrical resistance was observed with no changes in the optical properties of the AZO films. The elemental composition of the film was measured by X-ray photoelectron spectroscopy (XPS) and the change of crystal structure after DBD post annealing was measured by X-ray diffraction (XRD).

**Thin Film**

**Room: 10 - Session TF+EM+SE+NS-ThM**

**Nanostructuring Thin Films**

**Moderator: R.C. Davis, Brigham Young University**

8:00am **TF+EM+SE+NS-ThM1 Plasma Effects in Nanostructuring Thin Films**, K. Ostrikov, CSIRO Materials Science and Engineering, Australia **INVITED**

In this presentation, several examples of uniquely plasma-enabled nanostructuring of thin film materials for applications in energy conversion and storage, environmental monitoring, and bio-sensing. Strong emphasis is

made on atom-, energy-efficiency, and environment-friendliness of plasma-based nanotechnologies.

**1. Introduction:** Atom- and energy-efficient nanotechnology is the ultimate Grand Challenge for basic energy sciences as has recently been road-mapped by the US Department of Energy. This ability will lead to the energy- and matter-efficient production of functional nanomaterials and devices for a vast range of applications in energy, environmental and health sectors that are critical for a sustainable future. Here we present examples related to atom- and energy-efficient nanoscale synthesis of advanced nanomaterials for energy conversion and storage, environmental sensing, and also discuss effective cancer cell treatment using low-temperature plasmas.

**2. Atom- and energy-efficient nanostructure production for energy storage:** Here we show an example of a recent achievement of a very low amount of energy per atom (~100 eV/atom) in the synthesis of MoO<sub>3</sub> nanostructures for energy storage (e.g., Li-ion battery) applications. This was achieved by using time-programmed nanosecond repetitive spark in open air between Mo electrodes. Highly-controlled dosing of Mo and O atoms was achieved through the controlled evaporation and dissociation reactions and maintaining reactive chemistry in air. These nanomaterials show excellent electrochemical and energy storage performance.

**3. Environment-friendly, single-step solar cell production:** Highly-efficient (conversion efficiency 11.9%, fill factor 70 %) solar cells based on the vertically-aligned single-crystalline nanostructures have been produced without any pre-fabricated p-n junctions in a very simple, single-step process of Si nanoarray formation by etching p-type Si wafers in low-temperature environment-friendly plasmas of argon and hydrogen mixtures. The details of this process and the role of the plasma are discussed.

**4. Metal-nanotube/graphene environmental and bio-sensors:** Plasma processing was successfully applied for the fabrication of hybrid nanomaterials based on metal-decorated carbon nanotubes and vertically aligned graphenes. The applications of these structures in environmental (gas) and bio-sensing (SERC/plasmonic) platforms are presented. The vertically-aligned graphene structures have been grown without catalyst and any external substrate heating, owing to the unique plasma properties.

8:40am **TF+EM+SE+NS-ThM3 Directed, Liquid Phase Assembly of Patterned Metallic Films by Pulsed Laser Dewetting.** *Y. Wu*, University of Tennessee, *J.D. Fowlkes, M. Fuentes-Cabrera*, Oak Ridge National Laboratory, *N.A. Roberts, P.D. Rack*, University of Tennessee

Self-assembly of materials offer the potential to synthesize complex systems by defining the *initial and bounding* conditions if the fundamental scientific principles guiding the assembly are known. Much work has been performed studying the assembly of continuous thin polymer and metal films which reveal interesting dewetting phenomenon. Less work has been devoted to the directed assembly and pattern formation of confined or patterned metallic thin films. Meanwhile, the synthesis of functional metallic nanomaterials via self-assembly has been an effective and low-cost approach to realize many critical applications of nanoscience and nanotechnology. In this study, the dewetting and nanopattern formation of nanolithographically pre-patterned thin films of various shapes via pulsed nanosecond laser melting were investigated to understand how initial boundary conditions facilitate precise assembly. Specifically we will show experimental and computational results (continuum and molecular dynamics) illustrating how so-called synthetic perturbations can vary the dispersion of the resultant nanoparticle size and shape distribution of pseudo-one-dimensional liquid metal wires. Furthermore, we will show how controlling the shape and size of bi-metallic nanostructures, the assembly of multifunctional nanoparticles can be assembled.

9:00am **TF+EM+SE+NS-ThM4 Nanosphere Lithography for Bit Patterned Media.** *A.G. Owen, H. Su, A.M. Montgomery, S.M. Kornegay, S. Gupta*, University of Alabama

Nanosphere lithography 1-4 has been used to pattern perpendicular magnetic anisotropy Co/Pd multilayers into nanopillars for the first time for bit-patterned media applications. A multilayer stack of Pd<sub>10</sub>/[Co<sub>0.3</sub>Pd<sub>1.9</sub>]/Pt<sub>5</sub> nm nanolayers was deposited onto a bare silicon wafer. The nanospheres were spin-coated into a uniform monolayer and then reduced in size by plasma ashing in oxygen. The Co/Pd multilayer films were subsequently ion milled into nanopillars using the reduced nanospheres as masks. We tested two ranges of nanosphere sizes, one at about 100 nm, and the other at about 1000 nm. In order to optimize the ashing of the nanospheres, response surface methodology (RSM) was performed to optimize the ashing power and time. It was seen that ashing at low powers of less than 100 W for longer times was more effective than higher powers for short times in shrinking the nanosphere masks without damage. The subsequent ion milling of the Co/Pd films was performed at a near-perpendicular angle to minimize shadowing by the nanospheres. We will discuss some of the complex shapes the nanospheres were patterned into after ashing, and how

they translated into variously sized and shaped nanopillars of Co/Pd multilayers after ion milling. Magnetometry was used to characterize the films before and after patterning, showing an improvement in the coercivity and squareness of the media after patterning with nanospheres that were shrunk, but not damaged, by ashing. Micromagnetic simulations using Object Oriented Micromagnetic Framework (OOMF) have been carried out to produce a simulated hysteresis loop which is then compared with the experimental results.

#### Acknowledgements

The NSF ECCS 0901858 grant, entitled "GOALI: Nanopatterned graded media" is acknowledged for support. Alton Highsmith is acknowledged for support in the UA Microfabrication Facility.

#### References

1. Xiao Li, T. R. Tadisina, S. Gupta, J. Vac. Sci. Technol. A **27**, Jul/Aug 2009, 1062
2. Kosmas Ellinis, A. Smyrnakis, A. Malainou, A. Tseripi, E. Gogolides, Microelectronic Engineering, **88**, 2011, 2547-2551
3. C. L. Haynes, R. P. Van Duyne, J. Phys. Chem. B **105**, 5599, 2001
4. S. M. Weekes, F. Y. Ogrin, W. A. Murray, Langmuir **20**, 11208, 2004

9:20am **TF+EM+SE+NS-ThM5 Effects of Nanometer Scale Periodicity on the Self-Propagating Reaction Behaviors of Sputter-Deposited Multilayers.** *D. Adams, R. Reeves*, Sandia National Laboratories

Nanometer-scale, vapor-deposited multilayers are an ideal class of materials for systematic, detailed investigations of reactive properties. Created in a pristine vacuum environment by sputter deposition, these high-purity materials have well-defined reactant layer thicknesses between 1 and 1000 nm, minimal void density and intimate contact between layers. If designed appropriately, these energetic materials can be ignited at a single point and exhibit a subsequent, high-temperature, self-propagating formation reaction. The nanometer-scale periodicity set through design tailors the effective diffusion length of the subsequent self-propagating reaction.

With this presentation, we describe effects of the nanometer-scale, multilayer periodicity on i) the reactivity of multilayers in different surrounding gaseous environments and ii) the reaction front morphology as viewed in the plane of the multilayer. We show that nickel/titanium and titanium/boron multilayers are affected by the surrounding gaseous environment, and describe how the magnitude of average propagation speed depends on multilayer periodicity. Fine multilayer designs are characterized by fast reaction waves, and there is no difference in average propagation speed when reacted in air (atm. pressure) versus vacuum (1 mTorr). Coarse multilayer designs are generally slower and are affected by secondary oxidation reactions when conducted in air. These thick multilayer designs are affected by the pressure of the surrounding gaseous environment with enhanced propagation speeds owing to the highly exothermic reaction of Ti with O. Regarding the effects of nanometer-scale multilayer periodicity on reaction front morphology, we show that reactive multilayers often have a smooth reaction front when layer periodicity is small. However, multilayers having larger periodicity (and hence larger effective diffusion lengths) exhibit reaction front instabilities and complex reaction front morphologies.

In this talk, we also stress how the propensity to oxidize and the propensity to form reaction front instabilities (as affected through nanometer-scale design) impact final properties of the multilayers for applications such as localized joining.

Sandia is a multiprogram laboratory managed and operated by Sandia Corporation, a wholly owned subsidiary of Lockheed Martin Company, for the United States Department of Energy's National Nuclear Security Administration under Contract DE-AC04-94AL85000.

9:40am **TF+EM+SE+NS-ThM6 Ag Nanoparticles Supported by (111) Facets on Biaxial CaF<sub>2</sub> Nanoblades.** *M. Auer, D. Ye*, Virginia Commonwealth University

Silver nanoparticles of different diameters were grown in an effort to study methods of preferentially orienting the geometry of metal nanoparticles. Arrays of calcium fluoride nanorods were grown on silicon substrates using oblique angle deposition at 75° incident angle. A method was then developed to grow silver nanoparticles exclusively on the (111) facet of the calcium fluoride tips. Cross sectional scanning electron microscopy and transmission electron microscopy imaging was used to verify that the nanoparticles adhered exclusively to the desired facet of the tip. Using selected area diffraction and dark field in the TEM, it was shown that the nanoparticles did grow at a [111] orientation at the interface between them and the calcium fluoride rods. Different thicknesses and diameters of nanoparticles were then grown to determine what an ideal size was to achieve the most [111] orientation of the nanoparticles.

## Thin Film

Room: 11 - Session TF+NS+EM-ThM

### Thin Films: Growth and Characterization-II

Moderator: C. Vallee, LTM - MINATEC - CEA/LETI, France

8:00am **TF+NS+EM-ThM1 Plasma-enhanced Atomic Layer Epitaxy of AlN Films on GaN**, *N. Nepal, J.K. Hite, N. Mahadik, M.A. Mastro, C.R. Eddy, Jr.*, U.S. Naval Research Laboratory

AlN and its alloys with GaN and InN are of great interest for number of applications. In a device structure that employs an ultrathin layer of these materials, thickness control at the atomic scale is essential. Atomic layer epitaxy (ALE) is one of the most promising growth methods for control of epilayer thickness at the atomic scale. There are reports on atomic layer deposition of AlN on GaN and Si substrates [1]. In those reports, the AlN layers were either amorphous or composed of nm-sized crystallites. Since ALE is a low temperature growth process, there is significantly reduced thermal energy for adatoms to bond at preferred lattice sites and promote growth of crystalline material, therefore, surface preparation plays a very important role to ensure a crystalline layer.

In this work, we present recent efforts to improve the crystalline quality of ALE AlN layers on MOCVD grown GaN/sapphire templates, including the influence of *ex situ* and *in situ* surface pretreatments to promote uniform two-dimensional (2D) nucleation of AlN layers and ALE growth of crystalline AlN films thereupon. AlN layers were grown at 500°C by ALE simultaneously on Si(111) and GaN/sapphire templates and characterized using spectroscopic ellipsometry (SE), x-ray diffraction (XRD), and atomic force microscopy measurements. The SE measurements indicate that the AlN growth on Si(111) is self-limited for trimethylaluminum (TMA) pulse of length 0.04 to 0.06 sec. However, the AlN nucleation has a bimodal island size distribution for TMA pulses < 0.06 sec. The AlN nucleation becomes uniform and 2D for a pulse length of 0.06 sec, therefore, this pulse length was used to study the GaN surface pretreatment on the nucleation of AlN layer. GaN surfaces were pre-treated *ex situ* with HF and HCl wet chemical etches. Alternating pulses of trimethylgallium and hydrogen plasma followed by an hour of annealing at 500°C (emulating a Ga-flash-off process) were employed *in situ* before growing an AlN layer. For 3 cycles of Ga-flash-off the AlN nucleation is uniform and replicates the GaN surface morphology on both HF and HCl pretreated GaN. XRD measurements on 36 nm thick AlN films reveal that the ALE AlN on GaN/sapphire is crystalline with only a wurtzite structure and a (0002) peak rocking curve FWHM of 630 arc-sec, which is close to the typical value for AlN grown by MBE and MOCVD [2,3]. Electrical characterization of 2D electron gas at the AlN/GaN interface will also be presented.

References:

1. M. Alevli et al., Phys. Status SolidiA **209**, 266 (2012), and references therein.
2. T. Koyama et al., Phys. Stat. Sol. (a) **203**, 1603 (2006).
3. K. Balakrishnan et al., Phys. Stat. Sol. (c) **3**, 1392 (2006).

8:20am **TF+NS+EM-ThM2 In Situ Infrared Spectroscopy Study of Cobalt Silicide Thin Film Growth by Atomic Layer Deposition**, *K. Bernall Ramos*, University of Texas at Dallas, *M.J. Saly*, SAFC Hitech, *J. Kwon*, University of Texas at Dallas, *M.D. Halls*, Materials Design Inc., *R.K. Kanjolia*, SAFC Hitech, *Y.J. Chabal*, University of Texas at Dallas  
Cobalt silicide has potential applications in microelectronics. For instance, the drive to scale down integrated circuitry (IC) has led to the consideration of cobalt silicide (CoSi<sub>2</sub>) as an alternative contact material for titanium silicide (TiSi<sub>2</sub>) in future self-aligned silicide technology due to its wider silicidation window and superior thermal and chemical stability. Studies of the growth mechanisms during film deposition are critical to better understand and control thin film formation.

This work focuses on the atomic layer deposition (ALD) of cobalt silicide (CoSi<sub>2</sub>), using (tertiarybutylalyl)cobalttricarboxyl ((tBuAllyl)Co(CO)<sub>3</sub>) and trisilane on H-terminated silicon to uncover the film growth mechanisms. The first pulse of (tBuAllyl)Co(CO)<sub>3</sub> reacts completely with the H-terminated Si surface forming one monolayer of metallic silicide through the reduction of the allyl ligand by transfer of the surface hydrogen and the formation of Co-Si bonds. In situ infrared absorption spectra show the complete loss of H-Si bonds, and the appearance of surface-bound carbonyl and CH<sub>x</sub> ligands after the first (tBuAllyl)Co(CO)<sub>3</sub> pulse on H/Si(111). Further deposition of CoSi<sub>2</sub> is possible only after the linear carbonyl groups (initially observed, on the surface after the first (tBuAllyl)Co(CO)<sub>3</sub>) are removed by subsequent ALD cycles. Further ALD cycles give rise to cobalt silicide growth through ligand exchange after a

nucleation period of 2–4 cycles. The resultant CoSi<sub>2</sub> films are characterized by a low concentration of carbon impurities in the bulk according to X-ray photoemission spectroscopy (XPS).

1 Kwon et al. Chem. Mater. 2012, 24, 1025–1030

8:40am **TF+NS+EM-ThM3 Thin Film Growth: From Gas Phase to Solid Phase – Links and Control**, *P. Raynaud*, CNRS and University Paul Sabatier – Toulouse – France

INVITED

PECVD, PVD, ALD, sputtering processes, are widely used for thin film growth. Nevertheless, the growth mechanisms need to be controlled and understood to be able to propose stable, adaptable and reproducible processes. Gas, plasma or “volume” phase is one parameter; interaction with surfaces to be treated is the second one, the last one being the final property (ies) to be reached. The Gas phase is controlled by external parameters (pressure, power, polarization, temperature, gas mixture, type of power supply in plasma processes, type of target, duty cycle,). Moreover, these external parameters are linked to internal parameters such as: density and energy of species, type of species (neutrals, ions, electrons, radicals, photons ...), temperature, bombardment energy... Thus, interaction with surfaces and growth process (growth mode, growth rate...) are obviously controlled by these internal parameters and the couple “Gas phase/surface (nature of substrate)”. The purpose of this talk is to explain through examples (In situ Infrared spectroscopy of gas phase, OES, MS, Growth modes characterization by in situ ellipsometry, RBS, ARXPS...) how to characterize (in or ex situ) the gas phase et solid phase to find links between these two phases and give some explanation of the processes “from power supply to final properties of the layer”.

9:20am **TF+NS+EM-ThM5 Investigation of Precursor Infiltration and ALD Growth on Polymers and Effect on Fiber Mechanical Properties**, *R.P. Padbury, J.S. Jur*, North Carolina State University

Atomic layer deposition (ALD) provides the opportunity to unite the properties of organic fiber forming polymers and nanoscale inorganic films creating a hybrid material interface. Prior research has shown that ALD materials nucleation on polymers varies in composition and structure based on how the precursor interacts with the polymer chemistry and the process conditions. The purpose of this work is to explore the effect of this processing on the mechanical behavior of fibrous materials. To study this in more detail, *in-situ* quartz crystal microgravimetry (QCM) is employed to understand the material growth mechanisms of ALD TiO<sub>2</sub>, ZnO, and Al<sub>2</sub>O<sub>3</sub> on poly (acrylic acid), polyamide-6, and polyethylene terephthalate. Particular emphasis is placed on controlling the ALD precursor diffusion into the sub-surface region of these polymers. *In-situ* QCM data was complemented by *ex-situ* characterization methods such as FT-IR and TEM to examine the interaction between the precursor and polymer and the compositions of the inorganic films. Finally, these results are correlated to the mechanical performance of the ALD treated fabrics. This work has important implications on sustainable textiles processes as well as the introduction of hybrid material properties to textile systems.

9:40am **TF+NS+EM-ThM6 Atomic Layer Deposition Enabled Synthesis of Nanostructured Composite BiFeO<sub>3</sub>/CoFe<sub>2</sub>O<sub>4</sub> Thin Films for Multiferroic Applications**, *C.D. Pham, J.P. Chang*, University of California at Los Angeles

Multiferroic materials, that can either exist as single-phase materials or multi-phase composites, exhibit two or more forms of ferroic order such as (anti)ferroelectricity, (anti)ferromagnetism, or ferroelasticity and have been proposed for use in future non-volatile memory technology. Atomic layer deposition (ALD) is proposed as a scalable approach to synthesize multiferroic thin films and to enable the synthesis of multiferroic composites which utilize conformal deposition onto 3-D nanostructures. Challenges that must be overcome in the ALD of multiferroic materials is the amorphous nature of as-deposited films and the difficulty in attaining the desired crystallinity and structure that would enable multiferroic properties to emerge from these materials.

In this work, multiferroic BiFeO<sub>3</sub> was deposited by ALD as a single-phase multiferroic thin film as well as the ferroelectric component in a composite multiferroic using a ferrimagnetic CoFe<sub>2</sub>O<sub>4</sub> mesoporous template that was synthesized using an evaporation induced di-block copolymer self-assembly technique. The ALD process used the metallorganic precursors Bi(tmhd)<sub>3</sub> (tmhd = 2,2,6,6-tetramethylheptane-3,5 dione) and Fe(tmhd)<sub>3</sub> alongside oxygen atoms produced from a coaxial waveguide microwave powered atomic beam source. A variety of ALD process conditions were studied, such as the effects of process temperature, precursor pulsing time, and precursor pulsing ratio on film composition, growth rate, and crystallization. The ALD films were able to be grown with a composition ratio Bi:Fe close to unity and with a controlled nanostructure and growth rate of ~0.7 Å/cycle. In order to achieve the desired crystalline material

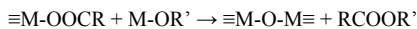
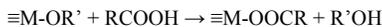
after rapid thermal processing, the composition and nanostructure of the as-deposited films must first be controlled via the ALD process to fit within narrow windows.

To compare the performance of the multiferroic ALD films to more well established synthesis methods, measurements of magnetic and ferro/piezoelectric properties were accomplished using SQUID magnetometry and piezoresponse force microscopy, respectively. Magnetic measurements showed that the out-of-plane remnant magnetization of a composite film at room temperature was approximately 66.4 emu/cm<sup>3</sup> while the coercive field was approximately 1950 Oe which was comparable to epitaxial films grown by other methods such as PLD. The magnetoelectric coupling effects in the composite films were studied to assess the effectiveness of the nanostructured material approach.

10:40am **TF+NS+EM-ThM9 In Situ Infrared Spectroscopic Study of Atomic Layer Deposited TiO<sub>2</sub> Thin Film Formation Using Non-Aqueous Routes**, *K. Bernal Ramos*, University of Texas at Dallas, *G. Clavel*, Université Montpellier 2, France, *C. Marichy*, Universidade de Aveiro / CICECO, Portugal, *W. Cabrera*, The University of Texas at Dallas, *N. Pinna*, Universidade de Aveiro / CICECO, Portugal, *Y.J. Chabal*, University of Texas at Dallas

Atomic layer deposition (ALD) is a unique technique for the deposition of conformal and homogenous thin films, by the use of successive self-limited surface reactions. Non-aqueous sol-gel routes are elegant approaches for the synthesis of metal oxide nanomaterials.<sup>1</sup> High quality inorganic nanocrystals,<sup>1</sup> ordered hybrid materials<sup>2</sup> or ALD thin films<sup>3</sup> can be obtained.

Our ALD approach makes use of metal alkoxides and carboxylic acids as metal and oxygen source, respectively.<sup>4</sup> It is expected that the reaction of carboxylic acids with the surface alkoxide species leads to surface carboxylate species (eq. 1), in a second step an aprotic condensation reaction between surface carboxylate species and metal alkoxides leads to metal-oxide bond formation (eq. 2).



Characterization of interface properties by in situ investigation of surface reaction mechanisms during deposition of high-*k* materials provides critical information for the development of semiconductor devices, where sharp interfaces and impurity free films are sought after.

In this work, in-situ IR spectroscopy is used to investigate the mechanisms for TiO<sub>2</sub> growth using either acetic acid or O<sub>3</sub> as oxygen source and titanium isopropoxide as metal source. It is believed to avoid intermediate OH group and to lead to sharp Si-high-*k* interfaces.

The IR results of the acetic acid process show clearly a ligand exchange leading to formation of acetates at the surface (vibrational bands at 1527 and 1440 cm<sup>-1</sup>) during the acetic acid pulse and then to their removal during the metal alkoxide pulse. These findings confirm the expected mechanism and demonstrate the absence of OH intermediate. However, the ligand exchange does not seem to be complete leading to accumulation of C impurities.

The in-situ study of O<sub>3</sub> based ALD demonstrates similarities with the above process. Indeed, formation of formate, carboxylate or carbonate species are observed function of the O<sub>3</sub> flow.<sup>5</sup> The formation of surface carboxylic species upon reaction with O<sub>3</sub> leads then to similar surface states as in the case of the reaction with carboxylic acids.<sup>4</sup> The mechanism of both approaches and their similarities and differences will be discussed.

1. N. Pinna and M. Niederberger, *Angew. Chem.-Int. Edit.*, 2008, **47**, 5292-5304
2. N. Pinna, *J. Mater. Chem.*, 2007, **17**, 2769-2774
3. G. Clavel, E. Rauwel, M. G. Willinger and N. Pinna, *J. Mater. Chem.*, 2009, **19**, 454-462
4. E. Rauwel, G. Clavel, M. G. Willinger, P. Rauwel and N. Pinna, *Angew. Chem.-Int. Edit.*, 2008, **47**, 3592-3595
5. J. Kwon, M. Dai, M. D. Halls, E. Langereis, Y. J. Chabal and R. G. Gordon, *J. Phys. Chem. C*, 2009, **113**, 654-660

11:00am **TF+NS+EM-ThM10 Nanomechanical Shaft-Loading Blister Testing of Thin Films**, *M. Berdova*, *A. Baby*, *J. Lyytinen*, Aalto University, Finland, *K. Grigoros*, *L. Kilpi*, *H. Ronkainen*, VTT Technical Research Center, Finland, *J. Koskinen*, *S. Franssila*, Aalto University, Finland  
Atomic Layer Deposition (ALD) is important in micro- and nanoelectromechanical systems, since it provides smooth, uniform, pin-hole free, and conformal layers. In particular, ALD aluminum oxide has excellent properties such as high mechanical strength and hardness, and chemical inertness.

We propose a new technique to measure the mechanical properties of ALD thin films. In the present work, a MEMS version shaft-loading blister test

used to evaluate the adhesion between ALD alumina and Cu, Cr/Cu, SiN<sub>x</sub>, SiC<sub>x</sub>, and Pt thin films. The test structure consists of microcylinders with diameters 1000 μm and 2000 μm, surrounded by etched annular rings making 50 μm, 100 μm and 200 μm gaps (Figure 1). The test structures are examined by applying the load along the microcylinder with a help of CSM Microindenter, inducing displacement which then causes the delamination between thin films and therefore, contributing to obtain the work of adhesion (Figure 2).

The fabrication of the test structure begins from the cleaning of double-side polished silicon wafer in hydrogen-peroxide-based (RCA) wet cleans. The following step is Atomic Layer Deposition of alumina on both sides of the wafer using trimethyl aluminium and water as precursors at 220 °C. 20 nm of Al<sub>2</sub>O<sub>3</sub> is grown on one side as the etch mask, and 200 nm of Al<sub>2</sub>O<sub>3</sub> is grown on another side to act both as an etch-stop mask and a testing layer. Next, the top layer is patterned to create alumina etch mask; and the rings are etched through silicon wafer by dry anisotropic Bosch process, forming this way a microcylinders supported only by 200 nm of Al<sub>2</sub>O<sub>3</sub> layer. Then, thin films (300 nm thick) are deposited by sputtering, or by PECVD techniques. The silicon nitride and silicon carbide were deposited at 300 °C. Magnetron sputtering was used for deposition of Pt, Cu, and Cr/Cu thin films at room temperature. Finally, those films are released by wet etching supporting alumina layer around the microcylinder.

As a result, we have not observed the delamination for nitride and carbide films: after certain reached displacement point (7 μm for nitride, 12 μm for carbide) the films start to break. For soft films as Pt and Cu, at similar displacement values we observed the starting of delamination. Comparing copper and copper with chromium layer underneath, the delamination of the film with adhesive layer starts at higher displacement and load values, proving the adhesive action of chromium. In the case of metal films large displacement and delamination can be achieved without breaking of the film (Table 1). The proposed MEMS shaft-loading blister test might become a valuable tool for all thin film adhesion testing.

11:20am **TF+NS+EM-ThM11 Phase Formation and Thermal Stability of Arc-Evaporated ZrAlN Thin Films**, *L. Rogström*, Linköping University, Sweden, *M.P. Johansson*, SECO Tools AB, Sweden, *M. Ahlgren*, Sandvik Tooling AB, Sweden, *N. Ghafoor*, Linköping University, Sweden, *J. Almer*, Advanced Photon Source, Argonne National Lab, *L. Hultman*, *M. Odén*, Linköping University, Sweden

Transition metal nitrides are widely used as wear protective coatings due to their high hardness also at elevated temperatures. Hence, TiAlN is one of the most common materials for coating of cutting tools. Its attractive mechanical properties are connected with the phase separation of the cubic TiAlN phase when the coating is exposed to high temperatures. The related ZrAlN system is less studied while its large miscibility gap with possibility for phase separation at elevated temperatures makes this material interesting for high temperature applications. Here, we present a comprehensive study of the phase formation in arc-evaporated ZrAlN thin films and their mechanical properties and thermal stability. Zr<sub>1-x</sub>Al<sub>x</sub>N thin films with a wide range of compositions (0.12 < x < 0.73) were grown by cathodic arc-evaporation. The structure of as-deposited and annealed films was characterized by x-ray diffraction and transmission electron microscopy and the mechanical properties were determined by nanoindentation.

The structure of the as-deposited ZrAlN thin films was found to depend on the Al-content. A low Al-content (x < 0.38) results in cubic (*c*) structure films while for high Al-content (x > 0.70) a hexagonal (*h*) ZrAlN phase is obtained [1]. In the compositional range between x = 0.38 and x = 0.70, the films exhibit a nanocomposite structure with a mixture of cubic, hexagonal, and amorphous phases [1, 2]. In all films, separation of ZrN and AlN takes place during annealing. In films with a nanocomposite structure, the phase transformation is initiated by nucleation and growth of *c*-ZrN in the ZrN-rich domains while the AlN-rich domains remain largely amorphous at 1100 °C [3]. Nucleation and growth of *h*-AlN is hindered by a high nitrogen content in the film and takes place at annealing above 1300 °C, simultaneously to loss of the excess nitrogen. The depletion of amorphous phase during annealing results in an improved hardness of the film. In the *h*-ZrAlN films, ZrN- and AlN-rich domains form within the hexagonal lattice during annealing above 900 °C. The formation of domains with different composition results in an increased hardness, from 24 GPa of the as-deposited film to 31 GPa of the annealed film. The *c*-ZrAlN phase is found to be stable to annealing temperatures of 1000 °C, while at higher temperatures, *h*-AlN nucleates and grows. This is different from the *c*-TiAlN system where spinodal decomposition occurs resulting in age hardening of the films.

[1] L. Rogström et al., *J. Vac. Sci. Technol. A* 30 (2012) 031504.

[2] L. Rogström et al., *Scr. Mater.* 62 (2010) 739.

[3] L. Rogström et al., *J. Mater. Res.*, In press (2012)

11:40am TF+NS+EM-ThM12 Ion-assisted Epitaxial Sputter-Deposition and Properties of Metastable  $Zr_{1-x}Al_xN(001)$  (0.05 x 0.25 ) Alloys, *AR.B. Mei, B.M. Howe*, University of Illinois at Urbana Champaign, *N. Ghafoor, E. Broitman*, Linköping University, Sweden, *M. Sardela*, University of Illinois at Urbana Champaign, *L. Hultman*, Linköping University, Sweden, *A. Rockett, J.E. Greene, I. Petrov*, University of Illinois at Urbana Champaign, *M. Oden, H. Fager*, Linköping University, Sweden

Single-phase epitaxial metastable  $Zr_{1-x}Al_xN/MgO(001)$  ( 0.05 x 0.25 ) thin films were deposited by ultra-high vacuum magnetically-unbalanced reactive magnetron sputtering from a single  $Zr_{0.75}Al_{0.25}$  target at a substrate temperature of 650°C. We control the AlN content,  $x$ , in the films by varying the ion energy ( $5 < E_i < 55$  eV) incident at the film growth surface with a constant ion to metal flux ratio of 8. The net atomic flux was decreased from  $3.16$  to  $2.45 \times 10^{15}$  atoms  $cm^{-2}s^{-1}$ , due to efficient resputtering of deposited Al atoms (27 amu) by  $Ar^+$  ions (40 amu) neutralized and backscattered from heavy Zr atoms (91.2 amu). Consequentially, films varied in thickness from 400 nm to 290 nm during 20 min depositions. HfN buffer layers were deposited on the  $MgO(001)$  substrates to reduce the lattice mismatch from ~8 to ~0.5%. High resolution x-ray diffraction  $\omega$ -2 $\theta$  scans and reciprocal lattice mapping revealed single-phase NaCl structure with a cube-on-cube orientation relative to the substrate,  $(001)_{Zr_{1-x}Al_xN} \parallel (001)_{MgO}$ , and relaxed lattice parameters varying from 4.546 with  $x = 0.25$  to 4.598 Å with  $x = 0.05$ . Film nanoindentation measurements showed that hardness decreases from 28.6 to 23.3 Gpa and Young's modulus increases from 263 Gpa to 296.8 GP as  $x$  is varied from 0.25 to 0.05. For the same range in  $x$ , electronic transport measurements established the films to have electron mobilities increasing from 2.67 to 462  $cm^2V^{-1}s^{-1}$ , resistivities decreasing from 162.4 to 25.4  $\mu\Omega$ -cm, and positive temperature coefficients of resistivity spanning from 0.3164 to 1.307  $\Omega$ -cm  $K^{-1}$ . Films deposited with incident ion energy above 35 eV ( $x < 0.08$ ) exhibited superconductivity with  $T_c$  of 8.26 K.

# Thursday Afternoon, November 1, 2012

## Electronic Materials and Processing

Room: 9 - Session EM+MI-ThA

### Semiconductor Heterostructures II + Heusler Alloys

Moderator: J.E. Ayers, University of Connecticut, B.D.

Schultz, University of California, Santa Barbara

2:00pm **EM+MI-ThA1 Dislocation Compensation in Ungraded ZnS<sub>y</sub>Se<sub>1-y</sub>/GaAs (001) Heterostructures.** T.M. Kujofsa, J.E. Ayers, University of Connecticut

Control of strain and dislocation dynamics are important in determining the performance and reliability of semiconductor devices such as light-emitting diodes and photo-detectors. Experimental studies of ZnS<sub>y</sub>Se<sub>1-y</sub>/GaAs (001) heterostructures show that a dislocation compensation mechanism is active in structures involving abrupt interfaces. This mechanism involves the bending over of threading dislocations associated with misfit segments of one sense by misfit dislocations having the opposite sense, and it allows removal of threading dislocations from device structures.

Semiconductor device structures may be designed to take advantage of the dislocation compensation with the aid of a dislocation dynamics model accounting for misfit-threading interactions. To develop such a model we studied strain relaxation in ZnSe/GaAs (001) and ZnS<sub>y</sub>Se<sub>1-y</sub>/GaAs (001) heterostructures to determine the kinetic material parameters associated with dislocation glide and multiplication. Based on these results and by including misfit-threading interactions we developed a dislocation dynamics model which predicts dislocation compensation in arbitrary ZnS<sub>y</sub>Se<sub>1-y</sub>/GaAs (001) heterostructures.

Whereas our previous experimental work involved graded structures, this work focuses on the study of theoretical heterostructures comprising a device layer (DL) of ZnS<sub>y</sub>Se<sub>1-y</sub> on a ungraded buffer layer (BL) of ZnS<sub>y</sub>Se<sub>1-y</sub> deposited on a GaAs (001) substrate. We show that for a given device layer thickness and compositional change at the buffer-device layer interface there exists an optimum thickness of the ungraded buffer layer where the mobile threading dislocation density can be removed entirely. The optimum buffer layer thickness decreases monotonically with the compositional difference between buffer and device layer.

2:20pm **EM+MI-ThA2 Dynamical X-ray Diffraction from Semiconductor Heterostructures with Asymmetrical Dislocation Densities.** P.B. Rago, J.E. Ayers, University of Connecticut

We extend the dynamical theory of Bragg x-ray diffraction to include asymmetrical dislocation densities on the two types of active slip systems in zinc blende semiconductor heterostructures with (001) orientation. In such structures the dislocations exist in eight active slip systems of two basic types distinguished by the orientation of their misfit segments, which are oriented along either the [1-10] or [110] direction. Variation of the incident x-ray beam azimuth results in a change in the shape of the diffraction profile if the two types of slip systems exhibit an asymmetry in dislocation densities. Our work allows simulation of the x-ray diffraction profile of an arbitrary zinc blende semiconductor heterostructure, and through comparison to experimentally measured data, the two dislocation densities of an experimentally measured sample can be extracted. In this work we have demonstrated use of the model by applying it to the ZnSe/GaAs (001) and HgCdTe/CdTe (001) material systems.

3:40pm **EM+MI-ThA6 Epitaxial Growth and Electronic Bandstructure of the Semiconducting Half Heusler Compound CoTiSb.** J. Kawasaki, University of California Santa Barbara, L. Johansson, M. Hjort, R. Timm, Lund University, Sweden, B. Shojaei, University of California Santa Barbara, A. Mikkelsen, Lund University, Sweden, B.D. Schultz, C. Palmstrom, University of California Santa Barbara **INVITED**

The Heusler compounds are an exciting class of intermetallics due to their ability to adopt a wide range of tuneable electrical and magnetic properties. These properties include ferromagnetism, paramagnetism, half-metallic ferromagnetism, large thermoelectric figures of merit, and both semiconducting and metallic behaviour. Additionally, some of the semiconducting Half Heuslers have been theoretically proposed to be topological insulators, making the Heusler compounds a promising system for multifunctional heterostructure devices. However, due to challenges in controlling defects and stoichiometry, little is known about the experimental band structure of the semiconducting Half Heuslers. We demonstrate the epitaxial growth of the Half Heusler compound CoTiSb by molecular beam epitaxy. Samples consist of an InP (001) substrate, lattice matched In<sub>x</sub>Al<sub>1-x</sub>As buffer layer, and CoTiSb layer. The films are single crystalline and of

high structural quality, as measured *in situ* by reflection high energy electron diffraction (RHEED) and scanning tunnelling microscopy (STM) and *ex situ* by X-ray diffraction (XRD), with an out of plane lattice mismatch of less than 0.5%. For growth temperatures of less than 400°C the films grow in a layer-by-layer mode as demonstrated by RHEED intensity oscillations. Under stoichiometric growth conditions the films have a (2x1) surface reconstruction and for Sb-rich conditions the films have a (1x1) reconstruction. Electrical transport measurements show the resistivity of the films decreases as a function of temperature down to 10K, consistent with semiconducting behaviour, and using tunnelling differential conductance spectroscopy (dI/dV) we measure a band gap on the order of 160 meV. However, this band gap is much smaller than the value of 1.0 eV predicted by density functional theory. Angle resolved photoemission spectroscopy (ARPES) measurements were also performed at the MAX-Lab synchrotron facility in Lund, Sweden. A protective Sb capping and decapping scheme was developed to maintain the surface quality of the films as the samples are transported to the characterization facility and exposed to air. The structural, chemical, and electrical properties of the single crystal CoTiSb films will be presented to provide insights into the band structure of the semiconducting Half Heuslers. This work was supported in part by the Office of Naval Research and the National Science Foundation.

4:20pm **EM+MI-ThA8 Application of Magnetic Heusler Alloys to All-Metal Sensors for Ultrahigh-Density Magnetic Recording.** J.R. Childress, HGST San Jose Research Center **INVITED**

Magnetic Heusler alloys are attractive materials for a number of applications in spintronics due to their potential high spin-polarization at the Fermi level, advantageous for spin-injection experiments and magnetoresistive devices. In the magnetic recording heads used in today's hard-disk drives (HDD's), the magnetoresistive thin-film sensors are multilayer spin-valves which operate in the current-perpendicular-to-film-plane (CPP) geometry, and rely on the spin-filtering properties of ultrathin MgO tunnel barriers (junction resistance < 1 Ohm-micron<sup>2</sup>) to achieve large tunnel-magnetoresistance (TMR) values using standard CoFe and CoFeB magnetic alloys as electrodes. Sensors with lower resistance (and thus lower-noise) are continuously required as sensor dimensions are reduced to keep up with the increased areal density of recorded data (approaching 1 Tb/in<sup>2</sup>). Intrinsically, an all-metal sensor can operate similarly to TMR sensors and will be able to achieve much lower resistances (~ 0.05 Ohm-micron<sup>2</sup>) and lower noise, but also requires a relatively large giant magnetoresistance (GMR) ratio to achieve sufficiently large signal to noise ratios (SNR). A number of Co-based full-Heusler alloys have the required magnetization, high T<sub>Curie</sub> and a predicted half-metallic behavior at low temperatures, and are therefore of interest for this application. But while the high spin-polarization in these Heusler alloys can significantly increase the GMR signal, integrating these materials in recording head sensors is a challenge due to their complex crystalline structure which typically requires high-temperature processing, and strong sensitivity to compositional disorder. In addition, the high polarization and low magnetic damping observed in these materials results in a high sensitivity to spin-torque excitations which limits the maximum allowable bias voltage, and is also a source of noise which limits the signal to noise (SNR) ratio. The geometrical, thermal, and magnetic constraints which influence the integration of Heusler alloys in magnetic recording head sensors will be presented, along with some examples of materials characterization and multilayer stack optimization required to improve the properties and robustness of the devices. It is found that practical spin-valves with Heusler alloy-based magnetic layers can be fabricated with CPP-GMR ratios which can be increased to >10%, more than 2x larger than for conventional ferromagnetic alloys. The outlook for applicability of such sensors to magnetic recording at high densities > 1 Tb/in<sup>2</sup> will be discussed.

5:00pm **EM+MI-ThA10 Growth of Epitaxial Co<sub>2</sub>MnSi/MgO/Co<sub>2</sub>MnSi Magnetic Tunnel Junctions by Molecular Beam Epitaxy.** S. Patel, A. Kozhanov, B.D. Schultz, C. Palmstrom, University of California, Santa Barbara

Epitaxial magnetic tunnel junctions (MTJs) have the potential to be used as low-energy non-volatile random access memory. The use of half metallic ferromagnets as electrodes has drawn great interest due to the predicted 100% spin polarization at the Fermi level. Co<sub>2</sub>MnSi is predicted to be half-metallic[1], with a Curie temperature of 985K [2], and is a strong candidate for use in magnetic random access memory devices. These devices, however, are highly sensitive to interfacial and bulk disorder, which may result in the loss of a minority spin gap [3]. Therefore it is critical to understand the fundamental properties of the Heusler alloy films and correlate these properties with device performance. We have successfully grown highly-ordered, epitaxial Co<sub>2</sub>MnSi(001) films by molecular beam

epitaxy (MBE) using a "seeded growth" technique to form a crystalline seed layer on various substrates, including MgO (001) and a Sc<sub>0.3</sub>Er<sub>0.7</sub>As lattice-matched diffusion barrier layer on GaAs (001). The lattice mismatch between GaAs and Co<sub>2</sub>MnSi is only -0.06% and x-ray diffraction of the MBE grown thin films show the two are nearly lattice matched. These films also have relatively smooth surfaces and coercivities down to 4 oersteds for stoichiometric films. Composition is also found to play a large role in the magnetic properties of the films. Off-stoichiometry films display lower saturation magnetization as well as higher coercivities. We have subsequently been able to grow epitaxial MTJ heterostructures of Co<sub>2</sub>MnSi/MgO/Co<sub>2</sub>MnSi with different switching fields for the top and bottom electrodes. We have characterized the structure of each layer and interfaces with reflection high-energy electron diffraction (RHEED), low-energy electron diffraction (LEED), scanning tunneling microscopy (STM) and cross-sectional transmission electron microscopy (XTEM) and the corresponding magnetic properties using vibrating sample magnetometry (VSM) and a superconducting quantum interference device (SQUID) to better understand the fundamental properties of these epitaxial heterostructures. This work was supported in part by the Semiconductor Research Corporation under award number 2011-IN-2153.

#### References

- [1] S. Picozzi, A. Continenza, and A. J. Freeman. Phys. Rev. B 69 (9), 094423 (2004)
- [2] P.J. Webster and K.R. Ziebeck. J. Phys. Chem. Solids 32, 1221 (1971)
- [3] B. Hülens, M. Scheffler, and P. Kratzer. Physical Review B 79 (9), 094407 (2000)

5:20pm **EM+MI-ThA11 Fabrication of Highly Ordered Co<sub>2</sub>FeAl Thin Films by Reactive Ion Beam Deposition for Spintronic Devices**, Y.S. Cui, University of Virginia, S. Schäfer, T. Mewes, University of Alabama, M. Osofsky, Naval Research Laboratory, J.W. Lu, S.A. Wolf, University of Virginia

Co<sub>2</sub>FeAl (CFA) is a full Heusler alloy that has potentially very low damping parameter and high spin polarization, highly desired for spintronic devices such as magnetic tunnel junctions and spin valves. CFA with B2-type chemical ordering has shown an extremely low Gilbert damping parameter among the Heusler alloys, which facilitates spin dynamics such as spin current driven magnetization switching. A large tunnel magnetoresistance (TMR) has been reported in B2-CFA based magnetic tunnel junctions, which is ascribed to its intrinsic high spin polarization efficiency. The high spin polarization efficiency originates from the half-metal gap in some of its energy bands with certain symmetry. It was predicted by theory that both low damping parameter and high spin polarization can only be achieved with a high chemical ordering existing in the CFA crystal structure. We will present the synthesis of high quality CFA thin films, prepared by a novel deposition technology, Reactive Biased Target Ion Beam Deposition (RBTIBD). The surface roughness (RMS) was observed as low as 0.14 nm. It was determined that CFA thin films grew on MgO(001) epitaxially along both in-plane and out-of-plane directions with a B2-type chemical ordering, according to the results obtained in XRD and TEM. The chemical ordering can be significantly improved by properly choosing the post annealing parameters. The ferromagnetic resonance (FMR) measurements suggested an extremely small damping parameter (~0.002). The damping parameter was strongly correlated with the chemical ordering of B2 structure. In addition, the impact of chemical ordering on the spin polarization efficiency of CFA films based on PCAR measurements will be discussed.

## Electronic Materials and Processing

Room: 14 - Session EM+TF+AS-ThA

### Growth and Characterization of Group III-Nitride Materials

Moderator: N. Dietz, Georgia State University

2:00pm **EM+TF+AS-ThA1 AIN-based Technology for Deep UV and High-power Applications**, Z. Sitar, HexaTech, Inc. & North Carolina State University, B. Moody, S. Craft, R. Schlessler, R. Dalmau, J. Xie, S. Mita, HexaTech, Inc., T. Rice, J. Tweedy, J. LeBeau, L. Hussey, R. Collazo, B. Gaddy, D. Irving, North Carolina State University **INVITED**

For the first time in history of III-nitrides, the availability of low defect density (<10<sup>3</sup> cm<sup>-2</sup>) native AlN substrates offers an opportunity for growth of AlGaIn alloys and device layers that exhibit million-fold lower defect densities than the incumbent technologies and enable one to assess and control optical and electrical properties in absence of extended defects. Epitaxial AlN wafers are fabricated from AlN boules grown by physical vapor transport at temperatures between 2200 and 2300°C. Gradual crystal

expansion is achieved through a scalable, iterative re-growth process in which the high crystal quality is maintained over many generations of boules. Despite the excellent crystal quality, below bandgap optical absorption bands in the blue/UV range affect the UV transparency of wafers. We use density functional theory (DFT) to develop a model to understand the interplay of point defects responsible for this absorption. We show a direct dependence of the mid-gap absorption band with the carbon concentration within the AlN. Low defect density AlN and AlGaIn epitaxial films are grown upon these wafers that exhibit superior optical properties in terms of emission efficiency and line width and can be doped with an efficiency that is several orders of magnitude higher than possible in technologies using non-native substrates. UV LED structures and Schottky diodes were fabricated on these materials that exhibit low turn-on voltages and breakdown fields greater than 10 MV/cm. This presentation will review state-of-the-art AlN-based technology and give examples of potential applications in future devices and contrast these with other wide bandgap technologies.

2:40pm **EM+TF+AS-ThA3 Atomic Layer Deposition of AlN Thin Films as Gate Dielectrics for Wide Bandgap Semiconductors**, Y.-C. Perng, J.P. Chang, D. Chien, University of California at Los Angeles

Aluminum nitride (AlN) is a potential dielectric layer for wide bandgap semiconductor based power electronic devices, such as those demanded in radio frequency, high-speed and high-temperature communication, because of its wide bandgap and high dielectric constant. In particular, for 4H-SiC, AlN is also a promising interfacial layer due to their similar atomic arrangement, small lattice mismatch (1.3%) and comparable thermal expansion coefficients. Although various deposition techniques have been investigated to synthesize AlN thin films with atomic controllability over a large substrate remains a challenge. Atomic layer deposition (ALD) was thus used in this work to grow AlN thin films.

AlN deposition was performed in an ultra-high vacuum chamber with base pressure of 10<sup>-7</sup> Torr using trimethylaluminum (TMA) and ammonia (NH<sub>3</sub>) as precursors. It was discovered that ALD of AlN is possible only when the minute amount of moisture in NH<sub>3</sub>, which competed with and inhibited the nitride growth, was completely eliminated. The ALD window was found to be 500-570°C with a growth rate of 1.5 Å/cycle. The deposited film composition was evaluated via *in-situ* x-ray photoelectron spectroscopy (XPS) with Al/N determined to be 1.2. *In-situ* reflective high-energy electron diffraction (RHEED) measurements showed as-deposited AlN films were crystalline, which was confirmed by x-ray diffraction (XRD). AlN/4H-SiC MIS capacitors were fabricated to examine the electrical properties with the dielectric constant of AlN determined to be 8.3 and a leakage current density of 10<sup>-3</sup> A/cm<sup>2</sup> at 4.3 MV/cm. The 150 Å ALD AlN passivated AlGaIn/GaN hetero-structure demonstrated 11% increase in the carrier density and 3% decrease in mobility compared to those of non-passivated hetero-structure as 8.3x10<sup>12</sup>cm<sup>-2</sup> and 1100 cm<sup>2</sup>/V-s. While with amorphous 150Å Al<sub>2</sub>O<sub>3</sub> surface passivation, the mobility decrease by 22% with carrier density increase by 12%, showing that the crystalline AlN providing a superior property on passivating the hetero-structure.

3:00pm **EM+TF+AS-ThA4 Low-Temperature Behavior of the Surface Photovoltage in p-type GaN**, J.D. McNamara, M. Foussekis, A.A. Baski, M.A. Reshchikov, Virginia Commonwealth University

The effect of low temperature on the surface photovoltage (SPV) in semiconductors is rarely studied and not well understood. We studied the SPV behavior for Mg-doped, p-type GaN using a Kelvin probe at temperatures from 80 to 300 K. Under band-to-band UV illumination at room temperature, the measured SPV signal in p-type GaN becomes negative as electrons are swept to the surface. However, we observed that at low temperatures, the SPV signal becomes positive under UV illumination, contrary to the SPV behavior of p-type GaN at room temperature. This positive SPV resembles the behavior of an n-type semiconductor. We assume that under UV illumination and at low temperatures, the conductivity of Mg-doped GaN does indeed convert from p- to n-type. This conversion was predicted from photoluminescence studies on Zn-doped GaN.<sup>[1]</sup> At low temperatures, photo-generated electrons may accumulate in the conduction band which causes an upward shift in the bulk Fermi level towards the conduction band. This results in a positive SPV signal, since the Kelvin probe uses the bulk Fermi level as a reference for the measured SPV signal. Interestingly, the characteristic temperature at which we observe this transition from p- to n-type behavior depends on illumination intensity. As the excitation intensity increases from 10<sup>15</sup> to 10<sup>17</sup> cm<sup>-2</sup> s<sup>-1</sup>, the characteristic temperature increases from 130 to 170 K. This result also agrees with previously reported photoluminescence data and further authenticates the above assumption.<sup>[1]</sup>

[1] M. A. Reshchikov, A. Kvasov, T. McMullen, M. F. Bishop, A. Usikov, V. Soukhovuev, and V. A. Dmitriev, Phys. Rev. B **84**, 075212 (2011).

3:40pm **EM+TF+AS-ThA6 Controlling GaN Polarity on GaN Substrates**, J.K. Hite, M.E. Twigg, J.A. Freitas, Jr., M.A. Mastro, J.R. Meyer, I. Vurgaftman, S. O'Connor, N.J. Condon, F.J. Kub, S.R. Bowman, C.R. Eddy, Jr., U.S. Naval Research Laboratory

Gallium nitride is a high quality semiconductor widely used in both optical and electronic devices. The polarity of GaN (+/- c-direction) influences many properties of the resultant material, including chemical reactivity and electric field in these 'piezoelectric' materials. Control over the polarity of GaN grown on sapphire and SiC substrates has been previously demonstrated by controlling the growth conditions, doping levels, and buffer or nucleation layer properties. Further, in the case of heavily doped p-type layers, spontaneous polarity inversion has been demonstrated in GaN homoepitaxial layers, switching the doped layer from Ga-polar to N-polar. However, this approach leads to uncontrolled inversion domain boundaries and often results in dopant clustering within the film, impacting film quality and resultant device performance.

In this work we investigate the fabrication of Mg-free inversion layers (ILs) to control the polarity of MOCVD-grown GaN on GaN substrates. By changing the IL material, we demonstrate conversion of GaN polarity in both directions (N-polar to Ga-polar and Ga-polar to N-polar). By employing a patented selective growth method to deposit the IL, the lateral polarity of the GaN can also be alternated, allowing control of the polarity in both vertical and lateral directions. A one-dimensional grating of periodically oriented (PO) GaN stripes was achieved over square-centimeter (or large) areas. The boundaries between polarities are found to be both sharp and vertical, and the growth conditions have been adjusted to result in equal growth rates of both polarities. Chemical etching of the material verifies the polarity of the material. Transmission electron microscopy (TEM) rules out the presence of alternating polar inclusions in the inverted material while showing a strong inversion domain boundary at the vertical interfaces. Dislocation density and grain size are determined through the use of electron channeling contrast imaging. The MOCVD-grown PO GaN structures have been extended in thickness by further HVPE growth. TEM and photoluminescence imaging confirms that the PO GaN structure is maintained throughout the extended growth (up to 80  $\mu\text{m}$  in thickness). This method of GaN polarity inversion offers the promise of engineering both lateral and vertical polarity heterostructures and the potential of novel engineered polarity-based devices.

4:00pm **EM+TF+AS-ThA7 Direct Green and Yellow Light Emitting Diodes – Polarization Control and Epitaxy**, C. Wetzel, T. Detchprohm, Rensselaer Polytechnic Institute **INVITED**

Solid state lighting by means of GaInN/GaN light emitting diodes (LEDs) is rapidly progressing to a major factor in energy savings technology. By convergence of lighting and lighting control, however, smart lighting is an opportunity to elevate lighting to a holistic experience of human wellbeing beyond the obvious economic benefits. Full epitaxial control of the GaInN/GaN active region is prime to fulfill the promise of an optical bandgap tunable across the entire visible spectrum. As such it will serve both, as tunable absorption layer for multijunction solar cells and emitter for direct emitting LEDs. The later aspect is of particular promise to outperform the traditional phosphor conversion approach known from historic fluorescence lamps and current white light LEDs.

Rigorous defect reduction approaches have enabled us to continuously improve the emission efficiency in ever longer wavelength emission reaching beyond green, deep green to yellow and orange (590 nm). In contrast to conventional phosphor or AlGaInP-based LED, such emitters show a superior temperature stability of their light output performance. A further leap in defect reduction has been demonstrated by the implementation of heteroepitaxy on nanotextured templates. Unlike widely explored lateral epitaxial overgrowth, growth zones primarily coalesce without the generation of threading dislocations. Implemented at the sapphire substrate level in green LEDs, the texturing substantially boosts both, internal quantum efficiency and light extraction. Furthermore, by control of the crystallographic orientation of growth we achieve a modulation of the piezoelectric polarization within the active region. This for once results in the emission of highly linear polarized light but on the other hand holds the promise to move the actual sweet spot of LED performance from the blue into the green and yellow spectral region. We discuss our approaches in light of our latest achievements.

This work was supported by a DOE/NETL Solid-State Lighting Contract of Directed Research under DE-EE0000627. This work was supported in part by the Engineering Research Centers Program of the National Science Foundation under NSF Cooperative Agreement No. EEC-0812056.

4:40pm **EM+TF+AS-ThA9 The Influence of Substrate and Gas Phase Temperatures on the Properties of InN Epilayers**, M.K.I. Senevirathna, S.D. Gamage, R. Atalay, R.L. Samaraweera, A.G.U. Perera, Georgia State University, B. Kucukgok, A.G. Melton, I. Ferguson, University of North Carolina at Charlotte, N. Dietz, Georgia State University

The influence of the substrate growth temperature on the structural and optoelectronic properties of group III-nitride layers grown by various growth techniques has been extensively studied and reported on, due to the close relationship of substrate temperature with crystalline quality and the point defect chemistry of the alloy. Most thin film growth systems only control the substrate temperature and have limited control to adjust the gas phase decomposition dynamic independent to influence to growth surface chemistry.

In this contribution, we present results on the growth of InN epilayers grown the high-pressure chemical vapor deposition (HPCVD), studying in influence of and independent from the substrate temperature controlled gas phase temperature above the substrate reactor zone. The HPCVD reactor system has two heater elements: one that controls the substrate temperature and a second radiative heat source above, which allows the control of the gas phase temperature. While the substrate temperature dominantly controls the growth process and the crystalline layer properties, the heater above the substrate surface influences strongly the precursor decomposition processes and the diffusion and concentrations of the precursor fragments in the boundary layer and at the growth surface. InN epilayers grown with different gas phase heating settings were grown and analyzed with the respect to their short- and long-range crystalline ordering and their optoelectronic properties as function of the gas phase temperature. The long-range and the short-range crystalline order of the layers have been analyzed by x-ray diffraction  $2\theta-\omega$  scans FWHM and the Raman  $E_2$  (high) FWHM, respectively. The optoelectronic properties have been studied by reflectance spectroscopy and are related to the structural properties and the additional gas phase heating.

The figure depicts the FWHM values of Raman- $E_2$  (high) peak of the InN epilayers as a function of reactor pressure for higher (red line) and lower (blue line) gas phase temperature. The results indicate that there is an improvement of the short-range crystalline order of the layers with lower gas phase temperature. However, the FWHM values of XRD  $2\theta-\omega$  scans, which are not shown here, are indicating that there is an improvement of long-range crystalline order of the layers with increasing gas phase heating.

5:00pm **EM+TF+AS-ThA10 Absence of Electron Accumulation at InN(11-20) Cleavage Surfaces**, H. Eisele, Technische Universität Berlin, Germany, S. Schaafhausen, Forschungszentrum Jülich, Germany, A. Lenz, Technische Universität Berlin, Germany, A. Sabitova, Forschungszentrum Jülich, Germany, L. Ivanova, M. Dähne, Technische Universität Berlin, Germany, Y.-L. Hong, S. Gwo, National Tsing-Hua University, Taiwan, P. Ebert, Forschungszentrum Jülich, Germany

InN in principle opens up the possibility of using only one ternary III-V semiconductor alloy (InGaN) in optoelectronic devices to cover the whole visible spectral range. Despite this, key material properties of InN are still under debate. The intrinsic energetic position of the Fermi level is unclear, i.e., whether the Fermi level is located within the fundamental band gap or shifted slightly into the conduction band. The latter case induces electron accumulation at the surfaces of the crystal. Such an electron accumulation is typically observed at InN surfaces upon air contact, raising the question whether it is an intrinsic material property or not?

In order to probe intrinsic bulk properties by STM and not only contamination or surface effects, a clean and stoichiometric surface is necessary. This can be achieved by cleaving InN along non-polar planes. To analyze the origin of the different electronic states in detail, we investigated the clean non-polar (11-20) cleavage surface using cross-sectional scanning tunneling microscopy (XSTM) and spectroscopy (XSTS).

Using combined XSTM and XSTS we were able to locate an InN layer grown on an AlN buffer layer on top of a Si(111) substrate [1]. XSTS spectroscopy on the InN(11-20) cleavage surface yield normalized conductivity spectra, where three contributions to the tunneling current can be observed: (i) the contribution from the conduction band density of states for biases above the conduction band minimum at +0.3 V, (ii) a defect induced current, dominating the spectra between biases of 0 and -0.4 V, and (iii) a valence band related tunneling current rising at a bias of about -0.4 V and dominating the spectrum for biases below. The defect induced current arises from semi-filled defect states being present at the surface steps, and probably also from other (point) defects at the surface. Within the bulk band gap of  $E_G = 0.7$  eV no intrinsic surface states could be observed. Furthermore, the Fermi level pinning at about 0.3 eV below the conduction band minimum indicates the absence of an electron accumulation layer.

The results illustrate that electron accumulation at InN surfaces is not a universal property on InN. For clean stoichiometric cleavage surfaces no electron accumulation is observed. Thus, electron accumulation results

primarily from the details of the surface structure and is hence not an intrinsic property of the bulk InN material.

[1] Ph. Ebert, S. Schaffhausen, A. Lenz, A. Sabitova, L. Ivanova, M. Dähne, Y.-L. Hong, S. Gwo, and H. Eisele, *Appl. Phys. Lett.* **98**, in press (2011).

5:20pm **EM+TF+AS-ThA11 Dependence of Gallium Incorporation and Structural Properties of Indium-rich  $\text{In}_x\text{Ga}_{1-x}\text{N}$  Epilayers on Ammonia - MO Precursor Pulse Separation**, S.D. Gamage, R. Atalay, M.K.I. Senevirathna, R.L. Samaraweera, Georgia State University, A.G. Melton, I. Ferguson, University of North Carolina at Charlotte, N. Dietz, Georgia State University

The large band gap tunability of ternary  $\text{In}_x\text{Ga}_{1-x}\text{N}$  alloys has opened new avenues in the field of advanced optoelectronics devices fabrication. However, the growth process of the epilayers of these materials is yet to be well explored. In this contribution, the growth of  $\text{In}_x\text{Ga}_{1-x}\text{N}$  epilayers under super atmospheric pressure is studied. In order to mitigate the gas phase reactions and the gap of dissociation temperatures between the binary alloys GaN and InN, and to improve the phase stability, high growth chamber pressure has been used together with a pulsed precursor injection system. This pulsed precursor injection scheme introduces two important process parameters; the precursor separation times between the metal organic (MO) sources (TMI and TMG) and ammonia ( $\text{S}_1$ ), and ammonia and MO ( $\text{S}_2$ ).

With the aim to find the optimum  $\text{S}_2$  separation for high quality indium-rich InGaN epilayers, a set of  $\text{In}_x\text{Ga}_{1-x}\text{N}$  samples with nominal  $x=0.9$  has been grown with different  $\text{S}_2$  timings. It will be shown that the  $\text{S}_2$  separation is critical for the incorporation of gallium into the epilayers. In order to maintain single-phase epilayers, the  $\text{S}_2$  separation has to be increased from  $\text{S}_2=400$  ms for InN to over 1200 ms for  $\text{In}_x\text{Ga}_{1-x}\text{N}$ . Raman spectroscopy and X-ray diffraction (XRD) spectroscopy are used to study the structural properties while the Fourier Transform Infra-red (FTIR) and transmission spectroscopy are utilized to investigate the electrical and optical properties of the epilayers.

5:40pm **EM+TF+AS-ThA12 MBE-Growth of Coherent-Structure InN/GaN Short-Period Superlattices as Ordered InGaN Ternary Alloys for III-N Solar Cell Application**, A. Yoshikawa, K. Kusakabe, N. Hashimoto, T. Okuda, T. Itoi, Chiba University, Japan

We have recently proposed “SMART” III-N tandem solar cells in which all sub-cells could be coherent-structure high-quality pn junctions with low leakage current, resulting in high performance solar cells. SMART means “Superstructure Magic Alloys fabricated at Raised Temperature”. The most important feature in the proposed SMART solar cell is a novel idea for realizing ordered and/or quasi InGaN-ternary alloys with InN/GaN Short-Period Superlattices (SPS) enabling coherent-structure band engineering for the  $(\text{InN})_n/(\text{GaN})_m$  SPSs with simple integer pairs of  $(n, m) \leq 4$ . In this symposium, detailed epitaxy processes, structural and physical properties of SPSs, and also the idea and features of proposed “SMART” III-N tandem solar cells are reported.

We have ever reported successful growth of fine and coherent-structure 1-ML InN/GaN matrix QWs, and they can be fabricated so under self-limiting and self-ordering growth processes at remarkably higher and/or “raised” temperatures ( $\sim 650$  °C) than the critical one ( $\sim 500$  °C) for growing thick InN layer under +c growth regime in MBE. We are now underway to extend this understanding and the corresponding epitaxy technology to realize the proposed  $(\text{InN})_n/(\text{GaN})_m$  SPSs, and we have started to achieve  $(\text{InN})_1/(\text{GaN})_m$  ( $m=1-20$ ) SPSs. When fabricating high structural quality those SPSs, very careful surface stoichiometry control such as  $(\text{In}+\text{Ga})/\text{N}$  and In/Ga composition in adlayers, and also periodical complete surface dry-up of In and Ga for each one-cycle growth of SPSs are necessary and quite important.

In brief, 50-100 periods of  $(\text{InN})_1/(\text{GaN})_m$  SPSs were grown on MOCVD-grown +c-GaN template at 650 °C by a conventional plasma-assisted MBE. Surface stoichiometry and surface dry up were quite carefully monitored and controlled by in-situ Spectroscopic-Ellipsometry. First, structural properties of 50 periods of  $(\text{InN})_1/(\text{GaN})_m$  SPSs were characterized with XRD diffraction patterns taking the  $m$  as a parameter. It was found that coherent structure SPSs could be fairly easily fabricated even when the  $m$  was decreased down to 4. Generally, much more careful surface stoichiometry control was necessary with decreasing the  $m$ , though it was confirmed coherent structure  $(\text{InN})_1/(\text{GaN})_4$  SPSs could be grown finally after quite careful control, such as selective re-evaporation between In and Ga consuming a long time. This leads to complete In re-evaporation leaving only some Ga metals on the surface. Of course those Ga metals must be completely dried up with irradiating plasma-excited nitrogen just before the following deposition of 1ML InN on it. It is still difficult at present, however, to grow fine structure InN/GaN SPSs with the  $m$  below 3.

## Graphene and Related Materials Focus Topic Room: 13 - Session GR+EM+NS+SS+TF-ThA

### Beyond Graphene: BN and Other 2D Electronic Materials; 2D Heterostructures

Moderator: I.I. Oleynik, University of South Florida

2:00pm **GR+EM+NS+SS+TF-ThA1 X-ray Photoelectron Spectroscopy Investigation of the Valence and Conduction Band Offset at Hexagonal a-BN:H/Si Interfaces**, S. King, M. French, J. Bielefeld, Intel Corporation, M. Jaehnig, Intel Corporation, M. Kuhn, B. French, Intel Corporation

Due to a wide band gap ( $\sim 6$  eV) and close lattice matching, hexagonal boron nitride (h-BN) is of interest as a potential gate dielectric in graphene channel transistor devices. A key property for the success of h-BN as a gate dielectric in such devices is the valence and conduction band offsets at the h-BN/graphene and h-BN/gate electrode interfaces. In many graphene channel devices, amorphous or poly-Si is a desirable gate electrode material for compatibility in standard CMOS processing. In this regard, we have utilized x-ray photoelectron spectroscopy (XPS) to determine the valence band offset present at the interface between plasma enhanced chemically vapor deposited hexagonal a-BN:H and a (100) Si substrate. Combined with Reflection Electron Energy Loss Spectroscopy measurements of the a-BN:H band gap, we have also been able to determine the conduction band offset at this interface. The combined measurements indicate a type I alignment with valence and conduction band offsets of  $1.95 \pm 0.1$  and  $2.15 \pm 0.17$  eV respectively.

2:20pm **GR+EM+NS+SS+TF-ThA2 Monolayer Graphene-Boron Nitride 2D Heterostructures**, R. Cortes, J. Lahiri, E. Sutter, P.W. Sutter, Brookhaven National Laboratory

Unusual electronic properties have been predicted for monolayer graphene-boron nitride heterostructures, but access to these properties depends on methods for controlling the formation of graphene-boron nitride interfaces [1]. Here we report on the growth and interface formation of monolayer graphene (MLG)-hexagonal boron nitride (h-BN) 2D heterostructures on Ru(0001), investigated by a combination of real-time low-energy electron microscopy (LEEM) and scanning tunneling microscopy (STM).

LEEM observations of sequential chemical vapor deposition growth show that h-BN attaches preferentially to the edges of existing MLG domains, while nucleation of h-BN on the Ru surface away from MLG is not observed at the conditions considered here. With increasing coverage, h-BN expands anisotropically and, ultimately, the substrate is covered by a continuous 2D membrane of MLG domains embedded in h-BN. The study of the 1D interface between MLG and h-BN in these membranes by STM demonstrates that, following sequential growth at high temperatures, the interface is not abrupt, but contains an intermixed zone consisting of h-BN with embedded carbon atoms. Using quantitative LEEM, we have identified processes that eliminate this intermixing and pave the way to atomically sharp graphene-boron nitride boundaries, as confirmed by STM. The application of a similar growth procedure to terminate the edges of atomically controlled graphene nanoribbons with h-BN, embedding them in a h-BN membrane, will be considered.

[1] P. Sutter, R. Cortes, J. Lahiri, and E. Sutter. *Submitted* (2012).

2:40pm **GR+EM+NS+SS+TF-ThA3 Large Area Vapor Phase Growth and Characterization of  $\text{MoS}_2$  Atomic Layers**, J. Lou, S. Najmaei, Z. Liu, Y. Zhan, P. Ajayan, Rice University

**INVITED**  
Monolayer Molybdenum disulfide ( $\text{MoS}_2$ ), a two-dimensional crystal with a direct bandgap, is a promising candidate for 2D nanoelectronic devices complementing graphene. Unlike conductive graphene and insulating h-BN, atomic layered  $\text{MoS}_2$  is a semiconductor material with a direct bandgap, offering possibilities of fabricating high performance devices with low power consumption in a more straight-forward manner.

In this talk, we will discuss our recent efforts on the large area growth of  $\text{MoS}_2$  atomic layers by a scalable chemical vapor deposition (CVD) method. The as-prepared samples can either be readily utilized for further device fabrication or be easily released from the growth substrate and transferred to arbitrary substrates. High resolution transmission electron microscopy and Raman spectroscopy on the as grown films of  $\text{MoS}_2$  indicate that the number of layers range from single layer to a few layers.

Our results on the direct growth of MoS<sub>2</sub> layers on dielectric leading to facile device fabrication possibilities show the expanding set of useful 2D atomic layers, on the heels of graphene, which can be controllably synthesized and manipulated for many applications.

**3:40pm GR+EM+NS+SS+TF-ThA6 Formation of Silicene and 2D Si Sheets on Ag(111): Growth Mode, Structural and Electronic Properties, P. Vogt, Technical University of Berlin, Germany, T. Bruhn, A. Resta, B. Ealet, CNRS CiNaM, Marseille, France, P. De Padova, CNR-ISM, Rome, Italy, G. Le Lay, CNRS CiNaM, Marseille, France**

Since the discovery of graphene enormous efforts have been invested to discover other similar 2-dimensional materials, like e.g. silicene. These 2D materials share similar structural, electronic and optical properties as graphene but are expected to differ in terms of their respective chemical reactivity and thus their applicability for electronic devices. In particular silicene could more easily be integrated into current Si-based electronics than graphene. Silicene has been predicted theoretically [1,2] but does not seem to exist in nature.

Recently, we could synthesize silicone layers grown epitaxially by depositing Si on Ag(111) surfaces. The electronic properties of these silicene layers were shown to behave as theoretically predicted [3] and the structural and electronic properties are very similar to graphene. In STM images the hexagonal 2D silicone sheet gives rise to triangular structures situated in a honeycomb arrangement with (4×4) symmetry with respect to the Ag(111) surface. A structural model derived from the STM measurements showed a very good agreement with DFT results and exhibited a downward conical electronic dispersion resembling that of relativistic Dirac fermions at the Si K-points [3]. Depending on the growth conditions the formation of different 2D silicon arrangements can be observed: 1) Si-clusters at low deposition temperatures, 2) the formation of less ordered 2D hexagonal Si-based structures at temperatures up to 180°C, 3) the formation of the (4×4) silicene sheet around 220°C and 4) a 2D Si structure with a ( $\sqrt{13}\times\sqrt{13}$ )-like periodicity at higher growth temperatures exhibiting a very regular, wide range ordered Moiré-like surface pattern in STM.

Here, we will discuss the formation and epitaxial growth mode of these different 2D Si structures and the dependence on the growth parameters. We will also investigate whether these different 2D Si layers all refer to similar silicene sheets which give rise to different appearances in STM due to a varying rotation with respect to each other.

Keywords: silicene, 2D materials, graphene, Dirac fermions

References:

- [1] S. Cahangirov et al., Phys. Rev. Lett. **102**, 236804 (2009)
- [2] G. G. Guzman-Verri and L. C. Lew Yan Voon, Phys. Rev. B **76**, 75131 (2007)
- [3] P. Vogt et al., Phys. Rev. Lett. **108**, 155501 (2012)

**4:00pm GR+EM+NS+SS+TF-ThA7 Yttria-monolayer on Pt(111) Supported Graphene: A Novel Two Dimensional Heterostructure and its Affect on Charge Doping of Graphene, R. Addou, A. Dahal, M. Batzill, University of South Florida**

Yttrium oxide (Y<sub>2</sub>O<sub>3</sub>) is a high-k dielectric material, with promising wetting behavior of graphene [1]. In our study we grew yttria by reactive MBE on Pt(111) supported graphene to investigate the structural and electronic properties of the graphene/yttria interface. Photoemission measurements indicate that the graphene layer is covered by yttria. Scanning tunneling microscopy (STM) and low energy electron diffraction reveal that at annealing temperatures higher than 600 °C yttria forms an ordered monolayer on top of graphene. In STM, a moiré pattern is observed that is a consequence of super-positioning of a hexagonal yttria monolayer lattice with that of graphene. X-ray photoemission indicates a shift of the C1s peak by 1 eV to higher binding energy upon depositing of the yttria film. This peak shift is explained by charge doping of graphene by the underlying Pt substrate due to the change in the work function of the yttria coated graphene.

[1] Z. Wang et al. Nano Lett. **2010**, *10*, 2024–2030; L. Ding et al. Nano Lett. **2009**, *9*, 4209–4214.

**4:20pm GR+EM+NS+SS+TF-ThA8 Probing the BCN-triangle by Computations—Outside the Carbon Corner, Jakobson, Rice University**

INVITED  
We will discuss recent work on modeling 2D-materials “beyond graphene” [1-2]: two dimensional hexagonal h-BN, pure B polymorphs, MoS<sub>2</sub>, etc. Lessons from graphene studies remain invaluable as they offer general approach and views on the edges [3] and interface structures and energies, and especially organization of the grain boundaries [4,5]. New dislocation

cores in BN (both 5/7 and 4/8 types) lead to accordingly new physical properties of emerging polar GB [6]. Similarly, we identify the dislocation cores and the grain boundary structure for more complex polar layer-material, MoS<sub>2</sub> (X. Zou, unpublished). Our analysis of edge and cleavage energies helps to explain fracture patterns emerging in the course of synthesis. In principle, computations suggest possibility of metastable 2D-layers of GaN or ZnO or even their hybrids. Finally, it is important to mention clear opportunities of designing 2D-circuits by combining 2D-materials in specific functional patterns like proposed nanoroads and quantum dots [7-8] which now become a subject of experimental laboratory work.

- [1] Y. Liu et al. Nano Lett. **11**, 3113 (2011).
- [2] E. Penev, et al, Nano Lett. **12**,2441 (2012).
- [3] Y. Liu et al. Phys. Rev. Lett. **105**, 235502 (2010).
- [4] BIY and F. Ding, ACS Nano **5**, 1569 (2011).
- [5] Ajayan and BIY, Nature Mater. **10**, 415 (2011).
- [6] Y. Liu et al. ACS Nano (2012).
- [7] A. Singh and BIY, Nano Lett., **9**, 1540 (2009).
- [8] A. Singh, E. Penev, and BIY, ACS Nano, **4**, 3510 (2010).

**5:00pm GR+EM+NS+SS+TF-ThA10 Single-layer MoS<sub>2</sub> Devices and Circuits, A. Kis, EPFL, Switzerland**

INVITED  
Single layer MoS<sub>2</sub> is a recent addition to the family of 2D materials and is reminiscent of graphene except that it is an intrinsic direct band gap semiconductor with a 1.8 eV gap. We have exfoliated single layers 6.5 Angstrom thick from bulk crystals of semiconducting MoS<sub>2</sub>, using the micromechanical cleavage technique commonly used for the production of graphene. Our nanolayers are mechanically and chemically stable under ambient conditions. We have fabricated transistors based on single-layer MoS<sub>2</sub> which demonstrate that this material has several advantages over silicon for potential applications in electronics. Our transistors have room-temperature current on/off ratios higher than 10<sup>8</sup>, mobility higher than 780 cm<sup>2</sup>/Vs and leakage currents in the fA range. Integrated circuits based on MoS<sub>2</sub> have the capability to amplify signals and perform logic operations. Finally, I will show our work on suspended MoS<sub>2</sub> membranes that show ripples similar to those observed in graphene. MoS<sub>2</sub> also has superior mechanical properties: higher stiffness than steel and 30 times its breaking strength which makes it suitable for integration in flexible electronics.

References

1. B. Radisavljevic, A. Radenovic, J. Brivio, V. Giacometti, and A. Kis. Single-layer MoS<sub>2</sub> transistors. Nature Nanotechnology **6**, 147, 2011. doi: 10.1038/nnano.2010.279
2. M.M. Benameur, B. Radisavljevic, J.S. Heron, S. Sahoo, H. Berger, and A. Kis. Visibility of dichalcogenide nanolayers. Nanotechnology **22**, 125706, 2011. doi: 10.1088/0957-4484/22/12/125706
3. B. Radisavljevic, M.B. Whitwick, and A. Kis. Integrated circuits and logic operations based on single-layer MoS<sub>2</sub>. ACS Nano **5**, 9934, 2011. doi: 10.1021/nn203715c
4. J. Brivio, D.T.L. Alexander, and A. Kis. Ripples and Layers in Ultrathin MoS<sub>2</sub> Membranes. Nano Letters **11**, 5148, 2011. doi: 10.1021/nl2022288
5. S. Bertolazzi, J. Brivio, and A. Kis. Stretching and Breaking of Ultrathin MoS<sub>2</sub>. ACS Nano **5**, 9703, 2011. doi: 10.1021/nn203879f

**Thin Film**

**Room: 10 - Session TF+EM+SS-ThA**

**Applications of Self-Assembled Monolayers and Layer-by-Layer Assemblies**

**Moderator: M.R. Linford, Brigham Young University**

**2:00pm TF+EM+SS-ThA1 Light-Directed Nanosynthesis: Near-Field Optical Approaches to Integration of the Top-Down and Bottom-Up Fabrication Paradigms, G.J. Leggett, University of Sheffield, UK**

INVITED  
The integration of top-down (lithographic) and bottom-up (synthetic chemical) methodologies remains a major goal in nanoscience. At larger length scales, light-directed chemical synthesis, first reported two decades ago, provides a model for this integration, by combining the spatial selectivity of photolithography with the synthetic utility of photochemistry. Work in our laboratory has sought to realise a similar integration at the nanoscale, by employing near-field optical probes to initiate selective chemical transformations in regions a few tens of nm in size. A combination of near-field exposure and an ultra-thin resist yields exceptional performance: in self-assembled monolayers, an ultimate resolution of 9 nm (ca.  $\lambda/30$ ) has been achieved. A wide range of methodologies, based on monolayers of thiols, silanes and phosphonic acids, and thin films of nanoparticles and polymers, have been developed for use on metal and

oxide surfaces, enabling the fabrication of metal nanowires, nanostructured polymers and nanopatterned oligonucleotides and proteins. Strategies based upon the use of nitrophenyl-based photocleavable protecting groups have enabled the introduction of synthetic chemical methodology into nanofabrication. Nanoscale control of chemistry over macroscopic areas remains an important challenge. Recently parallel near-field lithography approaches have demonstrated the capacity to pattern macroscopic areas at high resolution, yielding feature sizes of ca. 100 nm over an area four orders of magnitude larger; they have also demonstrated the ability to function under fluid, yielding feature sizes of ca. 70 nm in photoresist under water and suggesting exciting possibilities for surface chemistry at the nanoscale. Finally, the monolayer patterning methods we have developed are by no means restricted to near-field lithography; all that is required is a suitable means of confining the optical excitation. For example, SAM photochemistry has been combined with interferometric exposure to facilitate the fabrication of periodic nanostructures over macroscopic areas in fast, simple, inexpensive processes, underlining the versatility of photochemistry as a nanofabrication tool.

**2:40pm TF+EM+SS-ThA3 Molecular Layer Deposition (MLD) of Polymer Multiple Quantum Dots on TiO<sub>2</sub>.** *T. Yoshimura, S. Ishii*, Tokyo University of Technology, Japan

**[Introduction]** We previously proposed oxide-semiconductor-based sensitized solar cells, in which polymer multiple quantum dots (MQDs) are utilized for sensitizing layers, and fabricated the polymer MQDs on glass substrates by Molecular Layer Deposition (MLD) [1]. In the present study, we grew polymer MQDs on TiO<sub>2</sub> by MLD. The polymer MQD growth on TiO<sub>2</sub> was confirmed by photoluminescence (PL) spectra.

**[Proposed Solar Cells Sensitized by Polymer MQDs]** The proposed sensitized solar cell consists of an oxide semiconductor layer and polymer MQDs on the surface. The polymer MQD contains different-length quantum dots (QDs) in the backbone wire, and consequently, a wide absorption band is obtained by superposition of narrow absorption bands of the individual QDs. This spectral division with the narrow bands can reduce the energy loss arising from the heat generation due to excess photon energy in light absorption processes.

**[Absorption/Photoluminescence Spectra of Polymer MQDs]** Reference samples of poly-azomethine (AM) and polymer MQDs: OTPTPT, OTPT, and OT were grown on glass substrates by connecting terephthalaldehyde (TPA), *p*-phenylenediamine (PPDA), and oxalic dihydrazide (ODH) with designated orders using MLD. The QD lengths in OTPTPT, OTPT and OT are respectively ~3, ~2 and ~0.8 nm. With decreasing the QD length, while the absorption peak shifts to high-energy side due to the quantum confinement, the PL peak shifts to low-energy side due to the Stokes shift. Namely, in the order of poly-AM to OT, the electrons become highly localized to increase the surrounding atoms' displacement caused by the electron transitions, resulting in the Stokes shift enhancement.

**[Growth of Polymer MQDs on TiO<sub>2</sub>]** We performed MLD to grow poly-AM on ZnO and TiO<sub>2</sub> powder layers. A yellow film of poly-AM was observed on TiO<sub>2</sub>. For ZnO, however, no film growth was observed because of weak hydrophilic characteristics of ZnO surfaces. We grew poly-AM and polymer MQDs of TO on the TiO<sub>2</sub> powder layers by MLD, and measured their PL spectra. The PL spectrum of TO was located at lower-energy side than that of poly-AM, which is parallel to the tendency observed in the PL spectra of the reference samples. From this result, it is concluded that polymer MQDs can be grown on TiO<sub>2</sub> by MLD as the sensitizing layers for solar cells.

[1] T. Yoshimura, R. Ebihara, A. Oshima, "Polymer Wires with Quantum Dots Grown by Molecular Layer Deposition of Three Source Molecules for Sensitized Photovoltaics," *J. Vac. Sci. Technol. A*, **29**: 051510-1-6 (2011).

**3:00pm TF+EM+SS-ThA4 Thiol-yne Click Chemistry: Old Concept & New Applications in Surface Science.** *N.S. Bhairamadgi, H. Zuilhof*, Wageningen University, Netherlands

Click chemistry reactions have opened new horizons in the field of surface chemistry, as these reactions are easy to perform on surfaces. A nice example is the addition of thiol moieties onto C=C bonds, which have been shown to be highly efficient, orthogonal to many other reactions, highly selective, etc. Recently we and others have shown that thiol-ene click reactions can be used efficiently for the modification of semiconductor surfaces and nanoparticles with a wide range of materials. In the current presentation we show an improved procedure involving C≡C bonds, i.e. thiol-yne click reactions.

We modified oxide-free Si(111) surfaces with alkene-terminated and alkyne-terminated monolayers, and these surfaces were further modified with various thiols such as thioglycolic acid, thioacetic acid, thioglycerol, thio-β-D-glucose tetraacetate lactose and 9-fluorenylmethoxy-carbonyl cysteine by using thiol-ene and thiol-yne click reactions. Upon detailed surface analysis it was found that after some optimization the thiol-yne click

reaction yielded 20 – 80 % more surface coverage compared to thiol-ene click reactions. Thus surface modification with thiol-yne click reactions promise to be the next step in surface-bound thiol click chemistry.

References:

1. Campos, M. A. C.; Paulusse, J. M. J.; Zuilhof, H., Functional monolayers on oxide-free silicon surfaces via thiol-ene click chemistry. *Chem. Commun.* 2010, 46 (30), 5512-5514.
2. Lowe, A. B.; Hoyle, C. E.; Bowman, C. N., Thiol-yne click chemistry: A powerful and versatile methodology for materials synthesis. *J. Mater. Chem.* 2010, 20 (23), 4745-4750.
3. Ruizendaal, L.; Pujari, S. P.; Gevaerts, V.; Paulusse, J. M. J.; Zuilhof, H., Biofunctional Silicon Nanoparticles by Means of Thiol-Ene Click Chemistry. *Chem. Asian J.* 2011, 6 (10), 2776-2786.
4. Wendeln, C.; Ravoo, B. J., Surface Patterning by Microcontact Chemistry. *Langmuir* 2012, 28 (13), 5527-5538.
5. Wendeln, C.; Rinnen, S.; Schulz, C.; Arlinghaus, H. F.; Ravoo, B. J., Photochemical Microcontact Printing by Thiol-Ene and Thiol-Yne Click Chemistry. *Langmuir* 2010, 26 (20), 15966-15971.

**3:40pm TF+EM+SS-ThA6 Attachment of Conjugated Diruthenium Alkynyl Compounds by Click Chemistry.** *S. Pookpanratana*, National Institute of Standards and Technology, *S.P. Cummings, T. Ren*, Purdue University, *C.A. Richter, C.A. Hacker*, National Institute of Standards and Technology

Attaching electrochemically-active molecules to a variety of different surfaces is of particular interest for applications in photovoltaic devices, catalysis, and molecular electronics. The family of diruthenium 2-anilino-pyridinate (ap) molecules is redox active [1], which makes it an ideal candidate to incorporate on surfaces for molecular catalysis, photoelectrochemical cells for water splitting, and as an active component in molecular electronic devices. Often times, the attachment of a tailored-molecule requires the additional design challenge to incorporate a specific anchoring group (e.g., thiol). Click chemistry has been demonstrated as an effective method to incorporate bulky and complex molecules to a variety of surfaces [2-6]. This route has introduced numerous possibilities of tailoring molecular surfaces.

Here, we have employed a Cu-catalyzed azide-alkyne cycloaddition (CuAAC) click reaction to attach Ru<sub>2</sub>(ap)<sub>4</sub>-(C≡C-C<sub>6</sub>H<sub>4</sub>-C≡CH), (henceforth referred to as Ru<sub>2</sub>-alkynyl) to Au and SiO<sub>2</sub> surfaces. First, we form an azide-terminated monolayer on Au and SiO<sub>2</sub> by using azidoundecanethiol and azidoundecyl trimethoxysilane, respectively. Next, the Ru<sub>2</sub>-alkynyl is linked to the azide-containing monolayers via a CuAAC reaction (adapted from Ref. 4). The clicked-on Ru<sub>2</sub>-alkynyl molecule was physically characterized by X-ray photoelectron spectroscopy (XPS) and infrared (IR) spectroscopy. The formation of the azide monolayer on Au and SiO<sub>2</sub> surfaces is confirmed by IR measurements. After the CuAAC click reaction of the Ru<sub>2</sub>-alkynyl to the azide-treated surfaces, there is a reduction of the azide stretch in the IR which indirectly confirms the progress of the click reaction. The incorporation of Ru<sub>2</sub>-alkynyl is confirmed by XPS, where we estimate the Ru<sub>2</sub>-alkynyl covers about 10% of the azide sites.

The formation of molecular electronic junctions (Au/Ru<sub>2</sub>-alkynyl/Si structures) by flip-chip lamination [7] for electrical and backside IR [8] characterizations is currently ongoing. With these results, we are able to obtain a thorough picture linking electrical properties with physical and chemical structure of the diruthenium molecular junctions.

S. P. Cummings et al., *Organometallics* 29, (2010) 2783 – 2788.

R. Chelmowski et al., *Langmuir* 25, (2009) 11480-11485.

G. Qin et al., *J. Am. Chem. Soc.* 132, (2010) 16432-16441.

R. E. Ruther et al., *J. Am. Chem. Soc.* 133, (2011) 5692 – 5694.

A. C. Cardiel et al., *ACS Nano* 6, (2012) 310-318.

P. K. B. Palomaki and P. H. Dinolfo, *Langmuir* 26, (2010) 9677 – 9685.

M. Coll et al., *J. Am. Chem. Soc.* 131, (2009) 12451-12457.

C. A. Richter et al., *J. Phys. Chem. B* 109, (2005) 21836 - 21841.

**4:00pm TF+EM+SS-ThA7 Vapor Phase Surface Functionalization using Hybrid SAMs / ALD Heterostructures.** *L. Lecordier, M.J. Dalberth, G. Sundaram, J.S. Becker*, Cambridge Nanotech, Inc.

Self-assembled monolayers and atomic layer deposition are two methodologies commonly used to tailor surface properties at the atomic scale and achieve thin films with excellent electrical, chemical, mechanical or optical performances thus leading to a broad portfolio of applications from thin films for flexible electronics to biological surface functionalization.

While ALD film growth is the result of a discretized process where inorganic monolayers are built upon one another through a sequence of reactant exposure/purge cycles until the desired film thickness is achieved (typically 1-100nm), SAMs on the other hand allow the deposition of a single ordered organic monolayer. Both processes are driven by self-limited chemisorbed surface reactions and can be deposited under vacuum conditions at relatively low temperatures, facilitating the integration of these two processes on a single platform.

The current work was implemented on a commercial Cambridge Nanotech hybrid ALD/SAMs platform. The tool is based on a Savannah S200 ALD reactor and integrates a SAMs kit for the accurate delivery of a variety of SAMs reactants. Stable SAMs monolayers are deposited under vacuum conditions using exposure mode (EXPO) characteristic of Cambridge Nanotech ALD tools. Key process metrics such as precursor pulse and exposure times, source and reactor temperatures were investigated for a variety of precursors including non-polar hydrophobic alkylsilanes (DTS), oleophobic fluorinated silanes (FOTS), hydrophilic polyethylene glycol (PEG) and thiols. In all cases, the self-limited surface saturation was achieved within 1 to 15 min minute exposures to the precursor at temperature ranging from 50 to 110°C.

In some instances, oxide ALD films were used to deposit a very thin seed layers (<5Å) to promote the adhesion of a SAM without prior surface cleaning/conditioning. Heterostructures based on oxide ALD (Al<sub>2</sub>O<sub>3</sub>, ZrO<sub>2</sub>, SiO<sub>2</sub>) and SAMs were also obtained to develop efficient water moisture barriers to be used for encapsulation. Overall the integration of these processes in a single platform provides a versatile and scalable method to surface functionalization where surface properties such as wettability can be tuned by controlling at the atomic level the structures of these hybrid coatings.

**4:20pm TF+EM+SS-ThA8 Chemically and Mechanically Stable Hydrophobic Thin Films Prepared by Combination of Layer-By-Layer Approach and Thiolen Chemistry, N. Madaan, J.A. Tuscano, N.R. Romriell, M.R. Linford, Brigham Young University**

The current aim of our research is to create robust hydrophobic thin films, for glass/silicon substrates, which can withstand extreme pH conditions and temperatures, have good release properties, and at the same time are mechanically durable. This approach consists of deposition of 3-aminopropyltriethoxy silane (APTES) on a silicon substrate followed by layer-by-layer deposition and cross-linking of alternating layers of poly(acrylic acid) (PAA) and poly(allylamine hydrochloride) (PAH). These nylon-like cross-linked layers have already been demonstrated to possess stability in extreme pH conditions. Their permeability can be controlled by the extent of crosslinking, which depends on the time and temperature of crosslinking. A careful study using X-ray photoelectron spectroscopy in our lab showed 71% cross-linking when these assemblies were heated at 250 °C for 2 h. We also found that the ratio of ammonium to amine groups in these bilayers is 2:1, and that there is a potential to impart additional properties to the films by utilizing these residual amine groups. This was part of an experimental design over a series of times and temperatures. These substrates can further be modified using a variety of chemistries. One approach is to expose these substrates to basic NaOH solution (pH ~ 10) in order to deprotonate the ammonium groups of the terminal PAH layer followed by treatment with Traut's reagent to convert amine groups into thiol groups. The thiol groups are then reacted with 1,2-polybutadiene and a perfluoroalkane thiol using thiol-ene chemistry. Another approach is to use hydrolyzed poly(maleic anhydride alt 1-octadecene) as a terminal electrostatic anionic layer. A chemical and tribological stability comparison will be performed between the above prepared films and a perfluoroalkane silane film on Si substrates. The effect of the total thickness of cross-linked PAH-PAA bilayers on the stability of prepared films will be studied. The substrates are thoroughly analyzed at each surface modification step using X-ray photoelectron spectroscopy, time-of-flight secondary ion mass spectrometry, ellipsometry, water contact angles, and atomic force microscopy.

**4:40pm TF+EM+SS-ThA9 A Detailed Investigation of the Conditions for Monolayer Deposition from Silane Precursors, J. Knauf, Advanced Molecular Films GmbH / RWTH Aachen University, Germany, L. Reddemann, Advanced Molecular Films GmbH / Universität zu Köln, Germany, A. Böker, RWTH Aachen University, Germany, K. Reihs, Advanced Molecular Films GmbH, Germany**

We have systematically investigated the process parameters for the vapor-phase deposition of monolayers from fluoroalkylated silane precursors. Our study reveals the influence of many process parameters on the molecular structure of the monolayers. Of particular interest to us are wetting and frictional properties of the monolayer obtained from the variation of process conditions. For reproducibly preparing high quality films particular parameters have to be meticulously controlled in a very narrow range which is not achievable without advanced deposition equipment.

Although the deposition of monolayers from silane precursors has been accomplished by various methods and has been subject to numerous studies, the properties and reproducibility of the resulting films remain unsatisfying for many applications. As an example, fluid wall slippage strongly depends on small changes in monolayer processing conditions which sensitively influence the structure of the monolayer deposited on structured surfaces [1].

Self-assembled monolayers (SAMs) were prepared by controlling a variety of process parameters, such as processing sequence and partial pressures of reactive compounds, deposition temperatures, adsorption/desorption times. These conditions were investigated for linear fluoroalkylated silane precursors of different chain lengths.

SAMs were deposited from fluoroalkylated silane precursors on pre-treated Si-wafers. Samples were examined by dynamic contact angle measurements, x-ray photoelectron spectroscopy (XPS), and static secondary ion mass spectrometry (SSIMS). The precursors applied were linear 1H,1H,2H,2H-Perfluoroalkyltrichlorosilanes and varying chain lengths of the fluoroalkyl part were used for comparative studies based on detailed investigations using 1H,1H,2H,2H-Perfluorododecyltrichlorosilane. Short-chain precursors were commercially available in ready-to-use quality whereas longer-chain compounds starting from 1H,1H,2H,2H-Perfluorododecyltrichlorosilane were synthesized in our labs. While the short-chain compounds could be processed by routine measures special precautions had to be applied for storage and handling of longer-chain compounds due to their higher reactivity.

Results of the study of deposition conditions will be presented and discussed and may serve as a guideline for the reproducible preparation of well-defined monolayers from silane precursors.

[1] L. Reddemann, J. Knauf, A. Böker, K. Reihs, 14th International Conference on Organized Molecular Films (ICOMF14) - LB14, Abstract 146 (2012)

**5:00pm TF+EM+SS-ThA10 Self Limiting Behavior in the Directed Self-Assembly of Mounds on Patterned GaAs(001), C.-F. Lin, University of Maryland, C.J.K. Richardson, Laboratory for Physical Science, H.-C. Kan, University of Maryland, N.C. Bartelt, Sandia National Laboratories, R.J. Phaneuf, University of Maryland**

We present results demonstrating directed self assembly of nm scale mounds during molecular beam epitaxial growth on patterned GaAs(001) surfaces. In the initial stages of growth, a lithographically-defined pattern directs the spontaneous formation of multilayer islands at the centers of bridges between near-neighbor nanopits along [110] crystal orientation, seemingly due to the presence of an Ehrlich-Schwoebel barrier. As growth continues, the heights of mounds at these 2-fold bridge sites "self-limit". Beyond this point mounds at other, 4-fold bridge sites dominate the topography, but these self-limit as well. This behavior suggests the existence of a minimum, 'critical terrace width' for nucleation of islands during growth, and provides a physical mechanism for understanding the transient nature of the observed instability during growth on these patterned surfaces

**5:20pm TF+EM+SS-ThA11 Characterization of Fully Functional Spray-on Antibody Thin Film, J.J. Figueroa, S. Magana, D. Lim, R. Schlaf, University of South Florida**

Physical adsorption (solid-liquid interface) is known as a simple and rapid option to immobilize biomolecules on various surfaces. Proteins, receptors and antibodies are attached via physisorption to different surfaces by various attachment protocols. However, physical adsorption has been often labeled in the past with disadvantages like variability, reversibility and low surface density of immobilized biomolecules. In contrast, the presented research demonstrates that spray deposition with a pneumatic nebulizer can be used to immobilize fully functional and stable physisorbed antibody coatings on glass surfaces with high reproducibility.

The experiments were performed using a low flow concentric nebulizer (commonly used on mass spectrometry), regular glass slides as a substrate and *E. coli* O157:H7 antibody as prototypical test system. The antibody films were examined for functionality, specificity and shelf life. A series of films with varying thickness and deposition conditions was characterized with respect to functionality, mechanical stability, surface morphology and antibody density. The results demonstrate that the films are comparable to films prepared with the standard covalent attachment protocol (avidin-biotin). They show low denaturation or conformational changes, minimal

loss during the rinsing process suggesting good attachment to the surface, and they perform as well with regard to sensitivity, specificity and shelf-life. The morphology studies suggest that the non-oriented attachment of the spray deposited antibodies (compared to the oriented attachment achieved with the covalent attachment scheme) is compensated by a higher antibody density enabled by the non-equilibrium spray deposition process.

# Thursday Afternoon Poster Sessions

## Electronic Materials and Processing Room: Central Hall - Session EM-ThP

### Electronic Materials and Processing Poster Session

**EM-ThP1 Proton Irradiation of Lattice Matched InAlN/GaN High Electron Mobility Transistors.** C.-F. Lo, L. Liu, T.S. Kang, F. Ren, University of Florida, C. Schwartz, E. Flitsiyani, L. Chernyak, University of Central Florida, H.-Y. Kim, J. Kim, Korea University, Republic of Korea, O. Laboutin, Y. Cao, J.W. Johnson, Kopin Corporation, P. Frenzer, S.J. Pearton, University of Florida

The DC characteristics of InAlN/GaN High Electron Mobility Transistors (HEMTs) were measured before and after irradiation with 5, 10 or 15 MeV protons at doses up to  $2 \times 10^{15} \text{ cm}^{-2}$ . At 5 MeV, the on/off ratio degraded by two orders of magnitude for the highest dose, while the sub-threshold slope increased from 77 to 122 mV/decade. There was little change in transconductance or gate or drain currents for doses up to  $2 \times 10^{13} \text{ cm}^{-2}$ , but for the highest dose the drain current and transconductance decreased by ~40% while the reverse gate current increased by a factor of ~6. The minority carrier diffusion length was around 1  $\mu\text{m}$  independent of proton dose. The InAlN/GaN heterostructure is at least as radiation hard as its AlGaIn/GaN counterpart.

**EM-ThP2 Effects of 2MeV Ge<sup>+</sup> Irradiation on AlGaIn/GaN HEMTs,** E.A. Douglas, P. Frenzer, S.J. Pearton, C.-F. Lo, L. Liu, T.S. Kang, F. Ren, University of Florida, E. Bielejec, Sandia National Laboratories

The DC characteristics of AlGaIn/GaN High Electron Mobility Transistors (HEMTs) were measured before and after irradiation with 2 MeV Ge<sup>+</sup> ions at doses from  $5 \times 10^{10}$  to  $5 \times 10^{12} \text{ cm}^{-2}$ . The drain current, gate leakage current and transconductance decreased monotonically with dose, while the drain-source resistance increased to a much greater extent than observed previously for proton irradiation of similar devices. The gate leakage current decreased with dose, as shown above. To understand the mechanism, we probed on-chip transmission line method (TLM) patterns receiving the same dose. Those irradiated with  $5 \times 10^{10} \text{ cm}^{-2}$  showed in a ~4x increase in sheet resistance and a 75% decrease in specific contact resistance. TLM patterns irradiated at  $5 \times 10^{11} \text{ cm}^{-2}$  and  $5 \times 10^{12} \text{ cm}^{-2}$  showed nA current (100mA prior to irradiation). Threshold voltage shifted to more positive values for increasing dose. There was no systematic effect of gate width or length (gate length from 0.1 to 1 micron and width from 100-200 micron) on the degree of degradation in device parameters. Reverse recovery switching times in the HEMTs were unaffected by the Ge<sup>+</sup> fluences we investigated. In contrast to proton implantation with moderate doses, which does not lead to high sheet resistivities of the implanted layers, the use of heavier ions like Ge<sup>+</sup> causes the sheet resistivity to be greatly increased. The basic degradation mechanism is still carrier loss from the channel as a result of trap formation in the AlGaIn layer and in the GaN buffer.

**EM-ThP3 Influence of AlInN Buffer Layer Thickness on the Properties of GaN Films on Si(111) Substrate using RF Metal-Organic Molecular Beam Epitaxy.** W.C. Chen, C.T. Lee, C.-N. Hsiao, Instrument Technology Research Center, National Applied Research Laboratories, Taiwan

Hexagonal structure GaN films were grown on silicon (111) substrate by radio-frequency metal-organic molecular beam epitaxy with Al<sub>x</sub>In<sub>1-x</sub>N buffer layers. We discussed the influence of AlInN buffer layer thickness on properties of GaN films. The thickness of the AlInN buffer layer can effectively counteract the tensile stress usually observed in the GaN layer deposited on Si(111). For a 10-nm-thick AlInN, crack density of  $2.4 \times 10^5/\text{mm}$  and a crystalline quality of 150 arcmin are obtained. Also, the average later thicknesses measured about 300 nm, and the growth rate about 0.2  $\mu\text{m}/\text{hr}$ . Also, Strong band-edge emission from GaN on Si(111) is observed at 3.39 eV with 70 nm-thick AlInN interlayer. The reduced lattice mismatch between the GaN film and Si(111) is responsible for improvement of GaN quality using the buffer-layer technique.

**EM-ThP4 Morphological Study of GaN Films Grown Under ALD Process Conditions as Well as Both Over- and Under- Saturated Growth Conditions.** J.C. Revelli, T.J. Anderson, University of Florida

Gallium Nitride films were grown by pulsed deposition of GaCl<sub>3</sub> and NH<sub>3</sub> using nitrogen as both carrier and purge gas. The pulse and purge times leading to self-limiting, ALD-mode growth were investigated at 585°C. ALD growth conditions led to a constant thickness increment per cycle. The ALD conditions were determined to be a 3-6 second GaCl<sub>3</sub> pulse, a 30

second NH<sub>3</sub> pulse, and 30 second nitrogen purge times in between. The surface morphology of all films were examined by AFM. ALD films showed RMS surface roughness of 0.3nm, similar to that of the underlying (0002) sapphire substrate, while films that had a GaCl<sub>3</sub> pulse below 3 seconds had an RMS roughness of 0.5nm and films oversaturated with GaCl<sub>3</sub> had an RMS roughness of 1.2nm. This result suggests that ALD can be used as a rapid and non-destructive method to identify ALD growth conditions.

**EM-ThP5 Structural, Compositional, and Thermal Stability Studies on In<sub>1-x</sub>Ga<sub>x</sub>N Epilayers.** A. Acharya, Georgia State University, M. Buegler, Technical University of Berlin, Germany, S.D. Gamage, N. Dietz, B. Thoms, Georgia State University

The structural and compositional properties of indium gallium nitride (InGaN) epilayers grown by high-pressure chemical vapor deposition have been studied using x-ray diffraction (XRD), Auger electron spectroscopy (AES) and high-resolution electron energy loss spectroscopy (HREELS). In addition, the thermal stability of the epilayers have been studied using temperature programmed desorption (TPD). The XRD pattern shows the InGaN (0002) Bragg reflex at 31.38 deg, indicating single-phase InGaN epilayers. Both XRD and AES measurements indicate a composition x of 4% gallium. The HREELS spectra of atomic hydrogen-exposed surfaces exhibit modes assigned to a surface N-H species, which were confirmed by observation of isotopic shifts following exposure to atomic deuterium. No In-H or Ga-H vibrations were observed suggesting the epilayer is N-polar. The thermal desorption study indicated that nitrogen desorption from the sample starts at 625 °C and peaks at 740 °C. No significant desorption of NH/NH<sub>2</sub><sup>+</sup> fragments have been observed. From an Arrhenius plot, an activation energy for the desorption of nitrogen of  $1.14 \pm 0.06 \text{ eV}$  was found.

**EM-ThP6 The Influence of the Group V/III Molar Precursor Ratio on the Structural and Optoelectrical Properties of InN Epilayers Grown by High-Pressure CVD.** R. Atalay, Georgia State University, M. Buegler, Technische Universität Berlin, Germany, S.D. Gamage, M.K.I. Senevirathna, Georgia State University, G. Durkaya, University of California Irvine, L. Su, UNC Charlotte, A.G.U. Perera, Georgia State University, I. Ferguson, UNC Charlotte, N. Dietz, Georgia State University

Over the last two decades, significant research efforts have been devoted to understand and improve the physical properties of InN epilayers. However, even today, there is still a significant lack of understanding how the different partial pressures of the precursor fragments of trimethylindium and ammonia affect the InN surface and growth chemistry and influence the materials properties.

In this study, high-pressure chemical vapor deposition (HPCVD) is used to control and suppress the disassociation of InN alloys at higher growth temperatures, together with a pulsed precursor injection approach to reduce gas phase reactions and to control the surface chemistry. In this contribution, we will present results on the influence of the group V/III molar precursor ratio on the structural and optoelectronic properties of InN epilayers grown on sapphire substrate with a reactor pressure of 8 bar. The group V/III molar precursor ratio was studied in molar V/III-ratio range of 900 to 3600. The structural analysis show for molar V/III-ratio of 2400 an optimum with, Raman and XRD having the lowest FWHM of 7.53 cm<sup>-1</sup> and 210 arcsec, respectively. The XRD results indicate improved grain size and reduced strain effect. Optical FTIR reflectance analysis of this epilayer found a free carrier concentration of  $1.7 \times 10^{18} \text{ cm}^{-3}$ , a mobility of 1020 cm<sup>2</sup> V<sup>-1</sup> s<sup>-1</sup> and a growth rate of 120 nm/h. The Raman analysis for these epilayers indicate that the non-polar phonon frequency with symmetry of E<sub>2</sub> is changes little within the studied molar V/III precursor ratio range; however, the polar phonon modes of both transverse optical (TO) and longitudinal optical (LO) are affected significantly. The studies showed also reveal that LO-phonon is influenced from the free carrier concentration (n<sub>e</sub>) and TO-phonon is influenced from the free carrier mobility (μ). In addition, surface morphology studies by AFM show an improved average grain size of  $8.51 \times 10^{-2} \mu\text{m}^2$  for the molar V/III-ratio of 2400.

**EM-ThP7 Prototype of Junctionless Transistor on SOI Wafers using Focused Ion Beam Milling.** L. Petersen Barbosa Lima, J. Alexandre Diniz, I. Doi, J. Godoy Filho, State University of Campinas, Brazil, H. Ivanov Boudinov, University of Rio Grande Do Sul, Brazil

Nowadays, Junctionless devices (JL) have gained much attention of microelectronics industry, because it is compatible with CMOS technology and can be useful for 3D devices. In this context, nMOS JL devices were fabricated on SOI substrates using Ga<sup>+</sup> Focused Ion Beam (FIB) milling and for depositions of SiO<sub>2</sub> (gate dielectric) and Pt layers (as gate, drain and source electrodes) of JL transistor. In this work, two methods to fabricate

the JL devices were used. One method is using on FIB system to milling the Si substrate and the other method used Reactive Ion Etching (RIE) and FIB system to etch the Si substrate. The samples with only FIB system were called JLFIB and samples with RIE plasma etch and FIB system were called JLRFB. First of all, the wafers JLFIB and JLRFB were doped with phosphorus, dose  $10^{19}$  cm<sup>-3</sup> and energy of 30 KeV, using ion implantation system. After that, Rapid Thermal Annealing (RTA) were used to anneal the SOI samples after the ion implantation procedure. 0.6- $\mu$ m-thick SiO<sub>2</sub> were obtained using a wet oxidation on conventional furnace to get thinner height of Si substrate on SOI wafer. So, lithography to define MESA structures and RIE Si etching were carried out only on JLRFB samples. Then JLFIB and JLRFB samples were insert on FIB system to get the JL fabrication. First of all, using a Ga<sup>+</sup> ion beam the Si substrates were milled to obtain the Si nanowire to define the gate, drain and source regions of JL transistor. Width, length and height dimensions of Si nanowire were about 100 nm, 4  $\mu$ m and 50-80 nm, respectively. Then, 10-nm-thick SiO<sub>2</sub> was deposited to be gate dielectric and finally, Pt were deposited to be gate, drain and source electrodes. Energy Dispersive X-Ray Spectroscopy (EDS) measurements were carried out to confirm the surface composition of Si nanowire, SiO<sub>2</sub> gate dielectric deposition and Pt electrodes deposition. In addition, EDS results show some Ga incorporation on Si nanowire surface, however, this incorporation was derived from Ga<sup>+</sup> FIB and no significant damage on Si nanowire was occurred. Finally, these devices were sintered in a conventional furnace in forming gas at 450°C for 10 and 20 minutes. Drain-source current ( $I_d$ ) x drain-source voltage ( $V_{ds}$ ) measurements of JLFIB and JLRFB devices were carried out, and indicate that the devices are working, like a gated resistor or JL device, with high Pt source and drain contact resistances, which lead to the distortions of  $I_d$  x  $V_{ds}$  curves. However, these distortions can be reduced using a longer time of contact sintering process and a Si nanowire height lower than 50 nm. Finally, our fabrication method using FIB process steps can be used to obtain JL devices.

**EM-ThP8 Simulation of Millisecond Laser Anneal on SOI: A Study of Dopant Activation and Mobility and its Application to Scaled FinFET Thermal Processing.** *T. Michalak, J. Herman, M. Rodgers, D. Franca, C. Borst*, University at Albany-SUNY

Next generation CMOS requires high activation and hyper-abrupt junction formation for low sheet resistance and device performance. The primary method of doping, ion implantation, provides excellent spatial control of dose. A high temperature anneal (>1000° C) is required to remove defects introduced from ion implantation and to electrically activate the implanted specie. A “diffusionless anneal” by which dopant is activated without significantly diffusing, would be ideal for ultra-shallow junction (USJ) formation. This work investigates one such technique, laser annealing, which uses a scanning laser to locally heat the wafer surface. We investigate the laser system via simulation to determine the peak temperature achieved in the active area during processing. We employed the Sentaurus TCAD software by Synopsys to perform a 2D simulation of a laser scanning across the active area of the device, solving the heat equation in both time and space (Fig 1). An absorber layer is deposited on the wafer surface to encourage the absorption of optical power and consequent heating of the wafer surface. An effective absorption coefficient of  $\alpha=8861$  cm<sup>-1</sup> was calculated for the absorber layer, calibrated with the experimental laser intensity of 52526 W/cm<sup>2</sup> required to melt silicon at a scan speed of 150 mm/s which lies within the range for amorphous carbon stated in literature (Fig 2). This absorption coefficient correctly predicts the silicon temperature as a function of power with any arbitrarily defined scan speed (Fig 3). To investigate the role of dopant activation, an SOI wafer was implanted at 25 keV, dose  $3e15$  cm<sup>-2</sup> and laser annealed in stripes of target temperatures ranging from 1100-1300 °C. The sheet resistance was measured on wafer showing Rs improvement with increasing laser temperature (Fig 4). The extracted temperature cycle from the 2D heat simulation was used as an equivalent millisecond RTA in a full 3D finFET process simulation to study dopant distribution and activation using Sentaurus Process Kinetic Monte Carlo (KMC), considering the effect of dopant clusters and point defects. The results of this simulation, supplemented with Hall mobility measurement and secondary ion mass spectroscopy (SIMS), show that there is no further activation of arsenic with increasing laser temperature (~ 25%) which suggests healing of the implant crystal damage may be reducing sheet resistance. As well, an electrical device simulation of the finFET was performed to compare device performance between RTA and laser annealing (schematic Fig 5). Simulation results show a theoretical improvement in drive current with the laser process over standard RTA.

**EM-ThP9 Equivalent-Circuit Model for Vacuum Ultraviolet Irradiation of Dielectric Films.** *H. Sinha, J.L. Shohet*, University of Wisconsin-Madison

VUV irradiation causes electron photoemission from dielectrics. Photoemission occurs from defect states in the dielectric band gap and results in trapped positive charges. We propose an equivalent-circuit model using which, once the circuit parameters are determined, charging of dielectric materials under VUV irradiation can be predicted. The circuit includes a dielectric capacitor, the intrinsic and photo conductivities of the dielectric and substrate, and the processes of photoemission and photoinjection. The model has the back of the substrate grounded through an ammeter to the vacuum chamber. The ammeter reads the substrate current. To simulate the circuit between the dielectric sample and the vacuum chamber that collects photoemitted electrons, a photodiode is used. The sample itself, *i.e.* the dielectric deposited on a Si substrate, is represented by a combination of capacitors, resistors and dependent voltage sources. An ideal dielectric can be expressed as a parallel-plate capacitor. However in a real dielectric leakage currents are present due to defect states. Thus, we include a resistor in parallel to the capacitor that represents the intrinsic conductivity. In addition, photoconductivity is introduced in the dielectric during VUV radiation, which is shown by another resistor in parallel to the capacitance. A dependent voltage source models the electron depopulation from the defect states. We represent the substrate, which is a semiconductor, by a resistor. This resistor signifies the intrinsic resistance. As VUV photons also cause electron-hole pair generation in substrate, a resistor as a photoconductivity component is added in parallel to the intrinsic resistor. The circuit components were determined using experimental photoemission/substrate current data for SiCOH. The prediction of photoemission/substrate current using the model was found to match experimental results over different thickness of SiCOH. To conclude, an equivalent circuit can model the effect of VUV radiation on charging and currents in dielectrics.

This work has been supported by Semiconductor Research Corporation under Contact No. 2008-KJ-1871 and the National Science Foundation under Grant CBET-1066231. The UW-Madison Synchrotron is funded by NSF under Grant DMR- 0537588.

**EM-ThP10 Surface Photoconductivity of SiO<sub>2</sub> and SiCOH Induced by Vacuum Ultraviolet Radiation.** *H. Zheng, M.T. Nichols, D. Pei*, University of Wisconsin-Madison, *G.A. Antonelli*, Novellus Systems, Inc., *Y. Nishi*, Stanford University, *J.L. Shohet*, University of Wisconsin-Madison

The change in the electrical surface conductivity of SiO<sub>2</sub> and SiCOH during exposure to vacuum ultraviolet radiation is investigated<sup>1</sup>. To measure the change in conductivity, special fabricated patterned titanium finger “comb structures” are deposited on dielectric films and exposed to synchrotron radiation in the range of 50–300 nm, which is in the energy range of most plasma vacuum-ultraviolet radiation. For the measurements of the VUV-induced currents along the surface of the layer in between the titanium fingers, electrical connections are made from the test structure to outside circuitry through vacuum feedthroughs. A numerical simulation shows that the bulk current is too small to account for the measured values and most of the current indeed flows across the surface of the dielectric film in the test structure. By measuring the I-V curve of the comb test structures under controlled fluxes of VUV light, we determine that the measured current per unit photon-flux density is linear with applied electric field up to a saturation value that is VUV flux limited. This permits the surface conductivity to be calculated based on a simple photoconductor model. The increase in surface conductivity induced by VUV radiation can be beneficial in limiting charging damage of dielectrics by depleting the plasma-deposited charge.

This work is supported by the National Science Foundation under Grant CBET-1066231 and the Semiconductor Research Corporation under contract 2008-KY-1781. We also thank M. Severson for helping set up the VUV exposure.

<sup>1</sup> C.Cismaru, J.L. Shohet and J.P. McVittie, *Applied Physics Letters*, **71** 2191 (2000).

**EM-ThP11 Spatial Volume Charge Distribution Measurement in Thin Dielectric Films: Electro-Acoustic Method.** *D. Pei, M.T. Nichols*, University of Wisconsin-Madison, *Y. Shkel*, Commet LLC, *Y. Nishi*, Stanford University, *J.L. Shohet*, University of Wisconsin-Madison

Trapped volume charge inside dielectric films can lead to breakdown permanently damaging the dielectric film. Measurement of the spatial volume charge distribution is critical to estimate the electric field and the change in properties of dielectric films. A pulsed electro-acoustic (PEA)[1-2] method is applied to measure the volume charge distribution throughout the thickness of the thin film dielectric. In this method, a high voltage pulse signal (1 kV, 10 ns) or a sinusoidally varying high-voltage signal (4 kV, 5

kHz) is applied across a thin film of low-density polyethylene. An acoustic wave is generated by the volume charge inside the film and transmitted to each side of the film. A piezoelectric transducer on one side of the dielectric film is used as a sensor to detect and measure the arrival times of the acoustic waves in the case of pulsed excitation or the shift in phase of the detected signal in the case of sinusoidal excitation. This allows spatial resolution of both the location and magnitude of the charge distribution.

This work was supported by the Semiconductor Research Corporation under Contract No. 2008-KJ-1871 and by the National Science Foundation under Grant No. CBET-1066231.

[1] T. Maeno, T. Futami, H. Kushibe, T. Takada and C. M. Cooke "Measurement of Spatial Charge Distribution in Thick Dielectrics Using the Pulsed Electroacoustic Method" IEEE Transactions on Electrical Insulation Vol. 23 No. 3, June 1988

[2] M. Abou-Dakka, S.S. Bamji and A.T. Bulinski, "Space Charge Distribution in XLPE by TSM, Using the Inverse Matrix Technique", *IEEE Trans. Dielect. And Electr. Insul.*, vol. 4, pp. 314-320, 199

#### **EM-ThP12 Investigation of Photoluminescent Characteristics and Structural Properties of Thin Film Zinc Silicate Doped with Manganese, K.H. Yoon, J.H. Kim, Chungbuk National University (CBNU), Republic of Korea**

The photoluminescent characteristics and structural properties of manganese-doped zinc silicate ( $Zn_2SiO_4:Mn$ ) thin films were investigated. The  $Zn_2SiO_4:Mn$  films were deposited by radio frequency magnetron sputtering, followed by post-deposition annealing at temperatures of 600 - 1200 °C. The  $Zn_2SiO_4:Mn$  films exhibited a pronounced optical absorption edge in the near ultraviolet wavelength region and the maximum transmittance reached approximately 0.922. The refractive index of the  $Zn_2SiO_4:Mn$  films showed normal dispersion behavior. X-ray diffraction and atomic force microscopy measurements revealed that the as-deposited  $Zn_2SiO_4:Mn$  films had an amorphous structure with a smooth surface morphology. The  $Zn_2SiO_4:Mn$  films became crystalline after annealing at 800 °C and the crystallinity of the films was continuously improved up to 1200 °C. The annealed  $Zn_2SiO_4:Mn$  films had a polycrystalline rhombohedral structure with no preferred crystallographic orientation of the crystallites. The photoluminescence spectra of the annealed  $Zn_2SiO_4:Mn$  films showed broad-band emissions with a peak maximum at about 523 nm. The PL emission intensity was enhanced as the annealing temperature increased, resulting from the improvement of the crystallinity of the  $Zn_2SiO_4:Mn$  films. The excitation band exhibited a peak maximum at around 243 nm in the near ultraviolet region, which was considered to be associated with the charge transfer transition of divalent manganese ion in the  $Zn_2SiO_4$  system.

#### **EM-ThP13 The Electrical and Thermal Properties of Nanoscale Multilayered $Bi_2Te_3/Sb_2Te_3$ and $Bi_2Te_3/Bi_2Te_{3-x}Se_x$ Thin Films, M. Hines, Z. Xiao, Alabama A&M University**

Nanoscale multilayered  $Bi_2Te_3/Sb_2Te_3$  and  $Bi_2Te_3/Bi_2Te_{3-x}Se_x$  thin films were grown using the e-beam evaporation. The in-plane and cross-plane micro thermoelectric devices were fabricated using the clean room-based microfabrication techniques such as UV lithography. The e-beam-grown multilayered thin films and the fabricated thermoelectric devices were measured and characterized. The nanoscale multilayered  $Bi_2Te_3/Sb_2Te_3$  and  $Bi_2Te_3/Bi_2Te_{3-x}Se_x$  thin films can have much higher thermoelectric figure of merit than their bulk materials. The measurement results on the electrical and thermal properties of the nanoscale multilayered  $Bi_2Te_3/Sb_2Te_3$  and  $Bi_2Te_3/Bi_2Te_{3-x}Se_x$  thin films will be reported in the conference.

#### **EM-ThP14 Mapping the Magnetic Detection Properties of Chip-Scale Optically Pumped Magnetometers, N. Ptschelintzew, P.H. Holloway, M.R. Davidson, University of Florida**

Magnetometers have a wide range of utilization from Nuclear Magnetic Resonance (NMR), to medical applications such as the Magneto-Encephalogram (MEG), Magnetocardiography (MCG), and Magnetic Resonance Imaging (MRI). However, these techniques often depend on superconducting quantum interference detection magnetometers or the detection of a radio frequency magnetic resonance in a paramagnetic target induced while in a large field. Chip-scale, low-power optical magnetometers can improve the cost and size as well as reduce the complexity of these devices. The directional variation of sensitivity of these detectors can be exploited to make devices that can form images. We have designed and instrument that will be the functional equivalent of a portable MRI that will be capable of near real-time imaging. The inverse algorithm of mapping a series of detector responses to a magnetic "image" has been calculated and an algorithm for rapidly calculating images from sparse optical magnetometer data sets has been developed. Experimental measurement of the directional sensitivity of Rb-based optical

magnetometers will be presented. A prototype imaging system for magnetic tomography is being constructed.

#### **EM-ThP15 Characterization of ZnO/CuO Nanolaminate Materials, S.T. King, L. Bilke, B. Oleson, J. Krueger, E. Tennyson, University of Wisconsin - La Crosse**

ZnO and its alloys have shown much promise to replace ITO as the transparent conducting layer in many electrical devices. However, ZnO typically does not exhibit a low enough resistivity for such applications. Beyond doping ZnO, much work has focused on developing heterostructures in which ZnO is layered with a metal on the nanometer scale [1]. A recent study has suggested that bilayers of ZnO and Cu exhibit properties which may allow such laminate materials to be employed in photovoltaic applications [2]. However, it is apparent that these Cu interlayers will oxidize over time resulting in the formation of CuO interlayers. Therefore, the properties of ZnO/CuO laminates must be understood to determine the effects of interlayer oxidation on these materials.

The current study has employed x-ray diffraction, spectroscopic ellipsometry, UV-Vis spectroscopy, and four-point resistivity measurements to examine the effects that CuO interlayer thickness has on the structural, optical, and electrical properties of ZnO/CuO nanolaminate films deposited by reactive DC sputter deposition. Results suggest that CuO interlayers may afford similar transmittance and resistivity results as Cu interlayers thus alleviating possible difficulties incurred from interlayer oxidation in nanolaminate materials.

[1] J.S. Cho, S. Baek, and J.C. Lee; SOLAR ENERGY MATERIALS AND SOLAR CELLS, **95**, 7, 1852-1858 (2011)

[2] J.G. Lu, X. Bie, Y.P. Wang, L. Gong, and Z.Z. Ye; JOURNAL OF VACUUM SCIENCE & TECHNOLOGY A, **29**, 3, 03A115 (2011)

#### **EM-ThP16 Small-Molecule Scaffolds for Directed Self-Assembly, P.L. Mancheno-Posso, A.J. Muscat, University of Arizona**

Functionalization of oxide surfaces with vinyltrichlorosilane (VTCS,  $CH_2=CH-SiCl_3$ ) was studied using water contact angle, ex situ ellipsometry, X-ray photoelectron spectroscopy (XPS), and atomic force microscopy (AFM). VTCS monolayers can be used as scaffolds for the deposition of a subsequent layer and keep it in close proximity to the surface due to its short length and terminal vinyl group. In this work, Si(100) samples were ultrasonically cleaned in acetone, methanol, and DI water for 5 min each. Native oxide was removed using a 1:100 (v/v) solution of 49% HF in water for 1 min. Subsequently, samples were hydroxylated with a 3:1 (v/v) solution of  $H_2SO_4$  and  $H_2O_2$  for 10 min at 60 °C. VTCS was adsorbed from 1:1000 (v/v) solutions in toluene, chloroform, and acetone. The layer thickness after 30 min in toluene was  $47.5 \pm 6.4$  Å, in chloroform  $7.1 \pm 0.9$  Å, and in acetone  $4.0 \pm 1.9$  Å. These results suggest acetone as the most appropriate solvent to produce a monolayer. The contact angle was near 0° on the piranha-treated surface and increased to  $25.3 \pm 0.5^\circ$  after VTCS adsorption. Addition of bromine atoms to the vinyl group was performed by immersing the samples in a 2% (v/v) solution of elemental bromine in dichloromethane for 2 hr. The contact angle was  $63.2 \pm 3.9^\circ$  after bromination. A Br 3d XPS peak at 70.0 eV (C-Br) demonstrated the chemical modification of the unsaturated bond of the VTCS molecule. AFM roughness analysis yielded an RMS value of 0.11 nm for the VTCS monolayer. The reaction of VTCS with hydroxyl groups at the surface was demonstrated on a thick hafnia layer by the presence of XPS peaks at 102.6 eV for Si 2p and 532.3 eV for O 1s, which correspond to Si-O bonds formed by VTCS and the substrate. Oxidation of the vinyl group with potassium permanganate (5 mM) and sodium periodate (195 mM) yielded a peak at 286.6 eV for C 1s, suggesting the formation of C-OH moieties.

# Friday Morning, November 2, 2012

## Electronic Materials and Processing

Room: 14 - Session EM+NS-FrM

### Low-Resistance Contacts to Nanoelectronics

Moderator: S. Zollner, New Mexico State University

8:20am EM+NS-FrM1 **Electrical Transport on Chemically Modified Silicon-on-Insulator Substrates**, *G.P. Lopinski*, National Research Council of Canada **INVITED**

Electrical transport of semiconductor surfaces and nanostructures are strongly influenced by interfacial processes. Adsorption and reaction events which result in charge re-distribution can modulate conductivity through long-range electric field effects. These effects are being exploited to tailor electronic properties of nanomaterials and devices as well as in the development of electrically-based chemical and biological sensors. Silicon-on-insulator(SOI) substrates, in which the top layer is thinner than the depletion length, are particularly well-suited for demonstrating and investigating the effects of surface processes on electrical transport. Measurements on hydrogen terminated H-SOI substrates (with both (100) and (111) orientations) have demonstrated that adsorption of certain polar molecules (water, pyridine and ammonia) results in large reversible increases in conductivity, attributed to charge transfer effects which induce accumulation of majority carriers on n-type and minority carrier channels (inversion) on p doped substrates. Adsorption of the prototypical electron acceptor tetracyanoethylene (TCNE) results in a strong decrease in conductivity on n-type substrates due to depletion of majority carriers. This effect is not fully reversible due to reactions of TCNE with the H-terminated surface. Use of SOI substrates also facilitates formation of point contact pseudo-MOSFETs, allowing transistor characteristics to be obtained without the need for device fabrication. This approach has been shown to be a simple and straightforward way to monitor the effect of adsorption and reaction events on the electronic properties of the silicon substrate. Pseudo-MOSFET measurements have been used to monitor surface reactions such as ambient oxidation of the H-terminated surface. Gas phase photochemical reaction of alkenes has been used to chemically passivate these surfaces while maintaining a low density of electrically active defects ( $<1 \times 10^{11} \text{ cm}^{-2}$ ). These alkyl monolayer passivated SOI surfaces show a large reversible response to TCNE, suggesting they can function as good ultrathin gate dielectrics for sensing applications.

9:00am EM+NS-FrM3 **Evidence for Single Electron Tunnel Junction using Gold Nanoparticles on Oxide-Free Si(111)**, *L. Caillard, O. Seitz, P. Campbell*, University of Texas at Dallas, *O. Pluchery*, Université Pierre et Marie Curie, France, *Y.J. Chabal*, University of Texas at Dallas

It has been suggested that the phenomenon of Coulomb blockade could be achieved by placing a metallic nanoparticle between two tunnel junctions. While the Coulomb blockade has been well established theoretically and demonstrated on metal substrates<sup>1</sup>, it is more challenging to observe on semiconductor surfaces due in part to the defective nature of the interfaces and to the depletion layer. We present an experimental study of two ultra small-capacitance normal tunnel junctions connected in series between the Si substrate and a STM tip. To achieve such a structure, we use an amine-terminated self-assembled monolayer (SAM) grafted on silicon (111) as the insulator layer, acting as a linker to attach gold nanoparticles on the surface. The SAM layer is grafted directly on oxide-free silicon through a Si-C bond formation using hydrosilylation reactions and is characterized by a low interface state density<sup>2</sup>. Moreover, this SAM layer provides a long-term passivation (weeks) of the interface that prevents oxidation of the substrate during Au nanoparticle deposition. The SAM quality is characterized using an extensive range of techniques, including in-situ IR spectroscopy, spectroscopic ellipsometry, X-ray photoelectron spectroscopy (XPS) and Atomic force microscopy (AFM). The second capacitance is formed by the gap between the gold nanoparticle and the tip of the Scanning tunneling microscope/spectroscopy (STM/S). The current-voltage measurements have been performed in ultra high vacuum. Several parameters have been investigated: silicon doping level, sample temperature, and size of the gold nanoparticles (AuNPs), ranging from 1 to 15 nm. The junction is achieved by either grafting synthesized AuNPs or depositing evaporated gold directly on the SAM. Preliminary data confirm that coulomb staircases are observed under different conditions, mostly clearly for highly doped substrates at low temperature (10K). The steps width and height of these Coulomb staircases depend on particle size. These results are an important step toward future control for single electron transistor and flash memory applications.

[1] Zhang, H.; Yasutake, Y.; Shichibu, Y.; Teranishi, T.; Majima, Y., Tunneling resistance of double-barrier tunneling structures with an alkanethiol-protected Au nanoparticle. *Phys. Rev. B*, 72, (20) (2005)

[2] D. Aureau, Y. Varin, K. Roodenko, O. Seitz, O. Pluchery and Y. J. Chabal, Controlled Deposition of Gold Nanoparticles on Well-Defined Organic Monolayer Grafted on Silicon Surfaces. *Phys. Chem. C*, 114 (33), pp 14180–14186 (2010)

9:20am EM+NS-FrM4 **A Distribution of Variable Size Sn-islands on 0.8 nm Oxide/ Si (111): Local MOS Properties and Tunneling Studied with Synchrotron Radiation**, *A. Silva*, Universidade Nova de Lisboa, Portugal, *K. Pedersen*, Aalborg University, Denmark, *Z.S. Li*, Aarhus University, Denmark, *P. Morgen*, University of Southern Denmark

The thinnest possible uniform and stable oxide layer grown thermally on Si (111) is 0.8 nm thick. This oxide is grown at around 500°C, in a self-limiting process, which has earlier been fully characterized with surface sensitive, high-resolution core level photoemission at the ASTRID storage ring facility at Aarhus, Denmark. Such oxides are too thin for use in current generations of CMOS-devices, yet they have potential applications in devices, where controlled tunneling could be of importance, or as diffusion barriers. To study the tunneling properties of this oxide covering the Si (111) surface isolated nanometer-sized Sn islands in different diameters and concentrations were deposited at 500°C and became negatively charged, with different charges depending on their size. The deposition was done from a Knudsen source in a way programmed to produce a systematic variation of the Sn coverage across about 2 cm of the surface. This is done to allow locally resolved photoemission characterization of the system, at a resolution (with a photon beam width) of around 150 micron. The resulting shifts of Si 2p and Sn 4d core levels at, and across the surface, with varying amounts of Sn, and charge on the Sn islands, are used to determine the local changes in band bending and fields in the oxide. This method thus offers a unique possibility to evaluate MOS properties of nano-systems in-situ without direct electrical contacts.

9:40am EM+NS-FrM5 **Signatures of Interface Band Structure and Parallel Momentum Conservation of Hot Electrons across Metal-Semiconductor Schottky Diodes**, *J. Garramone*, Northwestern University, *J. Abel*, *R. Balsano*, University at Albany-SUNY, *S. Barraza-Lopez*, University of Arkansas at Fayetteville, *V.P. LaBella*, University at Albany-SUNY

Understanding hot electron transport and scattering through materials and interfaces is important for conventional integrated circuit technologies and futuristic applications such as hot carrier photovoltaics and hydrogen sensing. In this presentation, the hot electron attenuation length of Ag is measured utilizing ballistic electron emission microscopy (BEEM) on nanoscale Schottky diodes for Si(001) and Si(111) substrates. Marked differences in the attenuation length are observed at biases near the Schottky barrier depending upon the substrate orientation, increasing by an order of magnitude only for Si(001), while remaining unchanged for Si(111). These results provide clear evidence that the crystallographic orientation of the semiconductor substrate and parallel momentum conservation affect the hot electron transport across these interfaces. A theoretical model reproduces the effect that combines a free-electron description within the metal with an ab-initio description of the electronic structure of the semiconductor.

10:00am EM+NS-FrM6 **Metal-Fullerene Interfaces: A Dynamic System**, *P. Reinke*, *J.B. McClimon*, *H. Sahalov*, University of Virginia

Fullerenes and other small organic molecules are used in organic solar cells, organic LEDs and molecular electronics system, and the interface between the organic layer and the metal electrode is critical to achieve the desired functionality. The majority of studies focusses on the interaction of molecules with metal surface, and the interaction of metals with organic surfaces has garnered much less attention. However, the addition of metal to an organic layer surface has been one of the bottlenecks in the fabrication of molecular electronics devices. We therefore present here a comprehensive study of the metal interaction with fullerene surfaces. Our past research has investigated the deposition of Au and Si on fullerene surfaces, and our presentation here focuses on the interface to transition metals Vanadium and Tungsten. All of these systems show a dynamic behavior: the metal atoms are highly mobile and thus perturb the C<sub>60</sub> matrix substantially.

The fullerene and metal atoms/films are deposited by electron beam and thermal evaporation, and the interface formation is observed with STM under UHV conditions in a sequential manner. V immediately diffuses into the fullerene matrix, and surface clusters are sparse. The STM images reflect the change in the local electronic structure of the molecules through

the interaction with sub-surface V: the apparent height of molecules in contact with V is reduced, and their rotation ceases and the molecular orbitals can be identified by the characteristic  $C_{60}$  substructure within the molecule.

We suggest that the subsurface V forms complexes with  $C_{60}$  where charge donation to the fullerene cage occurs, and preferential bonding to the hexagonal face determines the molecule orientation. The increase of V concentration leads to agglomeration of V-clusters and consequently the extension of regions with a smaller apparent height in the filled state images. The charge exchange between metal clusters and fullerene matrix allows to observe the V-cluster growth within the matrix. The empty state images are essentially flat, and show small variations in topography and cracks in the fullerene layer for large V-concentrations (~0.6 to 1 ML). We will present a comprehensive model for the diffusion of V through the matrix, the complex formation and cluster growth. The behavior of W is distinguished by a larger percentage of surface clusters, and the dynamics of cluster formation within the matrix will be compared to V. However, both transition metals do not destroy the  $C_{60}$  matrix, but only react to form carbides at elevated temperatures.

10:20am **EM+NS-FrM7 Scaling Silicide Contacts in Microelectronics: At What Size will Material Characteristics affect Device Properties ?**, **C. Lavoie**, IBM T.J. Watson Research Center **INVITED**

With the continued scaling of CMOS technology, the typical contact area to the source and drain of a CMOS device can now reach below  $1000 \text{ nm}^2$ . At these nano-dimensions, typical intrinsic contact resistivities of  $1 \times 10^{-8} \Omega\text{-cm}^2$ , easily lead to resistances exceeding the  $K\Omega$  solely for crossing the interface silicide-silicon. Such resistances are unacceptable as they dominate the overall resistance of a device. In an attempt to mitigate this increase in interfacial resistance with contact area reduction, much research has been performed concentrating on the tailoring of material properties of both the silicide and the semiconductor substrate as well as on the optimization of contact geometries and the advanced engineering of interfaces. As the size of the contact reaches dimensions that are similar or smaller than the typical microstructure of the expected poly crystalline material, some dramatic effects are to be anticipated. First, the presence of a single grain during the silicidation eliminates the typical dominant diffusion path: grain boundaries. As a result, phase nucleation and kinetics of growth can only proceed through the silicide bulk or the available interfaces. This will likely retard formation of the desired phases in the narrowest dimensions. Another expected disadvantage of very small contacts resides in the variability of the intrinsic contact resistance discussed above. It is accepted that the Schottky barrier height of a given silicide to a silicon substrate varies with substrate orientation. As a result, variation of crystal orientation from contact to contact may lead to dramatic effects on contact resistance. This orientation variation can originate from either a variation in silicide texture from contact to contact or a variation in device geometry (i.e. silicidation on Si(100), Si(110) or Si nanowire device depending on geometry). In this presentation, we will first explain how the importance of contact resistivity has caused a shift in contact engineering from yield and defect control towards the optimization of device performance. We will then describe some of the challenges involved in building arrays of nanostructures and characterizing them.

11:00am **EM+NS-FrM9 Compositional Dependence of the Dielectric Function and Optical Conductivity of NiPt Alloy Thin Films**, **L.S. Abdallah**, **T. Tawalbeh**, **I.V. Vasiliev**, **S. Zollner**, New Mexico State University, **C. Lavoie**, IBM T.J. Watson Research Center, **A. Ozcan**, IBM Systems and Technology Group, **M. Raymond**, GLOBALFOUNDRIES

Optical properties of metals are less well known than those of insulators and semiconductors, because it is hard to achieve similar purity and crystallinity in metals. Many metals are reactive and easily form oxides, or they exhibit significant surface roughness. We report the dielectric function and optical conductivity of Ni-Pt alloys as a function of composition (10 to 25 atomic % Pt) from 0.8 to 6.5 eV. Our films are 10 nm thick and were prepared by physical vapor deposition (co-sputtering from pure Ni and Pt targets). To avoid reaction between Si and the metal alloy, films were deposited on thick thermal oxides (220 nm). Some films were annealed at  $500^\circ\text{C}$  for 30 s. Similar Ni-Pt alloys are used as Ohmic contacts in CMOS device processing, to achieve highly stable low-resistance contacts between copper back-end metallization and front-end silicon transistors. Our results will enable in-line process control of Ni-Pt alloy deposition using spectroscopic ellipsometry.

Since our metal thickness is below the penetration depth, the interference from the thick  $\text{SiO}_2$  layers creates artifacts when extracting the optical conductivity. We minimize this issue by acquiring the ellipsometric angles over a broad range of incidence angles ( $20^\circ$  to  $80^\circ$ ), which varies the optical path length and thus shifts the interference problems to different energies. Our resulting dielectric functions are similar to those tabulated by Palik for pure Ni. The data are dominated by a Drude divergence due to free carriers

at low photon energies. We can remove this divergence by multiplying with the photon energy. We find several trends: (1) The optical conductivity of the annealed films is always greater than that of the as-deposited films, due to improvements in crystallinity and reduced grain boundary scattering after annealing. (2) All four alloys show conductivity peaks near 1.5 and 4 eV due to transitions from the d-like valence bands to the s-like conduction bands. (3) These peaks are significantly broader and weaker than those in pure Ni, but at the same energy. The broadenings increase with increasing Pt content. However, the amplitude of the 4 eV conductivity peak remains constant near  $3500/\Omega\text{cm}$ , independent of Pt content.

From electronic structure calculations for pure Ni and Pt and a  $\text{Ni}_3\text{Pt}$  ordered compound, we find that Ni, Pt, and Ni-Pt d-bands have similar energy, which explains why the 4 eV peak in the conductivity does not shift with Pt addition. Furthermore, the bandwidth of the Ni 3d bands is smaller than that of the Pt 5d bands, consistent with the increase in the broadening of the optical transitions.

This work was supported by NSF (DMR-11104934).

11:20am **EM+NS-FrM10 Ultra-Shallow Junction Formation for sub-22nm CMOS Technology and Characterization using High-resolution SIMS**, **M.J.P. Hopstaken**, **H. Wildman**, **D. Pfeiffer**, IBM T.J. Watson Research Center, **Z. Zhu**, **P. Ronsheim**, IBM Systems and Technology Group, **K.K. Chan**, **I. Lauer**, **J.S. Newbury**, **D.-G. Park**, IBM T.J. Watson Research Center

Secondary Ion Mass Spectrometry (SIMS) has shown great resilience over the last decades in keeping up with the aggressive downscaling of advanced CMOS technology. Major improvements contributing to the staying power of SIMS are lower primary ion beam energies to meet the ever more stringent depth resolution demands [1] and application of novel external standard-free calibration methods for quantification in the near-surface region [2]. Here we demonstrate state-of-the-art applications of SIMS to Ultra-Shallow Junction (USJ) formation and in-situ doped thin epitaxial layers.

We present As-USJ extension formation for nFET with junction depths below  $120 \text{ \AA}$ , obtained using low energy ion implantation and micro-second flash ( $\mu$ -flash) annealing. SIMS depth profiling employing a  $200 \text{ eV Cs}^+$  beam provides detailed information on diffusion and segregation of As at the sub-nm scale for different annealing conditions. Low energy implantation of P has been proposed as an alternative to As for the formation of Source/Drain (S/D) regions to reduce crystalline damage. This is crucially important for advanced CMOS technology based on Extremely Thin SOI or FinFET. Here, we present different analytical approaches to determine the most accurate quantification for shallow P concentration profiles in Si. Also, we have employed 3D atom probe tomography to independently determine in-depth [P] profiles for SIMS calibration purposes [3].

For pFET processes, nm-scale control of B-diffusion is instrumental to obtain highly activated and abrupt B-USJ. Here we present a novel doping strategy employing ultra-thin solid source Si:B diffusion sources—in combination with  $\mu$ -flash annealing—to form the B-USJ extensions. Presence of high [B] and minimal diffusion length necessitates use of ultra low  $\text{O}_2^+$  impact energy for accurate determination of junction depth and abruptness. Regarding S/D formation, In-Situ Boron Doped (ISBD) SiGe is an important technology element for pFET strain enhancement. Quantitative analysis of [B] in SiGe using reactive low energy  $\text{O}_2^+$  ion sputtering is complicated due to large yield variations as a function of [Ge] [4]. We present a calibration protocol based on multiple B-implanted epitaxial  $\text{Si}_{1-x}\text{Ge}_x$  standards on Si(100) with constant [Ge] ranging from 20 to 50 at.%. This approach allows for explicit correction of both SiGe sputter yield and  $\text{B}^+$  and  $\text{Ge}^+$  yield variations as function of [Ge], enabling quantitative analysis of ISBD SiGe.

[1] A. Merkulov et al., *JVST B* **28**(1) (2010) C1C48.

[2] W. Vandervorst et al., *AIP Conf. Proc.* **931**(1) (2007) 233-245.

[3] M.J.P. Hopstaken et al., *SIA*, DOI 10.1002/sia.4916 (2012).

[4] Z. Zhu et al., *SIA* **43**(1-2) (2011) 657-660.

11:40am **EM+NS-FrM11 A Deep Dive into the Liquid Fermi Sea**, **R.K. Schulze**, **J.C. Lashley**, **B. Mihaila**, **D.C. Wallace**, Los Alamos National Laboratory

We reexamine high resolution photoemission in some of the liquid metals accessible in a UHV environment. These include Ga, In, and Bi, and at a basic level, involves comparison of the DOS EDCs between the crystalline solid and liquid metal. The motivation is to gain an understanding of the fundamental differences between normal and anomalous melters. This includes a search for an understanding of the electronic contribution to the melt phase transformation. Normal melters, such as In, show a difference in liquid and crystal solid entropy at constant volume,  $\Delta S^* = 0.8 \pm 0.1 k_B/\text{atom}$ , and exhibit a volume expansion upon melting, while anomalous melters,

such as Ga and Bi, have  $\Delta S^* >> 0.8$  k<sub>B</sub>/atom, and show a volume collapse upon melting. Observed changes to the electronic structure near the Fermi energy upon crossing the solid-liquid phase boundary will be discussed.

## Graphene and Related Materials Focus Topic

Room: 13 - Session GR+EM+ET+MS+NS-FrM

### Graphene Device Physics and Applications

Moderator: A. Turchanin, University of Bielefeld, Germany

8:20am **GR+EM+ET+MS+NS-FrM1 Heterointegration of Graphene with Nano and Molecular Scale Structures for High Performance Devices, X. Duan**, University of California, Los Angeles **INVITED**

Nanoscale integration of dissimilar materials with distinct compositions, structures and properties has the potential to create a new generation of integrated systems with unique functions and/or unprecedented performance to break the boundaries of traditional technologies. In this talk, I will focus my discussion on the heterointegration of graphene with a variety of nano and molecular scale structures of designed architectures to open up exciting opportunities for nanoscale device engineering. In particular, I will discuss our recent effort in integrating graphene with a self-aligned nanowire gate to create the highest speed graphene transistors, integrating graphene with plasmonic nanostructures to create multi-color high speed photodetectors, integrating graphene with nanoscale templates for the creation of graphene nanostructures, and integrating graphene with various  $\pi$ -conjugating molecular systems for band gap engineering and molecular sensing.

9:00am **GR+EM+ET+MS+NS-FrM3 Graphene RF: From Fundamentals to Opportunities, J.S. Moon, H.-C. Seo, M. Antcliffe, S. Lin, A. Schmitz, D. Le, C. McGuire, D. Zehnder**, HRL Laboratories LLC, L.O. Nyakiti, V.D. Wheeler, R.L. Myers-Ward, C.R. Eddy, Jr., D.K. Gaskill, P.M. Campbell, Naval Research Laboratory, K.-M. Lee, P. Asbeck, UC San Diego **INVITED**

Graphene is a topic of very active research from basic science to potential applications. Various RF circuit applications are under evaluation, which include low-noise amplifiers, frequency multipliers, mixers and high-speed radiometers. Potential integration of graphene on Silicon substrates with CMOS compatibility would also benefit future RF systems. The future success of the RF circuit applications depends on vertical and lateral scaling of graphene MOSFETs to minimize parasitics and improve gate modulation efficiency in the channel. In this presentation, we highlight recent progress in graphene materials and devices. For example, with hydrogen intercalation, a graphene wafer showed an electron mobility of 2500 cm<sup>2</sup>/Vs at 6.8 x 10<sup>12</sup> cm<sup>-2</sup> carrier density, and sheet resistance of 230 ohm/square. The Ti-based ohmic contact resistance is below 100 ohm\* $\mu$ m and hysteresis in HfO<sub>2</sub>/Graphene MOSFET transfer curves are no longer concerns in RF applications. We will show graphene MOSFETs in mixer and detector applications with performances comparable to and better than the current state-of-the-art technologies. Also, we will present recent progress in graphene heterostructure based diodes with on/off ratio greater than 10<sup>6</sup>. In summary, while graphene is relatively new material, it shows a strong potential to become disruptive in RF applications.

This work was partially supported by DARPA, monitored by Dr. J. Albrecht, under SPAWAR contract number N66001-08-C-2048.

The views, opinions, and/or findings contained in this article/presentation are those of the author/presenter and should not be interpreted as representing the official views or policies, either expressed or implied, of the Defense Advanced Research Projects Agency or the Department of Defense.

[1] J. S. Moon and D. K. Gaskill, IEEE Trans. Microwave Theory and Techniques, p. 2702, 2011

9:40am **GR+EM+ET+MS+NS-FrM5 Graphene and Dielectric Integration: A Sticky Situation?, V.D. Wheeler, N.Y. Garces, L.O. Nyakiti, R.L. Myers-Ward, D.J. Meyer**, U.S. Naval Research Laboratory, A. Nath, George Mason University, C.R. Eddy, Jr., D.K. Gaskill, U.S. Naval Research Laboratory **INVITED**

Scalable high- $\kappa$  dielectric integration is needed to realize graphene-based THz transistors. Yet, the inert nature of graphene inhibits direct application of high-quality uniform atomic layer deposition (ALD) dielectrics. While several methods have rendered the surface more susceptible to ALD[1], they often degrade mobility and/or shift the Dirac voltage due to charges within the gate stack. Recently, we developed a dry chemical functionalization approach using XeF<sub>2</sub> that results in conformal, thin high- $\kappa$  ALD oxide films with a 10-25% improvement in graphene mobility[2], high

dielectric constants (HfO<sub>2</sub>=18.5, Al<sub>2</sub>O<sub>3</sub>=8.9), and small Dirac voltage shifts (HfO<sub>2</sub>=2V, Al<sub>2</sub>O<sub>3</sub>=0.1V), indicating the effectiveness of F functionalization. We will present in-depth details of our fluorination process, discuss its advantages and limitations with respect to other methods used to enhance ALD reactivity with graphene, and provide future directions for this field of study.

Fluorination of EG surfaces was performed in a Xactix X3 XeF<sub>2</sub> etcher operating in pulse mode. Results show that 15 nm pinhole-free Al<sub>2</sub>O<sub>3</sub> and HfO<sub>2</sub> films are obtained with an optimized XeF<sub>2</sub> surface treatment prior to ALD consisting of six, 20s pulses (XeF<sub>2</sub>=1 torr, N<sub>2</sub>=35 torr). This optimal treatment resulted in ~6% fluorine surface coverage, as semi-ionic C-F bonds (F1s ~687eV) only, which provided additional ALD reaction sites needed to obtain uniform oxide films. This unique semi-ionic nature of the C-F bond allows the graphene lattice to maintain planarity and minimize degradation to transport properties.

Theoretical studies suggest that the semi-ionic nature of the C-F bond is related to the graphene electron sheet carrier density ( $n_e$ ), requiring at least 10<sup>13</sup> cm<sup>-2</sup> to form[3]. To test this, EG samples with similar thickness but varying  $n_e$  (2x10<sup>12</sup>-1.3x10<sup>13</sup> cm<sup>-2</sup>) were fluorinated simultaneously using the optimal conditions above. Samples with  $n_e > 1 \times 10^{13}$  cm<sup>-2</sup> had only semi-ionic C-F bonding, but those with  $n_e < 1 \times 10^{13}$  cm<sup>-2</sup> had both covalent and semi-ionic bonding – verifying the theoretical calculations. The amount of covalent bonding increased as  $n_e$  decreased, and an increased pinhole density was seen in subsequent Al<sub>2</sub>O<sub>3</sub> films. This implies that the underlying EG properties can impact the effectiveness of this fluorination method. Yet, by adjusting the pulse conditions one can tailor this method to still obtain uniform ALD oxides on low carrier density and even p-type EG. To this end, results of our XeF<sub>2</sub> approach on p-type H<sub>2</sub> intercalated EG samples will be shown.

1. Garces, et.al. *J/ST B* **30(3)** 03D104 (2012)

2. Wheeler, et.al. *Carbon* **50** 2307 (2012)

3. Sofo, et.al. *Phys Rev B* **83(8)** 081411(R) (2011)

10:20am **GR+EM+ET+MS+NS-FrM7 Achieving Scaled Dielectrics on Graphene Using Atomic Layer Deposition, S. Jandhyala, G. Mordi, R.M. Wallace, J. Kim**, University of Texas at Dallas

In order to realize high-performance graphene-based field-effect-devices, local gating of graphene channel is one of the foremost requirements [1]. Therefore, deposition of high-quality, scalable dielectrics on graphene is required. The ability to precisely control thickness and conformally deposit materials makes atomic layer deposition (ALD) an ideal technique for achieving such dielectrics [2]. However, ALD is a surface-reaction limited process [2] and graphene, being sp<sup>2</sup> bonded, has no *out-of-plane* covalent functional groups [3] and this can cause difficulties in initiating the ALD reaction [4]. In previous studies we have shown that using a reversibly physisorbed ozone (O<sub>3</sub>) functionalization approach, we can deposit high quality ALD oxides (such as Al<sub>2</sub>O<sub>3</sub>) on graphene with thicknesses below 5 nm [5]. Further understanding regarding the interaction of O<sub>3</sub> and metal precursors with graphene is required for successfully applying the ozone process to deposit different oxides.

In this study, we will use *in-situ* electrical measurements of graphene devices inside an ALD chamber as a characterization technique in order to understand the adhesion mechanisms of oxidants (such as O<sub>3</sub> and H<sub>2</sub>O) and metal precursors (such as trimethylaluminum-TMA, titanium tetrachloride-TiCl<sub>4</sub>) on graphene surfaces. The characterization scheme used is packaged back-gated graphene-FETs which can detect the molecules adsorbed on the graphene surface. We will compare exfoliated graphene and chemical vapor deposited (CVD) graphene (which tends to have a higher number of defect sites). Using such *real-time* electrical measurements, the observed charge scattering mechanisms and the effect on mobility and doping due to the interaction of these molecules with graphene will be presented.

#### Acknowledgement

This work was funded through the South West Academy of Nanoelectronics (SWAN) program of NRI under SRC.

#### References

- [1] S. K. Banerjee, et al., Pro. of the IEEE **98** (12), pp. 2032-2046 (2010).
- [2] R. L. Puurunen, J. Appl. Phys. **97** (12), pp. 121301-121352, (2005)
- [3] A. H. Castro Neto, et al., Rev. Mod. Phys. **81** (1), pp. 109-162 (2009)
- [4] L. Liao, X. Duan, Mat. Sci. Eng. R **70** (3-6), pp. 354-370, (2010)
- [5] S. Jandhyala, et al., ACS Nano, **6** (3), pp. 2722-2730 (2012)

10:40am **GR+EM+ET+MS+NS-FrM8 Atomically-Smooth MgO Films Grown on Epitaxial Graphene by Pulsed Laser Deposition.** *S.C. Stuart, A.A. Sandin*, North Carolina State University, *O. Nayfeh, M.D. Dubey*, Army Research Laboratory, *J.E. Rowe, D.B. Dougherty*, North Carolina State University, *M.D. Ulrich*, Army Research Office

The growth of high quality insulating films on graphene is a crucial materials science task for the development of graphene-based spintronics because graphene is a potentially revolutionary material for electronic and spintronic applications. For efficient spin-injection, graphene is expected to suffer from the well known “conductivity mismatch” problem at metal-semiconductor spin electrode interfaces. The standard approach to mitigating this problem has been to grow thin, insulating tunnel barriers between the graphene and the magnetic metallic electrode to provide a spin-dependent resistance via the tunneling magnetoresistance effect. It has been demonstrated by several experiments that direct spin injection from a magnetic electrode to graphene is possible but using aluminum oxide or MgO tunnel barriers to assist injection in graphene spin-valve devices is more efficient if suitable oxide-graphene interfaces can be formed. To address this problem we have used pulsed laser deposition (PLD) to grow thin (1-1000 nm) magnesium oxide films directly on epitaxial graphene on SiC(0001). We observe very smooth film morphologies (typical rms roughness of ~0.4 nm) that are nearly independent of film thickness and conform to the substrate surface which had ~0.2 nm rms roughness. Surface roughness is less than 0.5 nm for thicknesses up to 1000 nm and is independent of deposition laser pulse energy within the range 300-700 mJ/pulse at rates of 1-50 Hz. X-ray diffraction shows predominant (111) and (100) orientations, indicating the possibility of doping the graphene by the polar (111) interface. Raman spectroscopy indicates that the graphene is not measurably damaged by magnesium oxide growth. This work shows that PLD is a good technique to produce graphene-oxide interfaces without pre-deposition of an adhesion layer. The films are free of defects or pinholes (that can be observed by atomic force microscopy) and can be grown at arbitrary thicknesses without increasing the roughness or damaging the graphene. The details and kinetics of the deposition process will be described with comparisons being made to other dielectric-on-graphene deposition approaches.

11:00am **GR+EM+ET+MS+NS-FrM9 Facile, Controllable Graphene-based P-N Junctions Using Self-Assembled Monolayers.** *J. Baltazar, H. Sojoudi, J. Kowalik, L. Tolbert, S. Graham, C.L. Henderson*, Georgia Institute of Technology

In this study we investigate the use of a self-assembled monolayer (SAM) to create a p-n junction in graphene films. Previous techniques rely on charge transfer from adsorbants or electrostatic gate/potentials. Here we demonstrate that, by successfully modifying the SiO<sub>2</sub> surface with an aminopropyltriethoxysilane (APTES) layer, and using intrinsically p-doped transferred CVD graphene films, a well-defined junction can be achieved. Field-effect transistors and p-n junction regions are fabricated prior to graphene film transfer, in order to preserve the pristine properties of the graphene. The I-V characteristic curve indicates the presence of two thermally-controllable neutrality points. This method allows a facile, controllable and low temperature fabrication of graphene p-n junctions.

11:20am **GR+EM+ET+MS+NS-FrM10 Impact of Cleaning Procedures on the Performance of Graphene-Based Field Effect Transistors.** *M. Lodge, M. Ishigami*, University of Central Florida

It is now widely accepted that surface contaminants have large effects on the performance of graphene-based field effect transistors. Various techniques are now available to clean processing residues from graphene, yet some of these techniques are chemically aggressive leaving concerns that they may damage graphene and affect the device performance. In addition, there are no consensus on the best method to produce the cleanest and, therefore, the best graphene devices.

Here, we have performed a study on the impact of various chemical treatments on the performance of field effect transistors fabricated from graphene grown using chemical vapor deposition. By measuring the impact of hydrogen-annealing, oxygen-annealing, and various solvent-based cleaning on 50 graphene field effect transistors, we generate a statistically-significant conclusion on the best cleaning technique for producing the highest performance. We will present our results along with our scanning tunneling microscopy images and Raman spectra to shed a light on the mechanism involved in each cleaning technique.

11:40am **GR+EM+ET+MS+NS-FrM11 High Efficiency Graphene Solar Cells by Chemical Doping.** *X. Miao, S. Tongay, M.K. Petterson, K. Berke, A.G. Rinzler, B.R. Appleton, A.F. Hebard*, University of Florida

We demonstrate single layer graphene/n-Si Schottky junction solar cells that under AM1.5 illumination exhibit a power conversion efficiency (PCE) of 8.6%. This performance, achieved by doping the graphene with

bis(trifluoromethanesulfonyl)amide, exceeds the native (undoped) device performance by a factor of 4.5 and is the **highest PCE** reported for graphene-based solar cells to date. Current-voltage, capacitance-voltage, and external quantum efficiency measurements show the enhancement to be due to the doping-induced shift in the graphene chemical potential that increases the graphene carrier density (decreasing the cell series resistance) and increases the cell's built-in potential (increasing the open circuit voltage) both of which improve the solar cell fill factor.

# Authors Index

**Bold page numbers indicate the presenter**

## — A —

Abbott, J.: LB+EM+GR+MN+TR-WeA3, 28  
Abdallah, L.S.: EL+TF+AS+EM+SS-TuP2, 22;  
EL+TF+BI+AS+EM+SS-MoA9, 10; EM+NS-  
FrM9, 56  
Abel, J.: EM+NS-FrM5, 55  
Abraha, P.: LB+EM+GR+MN+TR-WeA2, 28  
Acharya, A.: EM-ThP5, 52  
Adam, T.N.: EL+TF+AS+EM+SS+PS+EN+NM-  
MoM9, 2  
Adams, D.: TF+EM+SE+NS-ThM5, 40  
Adamska, L.: GR+AS+EM+NS+SS-WeA2, 26  
Addou, R.: GR+EM+NS+SS+TF-ThA7, 48  
Ahlgren, M.: TF+NS+EM-ThM11, 42  
Ahn, J.R.: GR+EM+NS+PS+SS+TF-MoM11, 5;  
GR+EM+NS+PS+SS+TF-MoM4, 4  
Ajayan, P.: GR+EM+NS+SS+TF-ThA3, 47  
Aksamija, Z.: EM+SS+AS+NS-ThM10, 33  
Akturk, A.: EM+OX-WeA9, 25  
Alexandre Diniz, J.: EM-ThP7, 52  
Alian, A.: EM+TF+OX+GR-MoA1, 10  
Alles, M.L.: EM+SS+AS+NS-ThM11, 34  
Almer, J.: TF+NS+EM-ThM11, 42  
Anderson, T.J.: EM-ThP4, 52;  
GR+EM+ET+NS+TF-MoA1, 12  
Ando, T.: EM+TF+OX+GR-MoA7, 11  
Antcliffe, M.: GR+EM+ET+MS+NS-FrM3, 57  
Antonelli, G.A.: EM-ThP10, 53  
Anwar, S.R.M.: EM+TF+OX+GR-MoA4, 10  
Appleton, B.R.: GR+EM+ET+MS+NS-FrM11, 58;  
LB+EM+GR+MN+TR-WeA7, 28  
Arenholz, E.: GR+AS+EM+MI+MN-TuM9, 18  
Argibay, N.: LB+EM+GR+MN+TR-WeA1, 28  
Arnold, M.S.: GR+AS+EM+NS+SS-WeA9, 27  
Aryal, P.: EL+TF+AS+EM+SS+PS+EN+NM-  
MoM1, 1  
Asbeck, P.: GR+EM+ET+MS+NS-FrM3, 57  
Atalay, R.: EM+TF+AS-ThA11, 47; EM+TF+AS-  
ThA9, 46; EM-ThP6, 52  
Attygalle, D.: EL+TF+AS+EM+SS+PS+EN+NM-  
MoM1, 1  
Aubry, O.: PS+EM-MoM3, 7  
Auer, M.: TF+EM+SE+NS-ThM6, 40  
Ayers, J.E.: EM+MI-ThA1, 44; EM+MI-ThA2, 44

## — B —

Baby, A.: TF+NS+EM-ThM10, 42  
Baddorf, A.P.: ET+NS+EM-ThM3, 36  
Bae, H.-B.: EM+OX-WeA11, 26  
Bahng, W.: EM-TuM10, 17  
Bakhru, H.: EM+TF+OX+GR-MoM3, 2  
Balci, S.: ET+NS+EM-ThM11, 38  
Balsano, R.: EM+NS-FrM5, 55  
Baltazar, J.: GR+EM+ET+MS+NS-FrM9, 58  
Banerjee, S.K.: EM+OX-WeA1, 25  
Barlam, D.: OX+EM+MI+NS+TF-MoM11, 6  
Barmak, K.: EM-TuA2, 19; EM-TuA7, 19  
Barraza-Lopez, S.: EM+NS-FrM5, 55  
Bartelt, N.C.: TF+EM+SS-ThA10, 50  
Barton, D.: EL+TF+AS+EM+SS+PS+EN+NM-  
MoM10, 2  
Baski, A.A.: EM+TF+AS-ThA4, 45; SS+EM-  
WeA1, 30  
Basu, D.: EM+OX-WeA1, 25  
Batzill, M.: GR+AS+EM+NS+SS-WeA8, 27;  
GR+EM+NS+SS+TF-ThA7, 48  
Baughman, W.: ET+NS+EM-ThM11, 38  
Becker, J.S.: TF+EM+SS-ThA7, 49  
Belyansky, M.P.: NM+NS+MS+EM-MoA4, 14  
Benavidez, T.: EL+TF+BI+AS+EM+SS-MoA3, 3  
Benedek, G.: EM+TF-WeM12, 24  
Bennett, B.: EM+TF+OX+GR-MoA10, 12  
Bent, S.F.: EM-TuA1, 19; SS+EM-WeA8, 30  
Berdova, M.: TF+NS+EM-ThM10, 42  
Berke, K.: GR+EM+ET+MS+NS-FrM11, 58

Bernal Ramos, K.: TF+NS+EM-ThM2, 41;  
TF+NS+EM-ThM9, 42  
Bernasconi, M.: EM+TF-WeM12, 24  
Besnier, J.-F.: EL+TF+AS+EM+SS+PS+EN+NM-  
MoM3, 1  
Beugin, V.: NM+NS+MS+EM-MoA6, 14  
Bezares, F.J.: GR+EM+ET+NS+TF-MoA1, 12  
Bhairamadgi, N.S.: TF+EM+SS-ThA4, 49  
Bhattacharyya, D.: EM+SS+AS+NS-ThM4, 33  
Bielefeld, J.: EM-TuA1, 19; GR+EM+NS+SS+TF-  
ThA1, 47  
Bielejec, E.: EM-ThP2, 52  
Bilke, L.: EM-ThP15, 54  
Bingham, N.: OX+EM+MI+NS+TF-MoM1, 5  
Bockstaller, M.R.: TC+EM+AS-WeA9, 32  
Böker, A.: TF+EM+SS-ThA9, 50  
Bolotin, K.I.: GR+EM+ET+NS+TF-MoA3, 12  
Boos, J.B.: EM+TF+OX+GR-MoA10, 12  
Boosalis, A.: LB+EM+GR+MN+TR-WeA10, 29  
Borchers, J.: OX+EM+MI+NS+TF-MoM10, 6  
Borgström, M.T.: ET+NS+EM-ThM6, 37  
Borner, K.: EM+TF-WeM5, 23  
Borsa, D.: TC+EM+AS+TF+EN-ThM2, 38  
Borst, C.: EM-ThP8, 53  
Bosch, R.: TC+EM+AS+TF+EN-ThM2, 38  
Bose, S.: OX+EM+MI+NS+TF-MoM10, 6  
Bostwick, A.: GR+EM+ET+NS+TF-MoA8, 13  
Bowman, S.R.: EM+TF+AS-ThA6, 46  
Boyce, M.C.: EM+TF-WeM11, 24  
Braunstein, P.: GR+EM+ET+NS+TF-MoA7, 13  
Breitweiser, R.: LB+EM+GR+MN+TR-WeA8, 28  
Brennan, B.: EM+TF+OX+GR-MoM5, 3; EM-  
TuM3, 16  
Brewer, J.R.: EL+TF+AS+EM+SS-TuP1, 22  
Broitman, E.: TF+NS+EM-ThM12, 43  
Brown, R.D.: EM+TF-WeM12, 24  
Bruhn, T.: GR+EM+NS+SS+TF-ThA6, 48  
Brumbach, M.T.: LB+EM+GR+MN+TR-WeA1,  
28  
Buegler, M.: EM-ThP5, 52; EM-ThP6, 52  
Buie, C.: EM+TF+OX+GR-MoA4, 10  
Butz, T.: GR+AS+EM+MI+MN-TuM9, 18

## — C —

Cabrera, W.: EM+TF+OX+GR-MoA6, 11;  
TF+NS+EM-ThM9, 42  
Caillard, L.: EL+TF+BI+AS+EM+SS-MoA2, 9;  
EM+NS-FrM3, 55  
Caldwell, J.D.: GR+EM+ET+NS+TF-MoA1, 12  
Campbell, P.: EM+NS-FrM3, 55  
Campbell, P.M.: GR+EM+ET+MS+NS-FrM3, 57  
Campi, D.: EM+TF-WeM12, 24  
Cantoro, M.: EM+TF+OX+GR-MoA1, 10  
Cao, Y.: EM-ThP1, 52  
Cartier, E.A.: EM+TF+OX+GR-MoA7, 11  
Casolo, S.: GR+AS+EM+NS+SS-WeA12, 27  
Caubet, P.: NM+NS+MS+EM-MoA6, 14  
Caymax, M.: EM+TF+OX+GR-MoA1, 10;  
LB+EM+GR+MN+TR-WeA12, 30  
Ceballos-Sanchez, O.: EM+TF+OX+GR-MoA9,  
11  
Chabal, Y.J.: EL+TF+BI+AS+EM+SS-MoA2, 9;  
EM+NS-FrM3, 55; EM+TF+OX+GR-MoA6,  
11; EM+TF-WeM4, 23; GR+AS+EM+NS+SS-  
WeA1, 26; SS+EM-WeA11, 31; SS+EM-  
WeA9, 31; TF+NS+EM-ThM2, 41;  
TF+NS+EM-ThM9, 42  
Chae, J.: GR+EM+ET+NS+TF-MoA10, 13  
Champlain, J.: EM+TF+OX+GR-MoA10, 12  
Chan, K.K.: EM+NS-FrM10, 56  
Chang, C.S.: GR+EM+ET+NS+TF-MoA6, 13  
Chang, J.P.: EM+TF+AS-ThA3, 45; TF+NS+EM-  
ThM6, 41  
Chang, M.H.: EM+SS+AS+NS-ThM12, 34  
Chang, Y.H.: EM+SS+AS+NS-ThM12, 34  
Chao, Y.C.: LB+EM+GR+MN+TR-WeA8, 28

Chapman, R.: EM+TF-WeM4, 23  
Chebiam, R.: EM-TuA12, 20  
Chen, J.: EL+TF+AS+EM+SS+PS+EN+NM-  
MoM4, 1  
Chen, W.C.: EM-ThP3, 52  
Cheng, S.-F.: GR+AS+EM+MI+MN-TuM1, 17  
Chernyak, L.: EM-ThP1, 52  
Chien, D.: EM+TF+AS-ThA3, 45  
Childress, J.R.: EM+MI-ThA8, 44  
Cho, H.K.: OX+EM+MI+NS+TF-MoM2, 6  
Cho, K.J.: GR+AS+EM+NS+SS-WeA1, 26  
Cho, T.S.: TC+EM+AS+TF+EN-ThM12, 39  
Choi, D.: EM-TuA7, 19  
Choi, J.: GR+EM+ET+NS+TF-MoA7, 13  
Choi, J.Y.: GR+EM+NS+PS+SS+TF-MoM11, 5  
Choi, K.: EM+OX-WeA9, 25; EM+TF+OX+GR-  
MoA7, 11  
Choi, S.H.: EM+OX-WeA11, 26  
Choi, Y.J.: EM-TuM4, 16  
Chu, D.: NM+NS+MS+EM-MoA2, 14  
Chuang, Y.: EM-ThM12, 36  
Chumbuni-Torres, K.: EL+TF+BI+AS+EM+SS-  
MoA3, 9  
Chun, S.H.: OX+EM+MI+NS+TF-MoM2, 6  
Churaman, W.: EM+OX-WeA9, 25  
Clark, K.: GR+EM+NS+PS+SS+TF-MoM2, 4  
Clarke, J.: EM-TuA12, 20  
Clavel, G.: TF+NS+EM-ThM9, 42  
Clendenning, S.: EM-TuA1, 19  
Cleveland, E.: EM+TF+OX+GR-MoA10, 12  
Coffey, K.R.: EM-TuA2, 19; EM-TuA7, 19  
Cohen, S.A.: EM-TuA8, 20  
Cohen, S.R.: OX+EM+MI+NS+TF-MoM11, 6  
Collazo, R.: EM+TF+AS-ThA1, 45  
Collins, R.W.: EL+TF+AS+EM+SS+PS+EN+NM-  
MoM1, 1; EL+TF+AS+EM+SS+PS+EN+NM-  
MoM4, 1  
Colón Santana, J.: GR+EM+ET+NS+TF-MoA7,  
13  
Condon, N.J.: EM+TF+AS-ThA6, 46  
Conley, J.F.: EM+OX-WeA12, 26  
Cook, K.: EL+TF+BI+AS+EM+SS-MoA10, 10  
Copel, M.W.: GR+EM+NS+PS+SS+TF-MoM8, 5  
Coraux, J.: GR+AS+EM+NS+SS-WeA10, 27  
Cortes, R.: GR+EM+NS+SS+TF-ThA2, 47  
Craft, S.: EM+TF+AS-ThA1, 45  
Creator, M.: EL+TF+AS+EM+SS+PS+EN+NM-  
MoM6, 2; TC+EM+AS+TF+EN-ThM2, 38  
Cui, Y.S.: EM+MI-ThA11, 45  
Culbertson, J.C.: GR+EM+NS+PS+SS+TF-  
MoM3, 4  
Cummings, S.P.: TF+EM+SS-ThA6, 49

## — D —

Dahal, A.: GR+AS+EM+NS+SS-WeA8, 27;  
GR+EM+NS+SS+TF-ThA7, 48  
Dähne, M.: EM+TF+AS-ThA10, 46  
Dalberth, M.J.: TF+EM+SS-ThA7, 49  
Dalmau, R.: EM+TF+AS-ThA1, 45  
Darbal, A.: EM-TuA7, 19  
Davidson, M.R.: EM-ThP14, 54  
Davis, K.O.: NM+NS+MS+EM-MoA9, 15  
Davis, R.C.: LB+EM+GR+MN+TR-WeA3, 28  
Dawahre, N.: ET+NS+EM-ThM11, 38  
De Padova, P.: GR+EM+NS+SS+TF-ThA6, 48  
Dean, C.: GR+EM+ET+NS+TF-MoA10, 13  
Dekoster, J.: EM+TF+OX+GR-MoA1, 10  
Demberger, C.: NM+NS+MS+EM-MoA9, 15  
Desplats, O.: EM+TF+OX+GR-MoA9, 11  
Detchprohm, T.: EM+TF+AS-ThA7, 46  
Dhar, N.K.: EM+OX-WeA9, 25  
Dhiman, R.: EM+SS+AS+NS-ThM3, 33  
Diebold, A.C.:  
EL+TF+AS+EM+SS+PS+EN+NM-MoM9, 2  
Dietz, N.: EM+TF+AS-ThA11, 47; EM+TF+AS-  
ThA9, 46; EM-ThP5, 52; EM-ThP6, 52

Doi, I.: EM-ThP7, 52  
 Dong, H.: EM+TF+OX+GR-MoM5, 3; EM-TuM3, 16  
 Doris, B.: EL+TF+AS+EM+SS+PS+EN+NM-MoM9, 2  
 Dornstetter, J.-C.:  
 EL+TF+AS+EM+SS+PS+EN+NM-MoM3, 1  
 Douidin, B.: GR+EM+ET+NS+TF-MoA7, 13  
 Dougherty, D.B.: GR+EM+ET+MS+NS-FrM8, 58  
 Douglas, E.A.: EM-ThP2, 52  
 Dowben, P.A.: GR+EM+ET+NS+TF-MoA7, 13  
 Downey, B.P.: EM+OX-WeA8, 25  
 Draws, J.: EM+SS+AS+NS-ThM3, 33  
 Duan, X.: GR+EM+ET+MS+NS-FrM1, 57  
 Dubey, M.D.: GR+EM+ET+MS+NS-FrM8, 58  
 Dugger, M.T.: LB+EM+GR+MN+TR-WeA1, 28  
 Dunin-Borkowski, R.E.: EM-ThM11, 36  
 Durkaya, G.: EM-ThP6, 52  
 Dussart, R.: PS+EM-MoM3, 7  
 Dussault, L.: NM+NS+MS+EM-MoA6, 14

— E —

Ealet, B.: GR+EM+NS+SS+TF-ThA6, 48  
 Ebert, P.: EM+TF+AS-ThA10, 46; EM-ThM11, 36  
 Eddy, Jr., C.R.: EM+OX-WeA8, 25; EM+TF+AS-ThA6, 46; EM+TF+OX+GR-MoM9, 3; GR+AS+EM+MI+MN-TuM1, 17; GR+EM+ET+MS+NS-FrM3, 57; GR+EM+ET+MS+NS-FrM5, 57; GR+EM+ET+NS+TF-MoA1, 12; GR+EM+NS+PS+SS+TF-MoM1, 4; GR+EM+NS+PS+SS+TF-MoM3, 4; SS+EM-WeA1, 30; TF+NS+EM-ThM1, 41  
 Eden, J.G.: PS+EM-MoM1, 7  
 Edgar, J.H.: EM+TF+OX+GR-MoM9, 3  
 Eggenspiele, D.: EM+TF-WeM11, 24  
 Eisele, H.: EM+TF+AS-ThA10, 46  
 Eizenberg, M.: LB+EM+GR+MN+TR-WeA12, 30  
 Elam, J.W.: TC+EM+AS+TF+EN-ThM6, 39  
 El-Khatib, S.: OX+EM+MI+NS+TF-MoM10, 6  
 Elliman, R.G.: LB+EM+GR+MN+TR-WeA7, 28  
 Elmquist, R.: LB+EM+GR+MN+TR-WeA10, 29  
 Emam, M.: EM-ThM4, 35  
 Endo, K.: EM-ThM1, 34  
 Enta, Y.: GR+EM+NS+PS+SS+TF-MoM10, 5  
 Esquinazi, P.: GR+AS+EM+MI+MN-TuM9, 18  
 Exarhos, A.L.: GR+AS+EM+MI+MN-TuM2, 18

— F —

Facchetti, A.: TC+EM+AS-WeA1, 31  
 Fadida, S.: LB+EM+GR+MN+TR-WeA12, 30  
 Fager, H.: TF+NS+EM-ThM12, 43  
 Feigelson, B.: GR+AS+EM+MI+MN-TuM1, 17  
 Felhofer, J.L.: EL+TF+BI+AS+EM+SS-MoA3, 9  
 Felix, V.: PS+EM-MoM3, 7  
 Ferguson, G.S.: EL+TF+BI+AS+EM+SS-MoA10, 10  
 Ferguson, I.: EM+TF+AS-ThA11, 47; EM+TF+AS-ThA9, 46; EM-ThP6, 52  
 Ferguson, J.D.: SS+EM-WeA1, 30  
 Ferreira, P.: EM-TuA7, 19  
 Figueroa, J.J.: TF+EM+SS-ThA11, 50  
 Firrincelli, A.: EM+TF+OX+GR-MoA1, 10  
 Fleetwood, D.M.: EM+SS+AS+NS-ThM11, 34  
 Flitsyan, E.: EM-ThP1, 52  
 Foussekis, M.: EM+TF+AS-ThA4, 45  
 Fowlkes, J.D.: TF+EM+SE+NS-ThM3, 40  
 França, D.: EM-ThP8, 53  
 Frank, M.M.: EM+TF+OX+GR-MoA7, 11  
 Franssila, S.: TF+NS+EM-ThM10, 42  
 Freitas, Jr., J.A.: EM+TF+AS-ThA6, 46  
 French, B.: EM-TuA9, 20; GR+EM+NS+SS+TF-ThA1, 47  
 French, M.: GR+EM+NS+SS+TF-ThA1, 47  
 Frenzer, P.: EM-ThP1, 52; EM-ThP2, 52  
 Fridmann, J.: LB+EM+GR+MN+TR-WeA7, 28  
 Fromm, F.: GR+EM+NS+PS+SS+TF-MoM10, 5  
 Fruchart, O.: GR+AS+EM+NS+SS-WeA10, 27  
 Fu, S.: TC+EM+AS-WeA9, 32  
 Fuentes-Cabrera, M.: TF+EM+SE+NS-ThM3, 40

Fukidome, H.: GR+EM+NS+PS+SS+TF-MoM10, 5

— G —

Gaddy, B.: EM+TF+AS-ThA1, 45  
 Galatage, R.V.: EM-TuM3, 16  
 Galatsis, K.: EM+SS+AS+NS-ThM11, 34  
 Gamage, S.D.: EM+TF+AS-ThA11, 47; EM+TF+AS-ThA9, 46; EM-ThP5, 52; EM-ThP6, 52  
 Ganesh, K.: EM-TuA7, 19  
 Gao, Y.: GR+EM+ET+NS+TF-MoA10, 13  
 Garces, N.Y.: EM+OX-WeA8, 25; EM+TF+OX+GR-MoM9, 3; GR+AS+EM+MI+MN-TuM1, 17; GR+EM+ET+MS+NS-FrM5, 57; GR+EM+NS+PS+SS+TF-MoM1, 4; GR+EM+NS+PS+SS+TF-MoM3, 4  
 Garcia, C.D.: EL+TF+BI+AS+EM+SS-MoA3, 9  
 Garramone, J.: EM+NS-FrM5, 55  
 Gartstein, Yu.N.: EL+TF+BI+AS+EM+SS-MoA2, 9  
 Gaskill, D.K.: GR+EM+ET+MS+NS-FrM3, 57; GR+EM+ET+MS+NS-FrM5, 57; GR+EM+ET+NS+TF-MoA1, 12; GR+EM+NS+PS+SS+TF-MoM1, 4; GR+EM+NS+PS+SS+TF-MoM3, 4  
 Gassilloud, R.: NM+NS+MS+EM-MoA6, 14  
 Gates, S.M.: EM-TuA8, 20  
 Gazquez, J.: OX+EM+MI+NS+TF-MoM10, 6  
 Geisler, H.: EM-TuA11, 20  
 Ghafoor, N.: TF+NS+EM-ThM11, 42; TF+NS+EM-ThM12, 43  
 Ghosh, S.: EM-ThM6, 35  
 Gila, B.: LB+EM+GR+MN+TR-WeA7, 28  
 Girshevitz, O.: OX+EM+MI+NS+TF-MoM11, 6  
 Gleason, K.K.: EM+SS+AS+NS-ThM4, 33; EM+TF-WeM11, 24  
 Go, D.B.: PS+EM-MoM11, 8  
 Godoy Filho, J.: EM-ThP7, 52  
 Goldman, R.S.: EM+SS+AS+NS-ThM13, 34  
 Goldsman, N.: EM+OX-WeA9, 25  
 Gong, C.: GR+AS+EM+NS+SS-WeA1, 26  
 Gotlib-Vainshtein, K.: OX+EM+MI+NS+TF-MoM11, 6  
 Govorkov, A.V.: EM-TuM9, 17  
 Gowda, M.H.: GR+AS+EM+MI+MN-TuM1, 17  
 Graham, S.: GR+EM+ET+MS+NS-FrM9, 58  
 Grampeix, H.: EM+TF+OX+GR-MoA9, 11  
 Greene, A.: EM+TF+OX+GR-MoM3, 2  
 Greene, J.E.: TF+NS+EM-ThM12, 43  
 Grigoras, K.: TF+NS+EM-ThM10, 42  
 Grill, A.: EM-TuA8, 20  
 Gu, Y.: ET+NS+EM-ThM12, 38  
 Guerrero, J.: EM+TF+OX+GR-MoA9, 11  
 Guo, J.H.: GR+EM+ET+NS+TF-MoA11, 13  
 Gupta, S.: TF+EM+SE+NS-ThM4, 40  
 Gwo, S.: EM+TF+AS-ThA10, 46

— H —

Haasch, R.T.: TC+EM+AS+TF+EN-ThM6, 39  
 Habenicht, B.: GR+AS+EM+NS+SS-WeA11, 27  
 Habermann, D.: NM+NS+MS+EM-MoA9, 15  
 Hacker, C.A.: TF+EM+SS-ThA6, 49  
 Halls, M.D.: TF+NS+EM-ThM2, 41  
 Han, S.M.: EM-ThM12, 36; EM-ThM6, 35  
 Handa, H.: GR+EM+NS+PS+SS+TF-MoM10, 5  
 Hannon, J.B.: GR+EM+NS+PS+SS+TF-MoM8, 5  
 Harada, Y.: GR+AS+EM+NS+SS-WeA12, 27  
 Harker, M.: LB+EM+GR+MN+TR-WeA3, 28  
 Hasegawa, H.: EM-TuM1, 16  
 Hashimoto, N.: EM+TF+AS-ThA12, 47  
 Hassibi, A.: EM+OX-WeA1, 25  
 Haverkamp, H.: NM+NS+MS+EM-MoA9, 15  
 He, C.: OX+EM+MI+NS+TF-MoM10, 6  
 Hebard, A.F.: GR+EM+ET+MS+NS-FrM11, 58; LB+EM+GR+MN+TR-WeA7, 28  
 Henderson, C.: EL+TF+BI+AS+EM+SS-MoA6, 9  
 Henderson, C.L.: GR+EM+ET+MS+NS-FrM9, 58  
 Herman, G.S.: TC+EM+AS+TF+EN-ThM5, 39

Herman, J.: EM-ThP8, 53  
 Hernández, S.C.: GR+EM+NS+PS+SS+TF-MoM1, 4  
 Herrera-Gomez, A.: EM+TF+OX+GR-MoA9, 11  
 Heyns, M.: EM+TF+OX+GR-MoA1, 10  
 Hicks, R.F.: PS+EM-MoM9, 8  
 Hikita, Y.: OX+EM+MI+NS+TF-MoM3, 6  
 Hines, M.: EM-ThP13, 54  
 Hinkle, C.L.: EM+TF+OX+GR-MoA4, 10; EM-TuM3, 16  
 Hite, J.K.: EM+TF+AS-ThA6, 46; SS+EM-WeA1, 30; TF+NS+EM-ThM1, 41  
 Hjort, M.: EM+MI-ThA6, 44; ET+NS+EM-ThM6, 37  
 Hoehne, R.: GR+AS+EM+MI+MN-TuM9, 18  
 Hofmann, T.: LB+EM+GR+MN+TR-WeA10, 29  
 Holloway, P.H.: EM+TF-WeM9, 23; EM-ThP14, 54  
 Hone, J.C.: GR+EM+ET+NS+TF-MoA10, 13  
 Hong, J.: TC+EM+AS+TF+EN-ThM12, 39  
 Hong, Y.-L.: EM+TF+AS-ThA10, 46  
 Hopstaken, M.J.P.: EM+NS-FrM10, 56  
 Hopwood, J.: PS+EM-MoM5, 7  
 Hordagoda, M.: OX+EM+MI+NS+TF-MoM1, 5  
 Horn, K.: GR+EM+ET+NS+TF-MoA8, 13  
 Horsfall, A.B.: GR+EM+NS+PS+SS+TF-MoM1, 4  
 Hosadurga, S.: EM-TuA8, 20  
 Hoskinson, A.: PS+EM-MoM5, 7  
 Hosono, H.: TC+EM+AS+TF+EN-ThM3, 38  
 Hossain, T.: EM+TF+OX+GR-MoM9, 3  
 Howe, B.M.: TF+NS+EM-ThM12, 43  
 Howe, J.: GR+EM+NS+PS+SS+TF-MoM3, 4  
 Hsiao, C.-N.: EM-ThP3, 52  
 Hsu, C.: ET+NS+EM-ThM12, 38  
 Hsu, C.C.: PS+EM-MoM4, 7  
 Hu, Y.C.: LB+EM+GR+MN+TR-WeA8, 28  
 Huang, E.: EM-TuA8, 20  
 Huang, L.W.: GR+EM+ET+NS+TF-MoA6, 13  
 Hughes, G.J.: EM-TuM5, 16  
 Hultman, L.: TF+NS+EM-ThM11, 42; TF+NS+EM-ThM12, 43  
 Hund, Z.M.: EM+TF-WeM12, 24  
 Hurley, P.K.: EM-TuM5, 16  
 Hussey, L.: EM+TF+AS-ThA1, 45  
 Hyde, R.H.: OX+EM+MI+NS+TF-MoM1, 5

— I —

Ianno, N.J.: EL+TF+AS+EM+SS-TuP1, 22  
 Ide, T.: GR+EM+NS+PS+SS+TF-MoM10, 5  
 Irving, D.: EM+TF+AS-ThA1, 45  
 Ishigami, M.: GR+EM+ET+MS+NS-FrM10, 58; GR+EM+ET+NS+TF-MoA2, 12  
 Ishii, S.: TF+EM+SS-ThA3, 49  
 Islam, M.F.: TC+EM+AS-WeA7, 32  
 Itoi, T.: EM+TF+AS-ThA12, 47  
 Ivanov Boudinov, H.: EM-ThP7, 52  
 Ivanova, L.: EM+TF+AS-ThA10, 46

— J —

Jaehnig, M.: GR+EM+NS+SS+TF-ThA1, 47  
 Jain, R.: EM+TF-WeM6, 23  
 James, C.D.: ET+NS+EM-ThM10, 37  
 Jandhyala, S.: GR+EM+ET+MS+NS-FrM7, 57  
 Jang, W.C.: EM+OX-WeA7, 25  
 Jensen, B.D.: LB+EM+GR+MN+TR-WeA3, 28  
 Jeon, H.T.: EM+OX-WeA7, 25  
 Jeon, H.Y.: EM+OX-WeA7, 25  
 Jezewski, C.: EM-TuA12, 20  
 Ji, S.-H.: GR+EM+NS+PS+SS+TF-MoM8, 5  
 Jiang, K.: NM+NS+MS+EM-MoA9, 15  
 Jiang, S.: EM+TF+OX+GR-MoA1, 10  
 Jiang, Y.: EM-ThM11, 36  
 Jiang, Z.: ET+NS+EM-ThM9, 37  
 Johansson, L.: EM+MI-ThA6, 44  
 Johansson, M.P.: TF+NS+EM-ThM11, 42  
 Johnson, J.W.: EM-ThP1, 52  
 Johnson, S.D.: GR+AS+EM+MI+MN-TuM1, 17  
 Jones, K.: LB+EM+GR+MN+TR-WeA3, 28  
 Joy, R.: TC+EM+AS+TF+EN-ThM2, 38  
 Jung, S.: GR+EM+ET+NS+TF-MoA10, 13

- Jung, W.: EM+OX-WeA1, 25  
 Jur, J.S.: TF+NS+EM-ThM5, 41  
 — **K** —  
 Kahng, S.-J.: EM+SS+AS+NS-ThM12, 34  
 Kalfon-Cohen, E.: OX+EM+MI+NS+TF-MoM11, 6  
 Kamimura, T.: ET+NS+EM-ThM5, 37  
 Kamineneni, V.: EM-TuA11, 20  
 Kan, H.-C.: TF+EM+SS-ThA10, 50  
 Kang, T.S.: EM-ThP1, 52; EM-ThP2, 52  
 Kanjolia, R.K.: TF+NS+EM-ThM2, 41  
 Karpov, S.Y.: EM-TuM9, 17  
 Kasouit, S.: EL+TF+AS+EM+SS+PS+EN+NM-MoM3, 1  
 Katoch, J.: GR+EM+ET+NS+TF-MoA2, 12  
 Katz, H.E.: TC+EM+AS-WeA3, 31  
 Kaufman Osborn, T.: LB+EM+GR+MN+TR-WeA11, 29  
 Kaufman-Osborn, T.: EM+TF+OX+GR-MoA3, 10  
 Kawai, Y.: GR+EM+NS+PS+SS+TF-MoM10, 5  
 Kawakami, R.: GR+AS+EM+MI+MN-TuM3, 18  
 Kawasaki, J.: EM+MI-ThA6, 44  
 Kent, T.J.: LB+EM+GR+MN+TR-WeA11, 29  
 Kessels, W.M.M.:  
 EL+TF+AS+EM+SS+PS+EN+NM-MoM6, 2;  
 TC+EM+AS+TF+EN-ThM2, 38  
 Kiantaj, K.: EM+TF+OX+GR-MoA3, 10;  
 LB+EM+GR+MN+TR-WeA11, 29  
 Kikkawa, J.M.: GR+AS+EM+MI+MN-TuM2, 18  
 Kilpi, L.: TF+NS+EM-ThM10, 42  
 Kim, B.: EM-TuA8, 20  
 Kim, D.H.: NM+NS+MS+EM-MoA8, 14  
 Kim, H.: EM+SS+AS+NS-ThM12, 34  
 Kim, H.J.: EM+OX-WeA11, 26; EM-TuM4, 16  
 Kim, H.-Y.: EM-ThP1, 52; EM-TuM10, 17  
 Kim, J.: EM+TF+OX+GR-MoM6, 3; EM-ThP1, 52; EM-TuM10, 17; GR+EM+ET+MS+NS-FrM7, 57  
 Kim, J.H.: EM-ThP12, 54  
 Kim, J.K.: EM-TuA8, 20  
 Kim, K.H.: TC+EM+AS-WeA7, 32  
 Kim, M.J.: EM+TF+OX+GR-MoA4, 10  
 Kim, P.: GR+EM+ET+NS+TF-MoA10, 13  
 Kim, S.: EM+SS+AS+NS-ThM11, 34  
 Kim, S.M.: ET+NS+EM-ThM11, 38  
 Kim, T.: ET+NS+EM-ThM3, 36  
 Kim, Y.-H.: EM+SS+AS+NS-ThM12, 34  
 King, S.: EM-TuA9, 20; GR+EM+NS+SS+TF-ThA1, 47  
 King, S.T.: EM-ThP15, 54  
 Kinoshita, T.: GR+EM+NS+PS+SS+TF-MoM10, 5  
 Kioussis, D.R.: EM-TuA8, 20  
 Kis, A.: GR+EM+NS+SS+TF-ThA10, 48  
 Klymko, N.: EM-TuA8, 20  
 Knauf, J.: TF+EM+SS-ThA9, 50  
 Knoops, H.C.M.:  
 EL+TF+AS+EM+SS+PS+EN+NM-MoM6, 2;  
 TC+EM+AS+TF+EN-ThM2, 38  
 Koenraad, P.M.: SS+EM-WeA3, 30  
 Koirala, P.: EL+TF+AS+EM+SS+PS+EN+NM-MoM4, 1  
 Kondo, T.: GR+AS+EM+NS+SS-WeA12, 27  
 Kong, L.: GR+EM+ET+NS+TF-MoA7, 13  
 Kornegay, S.M.: TF+EM+SE+NS-ThM4, 40  
 Koskinen, J.: TF+NS+EM-ThM10, 42  
 Kostov, K.: LB+EM+GR+MN+TR-WeA9, 29  
 Kotsugi, M.: GR+EM+NS+PS+SS+TF-MoM10, 5  
 Kowalik, J.: GR+EM+ET+MS+NS-FrM9, 58  
 Kozhanov, A.: EM+MI-ThA10, 44  
 Kozhukhova, E.A.: EM-TuM9, 17  
 Kravchenko, I.I.: EM-TuA2, 19  
 Krist, B.: EM-TuA12, 20  
 Krueger, B.: TC+EM+AS+TF+EN-ThM11, 39  
 Krueger, J.: EM-ThP15, 54  
 Ku, J.H.: EM-TuM4, 16  
 Kub, F.J.: EM+TF+AS-ThA6, 46;  
 GR+AS+EM+MI+MN-TuM1, 17  
 Kucukgok, B.: EM+TF+AS-ThA9, 46  
 Kuhn, M.: GR+EM+NS+SS+TF-ThA1, 47  
 Kujofsa, T.M.: EM+MI-ThA1, 44  
 Kulsreshath, M.: PS+EM-MoM3, 7  
 Kumar, A.: EL+TF+BI+AS+EM+SS-MoA8, 9;  
 PS+EM-MoM8, 7  
 Kumar, S.: EL+TF+BI+AS+EM+SS-MoA8, 9  
 Kummel, A.C.: EM+TF+OX+GR-MoA3, 10;  
 LB+EM+GR+MN+TR-WeA11, 29  
 Kung, P.: ET+NS+EM-ThM11, 38  
 Kusakabe, K.: EM+TF+AS-ThA12, 47  
 Kwon, J.: TF+NS+EM-ThM2, 41  
 Kwon, Y.H.: OX+EM+MI+NS+TF-MoM2, 6  
 — **L** —  
 LaBella, V.P.: EM+NS-FrM5, 55  
 Laboutin, O.: EM-ThP1, 52  
 Lacovig, P.: LB+EM+GR+MN+TR-WeA9, 29  
 Lahiri, J.: GR+EM+NS+SS+TF-ThA2, 47  
 Lam, K.: EM-ThM5, 35  
 Landrock, S.: EM-ThM11, 36  
 Larciprete, R.: LB+EM+GR+MN+TR-WeA9, 29  
 Lashley, J.C.: EM+NS-FrM11, 56  
 Lauer, I.: EM+NS-FrM10, 56  
 Lauhon, L.J.: ET+NS+EM-ThM1, 36  
 Laver, M.: OX+EM+MI+NS+TF-MoM10, 6  
 Lavoie, C.: EM+NS-FrM7, 56; EM+NS-FrM9, 56  
 Le Lay, G.: GR+EM+NS+SS+TF-ThA6, 48  
 Le, D.: GR+EM+ET+MS+NS-FrM3, 57;  
 GR+EM+ET+NS+TF-MoA2, 12  
 LeBeau, J.: EM+TF+AS-ThA1, 45  
 Lecordier, L.: TF+EM+SS-ThA7, 49  
 Lee, C.-M.: GR+EM+ET+NS+TF-MoA7, 13  
 Lee, C.T.: EM-ThP3, 52  
 Lee, I.: TC+EM+AS-WeA7, 32  
 Lee, J.H.: OX+EM+MI+NS+TF-MoM2, 6  
 Lee, J.S.: EM+OX-WeA7, 25; EM+TF+OX+GR-MoA3, 10  
 Lee, J.Y.: OX+EM+MI+NS+TF-MoM2, 6  
 Lee, K.-M.: GR+EM+ET+MS+NS-FrM3, 57  
 Lee, N.I.: EM-TuM4, 16  
 Lee, S.H.: EM-TuM4, 16  
 Lee, T.H.: EM-TuA8, 20  
 Lefauchaux, P.: PS+EM-MoM3, 7  
 Leggett, G.J.: TF+EM+SS-ThA1, 48  
 Leick, N.: EL+TF+AS+EM+SS+PS+EN+NM-MoM6, 2  
 Leighton, C.: OX+EM+MI+NS+TF-MoM10, 6  
 Lemaitre, M.: LB+EM+GR+MN+TR-WeA7, 28  
 Lenahan, P.: EM-TuM11, 17  
 Lenz, A.: EM+TF+AS-ThA10, 46  
 Leonhardt, D.: EM-ThM12, 36  
 Leroux, C.: NM+NS+MS+EM-MoA6, 14  
 Lewis, N.S.: EM+TF-WeM12, 24  
 Li, A.-P.: ET+NS+EM-ThM3, 36; ET+NS+EM-ThM4, 37; GR+EM+NS+PS+SS+TF-MoM2, 4  
 Li, C.: TC+EM+AS-WeA4, 32  
 Li, J.B.: TC+EM+AS-WeA4, 32  
 Li, L.J.: LB+EM+GR+MN+TR-WeA8, 28  
 Li, Q.: EM-ThM12, 36  
 Li, X.D.: ET+NS+EM-ThM4, 37  
 Li, Z.S.: EM+NS-FrM4, 55; EM+SS+AS+NS-ThM3, 33  
 Liao, Y.C.: PS+EM-MoM4, 7  
 Libera, J.A.: TC+EM+AS+TF+EN-ThM6, 39  
 LiCausi, N.: EM-TuA11, 20  
 Liddiard, S.: LB+EM+GR+MN+TR-WeA3, 28  
 Lim, D.: TF+EM+SS-ThA11, 50  
 Lim, H.J.: EM-TuM4, 16  
 Lim, W.: EM-TuM9, 17  
 Lin, C.-F.: TF+EM+SS-ThA10, 50  
 Lin, D.: LB+EM+GR+MN+TR-WeA12, 30  
 Lin, J.H.: EM-TuM5, 16  
 Lin, K.C.: LB+EM+GR+MN+TR-WeA8, 28  
 Lin, P.A.: PS+EM-MoM8, 7  
 Lin, Q.: EM-TuA10, 20  
 Lin, S.: GR+EM+ET+MS+NS-FrM3, 57  
 Lin, Y.: EM-TuA8, 20  
 Lin, Y.H.: EM+SS+AS+NS-ThM13, 34  
 Linder, B.P.: EM+TF+OX+GR-MoA7, 11  
 Linford, M.R.: TF+EM+SS-ThA8, 50  
 Liu, L.: EM-ThP1, 52; EM-ThP2, 52  
 Liu, X.: EM-TuA7, 19  
 Liu, Y.: EM-ThM1, 34; TC+EM+AS-WeA3, 31  
 Lizzit, S.: LB+EM+GR+MN+TR-WeA9, 29  
 Lo, C.-F.: EM-ThP1, 52; EM-ThP2, 52  
 Lodge, M.: GR+EM+ET+MS+NS-FrM10, 58  
 Lopinski, G.P.: EM+NS-FrM1, 55  
 Loscutoff, P.: EM-TuA1, 19  
 Lou, J.: GR+EM+NS+SS+TF-ThA3, 47  
 Lu, J.W.: EM+MI-ThA11, 45  
 Lu, L.: EM-TuM9, 17  
 Lu, N.: EM+TF+OX+GR-MoA4, 10  
 Lu, Y.W.: PS+EM-MoM4, 7  
 Lucero, A.T.: EM+TF+OX+GR-MoM6, 3  
 Lund, J.: LB+EM+GR+MN+TR-WeA3, 28  
 Luo, H.: EL+TF+BI+AS+EM+SS-MoA9, 10  
 Lyytinen, J.: TF+NS+EM-ThM10, 42  
 — **M** —  
 MacDonald, A.H.: EM+OX-WeA1, 25  
 Madaan, N.: TF+EM+SS-ThA8, 50  
 Madan, A.: EM-TuA8, 20  
 Madisetti, S.: EM+TF+OX+GR-MoM3, 2  
 Magana, S.: TF+EM+SS-ThA11, 50  
 Mahadik, N.: TF+NS+EM-ThM1, 41  
 Maidecchi, G.: EL+TF+BI+AS+EM+SS-MoA8, 9  
 Majer, M.: EM-TuA11, 20  
 Mak, T.: EM-ThM5, 35  
 Makabe, T.: PS+EM-MoM10, 8  
 Malko, A.V.: EL+TF+BI+AS+EM+SS-MoA2, 9  
 Mancheno-Posso, P.L.: EM-ThP16, 54  
 Marichy, C.: TF+NS+EM-ThM9, 42  
 Marinella, M.: ET+NS+EM-ThM10, 37  
 Marsillac, S.: EL+TF+AS+EM+SS+PS+EN+NM-MoM1, 1; EL+TF+AS+EM+SS+PS+EN+NM-MoM4, 1  
 Martin, F.: EM+TF+OX+GR-MoA9, 11  
 Martinez, E.: EM+TF+OX+GR-MoA9, 11  
 Masahara, M.: EM-ThM1, 34  
 Mastro, M.A.: EM+TF+AS-ThA6, 46; SS+EM-WeA1, 30; TF+NS+EM-ThM1, 41  
 Matsubayashi, A.: GR+AS+EM+NS+SS-WeA7, 27  
 Matsukawa, T.: EM-ThM1, 34  
 Matsumoto, K.: ET+NS+EM-ThM5, 37  
 Mau, X.: EM+OX-WeA1, 25  
 Mavrakakis, K.: EM-TuA10, 20  
 McClimon, J.B.: EM+NS-FrM6, 55  
 McGuire, C.: GR+EM+ET+MS+NS-FrM3, 57  
 McNamara, J.D.: EM+TF+AS-ThA4, 45  
 Medikonda, M.:  
 EL+TF+AS+EM+SS+PS+EN+NM-MoM9, 2  
 Medina, A.A.: EL+TF+AS+EM+SS-TuP2, 22  
 Mei, A.R.B.: TF+NS+EM-ThM12, 43  
 Melese, Y.G.: EL+TF+AS+EM+SS+PS+EN+NM-MoM6, 2  
 Melton, A.G.: EM+TF+AS-ThA11, 47;  
 EM+TF+AS-ThA9, 46  
 Meng, G.W.: ET+NS+EM-ThM4, 37  
 Menzel, D.: LB+EM+GR+MN+TR-WeA9, 29  
 Merckling, C.: EM+TF+OX+GR-MoA1, 10  
 Mewes, T.: EM+MI-ThA11, 45  
 Meyer III, H.M.: EM+TF+OX+GR-MoM9, 3  
 Meyer, D.J.: EM+OX-WeA8, 25;  
 GR+EM+ET+MS+NS-FrM5, 57  
 Meyer, J.R.: EM+TF+AS-ThA6, 46  
 Miao, X.: GR+EM+ET+MS+NS-FrM11, 58  
 Michalak, T.: EM-ThP8, 53  
 Michallon, P.: NM+NS+MS+EM-MoA6, 14  
 Michely, T.W.: GR+EM+NS+PS+SS+TF-MoM5, 5  
 Mickel, P.R.: ET+NS+EM-ThM10, 37  
 Mihaila, B.: EM+NS-FrM11, 56  
 Mikkelsen, A.: EM+MI-ThA6, 44; ET+NS+EM-ThM6, 37  
 Millunchick, J.M.: SS+EM-WeA2, 30  
 Mita, S.: EM+TF+AS-ThA1, 45  
 Miura, N.: PS+EM-MoM5, 7  
 Miyamoto, J.: LB+EM+GR+MN+TR-WeA2, 28

Miyashita, H.: GR+EM+NS+PS+SS+TF-MoM10, 5  
 Modine, N.A.: SS+EM-WeA2, 30  
 Molis, S.: EM-TuA8, 20  
 Montgomery, A.M.: TF+EM+SE+NS-ThM4, 40  
 Moody, B.: EM+TF+AS-ThA1, 45  
 Moon, J.S.: GR+EM+ET+MS+NS-FrM3, 57;  
 GR+EM+NS+PS+SS+TF-MoM1, 4  
 Moore, R.: EM+TF+OX+GR-MoM3, 2  
 Mordi, G.: GR+EM+ET+MS+NS-FrM7, 57  
 Morgen, P.: EM+NS-FrM4, 55; EM+SS+AS+NS-ThM3, 33  
 Mousa, M.B.: NM+NS+MS+EM-MoA8, 14  
 Mowll, T.: GR+EM+NS+PS+SS+TF-MoM2, 4  
 Mukherjee, D.: OX+EM+MI+NS+TF-MoM1, 5  
 Mukherjee, P.: OX+EM+MI+NS+TF-MoM1, 5  
 Murphy, C.J.: EM+SS+AS+NS-ThM9, 33  
 Muscat, A.J.: EM+TF-WeM6, 23; EM-ThP16, 54  
 Muthinti, G.R.:  
 EL+TF+AS+EM+SS+PS+EN+NM-MoM9, 2  
 Myers-Ward, R.L.: GR+EM+ET+MS+NS-FrM3, 57; GR+EM+ET+MS+NS-FrM5, 57;  
 GR+EM+ET+NS+TF-MoA1, 12;  
 GR+EM+NS+PS+SS+TF-MoM1, 4;  
 GR+EM+NS+PS+SS+TF-MoM3, 4  
 — N —  
 Nachimuthu, P.: TC+EM+AS+TF+EN-ThM5, 39  
 Nadezka, A.: LB+EM+GR+MN+TR-WeA7, 28  
 Nagaiyah, P.: EM+TF+OX+GR-MoM3, 2  
 Nagareddy, V.K.: GR+EM+NS+PS+SS+TF-MoM1, 4  
 Najmaei, S.: GR+EM+NS+SS+TF-ThA3, 47  
 Nakamura, J.: GR+AS+EM+NS+SS-WeA12, 27  
 Narayanan, S.: TC+EM+AS-WeA9, 32  
 Narayanan, V.: EM+TF+OX+GR-MoA7, 11  
 Nasir, A.N.: EM+OX-WeA12, 26  
 Nath, A.: GR+EM+ET+MS+NS-FrM5, 57;  
 GR+EM+ET+NS+TF-MoA1, 12;  
 GR+EM+NS+PS+SS+TF-MoM1, 4;  
 GR+EM+NS+PS+SS+TF-MoM3, 4  
 Nayfeh, O.: GR+EM+ET+MS+NS-FrM8, 58  
 N'Diaye, A.T.: GR+AS+EM+NS+SS-WeA10, 27  
 Nelson, C.M.: EL+TF+BI+AS+EM+SS-MoA9, 10  
 Nepal, N.: EM+TF+OX+GR-MoM9, 3;  
 GR+EM+ET+NS+TF-MoA1, 12; TF+NS+EM-ThM1, 41  
 Newbury, J.S.: EM+NS-FrM10, 56  
 Ng, A.: EM+TF-WeM6, 23  
 Nguyen, H.M.: EL+TF+BI+AS+EM+SS-MoA2, 9  
 Nichols, M.T.: EM-ThP10, 53; EM-ThP11, 53;  
 EM-TuA10, 20  
 Nishi, Y.: EM-ThP10, 53; EM-ThP11, 53  
 Novak, S.: EM+TF+OX+GR-MoM3, 2  
 Nyakiti, L.O.: GR+EM+ET+MS+NS-FrM3, 57;  
 GR+EM+ET+MS+NS-FrM5, 57;  
 GR+EM+ET+NS+TF-MoA1, 12;  
 GR+EM+NS+PS+SS+TF-MoM1, 4;  
 GR+EM+NS+PS+SS+TF-MoM3, 4  
 Nyns, L.: LB+EM+GR+MN+TR-WeA12, 30  
 — O —  
 O'Connor, S.: EM+TF+AS-ThA6, 46  
 Oden, M.: TF+NS+EM-ThM12, 43  
 Odén, M.: TF+NS+EM-ThM11, 42  
 Oh, Y.: TC+EM+AS-WeA7, 32  
 Ohkouchi, T.: GR+EM+NS+PS+SS+TF-MoM10, 5  
 Ohldag, H.: GR+AS+EM+MI+MN-TuM9, 18  
 Ohsiek, S.: EM-TuA11, 20  
 Ohuchi, F.S.: TC+EM+AS+TF+EN-ThM11, 39  
 Oktyabryskiy, S.: EM+TF+OX+GR-MoM3, 2  
 Okuda, T.: EM+TF+AS-ThA12, 47  
 Oldham, C.J.: NM+NS+MS+EM-MoA8, 14  
 O'Leary, L.E.: EM+TF-WeM12, 24  
 Oleson, B.: EM-ThP15, 54  
 Oleynik, I.I.: GR+AS+EM+MI+MN-TuM10, 18;  
 GR+AS+EM+NS+SS-WeA2, 26  
 Olmstead, M.A.: TC+EM+AS+TF+EN-ThM11, 39  
 Oshima, M.: GR+AS+EM+NS+SS-WeA12, 27

Osofsky, M.: EM+MI-ThA11, 45  
 Ostrikov, K.: TF+EM+SE+NS-ThM1, 39  
 Ouchi, S.: EM-ThM1, 34  
 Ouyang, W.: ET+NS+EM-ThM3, 36  
 Overzet, L.J.: PS+EM-MoM3, 7  
 Owen, A.G.: TF+EM+SE+NS-ThM4, 40  
 Ozcan, A.: EM+NS-FrM9, 56  
 — P —  
 Padbury, R.P.: TF+NS+EM-ThM5, 41  
 Pai, W.W.: LB+EM+GR+MN+TR-WeA8, 28  
 Paiella, R.: EM+SS+AS+NS-ThM1, 33  
 Palmstrom, C.: EM+MI-ThA6, 44  
 Palmström, C.: EM+MI-ThA10, 44  
 Pandey, A.: TC+EM+AS+TF+EN-ThM5, 39  
 Park, C.-Y.: GR+EM+NS+PS+SS+TF-MoM4, 4  
 Park, D.-G.: EM+NS-FrM10, 56  
 Park, J.G.: EM+OX-WeA7, 25  
 Park, J.-H.: GR+EM+NS+PS+SS+TF-MoM11, 5  
 Park, Y.: EM+OX-WeA11, 26  
 Parks, C.: EM-TuA8, 20  
 Parsons, G.N.: NM+NS+MS+EM-MoA8, 14  
 Patel, S.: EM+MI-ThA10, 44  
 Pearton, S.J.: EM-ThP1, 52; EM-ThP2, 52; EM-TuM9, 17  
 Peckerar, M.: EM+OX-WeA9, 25  
 Pedersen, K.: EM+NS-FrM4, 55  
 Pei, D.: EM-ThP10, 53; EM-ThP11, 53  
 Pei, L.: LB+EM+GR+MN+TR-WeA3, 28  
 Peixoto, T.: SS+EM-WeA11, 31  
 Pelissier, B.: NM+NS+MS+EM-MoA6, 14  
 Peng, W.: EM+TF-WeM4, 23  
 Perera, A.G.U.: EM+TF+AS-ThA9, 46; EM-ThP6, 52  
 Perez Medina, G.J.: GR+EM+ET+NS+TF-MoA7, 13  
 Perng, Y.-C.: EM+TF+AS-ThA3, 45  
 Perriot, R.: GR+AS+EM+MI+MN-TuM10, 18  
 Persson, O.: ET+NS+EM-ThM6, 37  
 Pesin, D.: EM+OX-WeA1, 25  
 Petersen Barbosa Lima, L.: EM-ThP7, 52  
 Petrov, I.: TF+NS+EM-ThM12, 43  
 Petterson, M.K.: GR+EM+ET+MS+NS-FrM11, 58  
 Pfeiffer, D.: EM+NS-FrM10, 56  
 Pham, C.D.: TF+NS+EM-ThM6, 41  
 Pham, H.: TC+EM+AS+TF+EN-ThM11, 39  
 Phaneuf, R.J.: TF+EM+SS-ThA10, 50  
 Piallat, F.: NM+NS+MS+EM-MoA6, 14  
 Pinna, N.: TF+NS+EM-ThM9, 42  
 Pipe, K.P.: EM+SS+AS+NS-ThM13, 34  
 Pluchery, O.: EM+NS-FrM3, 55  
 Podraza, N.J.: EL+TF+AS+EM+SS+PS+EN+NM-MoM1, 1; EL+TF+AS+EM+SS+PS+EN+NM-MoM4, 1  
 Polyakov, A.Y.: EM-TuM9, 17  
 Ponomarev, M.V.:  
 EL+TF+AS+EM+SS+PS+EN+NM-MoM6, 2;  
 TC+EM+AS+TF+EN-ThM2, 38  
 Pookpanratana, S.: TF+EM+SS-ThA6, 49  
 Porter, L.M.: TC+EM+AS-WeA9, 32  
 Potbhare, S.: EM+OX-WeA9, 25  
 Povey, I.M.: EM+TF+OX+GR-MoA6, 11  
 Pradhan, P.: EL+TF+AS+EM+SS+PS+EN+NM-MoM1, 1  
 Prasad, S.V.: LB+EM+GR+MN+TR-WeA1, 28  
 Prokes, S.M.: EM+TF+OX+GR-MoA10, 12  
 Ptschelinzew, N.: EM-ThP14, 54  
 Putkonen, M.: NM+NS+MS+EM-MoA1, 13  
 — Q —  
 Qin, S.Y.: ET+NS+EM-ThM3, 36; ET+NS+EM-ThM4, 37  
 Qin, X.: EM+TF+OX+GR-MoM5, 3  
 — R —  
 Rack, P.D.: TF+EM+SE+NS-ThM3, 40  
 Radja, A.: EL+TF+BI+AS+EM+SS-MoA2, 9  
 Rafik, A.: GR+AS+EM+NS+SS-WeA8, 27  
 Rago, P.B.: EM+MI-ThA2, 44  
 Rahman, T.S.: GR+EM+ET+NS+TF-MoA2, 12

Rajachidambaram, M.S.: TC+EM+AS+TF+EN-ThM5, 39  
 Ranjan, V.: EL+TF+AS+EM+SS+PS+EN+NM-MoM1, 1  
 Rao, M.V.: GR+EM+NS+PS+SS+TF-MoM1, 4  
 Raskin, J.-P.: EM-ThM4, 35  
 Raymond, M.: EM+NS-FrM9, 56  
 Raynaud, P.: TF+NS+EM-ThM3, 41  
 Real, M.: LB+EM+GR+MN+TR-WeA10, 29  
 Reddemann, L.: TF+EM+SS-ThA9, 50  
 Reddy, D.: EM+OX-WeA1, 25  
 Reeves, R.: TF+EM+SE+NS-ThM5, 40  
 Register, L.F.: EM+OX-WeA1, 25  
 Reihls, K.: TF+EM+SS-ThA9, 50  
 Reinke, P.: EM+NS-FrM6, 55  
 Ren, F.: EM-ThP1, 52; EM-ThP2, 52; EM-TuM9, 17; LB+EM+GR+MN+TR-WeA7, 28  
 Ren, T.: TF+EM+SS-ThA6, 49  
 Reshchikov, M.A.: EM+TF+AS-ThA4, 45  
 Resta, A.: GR+EM+NS+SS+TF-ThA6, 48  
 Restaino, D.: EM-TuA8, 20  
 Revelli, J.C.: EM-ThP4, 52  
 Reznicek, A.: EL+TF+AS+EM+SS+PS+EN+NM-MoM9, 2  
 Rice, T.: EM+TF+AS-ThA1, 45  
 Richardson, C.J.K.: TF+EM+SS-ThA10, 50  
 Richter, C.A.: TF+EM+SS-ThA6, 49  
 Rinzler, A.G.: GR+EM+ET+MS+NS-FrM11, 58  
 Ritz, E.: TC+EM+AS+TF+EN-ThM12, 39  
 Roberts, N.A.: TF+EM+SE+NS-ThM3, 30  
 Robertson, J.: EM+TF+OX+GR-MoM10, 3  
 Robinson, Z.R.: GR+EM+NS+PS+SS+TF-MoM2, 4  
 Roca i Cabarrocas, P.:  
 EL+TF+AS+EM+SS+PS+EN+NM-MoM3, 1  
 Rockett, A.: TF+NS+EM-ThM12, 43  
 Rodenhausen, K.B.: EL+TF+BI+AS+EM+SS-MoA1, 9  
 Rodgers, M.: EM-ThP8, 53  
 Rogers, J.A.: EM+SS+AS+NS-ThM5, 33  
 Rogström, L.: TF+NS+EM-ThM11, 42  
 Rohrer, G.: EM-TuA7, 19  
 Romriell, N.R.: TF+EM+SS-ThA8, 50  
 Ronkainen, H.: TF+NS+EM-ThM10, 42  
 Ronsheim, P.: EM+NS-FrM10, 56  
 Roodenko, K.: EL+TF+BI+AS+EM+SS-MoA2, 9  
 Rosa, L.: GR+EM+ET+NS+TF-MoA7, 13  
 Ross, F.M.: GR+EM+NS+PS+SS+TF-MoM8, 5  
 Rotenberg, E.: GR+EM+ET+NS+TF-MoA8, 13  
 Rougemaille, N.: GR+AS+EM+NS+SS-WeA10, 27  
 Routaboul, L.: GR+EM+ET+NS+TF-MoA7, 13  
 Rowe, J.E.: GR+EM+ET+MS+NS-FrM8, 58  
 Rozen, J.: EM+TF+OX+GR-MoA7, 11  
 Rumbach, P.: PS+EM-MoM11, 8  
 Ruppalt, L.: EM+TF+OX+GR-MoA10, 12  
 Ruzic, D.N.: TC+EM+AS+TF+EN-ThM12, 39  
 Ryan, E.T.: EM-TuA11, 20; EM-TuA8, 20  
 — S —  
 Sabitova, A.: EM+TF+AS-ThA10, 46  
 Safron, N.: GR+AS+EM+NS+SS-WeA9, 27  
 Sahalov, H.: EM+NS-FrM6, 55  
 Sakurai, M.: GR+AS+EM+NS+SS-WeA12, 27  
 Saly, M.J.: TF+NS+EM-ThM2, 41  
 Samaraweera, R.L.: EM+TF+AS-ThA11, 47;  
 EM+TF+AS-ThA9, 46  
 Samuelson, L.: ET+NS+EM-ThM6, 37  
 Sandin, A.A.: GR+EM+ET+MS+NS-FrM8, 58  
 Sankaran, R.M.: PS+EM-MoM11, 8; PS+EM-MoM8, 7  
 Sardela, M.: TF+NS+EM-ThM12, 43  
 Sarkar, A.: EL+TF+AS+EM+SS-TuP1, 22  
 Schaaflhausen, S.: EM+TF+AS-ThA10, 46  
 Schäfer, S.: EM+MI-ThA11, 45  
 Schlaf, R.: TF+EM+SS-ThA11, 50  
 Schlessner, R.: EM+TF+AS-ThA1, 45  
 Schmid, A.K.: GR+AS+EM+NS+SS-WeA10, 27  
 Schmidt, D.: EL+TF+BI+AS+EM+SS-MoA1, 9  
 Schmitt, J.: OX+EM+MI+NS+TF-MoM10, 6

- Schmitz, A.: GR+EM+ET+MS+NS-FrM3, 57  
 Schoenfeld, W.V.: NM+NS+MS+EM-MoA9, 15  
 Schrimpf, R.D.: EM+SS+AS+NS-ThM11, 34  
 Schubert, E.: EL+TF+BI+AS+EM+SS-MoA1, 9  
 Schubert, M.: EL+TF+BI+AS+EM+SS-MoA1, 9;  
 LB+EM+GR+MN+TR-WeA10, 29  
 Schultz, B.D.: EM+MI-ThA10, 44; EM+MI-ThA6, 44  
 Schulze, R.K.: EM+NS-FrM11, 56  
 Schwaederle, L.: PS+EM-MoM3, 7  
 Schwartz, C.: EM-ThP1, 52  
 Seitz, O.: EL+TF+BI+AS+EM+SS-MoA2, 9;  
 EM+NS-FrM3, 55; EM+TF-WeM4, 23  
 Semidey-Flecha, L.: GR+AS+EM+NS+SS-  
 WeA11, 27  
 Senevirathna, M.K.L.: EM+TF+AS-ThA11, 47;  
 EM+TF+AS-ThA9, 46; EM-ThP6, 52  
 Seo, H.-C.: GR+EM+ET+MS+NS-FrM3, 57  
 Seyller, Th.: GR+EM+ET+NS+TF-MoA8, 13;  
 GR+EM+NS+PS+SS+TF-MoM10, 5  
 Sharma, K.: TC+EM+AS+TF+EN-ThM2, 38  
 Sharma, M.: OX+EM+MI+NS+TF-MoM10, 6  
 Shen, G.: ET+NS+EM-ThM11, 38  
 Shepard, K.L.: GR+EM+ET+NS+TF-MoA10, 13  
 Shi, Z.: EM+TF-WeM5, 23  
 Shih, C.: ET+NS+EM-ThM3, 36  
 Shikano, T.: GR+AS+EM+NS+SS-WeA12, 27  
 Shin, H.: GR+EM+NS+PS+SS+TF-MoM4, 4  
 Shin, H.-J.: GR+EM+NS+PS+SS+TF-MoM11, 5  
 Shin, Y.J.: EM-TuM10, 17  
 Shkel, Y.: EM-ThP11, 53  
 Shohet, J.L.: EM-ThP10, 53; EM-ThP11, 53; EM-  
 ThP9, 53; EM-TuA10, 20  
 Shojaei, B.: EM+MI-ThA6, 44  
 Sholl, D.: GR+AS+EM+NS+SS-WeA11, 27  
 Shong, B.: SS+EM-WeA8, 30  
 Sibener, S.J.: EM+TF-WeM12, 24  
 Silva, A.: EM+NS-FrM4, 55  
 Sinha, H.: EM-ThP9, 53  
 Sinno, T.: EM-ThM12, 36  
 Siringhaus, H.: TC+EM+AS+TF+EN-ThM9, 39  
 Sitar, Z.: EM+TF+AS-ThA1, 45  
 Smirnov, N.B.: EM-TuM9, 17  
 Sodeman, I.: EM+OX-WeA1, 25  
 Sojoudi, H.: GR+EM+ET+MS+NS-FrM9, 58  
 Song, E.B.: EM+SS+AS+NS-ThM11, 34  
 Song, I.: GR+EM+NS+PS+SS+TF-MoM4, 4  
 Soudi, A.: ET+NS+EM-ThM12, 38  
 Sozias, S.: PS+EM-MoM3, 7  
 Speck, J.: EM-ThM9, 35  
 Spemann, D.: GR+AS+EM+MI+MN-TuM9, 18  
 Spies, M.: EL+TF+BI+AS+EM+SS-MoA9, 10  
 Srikanth, H.: OX+EM+MI+NS+TF-MoM1, 5  
 Steele, B.: GR+AS+EM+MI+MN-TuM10, 18  
 Stroschio, J.A.: GR+EM+ET+NS+TF-MoA10, 13  
 Stuart, S.C.: GR+EM+ET+MS+NS-FrM8, 58  
 Sugl, H.: TF+EM+SE+NS-ThM4, 40  
 Su, L.: EM-ThP6, 52  
 Suemitsu, M.: GR+EM+NS+PS+SS+TF-MoM10, 5  
 Sukenik, C.N.: OX+EM+MI+NS+TF-MoM11, 6  
 Sun, T.: EM-TuA7, 19  
 Sun, Z.: EM-TuA8, 20  
 Sundaram, G.: TF+EM+SS-ThA7, 49  
 Sutter, E.: GR+EM+NS+SS+TF-ThA2, 47  
 Sutter, P.W.: GR+AS+EM+NS+SS-WeA8, 27;  
 GR+EM+NS+SS+TF-ThA2, 47  
 Suzuki, T.: GR+AS+EM+NS+SS-WeA12, 27  
 Sykes, C.H.: EM+SS+AS+NS-ThM9, 33  
 Synowicki, R.A.:  
 EL+TF+AS+EM+SS+PS+EN+NM-MoM5, 1  
 — **T** —  
 Tan, X.: EL+TF+AS+EM+SS+PS+EN+NM-  
 MoM4, 1  
 Tantarini, G.F.: GR+AS+EM+NS+SS-WeA12, 27  
 Tawalbeh, T.: EM+NS-FrM9, 56  
 ten Elshof, A.: EL+TF+BI+AS+EM+SS-MoA8, 9  
 Teng, D.: GR+AS+EM+NS+SS-WeA11, 27  
 Tennyson, E.: EM-ThP15, 54  
 Teplyakov, A.V.: SS+EM-WeA12, 31  
 Thevuthasan, S.: TC+EM+AS+TF+EN-ThM5, 39  
 Thissen, P.: SS+EM-WeA11, 31  
 Thomas, J.C.: SS+EM-WeA2, 30  
 Thoms, B.: EM-ThP5, 52  
 Tillocher, T.: PS+EM-MoM3, 7  
 Timm, R.: EM+MI-ThA6, 44; ET+NS+EM-ThM6, 37  
 Tiwald, T.E.: EL+TF+BI+AS+EM+SS-MoA1, 9  
 Tokei, Z.: EM-TuA3, 19  
 Tokranov, V.: EM+TF+OX+GR-MoM3, 2  
 Tolbert, L.: GR+EM+ET+MS+NS-FrM9, 58  
 Tompkins, H.G.:  
 EL+TF+AS+EM+SS+PS+EN+NM-MoM8, 2  
 Toney, M.F.: EM-TuA2, 19; EM-TuA7, 19  
 Tongay, S.: GR+EM+ET+MS+NS-FrM11, 58;  
 LB+EM+GR+MN+TR-WeA7, 28  
 Torija, M.: OX+EM+MI+NS+TF-MoM10, 6  
 Trioni, M.L.: GR+AS+EM+NS+SS-WeA12, 27  
 Tromp, R.M.: GR+EM+NS+PS+SS+TF-MoM8, 5  
 Tsai, J.H.: PS+EM-MoM4, 7  
 Turk, M.E.: GR+AS+EM+MI+MN-TuM2, 18  
 Tuscano, J.A.: TF+EM+SS-ThA8, 50  
 Tweedy, J.: EM+TF+AS-ThA1, 45  
 Twigg, M.E.: EM+TF+AS-ThA6, 46  
 Tyagi, P.: GR+EM+NS+PS+SS+TF-MoM2, 4  
 Tyliczszak, T.: GR+AS+EM+MI+MN-TuM9, 18  
 Tzeng, Y.R.: LB+EM+GR+MN+TR-WeA8, 28  
 — **U** —  
 Ulrich, M.D.: GR+EM+ET+MS+NS-FrM8, 58  
 Ungureneanu, M.: GR+AS+EM+MI+MN-TuM9, 18  
 Urban, F.K.: EL+TF+AS+EM+SS+PS+EN+NM-  
 MoM10, 2  
 Ushigome, D.: GR+AS+EM+NS+SS-WeA12, 27  
 — **V** —  
 Vallée, C.: NM+NS+MS+EM-MoA6, 14  
 van de Loo, B.W.H.:  
 EL+TF+AS+EM+SS+PS+EN+NM-MoM6, 2  
 Van der Ven, A.: SS+EM-WeA2, 30  
 Van Elshocht, S.: LB+EM+GR+MN+TR-WeA12, 30  
 Van Derslice, J.: EL+TF+BI+AS+EM+SS-MoA1, 9  
 Van Fleet, R.: LB+EM+GR+MN+TR-WeA3, 28  
 Varela, M.: OX+EM+MI+NS+TF-MoM10, 6  
 Vasiliev, I.V.: EM+NS-FrM9, 56  
 Velden, M.: TC+EM+AS+TF+EN-ThM2, 38  
 Venkatachalam, D.K.: LB+EM+GR+MN+TR-  
 WeA7, 28  
 Ventrice, Jr., C.A.: GR+EM+NS+PS+SS+TF-  
 MoM2, 4  
 Vilayrganapathy, S.: TC+EM+AS+TF+EN-  
 ThM5, 39  
 Virwani, K.: EM-TuA8, 20  
 Vogel, E.M.: EM+TF-WeM4, 23; EM-TuM3, 16  
 Vogt, P.: GR+EM+NS+SS+TF-ThA6, 48  
 Vora, P.M.: GR+AS+EM+MI+MN-TuM2, 18  
 Vo-Van, C.: GR+AS+EM+NS+SS-WeA10, 27  
 Vurgaftman, I.: EM+TF+AS-ThA6, 46  
 — **W** —  
 Walker, A.V.: EM+TF-WeM5, 23  
 Wallace, D.C.: EM+NS-FrM11, 56  
 Wallace, R.M.: EM+TF+OX+GR-MoM1, 2;  
 EM+TF+OX+GR-MoM5, 3; EM-TuM3, 16;  
 GR+AS+EM+NS+SS-WeA1, 26;  
 GR+EM+ET+MS+NS-FrM7, 57  
 Walrath, J.C.: EM+SS+AS+NS-ThM13, 34  
 Walsh, L.A.: EM-TuM5, 16  
 Walter, A.: GR+EM+ET+NS+TF-MoA8, 13  
 Walton, S.G.: GR+EM+NS+PS+SS+TF-MoM1, 4  
 Wang, E.G.: EM-ThM11, 36  
 Wang, K.L.: EM+SS+AS+NS-ThM11, 34  
 Wang, L.: GR+EM+ET+NS+TF-MoA10, 13  
 Wang, X.: LB+EM+GR+MN+TR-WeA7, 28  
 Warren, A.P.: EM-TuA2, 19; EM-TuA7, 19  
 Watkins, J.: NM+NS+MS+EM-MoA10, 15  
 Weber, J.W.: EL+TF+AS+EM+SS+PS+EN+NM-  
 MoM6, 2  
 Wei, D.: EM+TF+OX+GR-MoM9, 3  
 Wei, S.-H.: TC+EM+AS-WeA4, 32  
 Weisheit, M.: EM-TuA11, 20  
 Weitering, H.: ET+NS+EM-ThM3, 36  
 Wetzel, C.: EM+TF+AS-ThA7, 46  
 Wheeler, V.D.: EM+OX-WeA8, 25;  
 GR+EM+ET+MS+NS-FrM3, 57;  
 GR+EM+ET+MS+NS-FrM5, 57;  
 GR+EM+ET+NS+TF-MoA1, 12;  
 GR+EM+NS+PS+SS+TF-MoM1, 4;  
 GR+EM+NS+PS+SS+TF-MoM3, 4  
 White, E.: EM+TF-WeM6, 23  
 Wilbert, D.S.: ET+NS+EM-ThM11, 38  
 Wildman, H.: EM+NS-FrM10, 56  
 Williams, T.S.: PS+EM-MoM9, 8  
 Witanachchi, S.: OX+EM+MI+NS+TF-MoM1, 5  
 Witzke, M.: PS+EM-MoM11, 8  
 Woicik, J.C.: EM-TuM5, 16  
 Wolf, S.A.: EM+MI-ThA11, 45  
 Wormeester, H.: EL+TF+BI+AS+EM+SS-MoA8, 9  
 Wu, C.: PS+EM-MoM5, 7  
 Wu, K.H.: EM-ThM11, 36  
 Wu, R.: ET+NS+EM-ThM3, 36  
 Wu, Y.: TF+EM+SE+NS-ThM3, 40  
 Wu, Y.L.: TC+EM+AS+TF+EN-ThM12, 39  
 — **X** —  
 Xiao, Z.: EM-ThP13, 54  
 Xie, J.: EM+TF+AS-ThA1, 45  
 Xing, G.: EM+OX-WeA3, 25  
 Xu, Y.: EL+TF+BI+AS+EM+SS-MoA9, 10;  
 GR+AS+EM+NS+SS-WeA11, 27  
 Xue, A.: PS+EM-MoM8, 7  
 Xue, J.: EM+TF-WeM9, 23  
 — **Y** —  
 Yagisawa, T.: PS+EM-MoM10, 8  
 Yague, J.L.: EM+TF-WeM11, 24  
 Yakimov, M.: EM+TF+OX+GR-MoM3, 2  
 Yakobson: GR+EM+NS+SS+TF-ThA8, 48  
 Yang, J.: EM+TF-WeM5, 23; PS+EM-MoM9, 8  
 Yang, Y.J.: PS+EM-MoM4, 7  
 Yanguas-Gil, A.: TC+EM+AS+TF+EN-ThM6, 39  
 Yao, B.: EM-TuA7, 19  
 Yekache, K.: EM+TF+OX+GR-MoA9, 11  
 Ye, D.: TF+EM+SE+NS-ThM6, 40  
 Yeh, P.: PS+EM-MoM9, 8  
 Yesilkoya, F.: EM+OX-WeA9, 25  
 Yin, J.: EM+TF-WeM11, 24  
 Yoo, H.: EM-TuA12, 20  
 Yoon, K.H.: EM-ThP12, 54  
 Yoshikawa, A.: EM+TF+AS-ThA12, 47  
 Yoshimura, T.: TF+EM+SS-ThA3, 49  
 Young, A.: GR+EM+ET+NS+TF-MoA10, 13  
 Yu, H.: PS+EM-MoM9, 8  
 — **Z** —  
 Zandvliet, H.J.W.: EL+TF+BI+AS+EM+SS-  
 MoA8, 9  
 Zapotok, D.W.: EM+OX-WeA8, 25  
 Zappe, M.: LB+EM+GR+MN+TR-WeA3, 28  
 Zehnder, D.: GR+EM+ET+MS+NS-FrM3, 57  
 Zhakhovsky, V.: GR+AS+EM+MI+MN-TuM10, 18  
 Zhan, Y.: GR+EM+NS+SS+TF-ThA3, 47  
 Zhang, B.: TC+EM+AS-WeA3, 31  
 Zhang, C.X.: EM+SS+AS+NS-ThM11, 34  
 Zhang, E.X.: EM+SS+AS+NS-ThM11, 34  
 Zhang, L.: GR+EM+ET+NS+TF-MoA11, 13  
 Zhang, Y.: ET+NS+EM-ThM3, 36  
 Zhao, Y.: GR+EM+ET+NS+TF-MoA10, 13  
 Zharnikov, M.: EM+TF-WeM1, 23  
 Zheng, H.: EM-ThP10, 53  
 Zheng, X.: TC+EM+AS+TF+EN-ThM11, 39  
 Zhernokletov, D.M.: EM-TuM3, 16  
 Zhitenev, N.B.: GR+EM+ET+NS+TF-MoA10, 13  
 Zhou, H.: EM-TuA1, 19  
 Zhou, R.: EM+TF-WeM9, 23

Zhu, J.F.: GR+EM+ET+NS+TF-MoA11, 13  
Zhu, Z.: EM+NS-FrM10, 56

Zollner, S.: EL+TF+AS+EM+SS-TuP2, 22;  
EL+TF+BI+AS+EM+SS-MoA9, 10; EM+NS-  
FrM9, 56  
Zufelt, K.: LB+EM+GR+MN+TR-WeA3, 28

Zuilhof, H.: EM+TF-WeM3, 23; TF+EM+SS-  
ThA4, 49  
Zunft, H.: NM+NS+MS+EM-MoA9, 15